Low-energy electron-induced decomposition of bimetallic and silicon-containing FEBID precursors: $HFeCo_3(CO)_{12}$, $H_2FeRu_3(CO)_{13}$, $SiC_5H_{10}Cl_2$, SiC_5H_{12} and $Si_3C_3H_{12}$

Ragesh Kumar T. Puthiyaveettil

Faculty of Physical Sciences
School of Engineering and Natural Sciences
University of Iceland
2017

Low-energy electron-induced decomposition of bimetallic and silicon-containing FEBID precursors: $HFeCo_3(CO)_{12}$, $H_2FeRu_3(CO)_{13}$, $SiC_5H_{10}Cl_2$, SiC_5H_{12} and $Si_3C_3H_{12}$

Ragesh Kumar T. Puthiyaveettil

Dissertation submitted in partial fulfillment of a
Philosophiae Doctor degree in Chemistry (Physical Chemistry)

Advisor
Prof. Oddur Ingólfsson

PhD Committee
Prof. D. Howard Fairbrother
Dr. Cornelis W. Hagen

Opponents
Dr. Lionel Amiaud, University Paris-Sud, France
Dr. Janina Kopyra, Siedlce University, Poland

Faculty of Physical Sciences
School of Engineering and Natural Sciences
University of Iceland
Reykjavik, December 2017

Low-energy electron-induced decomposition of bimetallic and silicon-containing FEBID precursors: $HFeCo_3(CO)_{12}$, $H_2FeRu_3(CO)_{13}$, $SiC_5H_{10}Cl_2$, SiC_5H_{12} and $Si_3C_3H_{12}$
Dissertation submitted in partial fulfillment of a *Philosophiae Doctor* degree in Chemistry (Physical Chemistry)

Faculty of Physical Sciences
School of Engineering and Natural Sciences
University of Iceland
Dunhaga 3
107, Reykjavik
Iceland

Telephone: 525-4000

Bibliographic information:
Ragesh Kumar T. Puthiyaveettil, 2017, *Low-energy electron-induced decomposition of bimetallic and silicon-containing FEBID precursors: $HFeCo_3(CO)_{12}$, $H_2FeRu_3(CO)_{13}$, $SiC_5H_{10}Cl_2$, SiC_5H_{12} and $Si_3C_3H_{12}$*, PhD dissertation, Faculty of Physical Sciences
School of Engineering and Natural Sciences, University of Iceland, 262 pp.

ISBN 978-9935-9320-4-4

Printing: Háskolaprent ehf., Fálkagötu 2, 107 Reykjavik
Reykjavik, Iceland, December 2017

Abstract

Focused electron beam induced deposition (FEBID) is a direct-write 3D nanofabrication technique, which works on the principle of electron-induced molecular decomposition. In FEBID, a high-energy focused electron beam dissociates the precursor molecules adsorbed on a substrate into volatile and non-volatile species. The volatile species can be pumped away from the substrate by vacuum pumps and the non-volatile species will be deposited on top of the substrate. Although FEBID is a potentially useful 3-D direct write nanofabrication technique, it still faces some critical challenges such as deposit impurity and lateral broadening of deposited structures. These challenges are mainly due to the spatial distribution of secondary electrons (SEs, electrons with energy < 50 eV) outside the focal point of the primary electron beam and the incomplete electron-induced decomposition of precursor molecules. Several dissociation mechanisms are active in the low-energy SE energy range: dissociative electron attachment (DEA), dissociative ionization (DI), dipolar dissociation (DD) and neutral dissociation (ND). In particular, DEA and DI have been shown to be relevant to the deposition of several FEBID precursors. Understanding electron interactions with precursor molecules in this low-energy SEs range can therefore aid in addressing the challenges facing FEBID. One potential approach to realize this is combining gas phase and surface studies of FEBID precursor molecules.

In gas phase studies, an electron beam of variable energy (0 - 80 eV) is crossed with an effusive molecular beam of FEBID precursor molecules under single electron-molecule collision conditions, and the subsequently formed ionic species are detected using a quadrupole mass spectrometer. In surface studies, FEBID precursor molecules are adsorbed onto a cold substrate (at -120 ^{0}C) under ultrahigh vacuum (UHV) conditions and irradiated with a broad beam of electrons (energy ~500 eV) from a flood gun. Different changes occur in the adsorbed precursor film due to electron-induced reactions can be monitored using X-ray photoelectron spectrometry (XPS), while the species desorbed from the film can be detected using a Mass spectrometer (MS) attached to the UHV chamber.

This thesis focuses on gas phase and surface studies of the bimetallic precursor molecules $HFeCo_3(CO)_{12}$ and $H_2FeRu_3(CO)_{13}$. The bimetallic nanostructures have many applications mainly in the semiconductor industry. The conventional method to fabricate bimetallic nanostructures in FEBID is mixing two different metal centered precursor molecules using a dual or multichannel gas injection system. However, this method has difficulties in reproducing the exact deposited structure and there is only limited control over the composition of the deposits. These difficulties in FEBID can be overcome by using bimetallic precursor molecules like $HFeCo_3(CO)_{12}$ and $H_2FeRu_3(CO)_{13}$. Although these are both bimetallic and structurally similar precur-

sor molecules, their performance in FEBID is significantly different. This different behavior of $HFeCo_3(CO)_{12}$ and $H_2FeRu_3(CO)_{13}$ in FEBID motivated us to conduct gas phase and surface studies of their electron-induced dissociation behavior. Gas phase studies presented in this thesis mainly contain DEA and DI of $HFeCo_3(CO)_{12}$ and $H_2FeRu_3(CO)_{13}$. Gas phase studies also included quantum chemical calculations to identify most probable electron attachment fragmentation channels in $HFeCo_3(CO)_{12}$ and $H_2FeRu_3(CO)_{13}$. The surface study part mostly discussed the electron induced bond breaking reactions of surface adsorbed $HFeCo_3(CO)_{12}$ and $H_2FeRu_3(CO)_{13}$. The observations made from gas phase and surface study are used in this thesis to discuss why these two bimetallic precursor molecules behaved differently in FEBID reactions.

Furthermore, in this thesis, the gas phase study of trisilacyclohexane (TSCH) and the FEBID study of TSCH, dichlorosilacyclohexane (DCSCH) and silacyclohexane (SCH) are discussed in relation to their different behaviour towards DEA and DI. The precursor molecules SCH and TSCH are completely inert to DEA within the sensitivity of our experimental set up, however DCSCH is active to DEA and all these precursor molecules are active to DI. How the inert behaviour of SCH towards DEA compared to DCSCH reflects in the electron beam induced deposition of these precursor molecules will be discussed in this thesis. The questions like 'does this inert behaviour of SCH compared to DCSH influence significantly to the electron induced growth dynamics of these precursor molecules?, comparatively more silicon content in the TSCH precursor will have any advantage in FEBID?' will be addressed in this thesis.

Útdráttur

Örprentun með skörpum rafeindageisla (e. Focused Electron Beam Induced Deposition, FEBID) er aðferð sem nota má til að prenta þrívíða strúktúra á yfirborð með rafeindahvötuðu niðurbroti svokallaðra forverasameinda. Það eru þó enn þónokkrar hindranir sem standa ı vegi fyrir notkun FEBID, þar á meðal óhreinindi í útfellingum og og breikkun þeirra. Þessar hindranir má að stúru leyti rekja til dreifingar lágorkurafeinda (rafeinda með hreyfiorku undir 50 eV) út fyrir brennipunkt rafeindageislans og ófullkomið niðurbrot á forverasameindunum. Nokkrar rafeindadrifnar niðurbrotsleiðir eru mögulegar á lágorkusviðinu: rjúfandi rafeindarálagning (Dissociative Electron Attchment, DEA), rjúfandi jónun (e. Dissociative Ionization, DI), tvískautssundrun (Dipolar Dissociation, DD) og hlutlaus sundrun (e. Neutral Dissociation, ND). Við hagnýtingu á FEBID getur vitneskja um hvörf drifin af lágorkurafeindum skipt sköpum. Ein möguleg nálgun við rannsóknir á þessum ferlum er samtvinnaðar mælingar á forverasamendum í gasfasa og á yfirborðum.

Tilraunir í gasfasa eru svokallaðar þvergeislatilraunir þar sem rafeindageisli (hreyfiorka rafeindanna er 0-80 eV) og sameindageisli mætast undir réttu horni. Þessar mælingar eru gerðar við lágan þrýsting, sem tryggir að hver sameind víxlverkar einungis við eina rafeind. Jónir sem myndast við þessa víxlverkan eru greindar með massagreini. Í yfirborðsmælingum aðsogast forverasameindir á kalt yfirborð (við 153 K) við mjög lágan þrýsting og eru síðan geislaðar með breiðum rafeindageisla (~500 eV). Þær breytingar sem eiga sér stað á efnunum á yfirborðinu eru reyndar með Röntgen ljósröfunarmæli (X-ray Photoelectron Spectrometer, XPS) og þau efni sem losna frá yfirborðinu eru mæld með massagreini.

Í thessari ritgerð er sjónum beint að gasfasa- og yfirborðsmælingum á forverasameindunum $HFeCo_3(CO)_{12}$ and $H_2FeRu_3(CO)_{13}$. thó báðar sameindirnar séu tvímálmar, með svipaða uppbyggingu og lögun, hefur reynslan af þeim í FEBID verið gjörólík. Því er samanburður milli þeirra í gasfasa- og yfirborðsmælingum áhugaverður. Gasfasatilraunirnar sem hér eru kynntar eru aðallega DEA og DI á $HFeCo_3(CO)_{12}$ and $H_2FeRu_3(CO)_{13}$. Að auki voru skammtafræðilegir útreikningar á sameindunum framkvæmdir til að meta líklegustu niðurbrotsleiðir. Yfirborðsmælingarnar voru síðan notaðar til að athuga hvaða áhrif yfirborðið hefur tengjarof á sameindunum. Niðurstöður mælinganna sýna hvers vegna þessar tvær sameindir eru svo ólíkar í FEBID.

Að auki eru FEBID mælingar á trisilacyclohexane (TSCH), dichlorosilacyclohexane (DCSCH) og silacyclohexane (SCH) og niðurbrot þeirra í DEA og DI borið saman. Forverasameindirnar SCH og TSCH sýna ekkert niðurbrot í DEA en DCSCH sýnir talsvert niðurbrot. Allar sameindirnar brotna niður við DI. Athyglinni er beint að spurningum eins og "hefur óhvarfgirni TSCH m.t.t. DEA samanborið við DCSH áhrif á FEBID?ǫg "Hefur aukið kísilsinnihaldi í TSCH einhver áhrif í FEBID?".

Dedication

To my wife and parents.

Contents

List of Figures

List of Tables

List of Publications

Publications included in the thesis

Article 1: Ragesh Kumar T P, Sven Barth, Ragnar Bjornsson and Oddur Ingólfsson.
Structure and energetics in dissociative electron attachment to $HFeCo_3(CO)_{12}$.
The European Physical Journal D, **70** 163 (2016)

Article 2: Ragesh Kumar T P, Ragnar Bjornsson, Sven Barth and Oddur Ingólfsson.
Formation and decay of negative ion states up to 11 eV above the ionization energy of the nanofabrication precursor $HFeCo_3(CO)_{12}$.
Chemical Science, **8** 5949-5952 (2017)

Article 3: Ragesh Kumar T P, Ilyas Unlu, Sven Barth, Oddur Ingólfsson and D. Howard Fairbrother.
Electron Induced Surface Reactions of $HFeCo_3(CO)_{12}$, a Bimetallic Precursor for Focused Electron Beam Induced Deposition (FEBID)
Submitted to The Journal of Physical Chemistry C, 2017

Article 4: Ragesh Kumar T P, Paul Weirich, Lukas Hrachowina, Marc Hanefeld, Ragnar Bjornsson, Helgi Rafn Hrodmarsson, Sven Barth, D. Howard Fairbrother, Michael Huth and Oddur Ingólfsson.
Electron Interactions with the heteronuclear carbonyl precursor $H_2FeRu_3(CO)_{13}$: from fundamental gas phase and surface science studies to focused electron beam induced deposition
Submitted to Beilstein journal of nanotechnology, 2017

Article 5: Ragesh Kumar T P, Sangeetha Hari, Krishna K Damodaran, Oddur Ingólfsson and Cornelis W. Hagen.
Electron beam induced deposition of silacyclohexane and dichlorosilacyclohexane; the role of dissociative ionization and dissociative electron attachment in the deposition process
Beilstein Journal of Nanotechnology, **8** 2376-2388 (2017)

Article 6: Ragesh Kumar T P, Sangeetha Hari, Oddur Ingólfsson and Cornelis W. Hagen.
Gas phase study and focused electron beam induced deposition of 1,3,5-trisilacyclohexane
Manuscript in preparation, 2017

Publications not included in the thesis

Article 1: Rachel M. Thorman, Ragesh Kumar T P, D. Howard Fairbrother and Oddur Ingólfsson.
The role of low-energy electrons in focused electron beam induced deposition: four case studies of representative precursors .
Beilstein journal of nanotechnology, **06** 1904 (2015)

Article 2: Ragesh Kumar T P, Benedikt Ómarsson, Stefán þ. Kristinsson and Oddur Ingólfsson.
Dissociative electron attachment to bromotrifluoromethane.
International Journal of Mass Spectrometry, **387** 78 (2015)

Article 3: Ragesh Kumar T P, B. Brynjarsson, Benedikt Ómarsson, D. Jones, M. Hoshino, H. Tanaka, M. J. Brunger, P. Limão-Vieira and Oddur Ingólfsson.
Negative ion formation through dissociative electron attachment to the group IV tetrachlorides: Carbon tetrachloride, silicon tetrachloride and germanium tetrachloride.
Submitted to International Journal of Mass Spectrometry, (2017)

Abbreviations

STM	Scanning Tunneling microscope
TEM	Transmission electron microscope
AFM	Atomic Force Microscope
FEBID	Focused electron beam induced deposition
SEM	Scanning electron microscope
SEs	Secondary electrons
BSE	backscattered electrons
DEA	dissociative electron attachment
DI	dissociative ionization
ND	neutral dissociation
DD	dipolar dissociation
TNI	transient negative ion
CVD	chemical vapour deposition
ALD	atomic layer deposition
UHV	ultrahigh vacuum
XPS	X-ray photoelectron spectrometer
MS	mass spectrometry
GIS	gas injection system
PCVD	photochemical vapor deposition
DCSCH	dichlorosilacyclohexane
SCH	silacyclohexane
TSCH	trisilacyclohexane
EBL	electron beam lithography
UVL	ultraviolet lithography
EUV	extreme ultraviolet lithography
IVR	intramolecular vibrational energy redistribution

Acknowledgments

First of all, I would like to thank my PhD supervisor Prof. Oddur Ingólfsson for giving me this wonderful opportunity. I am also very grateful for his kind, moral and scientific support that has been given for the last 4 years.

I would like to also thank the University of Iceland Research Fund for funding my PhD project. Additionally, I would like to thank the COST action CM1301 (CELINA) for funding 4 short term scientific missions (STSMs), which were very helpful for finishing my PhD project.

Of course, I could not complete my PhD work without the help of many good people. I would like to thank our former group members Dr. Benedikt Ómarsson and Dr. Frímann Haukur Ómarsson for teaching me the instruments and theory behind this project, as well as for their guidance provided at the beginning of my PhD study. I would also like to thank other former group members: Birkir, Baldur, Stefán, Ines and many more, for their help. I would like to thank our present group member Dr. Rachel Thorman for special assistance in editing all my documents, valuable feedback and all other support provided during my entire PhD life. I would like to thank the other present group members: Reza, Maicol and Ali, for all their help. I would like to give a special thanks to Dr. Ragnar Björnsson for teaching me how to do the quantum chemical calculations, as well as for his support and guidance with both the computations and with editing most of my manuscripts. I would also like to thank all the administrators and other people working in the Science Institute for all their support and help, especially Dr. Subham Saha for helping me in all the paperwork that was required during my visa processing. I would like to give a very special thanks to Dr. Helgi Rafn Hróðmarsson for his patience in reading my entire thesis and valuable corrections. Dr. Sven Barth has provided two lovely compounds - $HFeCo_3(CO)_{12}$ and $H_2FeRu_3(CO)_{13}$ - for my PhD study, so thank you very much, Sven. I would also like to thank Dr. Sven Barth for all his assistance and support in the writing of my manuscripts.

I would like to give a special thanks to Dr. Krishna Kumar Damodaran and Dr. Sreekala for considering me like a family member and all kind of help provided during my entire stay in Iceland.

There are many people helped me during my STSM visits. For my STSM visit to TU Delft in the Netherlands, I would like to thank Dr. Cornelis W Hagen for his constant support, hospitality and guidance provided to complete my STSM project, as well as for being on my PhD committee. I would also like to thank all the group members in the charged particle optics group at TU Delft, especially Dr. Sangeetha Hari, Marijke and Joesy for all their support and help during my stay in TU Delft.

For my STSM visit to Johns Hopkins University in Baltimore, USA, I would like to thank Prof. Howard Fairbrother for all the guidance, support and hospitality that

was necessary to complete my STSM project. I would also like to thank his special assistance in editing my manuscripts as well as being on my PhD committee. I would like to thank all the members in Fairbrother group especially Dr. Ilyas Unlu, Michael and Dr. Julie Spencer for all the support and help.

I would like to thank Dr. Lionel Amiaud, University Paris-Sud, France and Dr. Janina Kopyra, Siedlce University, Poland for taking the role of opponents in my doctoral defence.

My parents have always given me special care and love, and I would like to give a special thanks to them. I would also like to thank all my other family members, especially Malu and Kannan, for their love and support. I would like to give a very special thanks to my sweet wife Anju Viswanath (Chakku) for constant love, special care, encouragement and support.

Finally, I would like to thank all my friends especially Vivek, Abhijith, Shibin, Jobish, Rahul, Jithu, Shebi, Sucharitha, Midhun, Arnar and Dipankar for all valuable input, support and encouragement.

1 Introduction

A famous talk titled "There is plenty of room at the bottom" given by American physicist Richard Feynman at the annual meeting of the American Physical Society at California Institute of Technology (Caltech) [1] in 1959 is considered to be the starting point of nanotechnology. The word "nanotechnology" itself was first used by Norio Taniguchi [2] in 1974 to describe semiconductor processes such as thin film deposition, ion beam milling etc. (The word "nano" originates from the Greek word "nanos" which means "dwarf".) The field of nanotechnology started developing by the invention of two sophisticated tools, namely the Scanning Tunneling microscope (STM) and Atomic Force Microscope (AFM), respectively. The STM was invented by IBM researchers Gerd Binnig and Heinrich Rohrer in 1981. The AFM was invented by Gerd Binnig, Calvin Quate and Christoph Gerber in 1986. The word nanotechnology can be applied for creating and manipulating matter at nanometer scale (usually from one to a few hundred nanometers). After the invention of the STM, one example of manipulating matter at the nanoscale was an experiment carried out by Donald M. Eigler and Erhard Schweinzer in 1989 at IBM [3]. In that landmark experiment, using an STM, they dragged 35 xenon atoms one at a time on top of a nickel substrate to spell out the company's name (IBM). Another example which shows the potential of controlling matter at nanometer scale is the recent experiment conducted by researchers at Stanford University (SU), in which they were able to encode 35 bits of information per electron using an STM [4]. When matter is reduced down to below 100 nm, its physical and chemical properties can change dramatically [5]. We can utilise these changes for different purposes and exploit them for different applications. Many of which are beneficial for society. Today, we cannot even think of a world without nanotechnology. It has influenced the lifestyle of humanity in a significant way. Nanotechnology has promising applications in areas such as medicine and health care, materials and manufacturing, nanoelectronics, data storage, energy, biotechnology, information technology etc. Further, there are thousands of nanostructures in nature and we have only started identifying those after development of nanotechnology tools like the STM and the AFM. A perfect example of natural nanostructures are the gecko's feet [6, 7]. The adhesive force in the gecko's feet is due to the hundreds of nanostructures present in its setae [7] or foot hairs.

There are two main approaches to the fabrication of nanostructures; top-down and bottom-up. The difference between them is in how the nanostructures are fabricated. In the top-down approach, nanostructures are fabricated from bigger objects by breaking them down using different lithography techniques. In the bottom-up approach, complex nanostructures are fabricated by assembling single atoms and molecules using different methods. In the general case of nanolithography, a desired structural pattern will be transferred to the substrates using different lithographic techniques based on electron

beams [8], ion beams [9], UV-rays [10], X-rays [11, 12], EUV [13] etc. Recently, proton beams have been used to transfer nanostructure arrays into a substrate. This technique has the advantage of less secondary electron production in the substrate compared to electron beams [14, 15]. In nanolithography techniques, it is required to process the wafer layer either through subtractive or additive methods. In the subtractive method, desired patterns are transferred to a substrate by localized removal of non-functional material. In the additive method, on the other hand, the desired structures are transferred to a substrate by locally treating the specific area. All those nanolithography techniques have both advantages and disadvantages. For example, optical lithography, in comparison with electron and ion lithographic techniques, has less resolution [16]. In contrast, electron and ion lithographic techniques have less speed [9]. In the modern semiconductor industry, optical lithography remains the preferred choice for electronic chip manufacturing because of its relatively high speed and suitability for mass production. Although nanofabrication techniques based on top down approach are still dominant in the semiconductor industry, they have limitations. For example, they can only make nanostructures on planar substrates, they rely on photoresists and there are number of processing steps to transfer specific structure into substrates [17]. In contrast, the bottom up approach doesn't have any complications with resist layers and can be used to make nanostructures on top of almost any substrate, irrespective to its geometry [18]. Focused electron beam induced deposition (FEBID) is such a bottom-up approach nanofabrication technique based on electron beam induced molecular dissociation.

In FEBID, a focused high energy electron beam dissociates precursor molecule adsorbed on a substrates surface, into volatile and non-volatile fragments [18, 19]. The volatile fragments can be pumped out and the non-volatile fragments will deposit on top of the substrate and grow nanostructures. The ultimate chemical composition, size and other parameters of FEBID deposits depends on many factors, including electron-precursor molecule interactions, electron-substrate interactions, and substrate-precursor molecule interactions [19]. The most important factor is the electron-precursor molecule interactions. When a high energy primary electron (PE) beam is focused onto a substrate, a large number of secondary electrons (SE) and backscattered electrons (BSEs) will be produced due to the inelastic and elastic scattering of PEs. The SEs have a characteristic energy distribution within which different reactions with the precursor molecules may take place, which in turn complicates the FEBID process. Furthermore, the electron-precursor molecule interaction region is not confined to the focal point of the PE beam, but rather it depends on the radial electron flux distribution of the SEs and BSEs produced by interactions of the PE beam with the substrate. The calculated radial distribution of SEs and BSEs emitted by the interaction of zero diameter 3 keV PEs with a silicon substrate is in the order of 100 nm [18]. Monte Carlo simulations [20–22] as well as experiments [23, 24] showed that the lateral size of the deposited structures in FEBID is significantly higher than the probe size of PE beam. Many studies [25–31] attributed this lateral broadening to dissociation of precursor molecules by the interaction of SEs and BSEs that are emitted outside the focal point of PEs The lateral broadening of structures fabricated in FEBID is one of the main challenges in FEBID. More detailed description of the FEBID process is given in chapter 2. In the scattered electron energy range, there are different distinct dissociation mechanisms active, by

which precursor molecules dissociate. These dissociation mechanisms are dissociative electron attachment (DEA), dissociative ionization (DI), neutral dissociation (ND) and dipolar dissociation (DD) [32–36]. In DEA, an electron attaches to the molecule and forms a transient negative ion (TNI), the TNI dissociates into negative ion fragments and one or more neutral fragments. DEA is mainly active below the ionization energy of the molecule, generally in the energy range 0 to 10 eV, and by far most efficient close to 0 eV. Dissociative ionization proceeds through electron impact ionization of the molecule, the ionized molecule dissociates into a positive ion fragment and one or more neutral fragments. It is mainly active above the ionization energy of the molecule and it can be very extensive over higher energies. Neutral dissociation and DD proceeds through electronic excitation of the molecule. In ND, the electronically excited molecule dissociates into neutral fragments, that may be in their ground state or vibrationally or electronically excited. In the case of DD, the electronically excited molecule dissociates into a positive and negative ion fragments. Both ND and DD can be observed above the first excitation energy of the molecule (generally above 6 to 10 eV), and can be extensive even above 100 eVs. Detailed description of electron-precursor molecule interaction and different dissociation mechanisms are provided in chapter 3.

In addition to lateral broadening of deposited structures in FEBID, low-energy SEs and BSEs can cause incomplete decomposition of the precursor molecule, which ultimately leads to impurities in the FEBID deposit. For e.g. the reported Pt content of deposits created from $MeCpPtMe_3$ in FEBID is generally <20% [37–39] whereby the impurity is mostly through co-deposition of carbon. The investigation of electron induced dissociation of [37–39] through gas phase and surface study by S. Engmann *et al*. [26] and J. D. Wnuk *et al*. [40], respectively showed that the reason for the carbon impurities in the deposit is incomplete dissociation of ligands from $MeCpPtMe_3$. The principal reason for the organic contamination in FEBID nanostructures are rooted in their incomplete electron induced fragmentation. Almost all of the commonly used FEBID precursor molecules are initially designed for chemical vapour deposition (CVD) and atomic layer deposition (ALD), both of which work on the basis of thermal decomposition. The physics behind FEBID, however, are based on electron induced precursor dissociation. In order to address the challenges in FEBID, it is thus necessary to understand the interaction of electrons with FEBID precursor molecules, and eventually use that knowledge for the design of more suitable precursors.

Molecular level information on electron induced fragmentation of FEBID precursor molecules cannot be obtained from a typical FEBID experiment. The effective method to understand the molecular fragmentation reactions in FEBID is to combine gas phase and surface science studies [32]. In the gas phase studies, a low energy electron beam with well-defined electron energy (resolution ~100 to 120 meV) crosses with an effusive beam of FEBID precursor molecules inside a vacuum chamber. The ionic fragments produced by the electron-molecule collisions are monitored in dependence of the electron incident energy using a quadrupole mass spectrometer. More experimental details of gas phase studies can be found in chapter 4. Since the gas phase studies of FEBID precursor molecules are performed under single electron-molecule collision conditions they do not necessarily reflect all possible electron induced reaction paths of these precursor molecules in FEBID where reactions take place on a surface. This may be addressed with ultrahigh vacuum (UHV) surface science studies. In UHV

surface science studies, precursor molecules adsorb onto a cooled clean substrate and are subsequently exposed to a flux of electrons with energy ~500 eV. The changes in the stoichiometry of the adsorbed precursor molecules, due to electron interactions, can be monitored in situ using X-ray photoelectron spectrometry (XPS) and the gas phase species desorbing from the surface can be monitored using mass spectrometry (MS). A detailed experimental description of the surface science studies can be found in chapter 4.

There have been many gas phase and surface science studies conducted to understand the fundamental physics and chemistry behind the fragmentation of FEBID precursor molecules. The first gas phase study of a FEBID precursor molecule was conducted by S Engmann *et al*. [25, 29]. In their study, they measured the absolute DEA and DI cross sections for the FEBID precursor molecule $Co(CO)_3NO$. The first surface science study to elucidate the electron induced bond breaking reaction of a FEBID precursor molecule was carried out by J. D. Wnuk *et al*. [40]. The precursor molecule selected for their surface study was $MeCpPtMe_3$. During the initial electron induced dissociation of $MeCpPtMe_3$, the C/Pt ratio was reduced by 11% of its initial value which means that the electron irradiated film had ~11% platinum and 89% carbon. The 11% decrease in carbon corresponds to loss of 1 carbon from the parent $MeCpPtMe_3$ precursor molecule. The single carbon loss was attributed to breaking of one Pt-Me bond through electron attachment dissociation of $MeCpPtMe_3$. The analysis of the $MeCpPtMe_3$ stoichiometric change in these experiments was consistent with deposits created from $MeCpPtMe_3$ having only 10-20% platinum content [18, 39, 41]. Other gas phase and surface studies related to relevant FEBID precursor molecules can be found in a recent review by Thorman *et al*. [32]. Although these gas phase and surface science studies improved the understanding of FEBID processes, more combined gas phase and surface science studies are required to get better insight of the FEBID process.

The current work focussed on the combined gas phase and surface science study of bimetallic FEBID precursor molecules, namely $HFeCo_3(CO)_{12}$ and $H_2FeRu_3(CO)_{13}$. Both precursor molecules have been used in FEBID to fabricate bimetallic nanostructures. $HFeCo_3(CO)_{12}$ was the first bimetallic precursor molecule used in FEBID to fabricate bimetallic nanostructures. The use of bimetallic precursor molecules to fabricate alloy nanostructures through FEBID is a recent development [42]. Usually in FEBID, alloy nanostructures have been fabricated through co-depositing different metals from two separate homo-metallic precursor molecules using a dual or multichannel gas injection system (GIS). An example can be found in ref. [43], where F. Porrati *et al*. fabricated CoPt nanostructures by co-depositing Co and Pt simultaneously from the FEBID precursor molecules $Co_2(CO)_8$ and $MeCpPtMe_3$ using a dual GIS. However, with this approach to fabricating bimetallic nanostructures, it is difficult to get good control over the deposition of bimetallic nanostructures and the reproducibility has proven to be limited. So far, the metal content of bimetallic nanostructures fabricated with this approach have not gone above 60% [44]. These can be improved by using heteronuclear bimetallic FEBID precursor molecules and F. Porrati *et al*. used this technique in FEBID for the first time to fabricate FeCo magnetic alloy nanostructures from $HFeCo_3(CO)_{12}$ [45]. Although this precursor molecule was initially designed for CVD [46], the performance of $HFeCo_3(CO)_{12}$ in FEBID was very good. The nanostructures fabricated with $HFeCo_3(CO)_{12}$ in FEBID showed metal content >80% [45].

Based on the electric transport measurement, the deposited FeCo nanostructures showed a resistivity of 43 $\mu\Omega$cm at room temperature. Although this resistivity was higher than the resistivity of bulk Fe and Co [47], it was much lower than the resistivity reported for Fe and Co nanostructures fabricated using the FEBID technique [47]. The ferromagnetic property of deposited FeCo nanostructures was confirmed from Hall magneometric measurement on 50 nm x 250 nm FeCo nanobars. Because of the ferromagnetic nature of FeCo nanostructures, these nanostructures could be used to build magnetic data storage devices. Furhermore, new physics of 3D nanomagnetism can be studied efficiently using magnetic alloy nanostructures fabricated with FEBID [48]. Similar to the $HFeCo_3(CO)_{12}$ precursor, the $H_2FeRu_3(CO)_{13}$ precursor molecule was also initially designed for CVD and both precursor molecules give very good film deposition with accumulated organic impurities only <5% in CVD. However, the performance of $H_2FeRu_3(CO)_{13}$ precursor molecule in FEBID was not as good as $HFeCo_3(CO)_{12}$ precursor molecules. The nanostructures fabricated from $H_2FeRu_3(CO)_{13}$ show only <30% metal content [49] and also the Ru/Fe ratio shows variation from the initial value of 3. Based on the gas phase, surface science data and the quantum chemical calculation obtained for $HFeCo_3(CO)_{12}$ and $H_2FeRu_3(CO)_{13}$, the very significant difference in the performance of these precursors in FEBID is discussed in chapter 5.

In addition to the gas phase and surface science studies of $HFeCo_3(CO)_{12}$ and $H_2FeRu_3(CO)_{13}$, the electron beam induced deposition of dichlorosilacyclohexane (DCSCH), silacyclohexane (SCH) are also discussed in this thesis, specifically with respect to the role of DEA and DI in FEBID. Here DCSCH and SCH were chosen to study the role of DEA and DI in electron beam induced deposition, as in gas phase studies DCSCH was found to be sensitive to both DEA and DI, while SCH was inert to DEA but sensitive to DI. This means that the reaction of low-energy SEs with these precursor molecules during the FEBID process might be different and that will be reflected in the deposited structures. As a result, one should expect more lateral broadening and growth rate in the nanostructures fabricated with DCSCH compared to that of SCH. In order to study this, a series of nanopillars were deposited on a silicon substrate using these two precursor molecules. The pillar height, pillar base diameter, pillar volume, pillar cone formation and deposits composition was compared for these precursor molecules to obtain information on the role of DEA and DI in the deposition process. The effect of the SEs was further studied through systematic assessment of the broadening of the deposited pillar when pillars are grown in close proximity to each other (proximity effect). Finally similar FEBID experiments were conducted with and trisilacyclohexane (TSCH) in comparison with SCH and DCSCH and as a potential SiC source based on it's stoichiometric C:Si ratio. Observations made from these experiments will be discussed in chapter 5.

2 Focused electron beam induced deposition (FEBID)

Focused electron beam induced deposition (FEBID) is a resistless direct writing 3D nanofabrication technique that works on the basis of electron induced molecule dissociation. It has received considerable attention in the last few years as a powerful nanoscale manipulation tool. In FEBID, a high energy focused electron beam decomposes the precursor molecules adsorbed on the substrate surface into volatile and non-volatile fragments. The volatile fragments can be pumped out and the non-volatile fragments deposit on top of a substrate and grow as nanostructures [18, 19]. The starting point of FEBID was the observation made by Stewart *et al*. [50] in 1934 during his electron and ion beam bombardment experiments. In his experiments, he noted the formation of an insulating film on top of a substrate's surface irradiated by the electron beam. He attributed the insulated film formed on the surface to polymerization of organic vapors in the vacuum chamber by electron bombardment [50]. Other researchers also observed similar film formation inside an electron microscope [51–53]. They considered it as unwanted contamination deposited inside the electron microscope and reported it as a disadvantage for using the apparatus. A. E. Ennos *et al*. [54] later discovered that the real reason behind this contamination is electron induced dissociation of residual organic molecules, adsorbed on the electron bombarded surface. The deposited contamination was formed by the interaction of electron beams with residual organic molecules, which remains as a problem in all forms of electron microscopes. Only in the 1960's, researchers realized the applicability of this deposition process as a potential technique for fabricating desired nanostructures [55, 56]. After realizing the potential capability of FEBID, researchers tried to apply this technique to deposit functional materials like metals, semiconductors, dielectrics etc. Baker *et al*. was the first one who used this technique intentionally for depositing metallic thin films using organometallic precursor molecules like tetrabutyltin, tetramethyltin and tetraethyllead [56]. In the 1970's, FEBID had already shown its potential to fabricating sub100 nm metal structures and make patterned arrays [57,58]. At this stage, the FEBID technique had proved its potential to fabricate "nano" structures. Nowadays, FEBID can be used to fabricate different structures with sizes even less than 1 nm [59]. In the 1980's, different precursor molecules like $AuCl_3$, $Fe(CO)_5$, $Cr(C_6H_6)_2$, $Cr(CO)_6$, WF_6, $W(CO)_6$, $Os_3(CO)_{12}$, $Ru_3(CO)_{12}$, Si_2H_6 were introduced into FEBID systems with the intention to study deposits in hope of providing information about deposition of various functional materials and fabricating different structures like free standing rods [60]. In the 1990s, researchers started applying FEBID for different applications like fabricating tips for STM [61, 62], AFM [63], repairing lithography masks [64], creating metal depositions for field emitter arrays [62], and nanofabrication of solid

state Fresnel lenses [65]. In the following years, a considerable number of studies have focused on the FEBID processes (electron-substrate interactions, electron-precursor molecule interactions, substrate-precursor molecule interactions, to be explained in section 2.2). For example, in 2002, N. Silvis-Cividjian *et al.* modelled nanopillar growth in FEBID using Monte Carlo simulations for the first time and studied the role of SEs in the spatial growth of a FEBID pillars [20]. Other similar simulation studies can be found in Refs. [21, 66, 67]. Several gas phase experiments are conducted to study the electron and FEBID precursor molecule interactions (more details and literatures can be found in chapter 3). The interactions of electrons with FEBID precursor molecules adsorbed on the surface are most studied by the D. H Fairbrother's group at Johns Hopkins University [30, 31, 40, 68–74]. Some other groups have also performed similar surface studies related to different FEBID precursor molecules [36, 75–78]. For deeper insight into the many facets of the FEBID process and its fundamental aspects the reader is referred to the reviews [18, 19, 32, 79, 80].

2.1 FEBID system

Usually FEBID is performed in a scanning electron microscope (SEM) with a gas injection system (GIS) attached to it. Fig. 2.1 shows a schematic of a typical FEBID system. FEBID system mainly consists of a vacuum chamber, field emission gun (FEG) and gas injection system (GIS).

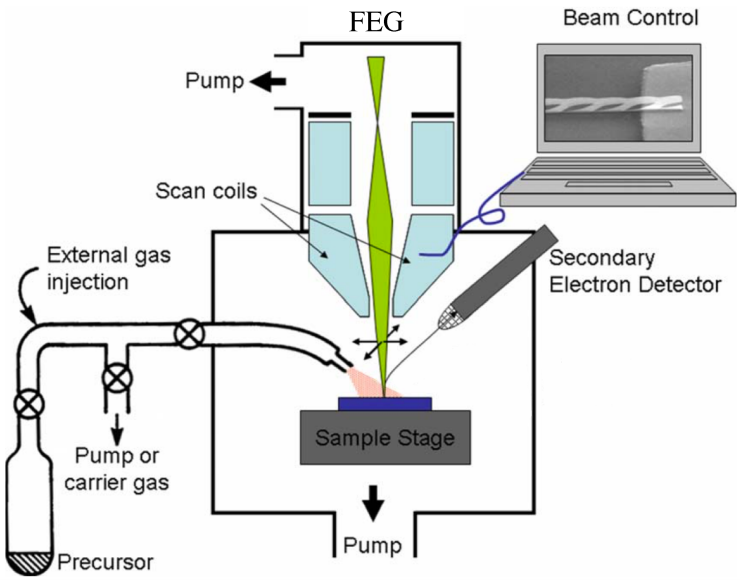

Figure 2.1. Schematic of FEBID system, reproduced with permission from ref [18], Copyright (2008) American Vacuum Society.

2.1.1 Focused electron beam

The electron beams available in SEM and TEM, are generally used in FEBID. Electron beams in SEM are widely used for FEBID because the instrument is simpler, cheaper and more easily accessible compared to STM and TEM. The important electron beam parameters that have influence on the quality (like resolution) of deposits are (i) the energy of the electron beam, (ii) the electron beam diameter, and (iii) the electron current density [18]. The electron energy in the SEM can generally vary in the range from 1 to 30 keV. With increasing the electron energy, generally the spatial resolution of fabricated structures increases mainly due to the reduction in the spatial distribution of scattered SEs [81, 82]. The minimum achievable electron beam size with increasing electron energy is ~1 nm [18]. The increase in electron current during FEBID will lead to an increase in the height of deposited pillar structures if it is within the electron current limited regime [19] (in electron current limited regime, there will be sufficient number of precursor molecules but limited electron flux and the electron flux determines the growth). The details of other electron beam parameters, which may have influence in FEBID can be found e.g. in Refs. [18, 19].

2.1.2 Gas injection system (GIS)

Fig. 2.2 shows a schematic of a typical gas injection system (GIS) used in FEBID. Desired FEBID precursor molecules can be loaded into the crucible as shown in Fig. 2.2. The needle at the end of the GIS is brought in close proximity to the focal point of the focused primary electron beam and hence, high local concentration of FEBID precursors is achieved in the substrate region where electron beam induced deposition takes place. The amount of FEBID precursor flow through a GIS needle is usually controlled by changing the temperature of the crucible which contains the FEBID precursor molecules.

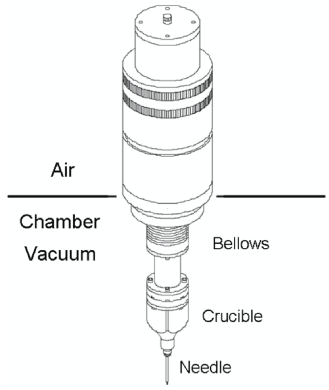

Figure 2.2. A schematic of a typical gas injection system used for FEBID, reprinted with permission from [83], Copyright (2010) IOP Publishing Ltd.

2.1.3 Precursor molecules

The ultimate product formed in FEBID is mostly determined by the nature of the precursor molecules. A typical FEBID precursor molecule is composed of two types of elements/ions. The first types are the elements which deposits on the surface and grows as structures by electron induced reactions. The second types are the elements which allow the transport of the first type into the FEBID system. The first type can be metals, semiconductors or metal alloys etc. The second type of elements are ligands. During electron beam induced reactions in FEBID, an ideal precursor dissociates completely and forms deposits with no trace of associated ligands. However, that is not the case in most FEBID processes, where an incomplete electron induced precursor dissociation commonly leads to impurities in the deposit. Most of the precursor molecules used in FEBID are initially designed for CVD, which works on the basis of thermal dissociation. Although FEBID has some similarities to CVD, the fundamental working principle of FEBID is electron induced dissociation, which is principally different from the thermal decomposition in CVD.

There are certain criteria that a precursor molecule should fulfill to be used in FEBID. One criteria is the precursor stability. FEBID precursor molecules should be stable at room temperature. Depending upon the storage time, container material and temperature variation, some precursor molecules may decompose. The precursor molecules should be volatile enough to get into the FEBID system. Volatility of precursor molecules is an important property which determines the amount of precursor molecules flown into a FEBID system. Importantly, the precursor molecules should also have high electron induced dissociation cross sections so that during FEBID processes most of the ligands in the precursor molecule are removed by the interacting electrons, and only the desired atom/ion is deposited. The sticking coefficient and residence time of precursor molecule also influences the FEBID process. Before choosing the FEBID precursor, one should also check its toxicity and any kind of chemical reactions that may cause damage to the FEBID instrument. Although there are no precursor molecules synthesized so far that fulfill all criteria described above, few examples of popular FEBID precursor molecules are $MeCpPtMe_3$, WF_6, $Co_2(CO)_8$ [18].

FEBID has many interesting applications particularly in the areas of mask repair [84–86], nano-sized circuit fabrication [87], wiring biomolecules [88–90], fabrication and modification of nanophotonic and nanoplasmonic devices [91–93], production of custom tips for STM [61] and AFM [94,95], fabrication of solid state Fresnel lenses [65] etc. Compared to other vacuum based nanofabrication techniques like electron beam lithography (EBL), ultraviolet lithography (UVL) and extreme ultraviolet lithography (EUV), FEBID has many advantages such as it can directly write an arrays of 3D nanostructures on top of almost any substrates irrespective of its geometry. Moreover, there is no need of any resist layer or solvent for fabricating nanostructures. Compared to Focused ion beam induced deposition (FIBID), FEBID can achieve higher spatial resolution [96] and no sputtering and Ga implantation.

Although FEBID has several advantages and applications, there are still challenges that need to be overcome to attain its full potential. The main challenges that need to be addressed to improve the performance of FEBID are

i) Lateral broadening of deposited structures

When a nanostructure is fabricated with FEBID, it is observed from both experiments [23, 24] and simulations [20–22] that the lateral size of deposited structures is considerably larger than the primary electron beam probe size, for example, the lateral size of nanostructures fabricated by Z. Q. Liu *et al*. [23] using FEBID with a probe size of 0.8 nm exceeds 60 - 65 nm. Similarly, Monte Carlo simulations of carbon deposition with 0 diameter electron beam shows a deposit with lateral size of > 20 nm [20, 21]. Several studies attributed this lateral broadening to flux of SE and BSE emitting from the region outside of primary electron beam focal point [21, 25, 28, 29, 32, 97] (more details in chapter 3).

ii) Impurities present in the deposited structures

So far, no FEBID precursors show 100% pure deposition in FEBID without any physical or chemical treatment during the deposition or after the deposition. The unwanted co-deposition of impurities (commonly carbon and oxygen) in the FEBID deposit adversely affect several important properties of FEBID deposit such as conductivity [98–100], magnetic behavior [101] and catalytic activity [98]. The impurities in the FEBID deposits mostly originate from the incomplete decomposition of precursor molecules and co-deposition of ligands by the electron induced reaction of FEBID precursor molecules. However, residual molecules like water and hydrocarbons present in the vacuum chamber may also contribute to the impurities in FEBID deposit.

iii) Low processing speed

Compared to other lithography techniques like ultraviolet lithography (UVL) and extreme ultraviolet lithography (EUV), the FEBID technique is slow. Main reason for the low speed of FEBID is the low growth rate and the fact that this approach has not been parallelized with multiple beams. The speed of FEBID could thus be increased by increased deposition rates and incorporation of multiple electron beams [102].

2.2 FEBID processes

Although FEBID is a simple 3D direct writing nanofabrication technique, the mechanism associated with FEBID is very complex. It involves substrate-precursor molecule interactions, electron-substrate interactions, electron-precursor molecule interactions (see Fig. 2.3) and an interplay between different factors like residence time of precursors on the substrate surface, the flow of precursor gas into the FEBID system, the orientation of the precursor source (GIS) with respect to the region of electron beam induced deposition, the residual gas in the chamber, the charge formation in the substrate and deposit, etc.

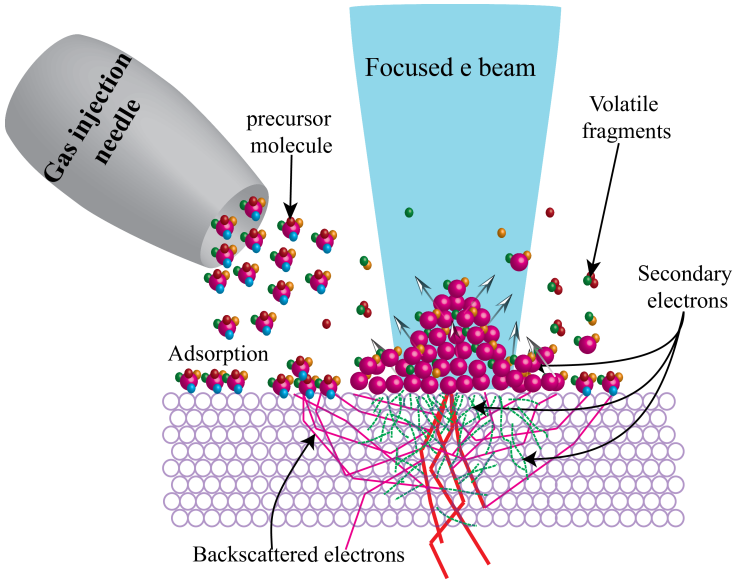

Figure 2.3. FEBID processes: Precursor molecules introduced to a substrate under high vacuum through a GIS, adsorb on the substrate's surface and dissociate by the focused high energy electron beam as well as back scattered and secondary electrons. Non-volatile fragments deposit on top of substrate and volatile fragments pump out using vacuum pumps. The thick red lines, violet lines and green dotted lines represents the transmitted primary electrons, BSE and SEs respectively.

2.2.1 Substrate - precursor molecule interactions

There are different interactions between the precursor molecules introduced into FEBID systems, and the substrate such as adsorption, desorption, and diffusion. The adsorption of FEBID precursor molecules on the surface of a substrate mostly occur through physisorption. Precursor molecules will adsorb on the substrate surface only for a specific time, called residence time τ of precursor molecules. After the residence time τ, precursor molecules desorb from the substrate's surface. A longer residence time increases the probability of electron induced dissociation of adsorbed precursor molecules. The constant supply and the dynamic equilibrium between the adsorption and desorption of FEBID precursor molecules maintains a constant precursor molecule coverage on the substrate surface. Precursor diffusion is the migration of precursor molecules from one adsorption site on the surface to an adjacent adsorption site and thus molecular transport to the place of decomposition. Surface diffusion of precursor molecules may thus play a significant role in electron beam induced deposition especially when growing tall pillars in FEBID [18].

2.2.2 Electron - substrate interactions

When high-energy electrons impinge on a solid substrate, the substrate can scatter electrons by elastic or inelastic interactions. The elastic interactions can alter the trajectory of the incident primary electrons (PE). Some energy of PEs will be lost by inelastic collision with substrate atoms. The inelastically scattered electrons with energy < 50 eV are defined as secondary electrons (SE), which are emitted by the atoms of the substrate through inelastic ionizing scattering of the primary and backscattered electrons (also the higher energy secondary electrons). These may be produced at the surface or reach the surface from inside the substrate. Auger electrons and X-rays can also be emitted from the substrate by inelastic electron collisions and PEs can be scattered back from the substrate (through elastic collisions). The scattered electrons (with energies > 50 eV) are defined as back scattered electrons (BSE), the forward scattered electrons (FSE) should also considered when growing structures like high aspect ratio pillars.

Both SEs and BSEs are capable of inducing chemical reactions. Therefore, it is important to study the electron energy distribution and spatial distribution of SEs and BSEs. Typical energy distribution of SEs and BSEs produced by the interaction of the PEs with the substrate is shown in Fig. 2.4a. The electron trajectory of scattered SEs and BSEs when high energy electron beams impinge on a flat substrate as well as on a 3D pillar geometry are schematically shown in Fig. 2.4b. The in-elastic and elastically scattered electrons inside the substrate form an onion shaped interaction volume just below the irradiation spot. The size and shape of the electron interaction volume inside the substrate material is directly dependent on the primary electron energy and inversely dependent on the material density and atomic number of the substrate's material. Using Monte Carlo simulations, one can model the interaction of primary electrons with a solid substrate and determine the interaction volume. The interaction volume formed when 5 keV electrons impinge on a silicon substrate is simulated using CASINO [103] and shown in Fig. 2.5. The spatial distribution of scattered electrons on the substrate's surface depends on the electron interaction volume of substrate's material. The scattered and secondary electrons are capable of dissociating precursor molecules through different dissociation mechanisms (details in chapter 3) and creating depositions. This is the main reason for lateral broadening of structures fabricated with the FEBID technique

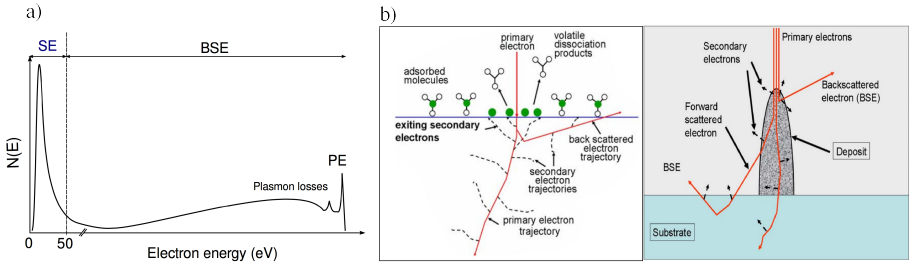

Figure 2.4. a) typical spectra of electrons emitting from a surface upon irradiation with high energy primary electrons. SE and BSE represent the secondary electrons and back scattered electrons respectively, (b) schematic for different electrons trajectory in a flat and pillar geometry. a) is adapted from ref [104] , b) is reproduced with permission from ref [18], Copyright (2008) American Vacuum Society.

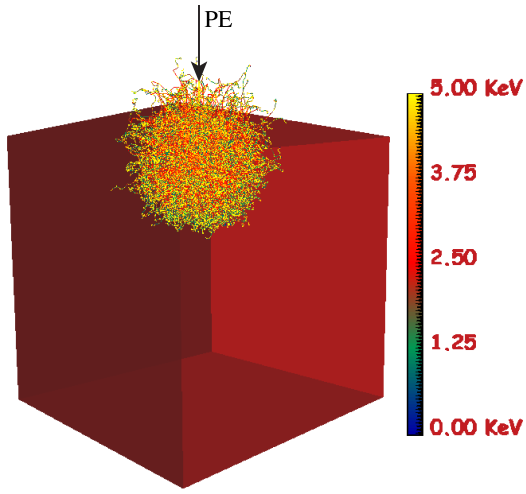

Figure 2.5. Simulated BSE trajectories in silicon substrate when a 5 keV electron beam with 1 nm diameter impinges on the substrate. The electron trajectories are simulated using CASINO version 3.2.0.4 [103] and 10000 electrons are simulated in the program. Width and height of silicon substrate used in the simulation was 1 μm.

2.2.3 Electron - precursor molecule interactions

Electron-precursor molecule interactions play a crucial role in determining the final deposit formed in FEBID. The probability of electron reaction with a precursor molecule and its fragmentation is generally expressed as its cross section (σ(E)). The electron induced precursor molecule dissociation cross section varies with electron energy, strength of different bonds present in the precursor molecule, and structure as well as electronic properties of the molecule in question.

There are different mechanisms such as dissociative electron attachment (DEA),

dissociative ionization (DI), dipolar dissociation (DD) and neutral dissociation (ND) by which electrons may induce dissociation of precursor molecules. Since the electron-precursor molecule interactions have crucial role in FEBID and the current work is related to electron-FEBID precursor molecule interactions, these will be described in more detail in the next chapter (chapter 3).

3 Electron interactions with precursor molecules

As discussed in the previous chapter, when primary electrons impinge on a substrate, large number of SEs and BSEs are emitted from the substrate. The emitted electrons are capable of dissociating the precursor molecules through different dissociation mechanisms i.e., DEA, DI, DD, and ND. The efficiency of the respective dissociation mechanisms is different in different electron energy ranges. Therefore, it is important to study the electron energy dependence for individual precursor dissociation. These studies cannot be performed in current FEBID or UHV surface science experiments because the surface adsorbed precursor molecules in these studies are simultaneously exposed to the whole energy distribution of the BSEs and low energy SEs as well as the PEs. The energy dependence and the extent of individual electron induced fragmentation processes for FEBID precursor molecules can be well studied using gas phase experiments carried out under single electron-precursor molecule collision conditions. In gas phase experiments, electrons of well-defined energy cross with an effusive beam of FEBID precursor molecules and the charged fragments formed by the collisions can be monitored using mass spectrometry. The first gas phase experiment performed with the objective to understand the energy dependent electron induced dissociation of FEBID precursor molecules was carried out by S. Engmann *et al.* in 2011 [25]. In that study, the absolute DEA and DI cross sections for electron interaction with the FEBID precursor molecule $Co(CO)_3NO$ in the energy range 0 to 140 eV were measured [25, 29]. DEA of $Co(CO)_3NO$ was by far most efficient close to 0 eV and the main DEA channel was loss of single CO. The onset of DI was in the range 9 - 15 eV with the cross section reaching a maximum close to 70 eV. Much at the same time, O. May *et al.* studied the electron interaction with the FEBID precursor molecule $Pt(PF_3)_4$ with the main focus on its absolute DEA cross sections [97] and M. Allan [105] measured the absolute cross sections for electronic excitation of this precursor. Further, early studies on low energy electron interactions with FEBID precursor molecules include studies on $W(CO)_6$ by K. Wnorowski *et al.* [27] and on $MeCpPtMe_3$ and $M(hfac)_2$ (M = Cu and Pd) by Engmann *et al.* [26, 28]. Since gas phase experiments are carried out using mass spectrometry, it is not possible to detect neutral fragments, i.e. we cannot study neutral dissociation using these gas phase experiments. However, it is possible to study ND to some extent using scattering experiments (for e.g. see electronic scattering experiments of $Pt(PF_3)_4$ [105]) and time dependent density functional theory (TDDFT) calculations (e.g. [106]). Although gas phase experiments are well suited to study the energy dependence and extent of electron induced FEBID precursor dissociation, they cannot completely map the electron induced reactions of precursor molecules adsorbed on a surface, as is the case in FEBID. At this point the role of UHV surface

science study comes into play. In the current UHV surface science studies, FEBID precursor molecules adsorbed onto a cold substrate situated inside a UHV chamber may be exposed to a flux of electrons with energy ~500 eV. The stoichiometric changes in the adsorbed molecules can be monitor using XPS and MS attached to the UHV chamber. The capability of UHV surface science experiments to monitor the electron induced bond breaking reactions of FEBID is demonstrated with many FEBID precursor molecules such as $Co(CO)_3NO$ [31], $MeCpPtMe_3$ [40], dimethyl-(acetylacetonate) gold (III) [68], $Pt(PF_3)_4$ [69], $W(CO)_6$ [30], $M(hfac)_2$ (where M = Pt, Pd and Cu) [71], (η^3-C_3H_5)$Ru(CO)_3Br$ [73], cis-$Pt(CO)_2Cl_2$ [74].

In order to better understand the processes occuring during FEBID, at the molecular level, both gas phase and surface studies of FEBID precursor molecules may contribute. The current chapter gives an overview of the theory of electron interactions with precursor molecules. A brief theoretical overview about the quantum chemical calculations is also included at the end of this chapter.

3.1 Electron - molecule interactions in gas phase

When an electron interacts with a molecule, it can scatter in two different ways i) direct scattering and ii) resonant scattering. In direct electron scattering, the electron - molecule interaction time will be shorter (in the order of magnitude of $1x10^{-16}$s), while for resonant electron scattering the interaction time can be longer (varies in the range $1x10^{-14}$s to $1x10^{-3}$s, depends upon the molecule size [107]). Such scattering process may be elastic, i.e., without energy transfer or inelastic and may thus induce changes in the molecule. These processes will be discussed in the following sections. For this purpose, a diatomic molecule; AB, is taken as an example to explain electron - molecule interaction processes and subsequent changes of the molecule, under single collision conditions. In the current gas phase experiments, positive ion formation through electron impact ionization and negative ion formation through resonant electron capture are mainly studied, therefor the theory of these processes will be discussed in more detail.

3.1.1 Electron impact ionization

If the energy of an electron interacting with the neutral molecule is efficiently transferred and it is greater than the ionization potential of the molecule (IE is typically in the range 7 - 15 eV, depends upon the molecule), the molecule gets ionized by the interacting electron. The ionization process in which the incoming electron directly removes one of the bound electrons from the molecule is called direct ionization. The scattered electron and the ejected electron will leave simultaneously or within $1x10^{-16}$s of each other; it is a very fast process [107]. Also, according to the Frank-Condon principle, the electron impact ionization occurs through a vertical transition of electrons (see Fig. 3.1) which takes place on a much faster time scale than is required to move the nuclei in the molecule. This means that during the ionization process, the separation between nuclei, i.e. bond lengths, remain unaltered.

If the incoming electron has sufficiently high energy, multiple electrons can be

ejected from the molecule. The ionization of a diatomic molecule AB can be represented as

$$AB + e^-(\varepsilon_1) \rightarrow AB^{(\ddagger)n+} + (n+1)e^- \tag{3.1}$$

The ionization efficiency of a molecule is usually expressed in terms of the ionization cross sections. The ionization cross section can be defined as an area through which an electron must travel to efficiently transfer the electron energy and consequently ionize the molecule. Since the ionization cross section is a measure of an area, it has the unit of square-meters. The behaviour of ionization cross section with respect to electron energy is similar for most molecules. It starts increasing above the ionization threshold of the molecule and peaks at around 70 eV. Therefore, electron impact ionization mass spectrum are usually measure at an electron energy of 70 eV.

When an electron is removed from the molecule by electron impact ionization, the molecule becomes destabilized. As a consequence, the excess energy may redistribute as vibrational energy and that will cause elongation of bonds in the ionized molecule. This destabilization of ionized molecule may lead to dissociation, i.e., dissociative ionization (DI).

3.1.1.1 Dissociative ionization (DI)

In dissociative ionization, the electron impact ionized parent molecule will dissociate into a positive ion and one or more neutral fragments. DI can be represented by the equation.

$$AB + e^-(\varepsilon_1) \rightarrow AB^{(\ddagger)+} + 2e^- \rightarrow A^{(\ddagger)+} + B^{(\ddagger)} + 2e^- \tag{3.2}$$

Where "$(\ddagger)$" denotes that the fragments are in vibrationally and/or electronically excited state. The DI process can be understood from a 2-D potential energy diagram of a diatomic molecule; AB, as shown in Fig. 3.1. In the initial step, the molecule ionizes by vertical transition of a bound electron into the ionization continuum of the molecule. If the incident electron energy is higher than the ionization energy of the molecule, part of the electron excess energy can be transferred to the molecule. The transferred excess energy may leave the parent cation in a vibrationally and/or electronically excited state, which may further lead to fragmentation of the parent cation. The extent of fragmentation in DI depends upon the electron energy transferred to the parent cation and the thermochemical threshold or activation energies of the respective fragmentation processes. The thermochemical threshold for the formation of positive ion fragments in DI can be written as

$$E_{th}(A^+) = BDE(AB) + IE(A) \tag{3.3}$$

Where BDE(AB) is the bond dissociation energy of AB and IE(A) is the ionization energy of A.

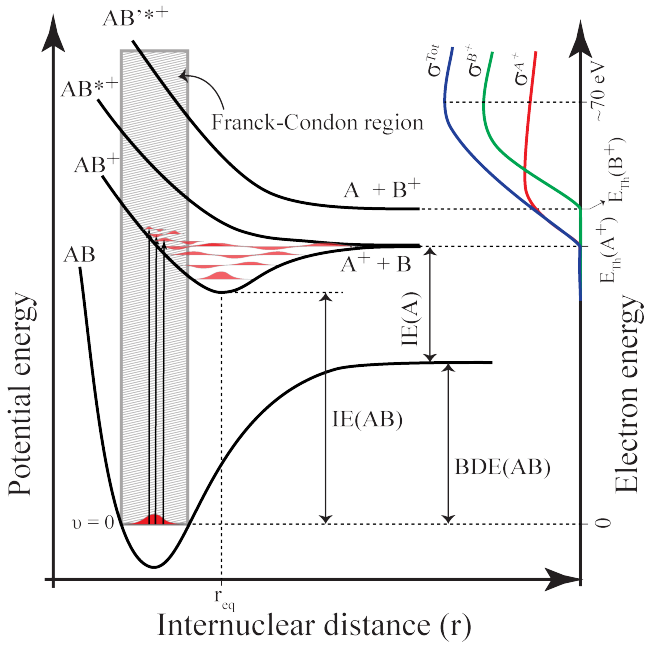

Figure 3.1. Simplified 2-D potential energy diagram for DI of a diatomic molecule AB. The potential energy curves AB, AB^+, AB^{*+}, AB'^{*+} represent the ground state of the neutral molecule and different ionized states. $E_{th}(A^+)$ and $E_{th}(B^+)$ are the threshold energies for forming A^+ and B^+ through dissociative ionization of AB, adapted with permission from ref. [32].

The total dissociation cross section of the molecule will increase with electron energy and generally shows a maximum at around 70 eV, and then diminishes again with further increase in energy. The decrease in dissociation cross sections at higher energy is mainly due to the short interaction time of the electron with the molecule and thus less efficient energy transfer. The DI process can be very extensive; it can be active from slightly above the ionization energy of the molecule to well above 100 eV with fairly high dissociation cross sections. In chapter 2 we saw that there is a large number of SEs emitted with energies between 10 - 100 eV during the FEBID processes. Therefore, DI can significantly contribute to decomposition of the precursor molecules in FEBID.

3.1.2 Resonant interactions; electron attachment

In resonant interactions, the interacting electron stays longer in the vicinity of the molecule than necessary for its transit through the dimension of the molecule (typically $> 1x10^{-14}$s). The electron attaches to the molecule during the interaction time and forms a transient negative ion (TNI). The lifetime of the TNI varies from a few vibrational periods ($1x10^{-14}$s) as in N_2 to the μs range (e.g. the measured lifetime of SF_6^- is > 100 μs [108]). The electron attachment is a resonant process and accordingly it occurs in a

specific energy range. Due to the complex nature of the electron attachment process, it usually is explained in terms of a quasi-diatomic molecule. Electron attachment to a diatomic molecule AB is shown in Fig. 3.4 using a two-dimensional potential energy diagram. From the diagram, the electron attachment process can be understood as a vertical electronic transition from the ground state of neutral molecule to the ground or any accessible excited states of the anion. The vertical transition takes place over a very narrow energy range within the Franck-Condon region. The transition probability (P_{trans}) in the electron attachment process is proportional to the Franck-Condon factor, which is given by the square of the overlap integral of the ground state wave function and the excited anionic state wave function.

$$(P_{trans}) \propto |\langle \psi^0 | \phi^* \rangle|^2 \tag{3.4}$$

The energy dependence of the electron attachment process can be graphically represented using the reflection principle [107], i.e. the shape of electron attachment curve will be a reflection of the molecule's ground state wave function overlap with the respective anionic state (see Fig. 3.4).

The stability of negative ions is determined by the electron affinity of the molecule. Electron affinity can be defined by the difference in energy between the ground state of the respective neutral molecule and its anionic ground state. By convention, if the anionic ground state is below the respective neutral ground state we can consider it as a positive electron affinity, and if the anionic ground state is above the respective neutral ground state we can consider it as negative electron affinity. In principle, the only prerequisite for the formation of a thermodynamically stable negative ion is the positive electron affinity i.e. the ground state of the anion should be lower than the ground state of neutral molecule. It is not necessary that all molecules with positive electron affinity show stable molecular anions in gas phase experiments under single collision conditions, for e.g., small molecules like CF_3Br [109], CCl_4 [110] with positive electron affinity did not show stable negative ions in the experimental measurements. The excess energy created in these molecules by electron attachment may not be efficiently removed or redistributed; hence it is not possible to form stable molecular anions under single collision conditions.

3.1.2.1 Negative ion resonances

Different types of resonances observed in the electron attachment are shape resonances and Feshbach resonances. Basic difference between the two resonances is that shape resonances lie energetically above the corresponding parent state and Feshbach resonances lie energetically below the corresponding parent state

Shape resonances

In shape resonance, an incoming electron attaches to the molecule due the shape of the potential created from the electron-molecule interaction (see below). If the incoming electron resides to a previously empty or half-filled molecular orbital of the ground state of the molecule without any change in the molecule electronic configuration, it is defined as single-particle shape resonance. Single particle shape resonances are usually observed in the energy range 0 to 4 eV [111, 112]. If the incoming electron is attached to the molecule due to the shape of the potential created by the electron-molecule interaction, and the electron attachment induces an electronic excitation of the molecule,

it is defined as two particles-one hole shape resonance or a core-excited shape resonance. Core excited resonances are observed at energies at or above the first excited states of the respective neutral molecules. Both single particle shape resonance and core excited shape resonance are open channel resonances because the electron detachment is open for these resonances. Both single-particle shape resonance and core excited shape resonance are illustrated in Fig. 3.2.

Feshbach resonances

Feshbach resonances are usually observed for molecules with positive electron affinities. As mentioned, Feshbach resonances lie energetically below the corresponding parent state and direct electron detachment is not possible. Feshbach resonances are thus closed channel resonances and generally have longer lifetime because the direct electron detachment channel is closed in these resonances. Similar to shape resonances, there are two types of Feshbach resonances, nuclear excited (also referred to as vibrational Feshbach resonances) and core-excited Feshbach resonances. In both Feshbach resonances, the TNI lies energetically below the respective ground or excited states of the parent molecule. Vibrational Feshbach resonances usually occur at very low energies with fairly high cross sections [113]. Both vibrational and core-excited Feshbach resonance are shown schematically in Fig. 3.2.

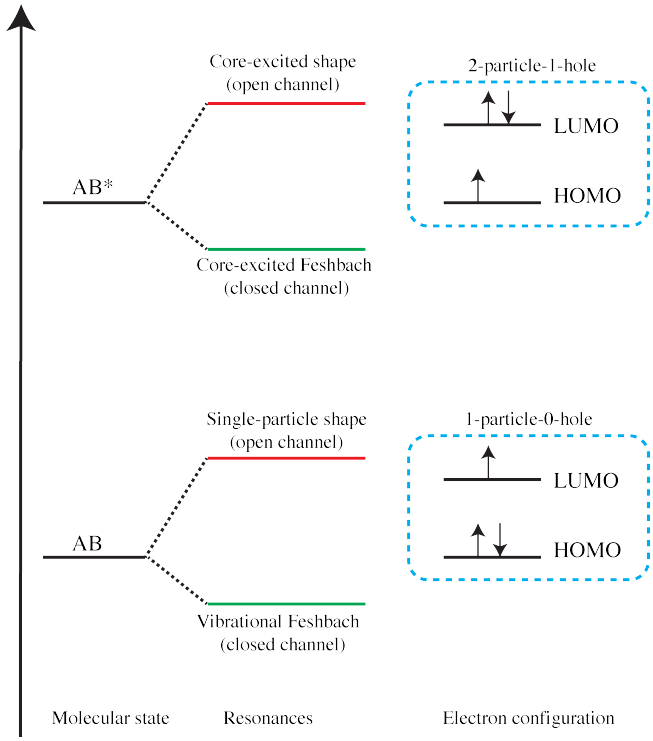

Figure 3.2. Schematic representing four types of resonances (vibrational Feshbach, single-particle shape, core-excited Feshbach and core-excited shape). AB and AB represents the ground and excited state of neutral molecule AB. 1-particle-0-hole means that there is single electron in the LUMO and no hole created in HOMO, 2-particle-1-hole means that there are 2 electrons in LUMO and one hole created in HOMO due to electron excitation.*

3.1.2.2 Mechanisms behind electron attachment

(a) Electron trapping mechanism in shape resonances: When an electron interacts with a molecule, we can consider the incoming electron as a plane wave containing different components of angular momentum, *l*. The incoming electron will attach to the molecule if it possesses an unfilled and energetically accessible molecular orbital whose symmetry fits to the incoming electron angular momentum [111, 112]. This kind of electron attachment results in shape resonances. This model simplifies the understanding of very complicated mechanisms of electron - molecule interactions [114–116].

When the incoming electron approaches to a non-polar molecule with non-zero polarizability (α), a temporary (charge induced) dipole will be induced in the molecule, which will weakly attract the incoming electron through a long range attractive polarization potential given by the equation

$$V_\alpha = -\frac{\alpha}{2r^4} \tag{3.5}$$

Because of the angular momentum of the electron, a repulsive centrifugal potential will be created between the electron and the molecule

$$V_l(r) = \frac{l(l+1)}{2r^2} \tag{3.6}$$

Therefore, the effective potential will be the sum of the attractive polarization potential $V_\alpha(r)$ and the repulsive centrifugal potential $V_l(r)$

$$V_{effective} = V_l(r) + V_\alpha(r) = \frac{l(l+1)}{2r^2} - \frac{\alpha}{2r^4} \tag{3.7}$$

The effective potential between an electron and a molecule for various l values is shown in Fig. 3.3. From equation 3.7 we can see that for l=0 (s-waves), the centrifugal term vanishes and therefore no potential barrier is formed for the incoming electron. This indicates that resonances formed by s-wave electron attachment are not shape resonance. For electron angular momenta $l > 0$, a clear potential barrier is formed. The height of the potential barrier increases with increasing electron angular momentum. When the electron-molecule distance becomes very short, a short-range repulsive force is created between the molecule's electron cloud and the trapped electron, explained by the Pauli Exclusion Principle. Therefore, in the real case, the total effective potential between the electron and the molecule will be a combination of this short-range repulsive force and the long range effective potential ($V_{effective}$). When an electron with $l \neq 0$ interact with the molecule, it most likely deflects from the molecule due to the potential barrier. However, there exists a certain probability that electron tunnel through the potential barrier and get trapped. The trapped electron creates a TNI. There also exists a certain probability that the electron tunneled through the potential barrier may tunnel back out. The time spent by the trapped electron in the potential barrier is basically the lifetime of the TNI [107]. When the trapped electrons tunnel back from the potential barrier, autodetachment occurs (see below).

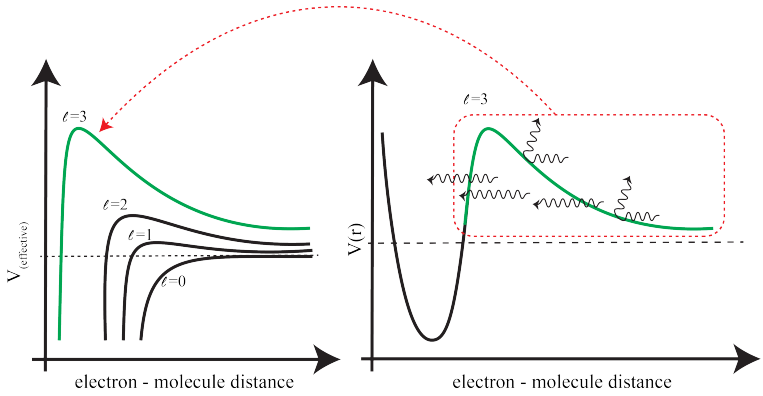

Figure 3.3. The left panel shows schematically the effective potential between the approaching electron and the respective molecule for various angular momentum (l). The right panel shows schematically the total effective potential between the electron and the respective molecule, electrons may deflect back due to the effective potential (shows with reflecting waves) but may also tunnel through the potential barrier (shows with straight waves) and thus become temporally trapped within the potential barrier.

(b) Electron trapping mechanism in Feshbach resonances: When an electron interacts with molecule which is capable of forming a stable molecular anion (i.e. a molecule with a positive electron affinity), the interacting electron may be trapped within the field of an excited (electronic or vibrational) molecule. Since the Feshbach resonances (both vibrationally and core excited) lie energetically below the respective parent state of the molecule, autodetachment of the attached electron via a one electron process is energetically not possible. The relaxation is only possible through a two-electron process; however, it requires significant rearrangement in the electronic structure of the molecule, which will lead to capture of electron for longer time [111].

3.1.2.3 Relaxation of temporary negative ion

During resonant electron-molecule interaction, the TNI is generally formed in an electronically or vibrationally excited state, therefore it needs to relax by removing its energy. There are mainly two pathways for relaxing the TNI, autodetachment (AD) and dissociative electron attachment (DEA). Additionally, TNI can also relax/stabilize through intramolecular vibrational energy redistribution (IVR). These processes can be represented by the equations

$$AD \quad : AB + e^-(\varepsilon_1) \quad \rightarrow \quad AB^{(\ddagger)-} \quad \rightarrow \quad AB^{(\ddagger)} + e^-(\varepsilon_2)(\varepsilon_2 < \varepsilon_1) \tag{3.8}$$

$$DEA \quad : AB + e^-(\varepsilon_1) \quad \rightarrow \quad AB^{(\ddagger)-} \quad \rightarrow \quad A^{(\ddagger)-} + B^{(\ddagger)} \tag{3.9}$$

$$IVR \quad : M + e^-(\varepsilon_1) \quad \rightarrow \quad M^{(\ddagger)-} \quad \rightarrow \quad M^- \tag{3.10}$$

Where AB represent a diatomic molecule and M stands for molecule with large number of vibrational degrees of freedom

3.1.2.4 Autodetachment

If the lifetime of the TNI is short (i.e. less than the vibrational period of the nuclei ~$10^{-14}s$), the temporarily attached electron re-emits without dissociation, and forms the neutral molecule in its ground state or excited states. The lifetime (τ_a) of a TNI with respect to AD is given by the Heisenberg uncertainty principle

$$\tau_a = \frac{\hbar}{\tau} \tag{3.11}$$

where ($\hbar$) is the reduced Plank constant and (τ) is the width of the negative ion state. Based on equation 3.11, the lifetime of a TNI will be higher for narrow resonances. As mentioned before, the lifetime of TNIs can vary from few femtoseconds for smaller molecules (like N_2) to milliseconds for larger molecules like $SF_6{}^-$ [108].

3.1.2.5 Relaxation through IVR

At very low energies, i.e. close to 0 eV, the molecular anion with sufficiently larger size can live longer through intramolecular vibrational energy redistribution (IVR). In this case, the molecular anion forms a metastable anion. The observation of molecular anion formation from electron attachment to SF_6 at 0 eV is the best example of a metastable anion. Other molecules like C_{60}, C_6F_6 [117, 118] can also form long lived metastable anion through IVR. Positive electron affinity is one requirement to form metastable molecular anion. The relaxation of the TNI through IVR reduces the chance to re-emit the attached electron through AD.

3.1.2.6 Dissociative electron attachment

In DEA, the formed TNIs relax through dissociation into a negative ion fragment and one or more neutral fragments. DEA of a diatomic molecule AB can be understood from its two-dimensional potential energy diagram as shown in Fig. 3.4. The DEA process consists here of the formation of a TNI by vertical transition from the molecule's ground state to the repulsive ground or excited state of the corresponding molecular anion. The relaxation of the TNI may occurs along the repulsive potential energy surface and after the crossing point r_c (crossing of neutral and anionic potential energy curve in Fig. 3.4) autodetachment is not possible and the molecule is bound to dissociate. In Fig. 3.4 this results in the formation of a neutral fragment A and an anionic fragment B^-. The survival probability of the TNI to cross r_c depends on the autodetachment lifetime (τ_{AD}) and the time t required for the internuclear distance r to exceed r_c. The survival probability of the TNI is given by the equation $P = e^{-\frac{\tau}{\tau_{AD}}}$. Based on the survival probability of the TNI, the DEA cross section can be written as

$$\sigma^{DEA} = \sigma^{EA} e^{-\frac{\tau}{\tau_{AD}}} \tag{3.12}$$

Where σ^{EA} is the electron attachment cross section.

As mentioned above, the lifetime of the TNI depends on the width of the negative ion state. At shorter inter-nuclear distances and higher energies, the width of the negative ion state is larger which reduces the lifetime of the TNI. This results in more efficient AD at higher energies. This is the reason why the DEA curve shown in Fig. 3.4 is red shifted compared to EA curve.

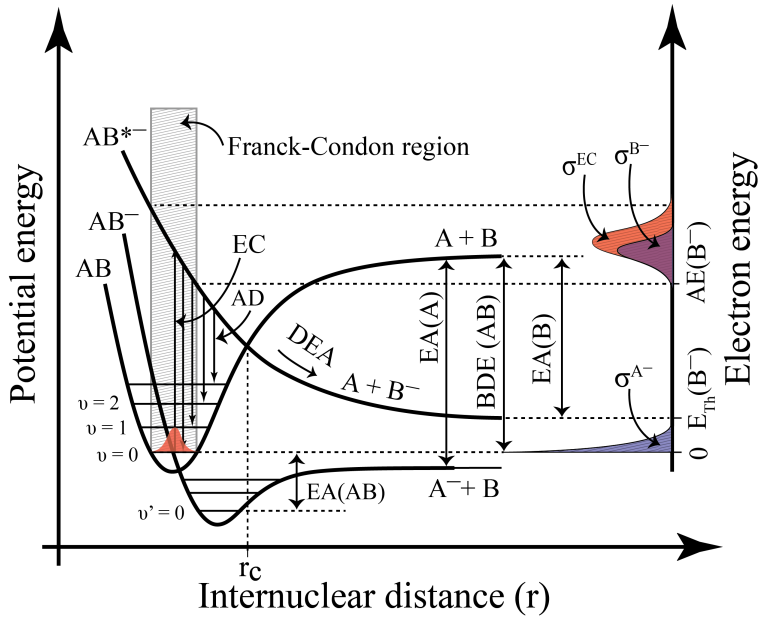

Figure 3.4. Simplified 2-D potential energy diagram for DEA to a diatomic molecule AB. The potential energy curves AB, AB^- and AB^{*-} represent the neutral ground states, anionic ground states and anionic excited states of molecule AB, $E_{th}(B^-)$ represent the thermochemical threshold for forming B^- through DEA of AB, the electron capture (EC) shows with a vertical arrow, adapted with permission from ref [32].

The thermochemical threshold for the formation of the neutral fragment A and the anionic fragment B^- from dissociative electron attachment to AB is given by

$$E_{th} \sim \Delta H_r = BDE(AB) - EA(B) \tag{3.13}$$

where BDE(AB) is the bond dissociation energy for the A-B bond and EA(B) is the electron affinity of fragment B.

In the general case, we can write the E_{th} as

$$E_{th} = \sum_{i=1}^{n} BDE(Educt)_i - \sum_{j=1}^{n} BDE(Product)_i - EA(X) \tag{3.14}$$

where $BDE(Educt)_i$ and $BDE(Product)_j$ are the bond dissociation energies for the respective broken and formed bonds, EA(X) is the electron affinity of charge retaining fragment X.

However, in the experimental measurement, the negative ions formed through the DEA process may appear above the respective thermochemical threshold value. The additional energy is distributed as the internal energy of the created fragments or as the translation energy of the neutral and negative ion fragments. Therefore, the appearance energy (AE) of the negative ion formed through DEA can be written as

$$AE(B^-) = E_{th} + E^* \tag{3.15}$$

where E^* is the additional energy distributed to the fragments as internal energy or translation energy.

In addition to DEA and DI, there are other electron induced dissociation mechanisms such as neutral dissociation (ND) and dipolar dissociation (DD). We didn't observe DD in the current work and with the experimental set up used for the current work we cannot study ND. A brief description of the theory for ND and DD are given below.

Neutral dissociation (ND)

In neutral dissociation of the electronically excited diatomic molecule AB*, it will dissociate into two neutral fragments and the process can be represented by the equation

$$AB + e^-(\varepsilon_1) \rightarrow AB^* + e^-(\varepsilon_2)(\varepsilon_2 < \varepsilon_1) \rightarrow A^\ddagger + B^\ddagger \tag{3.16}$$

where $(*)$ denotes that the species are electronically excited and $(\ddagger)$ denotes that the species may be in an electronically and/or vibrationally excited state.

Neutral dissociation will only occur if the initial electronic excitation energy is higher than the bond dissociation energy (BDE) of the molecule AB. It is not a resonant process and its threshold depends upon the BDE and the size of molecule. Many organic and inorganic molecules have first excitation energies as low as 2 to 5 eV [119], for e.g. in azulene it is 1.77 eV, the excitation energy of CrH is 1.62 eV [119], while the BDE of CrH is 1.7 eV [120]. Therefor ND can be active at low electron energies. The neutral dissociation of a diatomic molecule AB can be schematically represented using a two-dimensional potential energy diagram of AB as shown in Fig. 3.5. Above threshold, the ND cross section will gradually increase and at higher electron energies, new ND channels will open up and contribute to the total ND cross section of the molecule. Neutral dissociation may be very efficient for bigger molecules with large densities of electronically excited states. Depending upon the molecule density of electronically excited states and efficiency of electron energy transfer to the molecule, ND may maintain a high cross section in over a large electron energy range i.e. in the energy range 5 to > 100 eV.

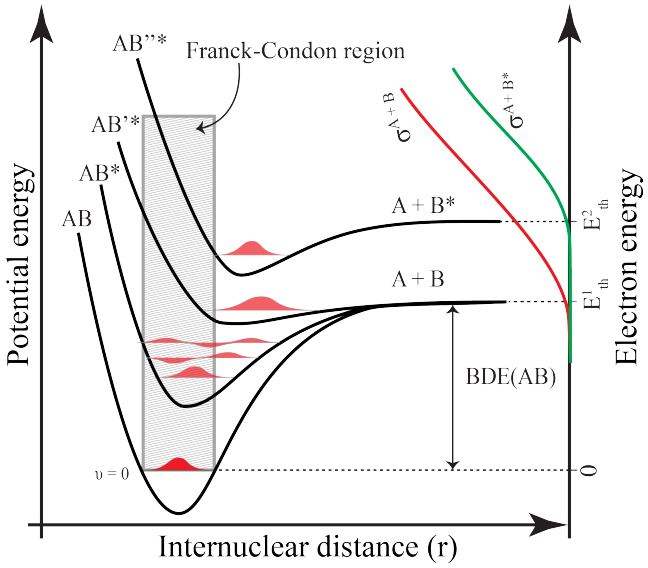

Figure 3.5. Simplified 2-D potential energy diagram for neutral dissociation of a diatomic molecule AB. The potential energy curves AB, AB, AB'*, AB"* represent the ground state and different excited states of the neutral molecule AB, E_{th} is the threshold energy for neutral dissociation, adapted with permission from ref [32].*

Since there are no charged fragments involved in the ND process, it is difficult to study ND using a mass spectrometric set up. However, using the electron scattering experiments it is possible to measure the electronic excitation cross section of a molecule and that may be informative about the potential ND cross sections. M Allan performed electron scattering experiment with the FEBID precursor molecule $Pt(PF_3)_4$ [105]. The experimental result showed a significant electronic excitation cross section for $Pt(PF_3)_4$ [105]. M. Zlatar *et al*. [106] recently characterized the ground and excited states of $Pt(PF_3)_4$ using TDDFT calculations and found that many of low energy excited states are either dissociative along the Pt-PF_3 bond or undergo a number of conical intersections which may open many dissociation pathways. An electron induced fluorescence apparatus (EIFA) developed by Š. Matejčík's group in Bratislava [121] recently used to study the dissociative excitation (DE) process of $Fe(CO)_5$ [122]. EIFA detects the photons (in the UV/Visible range) emitting from the excited neutral species, which produced by the electron-molecule collision and give energy dependant photon efficiency curves. These energy dependant photon efficiency curves are informative about the ND process of a molecule.

Dipolar dissociation

In DD, the resultant electronically excited state of AB* will induce ion-pair formation. It can be represented by the equation

$$AB + e^-(\varepsilon_1) \rightarrow AB^* + e^-(\varepsilon_2)(\varepsilon_2 < \varepsilon_1) \rightarrow A^{(\ddagger)+} + B^{(\ddagger)-} \tag{3.17}$$

DD will proceed similarly to ND, but for a DD to occur, the coulomb interactions

between the positively and negatively charged fragments must be overcome. If we observe non-resonant anion fragments above the excitation energy of a molecule, the anion is definitely formed through DD because there is no other non-resonant dissociation mechanism that exists to creates anion fragments above the excitation energy of a molecule. The other dissociation mechanism that creates anion fragments is DEA (described in section 3.1.2.6), however DEA is a resonant process and we can thus clearly distinguish DD from DEA. We can further confirm DD by measuring the counter cation formed through DD by utilizing the fact that the ion yield curves for these two partner ions will show the same (or very similar) profile. The DD for a diatomic molecule AB is schematically shown in Fig. 3.6 using a two-dimensional potential energy diagram of AB. The thermochemical threshold for DD of diatomic molecule AB can be calculate by

$$E_{th}(A^+ + B^-) = BDE(AB) + IE(A) - EA(B) \tag{3.18}$$

The thermochemical threshold for DD is generally higher than DEA and ND but lower than DI because ionization energy is generally higher than the electron affinity. Compared to DEA, DI and ND, dipolar dissociation is not a very efficient process. As I mentioned, in our study no DD was observed. There is a recent negative ion desorption study for $Fe(CO)_5$, which shows considerable intense ions formed through DD, [123]. No other efficient DD reported for FEBID precursor molecules.

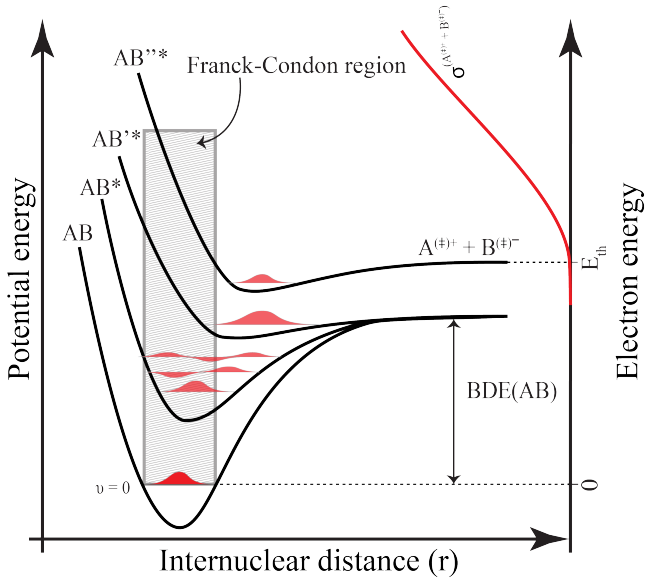

Figure 3.6. Simplified 2-D potential energy diagram for dipolar dissociation of diatomic molecule AB, The potential energy curves AB, AB, AB'*, AB"* represent the ground state and different excited states of neutral molecule AB, E_{th} is the threshold energy for dipolar dissociation, adapted with permission from ref [32].*

3.2 condensed phase

It is really important to consider the electron-molecule interactions in condensed phase because the typical FEBID process takes place on a surface. Knowledge about the electron-molecule interactions acquired from the gas phase experiments may be used to understand the electron-molecule interactions in the condensed phase, however the difference in environment of the molecule in condensed phase compared to gas phase need to take into account. The main factors which we need to be taken into account for modifying the electron-molecule resonant interaction in the gas phase in comparison with condensed phase are i) the polarization interaction of the molecule by the presence of electrons and transient anions, ii) fixed orientation of molecules with respect to the surface where it is adsorbed, iii) the probability of distortion and modification of the target molecule by the solid [124]. In the case of DEA, the negative ion yield and its energy dependence in condensed phase may also affect by electron scattering prior to electron attachment, kinetic energy required to overcome the polarization potential and post dissociation interactions. The surface influence like chemical activity due to impacted electrons [125] should also take into account when describing the electron-molecule interactions in condensed phase compared to gas phase.

The first experiment to study the DEA in condensed phase was carried out by Sanche *et al*. in 1984 [126]. In that study, they reported the formation of O^- from the electron attachment dissociation of surface adsorbed O_2 and CO [126], they also observed C^- formation from surface adsorbed CO. The comparison of negative ion formation by the electron attachment dissociation of surface adsorbed O_2 and CO with the similar observation in the gas phase O_2 and CO [127, 128] was interesting for a number of reasons. The O^- ion yield curve for adsorbed O_2 was slightly shifted to higher energies and became broader compared with the O^- ion yield curve in gas phase [129]. An additional peak was also observed at about 13 eV. In the case of O^- formation from condensed CO, the ion yield curve shifted to a higher energy region and an additional peak was observed at about 16 eV compared with the gas phase results [128]. For C^- formation from condensed CO, there was only one peak observed at about 14 eV, however this is significantly different from the gas phase results where two peaks were observed at about 10.5 eV and 11 eV [128]. The surface experiments related to precursor molecules like $MeCpPtMe_3$, $Au(acac)Me_2$, $Co(CO)_3NO$, $W(CO)_6$, $M(hfac)_2$ (M = Pt, Pd, Cu), $Pt(PF_3)_4$, (η^3- C_3H_5)$Ru(CO)_3Br$ and cis-$Pt(CO)_2Cl_2$ can be found in references [30, 31, 40, 68, 69, 71, 73, 74].

3.3 Quantum chemical calculations

The basis for all quantum chemical calculations is solving the Schrödinger equation to predict the probable distribution of electrons around the nuclei in molecular systems. The information about the electron distributions in the molecular system is the key point to understand its physical and chemical properties. The time-independent form of the Schrödinger equation is

$$H(r,R)\psi(r,R) = E\psi(r,R) \tag{3.19}$$

where the wavefunction ψ is function of electronic and nuclear coordinates, H is the Hamiltonian operator and E is the energy eigenvalue. When we solve the Schrödinger equation, we get the energy eigenvalues. The Hamiltonian H is the sum of kinetic energy and the potential energy of the system. For a one-particle system it is very simple, however, for many-particle systems the Hamiltonian operator H become complicated because in that case we need to consider the kinetic energy of all electrons ($\hat{T}_{\mathrm{e}}$), nucleus ($\hat{T}_{\mathrm{n}}$), coulomb attraction between electrons and nuclei ($\hat{V}_{\mathrm{ne}}$), electrostatic repulsion between the electrons ($\hat{V}_{\mathrm{ee}}$) and electrostatic repulsion between the nucleus ($\hat{V}_{\mathrm{nn}}$).

$$\hat{H} = \hat{T}_{\mathrm{e}} + \hat{T}_{\mathrm{n}} + \hat{V}_{\mathrm{ne}} + \hat{V}_{\mathrm{ee}} + \hat{V}_{\mathrm{nn}} \tag{3.20}$$

The Schrödinger equation for a complex system cannot be solved analytically mostly due to the interdependence nature of electrons in the system (the term $\hat{V}_{\mathrm{ee}}$), several approximations need to introduce to solve it practically. The main approximation is the Born-Oppenheimer approximation. In this approximation, it is assumed that the nuclear motion is much smaller than the electronic motion due to the larger mass of the nucleus. As long as the Born-Oppenheimer approximation is valid, the term $\hat{T}_{\mathrm{n}}$ is ignored and $\hat{V}_{\mathrm{nn}}$ become constant. The potential energy surface is a direct result of the Born-Oppenheimer approximation. Another approximation made is that electrons move independently of each other and thus the multi-electron wavefunction could be considered as the product of independent single-electron wavefunctions (orbitals), this approximation is the Hartree approximation [130]. The antisymmetric nature of orbital is missing in the Hartree approximation [131], the antisymmetric nature can be addressed by writing the total wavefunction as a Slater determinant (Hatree Fock (HF) approximation) [132]. In reality, these orbitals are written as linear combination of basis functions (basis sets). From the multi-electron wave function in HF approximation, the HF energy equation ($< \psi|H|\psi >$) can be solved by applying the variation principle, i.e. put different trial wavefunctions in the HF energy equation and minimize it with respect to molecular orbital (MO) coefficients. The main thing missing in the HF method is electron correlation. Although electron correlation can be improved using post-HF method such as coupled cluster theory, they are computationally expensive. Another approach, which addresses the problem of electron correlation from a different point of view is density functional theory (DFT). It has become the most popular quantum chemistry methodology.

Density functional theory (DFT) is based on the Hohenberg-Kohn (HK) theorems [133]. According to the HK theorems, the exact energy of the system can be expressed in terms of electron density. There exists a functional (function of electron density), which gives the exact energy of the system, the problem is that we need to find the right functional. The electron density can be obtained from the orbitals (that are described by basis functions), in the currentt work I used def2-TZVP and ma-def2-TZVP basis set (set of basis functions), where the term "TZVP" stand for polarized triple zeta i.e it using polarized 3 basis functions. The term "ma" adds diffuse function to the basis sets. If the electron density is known we can express the ground state energy of the system using Kohn-Sham DFT energy equation [134]

$$E[\rho(r)] = T_e^{KS}[\rho(r)] + V_{ek}[\rho(r)] + J[\rho(r)] + E_{xc}[\rho(r)] + V_{kk} \tag{3.21}$$

where $T_e^{KS}[\rho(r)]$ is the kinetic energy term for non-interacting electrons, this was introduced from the Kohn-Sham approach [134] i.e. kinetic energy term for non-interacting electrons can be calculated using orbitals, $V_{ek}[\rho(r)]$ is electron-nuclear attraction term, $J[\rho(r)]$ is electron-electron coulomb interaction term, $E_{xc}[\rho(r)]$ is the exchange correlation term for electron-electron repulsion and V_{kk} is the nuclear-nuclear interaction term, It is possible to find the exact solution for $T_e^{KS}[\rho(r)], V_{ek}[\rho(r)], J[\rho(r)], V_{kk}$, however, there is no exact solution for $E_{xc}[\rho(r)]$, only approximate ones. Different DFT functionals mostly differ by using different expressions for $E_{xc}[\rho(r)]$; nowadays there is a huge number of functionals available (PBE0, BP86, B3LYP etc.). For the current work we used the functionals BP86 [135, 136] and PBE0 [137, 138]. BP86 is a functional based on the generalized gradient approximation (GGA) while PBE0 is a hybrid functional that uses a mixture of exact exchange from Hartree-Fock theory (25%) and DFT exchange (75%). The performance of PBE0 in predicting the energetics of negative ion formation from DEA to $HFeCo_3(CO)_{12}$ was good compared to BP86.

4 Experimental section

This thesis contains gas phase, UHV surface and in *situ* FEBID experimental results. Quantum chemical calculations were also conducted to support the gas phase observations. All gas phase experimental studies were conducted using the crossed electron-beam/effusive-molecular-beam instrument; Simply a Gas-phase Machine (SIGMA) at the University of Iceland. The quantum chemical calculations were also conducted at the University of Iceland using ORCA [139]. All surface studies were conducted in a UHV chamber equipped with an X-ray photoelectron spectrometer (XPS) and a mass spectrometer (MS) at Johns Hopkins University. The FEBID experiments were conducted in an FEI NovaNanoLab 650 dual beam scanning electron microscope at the Technical University of Delft (TU Delft).

4.1 Precursor molecules

$HFeCo_3(CO)_{12}$ and $H_2FeRu_3(CO)_{13}$: Both bimetallic precursor molecules were supplied by Dr. Sven Barth at the Vienna University of Technology, Austria. The synthetic details of these precursor molecules can be found in articles 3 and 4.

Dichlorosilacyclohexane (DCSCH) and Trisilacyclohexane (TSCH): These silicon-based precursor molecules were purchased from Gelest Inc, Morrisville PA, US. The purchased precursor molecules were used as obtained without any processing.

Silacyclohexane (SCH): This precursor molecule was synthesized from DCSCH at the University of Iceland by Dr. Krishna, the synthetic details can be found in article 5 and in ref. [140].

4.2 Gas phase experimental

Gas phase experiments were conducted using SIGMA under single electron/molecule collision conditions. Fig. 4.1 shows a picture (top) and a schematic (bottom) of SIGMA. The usual base pressure of SIGMA is on the order of ~1x10^{-8} mbar. SIGMA consists of a trochoidal electron monochromator (TEM) used to produce a monochromatic electron beam, an effusive gas inlet system used to introduce the precursor molecules into the collision chamber and a HIDEN EPIC 1000 quadrupole mass spectrometer (Hiden Analytical, Warrington, UK) used to detect the subsequently produced ions. In the TEM shown in Fig. 4.1 (bottom), electrons with a broad energy distribution (~1 eV FWHM)

are emitted from a tungsten filament. The emitted electrons are then guided by the electric field generated by the lens components M2 - M4. The guided electrons then enter into a deflection region, where they experience a crossed electric field (from the M5 and M6 lenses) and magnetic field, which is generated with a pair of magnetic coils situated outside the vacuum chamber. Under this crossed electric and magnetic field, an electron will drift in the x-direction independent of its velocity in the z direction. The drift of an electron in the x direction is given by eq. 4.1 (it is also shown in Fig. 4.1):

$$v_x = \frac{E \times B}{|B|^2} \tag{4.1}$$

Since the electric and magnetic fields are perpendicular to one another, equation 4.1 can be rewritten as:

$$v_x = \frac{E}{B} \tag{4.2}$$

After passing through the deflection region, the electrons exit through the aperture of M7. This aperture is offset by 2.4 mm with respect to the aperture on M4; therefore, due to the electron drift in the x-direction only electrons with a narrowly selected velocity will exit through the M7 aperture. Therefore, after the deflection region, the trochoidal electron monochromator will produce electron beams of a significantly more narrow FWHM when compared to its original width of ~1 eV.

The monochromator lens voltages are referenced to a floating potential and collision lens voltages are referenced to ground. Particular electron energy can be achieved by ramping the monochromator's reference potential. Electrons with the desired energy then enter into the collision region (see Fig. 4.1), where they interact with an effusive beam of precursor molecules, forming ions as described in the previous chapter. The precursor molecules introduce into the vacuum chamber/collision region through an inlet system. The end side of the inlet system which connects to the vacuum chamber is a capillary tube which helps to get an effusive flow of precursor molecules. The ions formed in the collision region are then extracted by applying a weak electric field (~1V/cm) between lenses C2 and C3. The extracted ions are subsequently focused into the quadrupole mass spectrometer using the focus elements F1-F3 (see Fig. 4.1). Any electrons that traveled through the collision region are then collected in the faraday cup (see Fig. 4.1). This gives some insight into the electron current in the monochromator, as well as reducing the possibility of scattering transmitted electrons back into the collision region. In order to avoid charging on the monochromator lenses due to condensation or deposition of precursor molecules on their surfaces, the monochromator was maintained at a temperature of about 393 K.

For the measurement of $HFeCo_3(CO)_{12}$, the precursor was sublimed at 348 - 353 K, and the working pressure was ~4 x 10^{-7} mbar (base pressure was ~6 x 10^{-8} mbar). In the case of $H_2FeRu_3(CO)_{13}$, the precursor was sublimed at 338 - 343 K, with a working pressure of 2 - 4 x 10^{-7} mbar. Both $HFeCo_3(CO)_{12}$ and $H_2FeRu_3(CO)_{13}$ are introduced into the vacuum chamber/collision region through an inlet system and the precursor flow was controlled using a ball valve. The precursor molecule TSCH was sufficiently volatile at room temperature and was introduced into the vacuum chamber/collision region through the inlet system without heating. The TSCH flow was controlled using a

leak valve and a working pressure of about 1 x 10^{-6} mbar was used for its gas phase measurement.

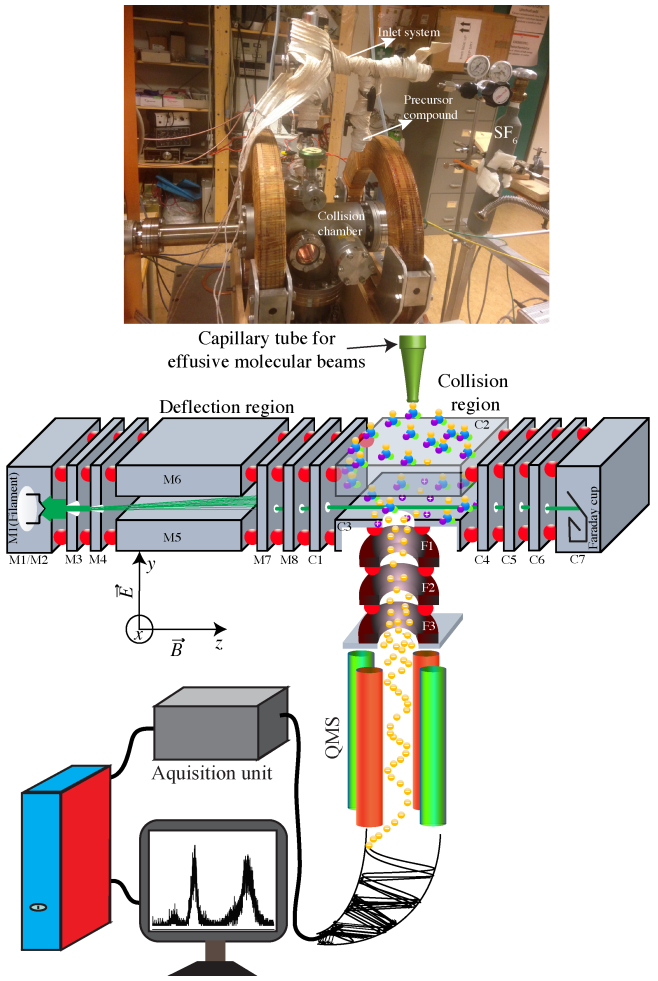

Figure 4.1. Upper side shows the picture of SIGMA used for the gas phase study and bottom side shows its schematic. The direction of electric and magnetic field in the deflection region is shown with black arrows, the drift of electron beams in the deflection region is shown with green lines. In the collision region energy selected electron beams crosses with effusive beam of precursor molecules. The ions formed in the collision region detects using QMS, detection of only negative ions is shown in the schematic.

Energy scale calibration

Electron energy scale was calibrated to the formation of SF_6^- from SF_6 at 0 eV. A typical negative ion yield curve for SF_6^-/SF_6 obtained during the gas phase measurement is

shown in Fig. 4.2. With an SF_6 pressure of 2 x 10^{-7} mbar, the intensity and FWHM of SF_6^- obtained here were 1.5 x 10^5 counts/s and 100 meV, respectively (see Fig. 4.2). It is well known that SF_6^-/SF_6 forms a very narrow energy resonant structure close to 0 eV with width of resonance <1 meV [141]. Due to this very narrow FWHM of SF_6^-/SF_6, energy calibration with SF_6^- gives a good estimation of the actual energy distribution.

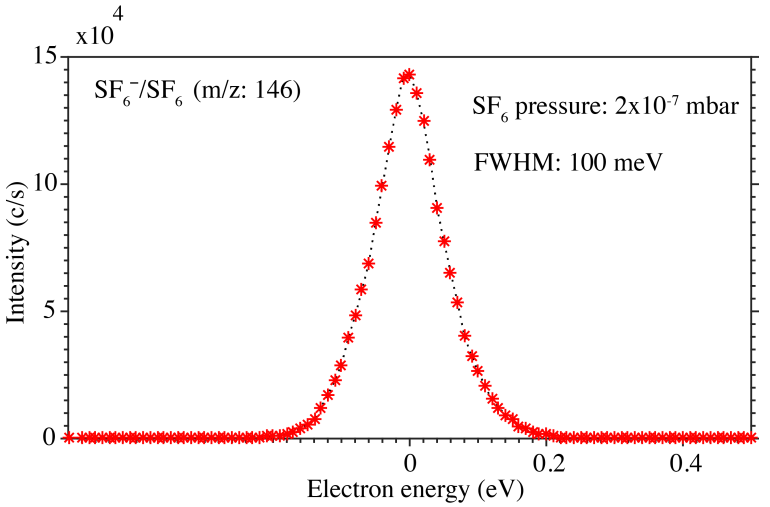

Figure 4.2. Typical ion yield curve obtained for SF_6^-/SF_6 during the gas phase measurements from SIGMA.

Appearance energy determination

There is actually no physically meaning ful approach to determine the appearance energy of negative ion formation in the DEA process. We tried finding appearance energy by fitting the rising part of negative ion yield curve using a Wannier type function [142,143], however it often shows deviation from the onset of negative ion yield curve. Because of the deviation, we used another approach in which appearance energy measurements were done by fitting a straight line to the rising side of the respective ion yield curves and extrapolating it to the base line of the ion yield curve. Examples of fitting and subsequent measurement of appearance energy for several fragments are shown in Fig. 4.3. For all negative ion fragments with sufficient signal-to-noise ratio, both the upper and lower limits of the appearance energy are determined from the straight-line fitting. The upper limit is estimated from the straight-line fitting to the extended portion of the rising side of the respective ion yield curves, the lower limit is estimated from the straight-line fitting to the base line of respective ion yield curve. For the negative ion fragments with low signal-to-noise ratio, the uncertainty is simply an estimate (see Fig. 4.3).

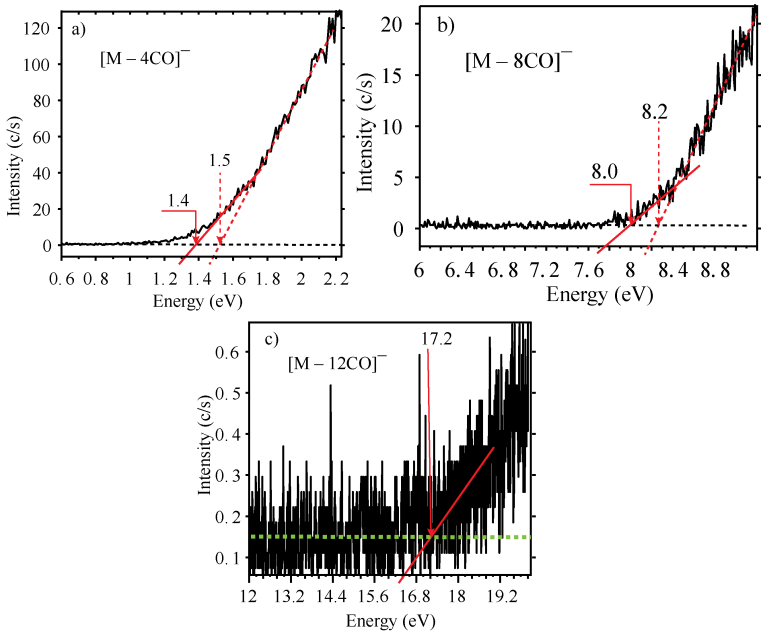

Figure 4.3. Examples for determining the appearance energy from straight line fitting to three fragments: $[M - 4CO]^-$, $[M - 8CO]^-$ and $[M - 12\ CO]^-$, where M is $HFeCo_3(CO)_{12}$. The upper and lower limits are indicated with dashed and solid red lines respectively. Because of the low signal-to-noise ratio, the lower and upper limits of the appearance energy for $[M - 12CO]^-$ (c) could not be directly measured from the fitting shown in (a) and (b), thus it is determined by visual inspection. Adapted with permission from ref. [144], Copyright EDP Sciences, SIF, Springer-Verlag Berlin Heidelberg 2016.

4.3 Surface experimental

All surface experiments were carried out in a UHV chamber. The UHV chamber is equipped with a flood gun used for electron irradiation, and an X-ray photoelectron spectrometer (XPS) and a mass spectrometer (MS) for analyzing the electron-induced surface reactions. More information about the UHV instrumental setup and its capabilities can be found in ref. [40, 68]. A picture and schematic of the UHV surface study experimental setup is shown in Fig. 4.4. In the work presented in this thesis, the IR analyzer was not used; all other analytical techniques shown in Fig. 4.4 were utilized. The UHV surface experimental details concerning the work presented in this thesis are discussed below.

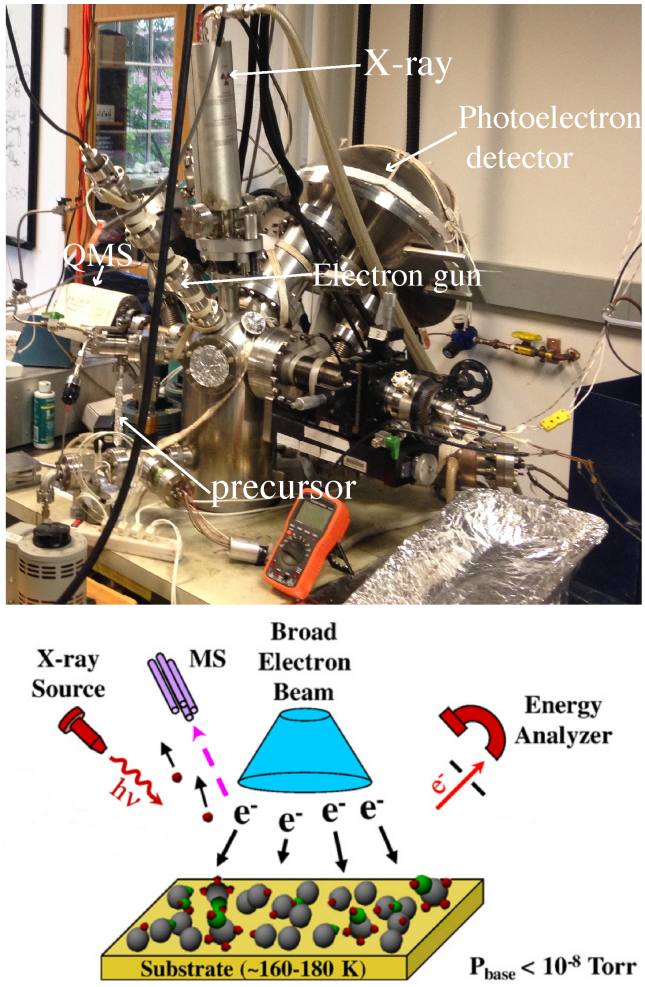

Figure 4.4. Picture of UHV surface study experimental setup (upper side) and its schematic (lower side), adapted with permission from ref. [70]. X-ray source and photoelectron detector (Energy analyzer) used to monitor the stoichiometric change in the film and MS used to detect the species desorbed from the surface during electron induced reactions.

Sample handling: Both the $HFeCo_3(CO)_{12}$ and $H_2FeRu_3(CO)_{13}$ precursors were individually loaded into a glass finger (shown in Fig. 4.4, labeled "precursor") inside a N_2 glove box and attached to a UHV-compatible precision leak valve, which helped to minimize any oxidation of the precursor molecules. The glass finger/UHV leak valve assembly was then attached to UHV chamber wherein the experiments took place. Due to the low volatility of $HFeCo_3(CO)_{12}$ and $H_2FeRu_3(CO)_{13}$, the glass finger could be evacuated by directly pumping through the leak valve at room temperature (RT). The

evacuation of the glass finger was repeated several times in order to remove any N_2 or degassed CO present in the glass finger.

Substrate: All surface experiments were conducted on a polycrystalline gold substrate. Gold was chosen as a substrate due to its inert behavior and lack of XPS peak overlap with the XPS peaks of elements present in the precursor molecules (C, O, Fe, Co and Ru). Prior to each surface experiment, the gold substrate was cleaned by sputtering with 4 keV Ar^+ ions and surface cleanliness was ensured by examining the XPS spectra in the C(1s) and O(1s) regions.

Creating $HFeCo_3(CO)_{12}$ and $H_2FeRu_3(CO)_{13}$ films: Since both precursor molecules were low volatility compounds, we heated the glass finger in order to get sufficient pressure of the precursor molecules. The precursor molecule $HFeCo_3(CO)_{12}$ was sublimed by heating to ~348 K, which increased the chamber pressure from a background pressure of ~7 x 10^{-9} Torr to ~8 x 10^{-7} Torr. The precursor molecule $H_2FeRu_3(CO)_{13}$ was more sensitive towards thermal decomposition, therefore that precursor molecule was heated in the range of 338 - 343 K. With this heating, the chamber pressure increased to ~3 x 10^{-7} Torr. After introducing the precursor into the UHV chamber, nanometer-thick films of these precursor molecules were formed by adsorption onto the sputter-cleaned gold substrate at a substrate temperature of 153 K. In the case of $H_2FeRu_3(CO)_{13}$, it was necessary to dose the precursor molecules continuously for 4 hours in order to obtain sufficiently thick $H_2FeRu_3(CO)_{13}$ films for the experiments; however, in the case of $HFeCo_3(CO)_{12}$, it was only required to dose the precursor molecules for 2 hours in order to get sufficiently thick $HFeCo_3(CO)_{12}$ films. The thickness of the deposited films was estimated by measuring the signal attenuation from the substrate Au(4f) XPS peak. For this estimation, an inelastic mean free path of 2 nm for Au(4f) photoelectrons was used [10]. A typical $HFeCo_3(CO)_{12}$ film thickness was estimated to be in the range of ~1.4 - 1.6 nm. In the case of $H_2FeRu_3(CO)_{13}$, the estimated film thickness was in the range of ~1.1 - 1.4 nm. These film thicknesses correspond to an average coverage of 1 - 2 monolayers for both precursor molecules. During the surface experiments, the substrate temperature was increased from 153 K to 213 K to ensure that any water co-adsorbed in the film had desorbed prior to electron irradiation.

Electron source: A commercial flood gun (Specs FG 15/40) was used for the irradiation of the adsorbed films. The electron flux was measured by recording the current in the substrate. By keeping the target current constant during the experiment, we maintained a constant electron flux for each particular XPS measurement. For all the surface results presented in this thesis, the electron flux is reported in terms of electron dose (electron dose = target current x electron exposure time). The incident electrons have energy of ~500 eV. This is the sum of the electron energy from the flood gun (+480 V) and a positive bias of +20 V, which was applied to prevent the escape of SEs generated by the primary electrons.

X-ray photoelectron spectroscopy: The XPS used to monitor the stoichiometric and elemental changes in the film was a PHI 5400 XPS using Mg Kα X-rays ($h\nu$ = 1253.6 eV). A commercial software CASA XPS was used to de-convolute the measured XPS spectra. The binding energy for all the elements (C(1s)/Ru(3d), O(1s), Fe(2p) and Co(2p)) were calibrated by aligning the Au($4f_{7/2}$) XPS peak to 84.0 eV.

Mass spectrometry: The species desorbing from the surface were monitored using a quadrupole mass spectrometer (Balzers Prisma QMS, 0-200 amu) located ~5 cm away from the sample.

4.4 FEBID experimental

All FEBID experimental work for DCSCH, SCH and TSCH was carried out in an FEI NovaNanoLab 650 dual beam scanning electron microscope. The precursor molecules were introduced into the electron microscope chamber using a home-built inlet system, which consists of a precision leak valve and stainless-steel sample container. Fig. 4.5 shows a picture of the FEBID setup and the inlet system. Usually in a FEBID system, a gas injection system (GIS) is used to introduce the precursor molecules; however, due to the high volatility of the precursor molecules (DCSCH, SCH and TSCH) used in the current work, it was not possible to use a commercially available GIS. With the leak valve attached to the FEBID system, we could more precisely control the flow of precursor molecules.

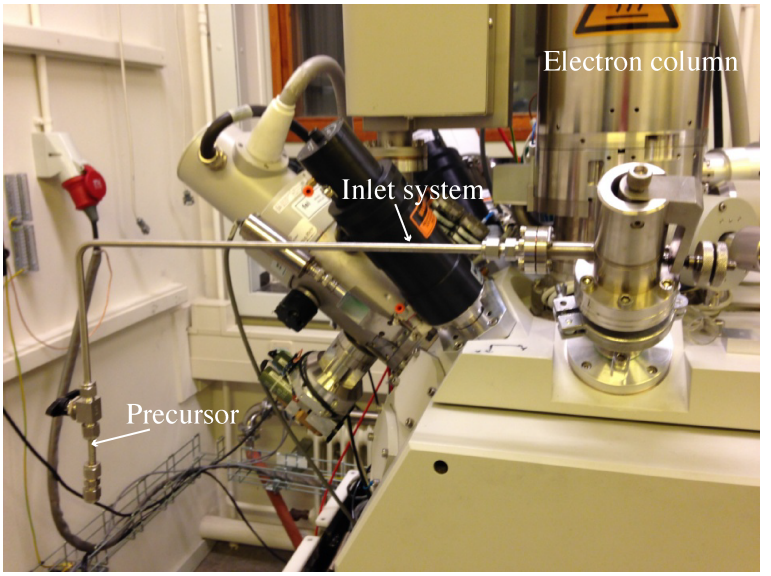

Figure 4.5. Picture of FEBID setup (NovaNanoLab 650 dual beam scanning electron microscope) with inlet system used to introduce the precursor molecules into FEBID chamber.

All FEBID experiments were performed at room temperature (25 ^{0}C). The typical background pressure in the FEBID chamber was ~7 - 9 x 10^{-7} mbar. By leaking the precursor molecules into the FEBID chamber through the leak valve, a precursor pressure of ~3 x 10^{-5} mbar was maintained for all three precursor molecules (DCSCH, SCH and TSCH) during the experiment. For the DCSCH and SCH FEBID experiments,

all pillars were deposited with a primary electron energy of 20 keV and current of 150 pA. For TSCH, pillars were deposited with three different primary electron beam energies: 20, 5 and 1 keV, the primary electron beam current was 150, 98 and 30 pA, respectively. All depositions were imaged using the same scanning electron microscope using a 20 keV, 150 pA primary electron beam. Pillar deposition was achieved by keeping the primary electron beam in the stationary mode. The position and exposure time of primary electron was controlled using a stream file generated with the help of MATLAB. In order to determine the elemental composition of the deposit, energy dispersive spectra (EDX) analysis of large volume deposits on gold substrate performed. The substrate used for all depositions was silicon, except for the EDX measurement, where gold substrates were used to avoid EDX overlap contribution from the substrate. In order to avoid any further deposition due to remaining precursor molecules and residual gases while imaging at least 90 minutes pump out time was allowed before imaging. After this waiting period, the pressure in the SEM chamber was reduced back to the initial background pressure of ~9 x 10^{-7} mbar.

The parameters of deposited pillars, such as pillar height and base diameter, are determined from the SEM images of pillars using image J program [145]. The base diameter for all pillars was measured by fitting an ellipse to the base plane of the pillars in an image taken at a tilted angle. The pillar height was also measured from the same tilted image by finding the distance between the center of the ellipse in the base plane to the apex of the pillar. The tilt correction was incorporated to get the actual pillar height. The pillar tip cone angle was measured by fitting a straight line to the edge of the pillar tip using the imageJ program [145]. The volume of the deposited pillars was measured by approximating the pillar as a combination of the lower cylindrical part and the upper conical part. The volume growth rate is then estimated from the measured volume of the pillars. The volume of the bulged structure observed on the top of pillars deposited from TSCH with 5 keV primary electron beam was estimated by assuming it as ellipsoid shape. For the EDX measurements, an Oxford instruments 80 mm^2 detector was used.

4.4.1 Thermochemical threshold calculations

The thermochemical threshold for negative ion formation of a general DEA process can be assumed as approximately the enthalpy of the reaction, given by:

$$\Delta H_r = \sum H(products) - H(educt) \tag{4.3}$$

where $\sum H(products)$ represents the total energy of both anionic and neutral fragments formed in the DEA process and H(educt) represents the energy of parent neutral molecule. The energy of the fragments and the neutral parent molecule can be calculate using quantum chemical calculations which are described below.

All quantum chemical calculations, which were performed for bimetallic precursor molecules $HFeCo_3(CO)_{12}$ and $H_2FeRu_3(CO)_{13}$, were carried out using the computational chemistry software ORCA [139]. The geometry optimizations for the relevant molecules and fragments were performed using the density functional theory (DFT) method BP86 [135, 136] and the def2-TZVP [146] basis set. Based on the optimized geometries, the single point energies were calculated with the hybrid DFT functional

PBE0 [137, 138] and the minimally augmented polarized triple zeta basis set ma-def2-TZVP [146, 147]. The zero-point energy contribution for the fragments were calculated at BP86/def2-TZVP level of theory. The thermochemical threshold for each fragment formation in DEA to $HFeCo_3(CO)_{12}$ and $H_2FeRu_3(CO)_{13}$ was estimated from the calculated single point energies by using equation (4.3) shown above. As the DEA experiments were performed at about 353 K for $HFeCo_3(CO)_{12}$ and at about 343 K for $H_2FeRu_3(CO)_{13}$, the calculated thermal energy of the neutral molecule at the respective temperatures were included in the thermochemical threshold estimation. The thermal energy of $HFeCo_3(CO)_{12}$ calculated at 353 K is about 1.2 eV and that for $H_2FeRu_3(CO)_{13}$ at 343 K is about 1.16 eV. The thermally-corrected values were then obtained by adding the thermal energy to the total energy of the parent molecule. At a given temperature, the internal energy of the molecule has Maxwell-Boltzmann distribution. Therefore, some DEA channels which are thermochemical not possible at 0 eV may active due to hot band transition of molecules associated with high energy tail of Maxwell-Boltzmann distribution. The molecular orbital diagram for $HFeCo_3(CO)_{12}$ and $H_2FeRu_3(CO)_{13}$ was calculated at BP86/def2-TZVP level of theory. All optimized geometries and iso-surfaces of molecular orbitals, as well as spin density maps for $HFeCo_3(CO)_{12}$ and $H_2FeRu_3(CO)_{13}$, were plotted using the VMD program [148].

5 Results and discussions

5.1 $HFeCo_3(CO)_{12}$

5.1.1 Gas phase study of $HFeCo_3(CO)_{12}$

5.1.1.1 Introduction and motivation for the study

For the last few years the awareness of the importance of low energy electron interactions with FEBID precursor molecules increased significantly because of its role in determining the chemical composition and resolution of structures fabricated with the FEBID technique. There are many gas phase studies reported for FEBID precursor molecules, however this is the first gas phase study for a bimetallic FEBID precursor molecule. $HFeCo_3(CO)_{12}$ is a heteronuclear metal complex first synthesized by Chini *et al* in 1960 [149]. $HFeCo_3(CO)_{12}$ has C_{3v} symmetry with an apex Fe and a Co_3 base plane. The apex Fe has 3 terminal CO ligands and the Co_3 base plane has 6 terminal CO ligands (two CO ligands for each Co) and 3 bridging CO ligands. The hydrogen is situated below the Co_3 base plane, coordinated to all Co atoms. The experimentally determined and computed structures of $HFeCo_3(CO)_{12}$ are shown in the results part of this section (see below). This precursor molecule has been used in chemical vapor deposition (CVD) [46] and photochemical vapor deposition (PCVD) [150] to fabricate mixed Fe/Co thin films. $HFeCo_3(CO)_{12}$ has also been used for the preparation of magnetic ferrofluids [151] which have applications in building nanoscale devices like nanomotors, nanogenerators and nanopumps [152] as well as in magnetically controlled drug targeting [153]. Very recently F Porrati *et al* [45] used this precursor molecule in FEBID for the fabrication of magnetic alloy FeCo nanostructures. $HFeCo_3(CO)_{12}$ is the first heteronuclear precursor molecule used in FEBID to fabricate bimetallic nanostructures. The fabrication of bimetallic nanostructures in FEBID is a recent development. A common method to fabricate bimetallic nanostructures in FEBID is co-depositing different metals simultaneously from separate precursor molecules using dual or multichannel gas injection systems. However, this method has limitations in reproducing the exact deposited structures and it is difficult to get good control over the composition of the deposit. These limitations can be overcome by using bimetallic precursor molecules like $HFeCo_3(CO)_{12}$. In the study by Porrati *et al* [45] the performance of $HFeCo_3(CO)_{12}$ in FEBID was found to be quite good in terms of its chemical composition (>80% metal content) and Fe:Co ratios (~1:3) in the deposit, the hall magnetometric measurements on 50 nm x 250 nm FeCo nanobars showed that the fabricated FeCo structure was ferromagnetic which is the basic property required for building magnetic data storage devices. These FeCo ferromagnetic nanostructures could also be used as a building block for creating nano-sized magnetic recordings read/write

heads [154]. By decreasing the read/write head size to 20 nm, the read/write density of hard disc could increase to 1000 Gbit/in^2 from the current density of 200 Gbit/in^2 [154]. The fabrication of 3D FeCo ferromagnetic structures using $HFeCo_3(CO)_{12}$ can be also useful to study the physics of 3D nanomagnetics and its potential applications [48].

The good performance of $HFeCo_3(CO)_{12}$ in FEBID and the lack of sufficient knowledge about the electron interaction with $HFeCo_3(CO)_{12}$ motivated the current gas phase study of $HFeCo_3(CO)_{12}$ under single electron/molecule collision conditions. In the current gas phase study of $HFeCo_3(CO)_{12}$, the negative ion formation through electron attachment dissociation of $HFeCo_3(CO)_{12}$ and the positive ion formation through electron impact ionization of $HFeCo_3(CO)_{12}$ will be mainly discussed. The quantum chemical calculations on the structure of $HFeCo_3(CO)_{12}$ and the energetics of negative ion formation through electron attachment to $HFeCo_3(CO)_{12}$ are used to aid the interpretation of gas phase data. The details of experimental and computational methods used for the gas phase study of $HFeCo_3(CO)_{12}$ can be found in section 4.2.

5.1.1.2 Results and discussions

Geometrical and electronic properties of the neutral and anionic ground state of $HFeCo_3(CO)_{12}$

The experimentally determined structure of neutral $HFeCo_3(CO)_{12}$ from single crystal X-ray diffraction is shown in Fig. 5.1a. The relaxed ground state neutral and anionic geometry of $HFeCo_3(CO)_{12}$ computed at BP86/def2-TZVP level of theory (i.e BP86 functional and def2-TZVP basis set are used, see section 3.3) are shown in Figs. 5.1b and 5.1c, respectively. A comparison of geometrical parameters like bond length and bond angles of neutral $HFeCo_3(CO)_{12}$ as determined from the single crystal X-ray diffraction along with the similar parameters calculated from the quantum chemical calculations can be found in article 1. The calculated metal-metal bonds, i.e., the Co-Co and Co-Fe bonds in $HFeCo_3(CO)_{12}$ are 2.509 Å and 2.540 Å, respectively, which matches well with the experimentally determined values of 2.492 and 2.550 Å. The experimentally determined average bond lengths for terminal CO groups: Fe-CO, Co-CO_{above} (above the Co_3 base plane) and Co-CO_{below} (below the Co_3 base plane) are 1.808, 1.778, and 1.839 Å, respectively. The calculated values for these bond lengths are slightly lower than the experimentally determined bond lengths, however the deviation from the experimental values are only 1.7, 1.0, and 2.8%, respectively. In the case of bond lengths for the Co-CO-Co bridging bond, the calculated value of 1.959 Å matches well with the experimentally determined value of 1.974 Å. Since the hydrogen atom is insensitive to X-ray diffraction experiments, it is not possible to determine the position of hydrogen in $HFeCo_3(CO)_{12}$ using X-ray diffraction, but our calculations suggest that the position of hydrogen atom is 0.964 Å below the Co_3 base plane. The H-Co bond length estimated from the calculated position of hydrogen and cobalt is 1.717 Å, which is in good agreement with neutron diffraction study on the H-Co bond length in $HFeCo_3(CO)_9(OCH_3)_3$ [155] . In the neutron diffraction study, the H-Co bond length is found to be 1.734 Å and the determined position of hydrogen atom is 0.978 Å below the Co_3 base plane.

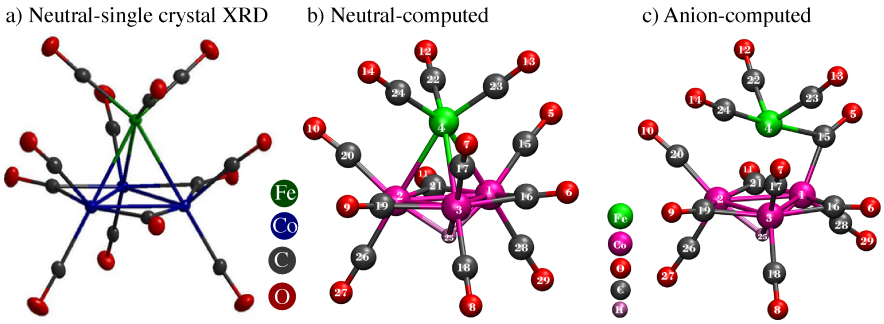

Figure 5.1. Geometry of neutral $HFeCo_3(CO)_{12}$ as determined a) experimentally and b) from quantum chemical calculations. c) Calculated ground state anionic geometry of $HFeCo_3(CO)_{12}$, adapted with permission from ref [144], Copyright EDP Sciences, SIF, Springer-Verlag Berlin Heidelberg 2016.

When an electron attaches to a neutral molecule, the molecule's geometry changes to redistribute the excess energy. The most noticeable changes that occur to the neutral ground state geometry of $HFeCo_3(CO)_{12}$ is the weakening of bonding between the Fe apex and Co_3 basal plane [144]. This is clearly reflected in the elongation of two of the three Fe-Co bonds (see positions of Co2 and Co3 in Fig 5.1b, c) from 2.54 Å in the neutral to 2.879 Å (Co2) and 2.868 Å (Co3) in the anion. The terminal CO ligand originally attached to Co1 changed to a bridging ligand, which connects Fe and Co1. As a consequence, the distance between Fe and C15 reduced from 2.866 Å in the neutral geometry to 2.124 Å in the anion geometry [144].

Some changes are observed in bond angles when converting ground state neutral $HFeCo_3(CO)_{12}$ to its anion. The most noticeable angle change occurs for the position of the $Fe(CO)_3$ apex group relative to the Co_3 base. As a result, the angle C24-Fe4-C19, changes from 73.7^0 in the neutral to 64.9^0 in the anion geometry. The angles C22-Fe4-C21 and C23-Fe4-C16 change from 73.6^0 and 73.7^0 in the neutral geometry to 80.3 and 80.6^0, respectively in the relaxed anion geometry. A detailed discussion of structural changes during electron attachment can be found in article 1.

The structural change, i.e. weakening of bonds between the apex Fe and the Co_3 base plane and transformation of one of the terminal Co-CO ligand to an Fe-(CO)-Co bridging ligand, occurs during the attachment of the electron to the neutral $HFeCo_3(CO)_{12}$. This is in good agreement with the observation of $[Fe(CO)_4]^-$ in DEA to $HFeCo_3(CO)_{12}$. $[Fe(CO)_4]^-$ is the second most intense fragment observed in DEA to $HFeCo_3(CO)_{12}$ (more details are discussed in the below sections) and appeared at 0 eV electron energy. This observation is also consistent with the analysis of HOMO and LUMO iso-surfaces of the neutral $HFeCo_3(CO)_{12}$ and the SOMO iso-surface of its anion as shown in Fig. 5.2. It is further consistent with the analysis of the spin density of anion shown in Fig. 5.3. From the HOMO iso-surface of neutral $HFeCo_3(CO)_{12}$, the metal-metal bonding character between the Fe apex and Co_3 base is very clear, while the LUMO iso-surface of neutral $HFeCo_3(CO)_{12}$ shows an anti-bonding metal-metal character between the Fe apex and Co_3 base. The SOMO of the $HFeCo_3(CO)_{12}$ anion has similar character as the LUMO of neutral $HFeCo_3(CO)_{12}$. The spin density of $HFeCo_3(CO)_{12}$ anion shown

in Fig. 5.3 is mostly located in the Fe apex region which indicates that the attached electron is localized around the Fe apex and makes significant changes to the Fe apex region [144].

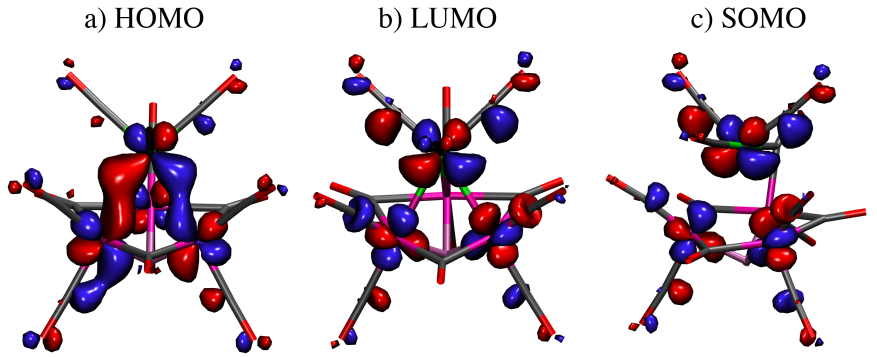

Figure 5.2. (a) The highest occupied molecular orbital (HOMO) and (b) the lowest unoccupied molecular orbital (LUMO) of $HFeCo_3(CO)_{12}$. (c) The singly occupied molecular orbital (SOMO) of the ground state anion; $[HFeCo_3(CO)_{12}]^-$ in its relaxed geometry, adapted with permission from ref. [144], Copyright EDP Sciences, SIF, Springer-Verlag Berlin Heidelberg 2016.

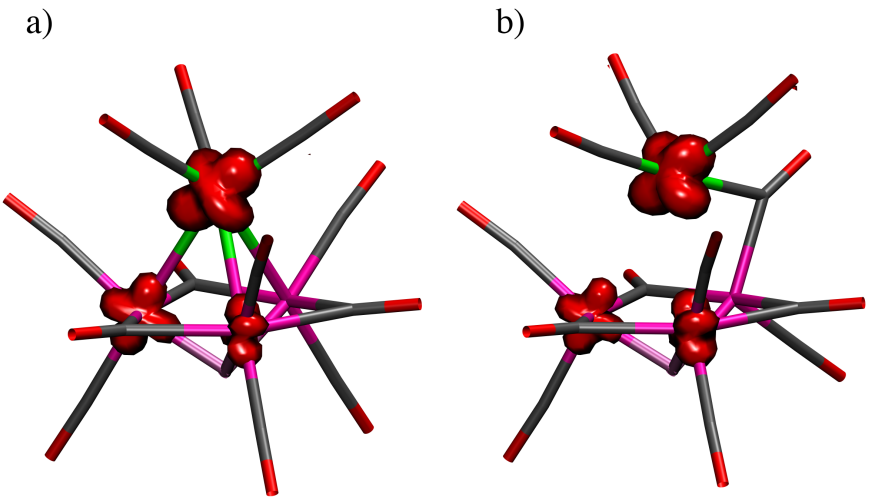

Figure 5.3. (a) Spin density of the anion; $[HFeCo_3(CO)_{12}]^-$ in the constrained geometry of the neutral (vertical transition) and (b) spin density of anion in its relaxed ground state geometry, adapted with permission from ref. [144], Copyright EDP Sciences, SIF, Springer-Verlag Berlin Heidelberg 2016.

Negative ion formation upon electron attachment to $HFeCo_3(CO)_{12}$

All the detectable negative ions formed from electron attachment to $HFeCo_3(CO)_{12}$ are identified by performing a full range negative ion mass scan (10 to 560 amu) at different incident electron energies (0, 1.5, 3.5, 4.5, 6, 8, 10.5, 13 and 19 eV). Three groups of negative ions along with the parent molecular anion are observed in the negative ion mass scan. Negative ions formed in the first group are $[M - n(CO)]^-$, where M is the parent molecule $HFeCo_3(CO)_{12}$ and n varies from 1 to 12. Negative ions formed in the second group are $[M - Co(CO)n]^-$, where n varies from 4 to 10. The third group of negative ions consist of $[Fe(CO)_2]^-$, $[Fe(CO)_3]^-$ and $[Fe(CO)_4]^-$. Although our measurements cannot provide insights into the structure and thermodynamical stability of the individual fragments, we can confidently say that the detected fragments are stable within the time scale of our mass spectrometric detection system. The most probable structure of fragments formed in the electron attachment dissociation of $HFeCo_3(CO)_{12}$ are computed with quantum chemical calculations. Some of them are shown in Fig. 5.4. Since our mass spectrometric measurements are only capable of detecting charged species, we don't have any information about the neutral species formed by the interaction of electrons with $HFeCo_3(CO)_{12}$. The three groups of negative ions formed by the electron attachment to $HFeCo_3(CO)_{12}$ can be schematically represented by the following equations.

$$e + M \rightarrow M^{(\ddagger)-} \rightarrow [M - n(CO)]^- + n(CO) \quad (n = 1 - 12) \tag{5.1}$$

$$e + M \rightarrow M^{(\ddagger)-} \rightarrow [M - Co(CO)_4 - n(CO)]^- + Co(CO)_4 + n(CO) \quad (n = 0 - 6) \tag{5.2}$$

$$e + M \rightarrow M^{(\ddagger)-} \rightarrow [Fe(CO)_n]^- + HCo_3(CO)_8 + (4 - n)(CO) \quad (n = 2 - 4) \tag{5.3}$$

Before discussing the details of negative ion yield curves for these fragments, the thermochemical threshold calculations of these fragments will briefly be discuss.

For all threshold calculations, the geometries are optimized at BP86/def2-TZVP level of theory. Based on the energy of optimized geometries, thermochemical threshold values are calculated at the same level of theory and also at PBE0/ma-def2-TZVP level of theory. The structural optimization is explored for various possibilities of removing CO ligands from different positions of the $HFeCo_3(CO)_{12}$ molecule; these can be found in article 1. From the structural optimization, it is found that the removal of CO ligand from the Fe apex is most favorable.

Fig. 5.4 shows the structure of lowest energy optimized $[M - n(CO)]^-$ species along with their experimentally determined appearance energy (AE) values, thermochemical threshold values calculated at BP86/def2-TZVP and PBE0/ma-def2-TZVP levels of theory, respectively, and thermally corrected threshold values calculated at the PBE0/ma-def2-TZVP level of theory. As we can see from Fig. 5.4, the thermally corrected thermochemical threshold values calculated at the PBE0/ma-def2-TZVP level of theory are much closer to the experimentally determined AE values. The threshold values calculated at the BP86/def2-TZVP level deviate from the experimental AE values; the deviation increases with the removal of CO ligands. Even when including the ZPE and thermal energy corrections, the deviation of the calculated thermochemical threshold

values from the experimental AEs are in the range from 0.7 to 3.5 eV for removing three CO to nine CO ligands, respectively.

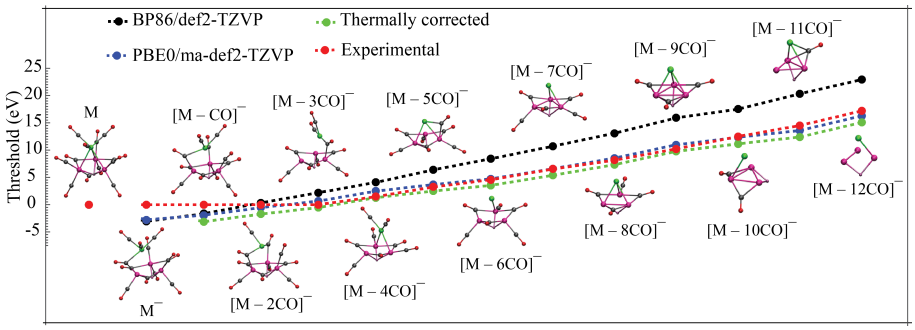

Figure 5.4. Calculated threshold values at BP86/def2-TZVP and PBE0/ma-def2-TZVP level of theory and the optimized geometries of the corresponding anions, adapted with permission from ref. [144], Copyright EDP Sciences, SIF, Springer-Verlag Berlin Heidelberg 2016.

Formation of the molecular anion and the first group of negative ions

The negative ion yield curve for the formation of the molecular anion and the first group of negative ions (sequential loss of CO ligands) upon electron attachment is shown in Fig. 5.5. The thermochemical threshold values calculated at PBE0/ma-def2-TZVP (discussed above), experimentally determined AE values, energy position of negative ion yield curve peak maxima, and integrated intensity of negative ion yield curves for all detected negative ions, are tabulated in Table 5.1. From Table 5.1 it is apparent that the adiabatic electron affinity of $HFeCo_3(CO)_{12}$, calculated at the PBE0/ma-def2-TZVP level of theory, is 2.77 eV and the loss of one, two and three CO ligands are found to be exothermic by 3.13, 1.74 and 0.54 eV, respectively. This is in accordance with the observation of the molecular anion and the loss of one, two and three CO ligands at 0 eV upon electron attachment to $HFeCo_3(CO)_{12}$. The relative intensity of the negative ion yield curves reflects the survival probability of negative ions towards autodetachment and further decompositions. The time required to extract the ions from the electron - molecule interaction zone of our instrument is ~10 μs and the time required for the ions to travel through the quadrupole mass filter is ~50 μs. This means that all the negative ions detected in our instrument are formed within the first ~10 μs and have lifetimes greater than 50 μs. The survival probability and lifetime of negative ions will be reflected in the intensity and energy dependence of their negative ion yield curves. Although losses of the initial three CO ligands are exothermic in nature, the most intense negative ion fragment observed was the loss of two CO ligands. This could be understood by considering the efficiency of the excess energy distribution. Loss of one CO ligand is exothermic by 3.13 eV, which may result in further dissociation, while losses of two CO ligands is exothermic by 1.74 eV which is probably lower or close to the threshold energy required for any further CO loss and may be efficiently distributed within the anion as vibrational energy. (It is noteworthy that $[M - 2CO]^-$ has 69 vibrational degrees of freedom).

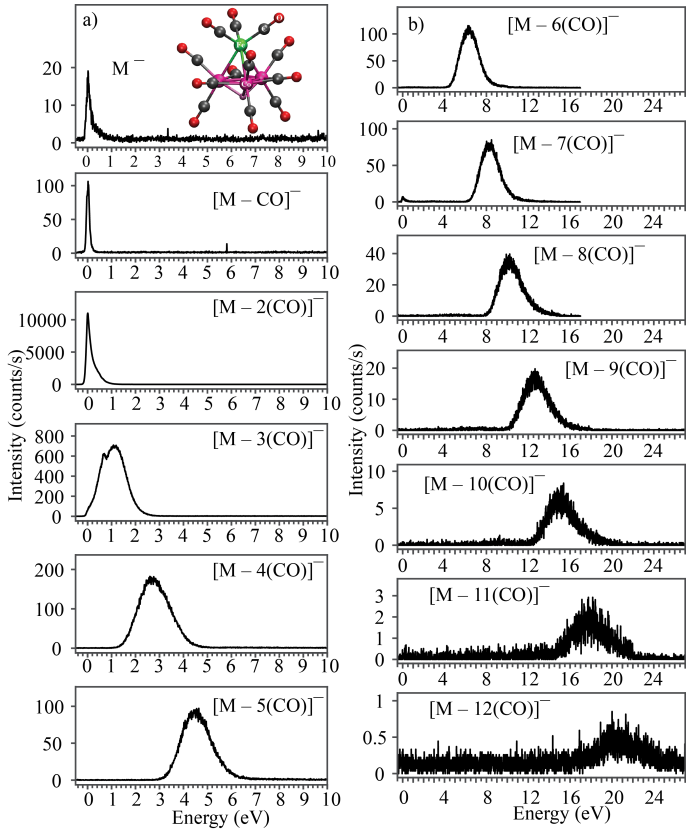

Figure 5.5. Negative ion yield curve corresponding to the formation of molecular anion M^- ($[HFeCo_3(CO)_{12}]^-$) and sequential loss of COs ($[M - n(CO)]^-$).

As discussed above, the detection of the $HFeCo_3(CO)_{12}$ molecular anion in our instrument indicates that $[HFeCo_3(CO)_{12}]^-$ has a lifetime of at least ~50 μs. There is only one previous report of metal carbonyl molecular anion detection, which was from electron attachment to $V(CO)_6$ [156]. Another organometallic precursor molecule, $Pd(hfac)_2$, also forms molecular anion upon electron attachment [28]. As we can see from its negative ion yield curve (see Fig. 5.5), the molecular anion at 0 eV competes with fragmentation channels such as the formation of $[M - CO]^-$, $[M - 2CO]^-$, $[M - 3CO]^-$ and $[Fe(CO)_4]^-$. Therefore, the intensity of the molecular anion at 0 eV is weak compared to the respective DEA channels.

Table 5.1. Calculated thermochemical threshold (E_{th}), measured appearance energy (AE), energy position of peak maxima (E.max), and integrated intensity of negative ions and measured intensity of positive ions.

Negative ions	Eth	AE	E.max	Integrated Intensity	Positive ions	Measured Intensity
M^-	-2.77	0	0	7.3E+02	M^+	15
$[M - CO]^-$	-3.13	0	0	3.0E+03	$[M - CO]^+$	6
$[M - 2(CO)]^-$	-1.74	0	0	3.4E+05	$[M - 2(CO)]^+$	5
$[M - 3(CO)]^-$	-0.54	0	0.7, 1.2	9.3E+04	$[M - 3(CO)]^+$	3
$[M - 4(CO)]^-$	1.28	1.4 ± 0.1	2.7	2.9E+04	$[M - 4(CO)]^+$	8
$[M - 5(CO)]^-$	2.49	3.1 ± 0.2	4.5	1.5E+04	$[M - 5(CO)]^+$	23
$[M - 6(CO)]^-$	3.52	4.5 ± 0.2	6.4	2.4E+04	$[M - 6(CO)]^+$	22
$[M - 7(CO)]^-$	5.36	6.4 ± 0.2	8.2	1.8E+04	$[M - 7(CO)]^+$	19
$[M - 8(CO)]^-$	7.32	8.0 ± 0.2	10.2	9.9E+03	$[M - 8(CO)]^+$	15
$[M - 9(CO)]^-$	9.77	10.1 ± 0.2	12.7	5.5E+03	$[M - 9(CO)]^+$	19
$[M - 10(CO)]^-$	11.14	12.4 ± 0.2	15	2.4E+03	$[M - 10(CO)]^+$	15
$[M - 11(CO)]^-$	12.39	14.4 ± 0.2	18	1.0E+03	$[M - 11(CO)]^+$	12
$[M - 12(CO)]^-$	15.05	17.2 ± 0.5	20.2	5.1E+02	$[M - 12(CO)]^+$	15
$[M - Co(CO)_4]^-$	-1.76	0	0, 1	1.0E+03	$[Co_2(CO)_2]^+$	10
$[M - Co(CO)_5]^-$	0.16	0.3 ± 0.2	1.8, 2.5	3.0E+03	$[Co_2]^+$	8
$[M - Co(CO)_6]^-$	2.22	2.3 ± 0.2	3.8, 5.2	1.2E+03	$[CoFe]^+$	12
$[M - Co(CO)_7]^-$	4.26	4 ± 0.2	5.7, 6.7	1.4E+03	$[Fe(CO)_5]^+$	13
$[M - Co(CO)_8]^-$	6.63	7.3 ± 0.2	9	3.0E+02	$[Fe(CO)_4]^+$	18
$[M - Co(CO)_9]^-$	9.54	9 ± 0.2	11.5	4.6E+02	$[Fe(CO)_3]^+$	8
$[M - Co(CO)_{10}]^-$	11.48	12.5 ± 0.2	15	2.6E+02	$[Fe(CO)_2]^+$	15
$[Fe(CO)_4]^-$	-0.78	0	0	2.3E+05	$[Fe(CO)]^+$	44
$[Fe(CO)_3]^-$	0.29	0.7	1.2, 3.5	1.6E+04	Fe^+	40
$[Fe(CO)_2]^-$	-	3	4.3	1.7E+03	-	-

The negative ion yield curve for the loss of three CO ligands shows three very close peaks centered around 0, 0.7 and 1.2 eV. The resonance structures centered at 0 and 0.7 eV are tentatively assigned as vibrational Feschbach resonances (VFR) associated with different molecular vibrational energy levels. This is based on the significance of s-wave attachment at these low energies making significant contributions through shape resonances unlikely.

The resonance structure centered at around 1.2 eV is likely to be associated with a single particle shape resonance. However, in the UV-Visible absorption spectra of the metal carbonyl complex $Co_4(CO)_{12}$, an intense absorption band is observed at 660 nm (1.8 eV) [157]. In our quantum chemical calculations of $HFeCo_3(CO)_{12}$ the energy difference between HOMO and LUMO obtained is ~2 eV. Therefore, it is also possible that the contribution centered at 1.2 eV is due to a core excited resonance enabled through the tail of the Maxwell Boltzmann distribution of internal energies. From Fig. 5.5 one can see that after three CO ligand loss, the negative ion yield contributions for further CO losses systematically shift to higher energies. The shift in energy is approximately equal to the bond dissociation energy of the CO units (~2 eV [144]). This

picture is clearer in Fig. 5.6, where combined negative ion yield curves for sequential loss of 3 - 12 CO ligands are shown. The progression of CO loss from the initially formed TNI and its presence even at 11 eV above the parent's ionization energy (8.5 eV (ref. [144])) is very interesting [158]. By looking at the ion yield structure in Fig. 5.6, one can see that the maximum intensity of $[M - n(CO)]^-$ coincides with the onset of next CO loss $[M - (n\text{-}1)CO]^-$. This is typical for sequential metastable loss where $[M - n(CO)]^-$ is the precursor for $[M - (n+1)CO]^-$ formation. In this case, however, a quasi-continuous electron attachment in the range few eV to about 20 eV would be required. The TNI formed by the electron attachment must also be sufficiently stable towards autodetachment (AD) over this range, to enable such extensive dissociation.

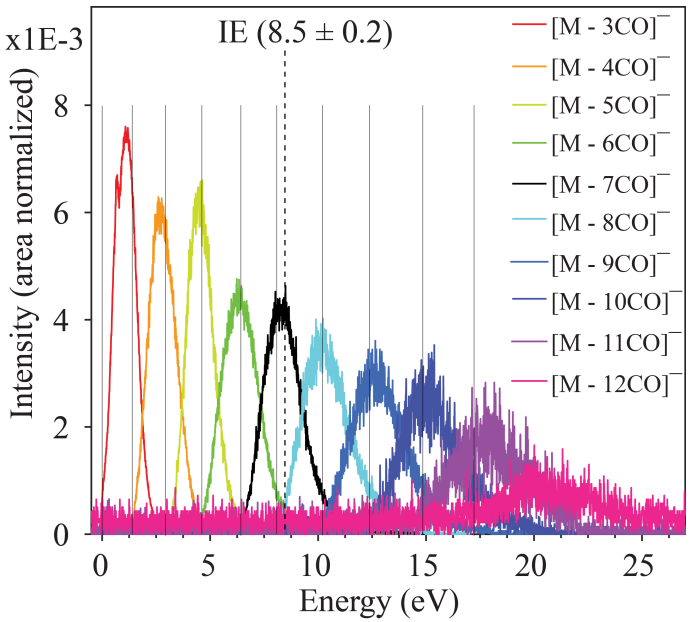

Figure 5.6. Combined negative ion yield curves for $[M - n(CO)]^-$ (n = 3 - 12) formed by DEA to $HFeCo_3(CO)_{12}$ in the energy range 0 - 27 eV. Solid vertical lines represent the AEs of the individual negative ions. The dotted vertical line shows the molecular ionization energy (IE) [144], adapted with permission from ref. [158].

For the quasi continuous electron attachment, there should be a large density of long lived electronic excited states involved in the formation of the TNI. The molecular orbital diagram of $HFeCo_3(CO)_{12}$ is calculated at the BP86/def2-TZVP level of theory to get a picture of the density of excited states [158]. Although the molecular orbital diagram does not reveal the actual anionic excited states, i.e., the state density, it is a reflection of the possible electronically excited states of $HFeCo_3(CO)_{12}$ in this energy range The MO diagram of the $HFeCo_3$ metal core along with those of the metal carbonyls $Fe(CO)_5$, $W(CO)_6$ and $Co_2(CO)_8$ and the hypothetical linear compound $Co_4(CO)_{12}$ (6 bridging COs) are calculated for the purposes of comparison. All of these calculated MO energy diagrams are shown in Fig. 5.7. It is clear that $HFeCo_3(CO)_{12}$ shows dense

"bands" of occupied/unoccupied molecular orbitals close to the HOMO-LUMO gap, while the molecular orbital distribution is very discrete for $Fe(CO)_5$ and $W(CO)_6$. The occupied/unoccupied molecular orbital density close to HOMO-LUMO gap increased for $Co_2(CO)_8$. In the case of hypothetical linear $Co_4(CO)_{12}$ the MO energy diagram is similar to $HFeCo_3(CO)_{12}$ [158].

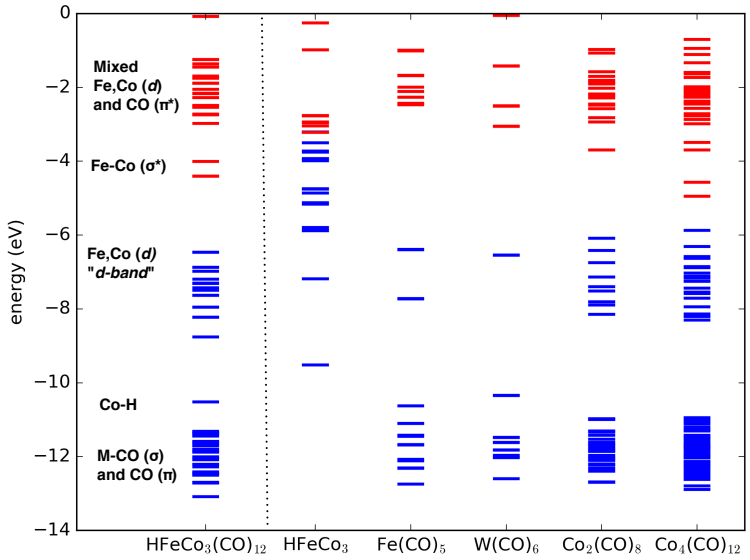

Figure 5.7. Molecular (valence) orbital diagram of $HFeCo_3(CO)_{12}$ (left) compared to the $HFeCo_3$ metal core and simpler carbonyl complexes and the hypothetical linear $Co_4(CO)_{12}$. Occupied orbitals are in blue and unoccupied orbitals red. Orbital labels refer to $HFeCo_3(CO)_{12}$, adapted with permission from ref. [158].

The nature of the molecular orbitals in $HFeCo_3(CO)_{12}$ are labeled in Fig. 5.7. The highest occupied MOs are mostly metal based σ bonding d orbitals. The orbitals situated below this band have Co-H bonding character. The unoccupied MOs are the metal-metal σ^* d-orbitals followed by a dense band of ligand CO π^* orbitals. For core-excited resonances observed at higher energies i.e. above 3 - 4 eV, the electronic transitions between the occupied d-band and the dense CO π^* orbitals might be playing a bigger role. The dense bands of molecular orbitals observed close to HOMO-LUMO gap of $HFeCo_3(CO)_{12}$ enables multiple electron excitation already at 7 eV and at higher energies multi-particle-multi-hole resonances associated with multiple electron excitation become dominant. The incident electron energy of 20 eV is sufficient enough to induce these kinds of transitions of 5 - 6 electrons [158]. Further discussions of the negative ion formation at higher electron energies (i.e. above IE of $HFeCo_3(CO)_{12}$) by electron attachment to $HFeCo_3(CO)_{12}$ can be found in article 2.

Second group of negative ions

The second group of negative ions consists of $[M - Co(CO)n]^-$, where M is the parent molecule and n varies from 4 to 10. The masses of these negative ions are equal

to those of $[M - CoFe(CO)n]^-$, where n varies from 2 to 8. From the structure of $HFeCo_3(CO)_{12}$ (Fig. 5.1) it is obvious that when Fe is removed, three associated CO ligands are also removed. Similarly, when Co is removed, at least two CO ligands associated with the leaving Co atoms will also be removed. Also, from the pattern of negative ion yield curves shown in Fig. 5.8a, it is very unlikely that $[M - CoFe(CO)n]^-$ is formed instead of $[M - Co(CO)n]^-$.

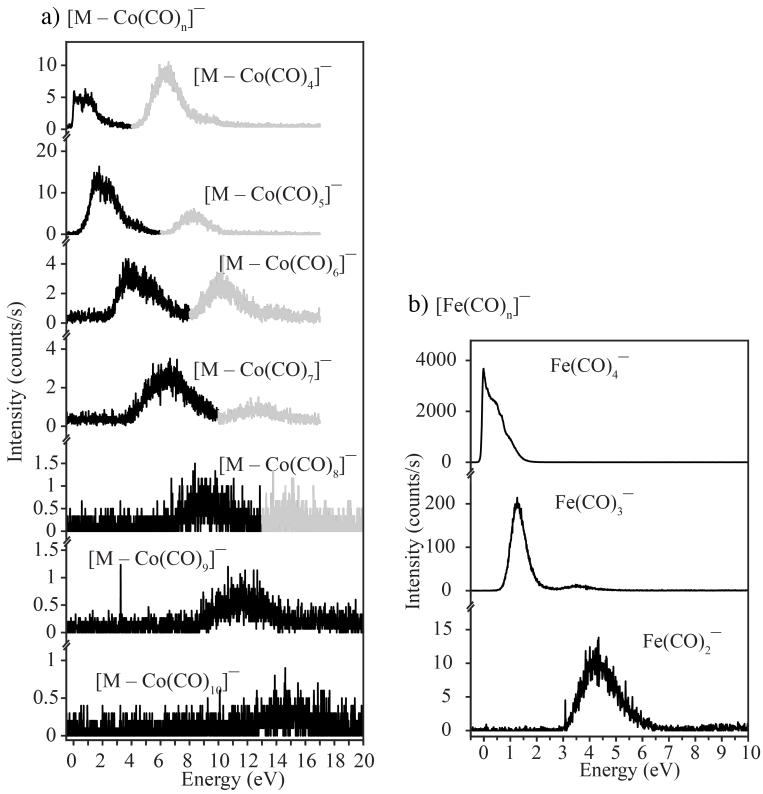

Figure 5.8. Negative ion yield curves of the second group of negative ions ($[M - Co(CO)n]^-$) and the third group of negative ions ($[Fe(CO)_n]^-$) formed from electron attachment dissociation of $HFeCo_3(CO)_{12}$, grey color curves are negative ion yield signal due to the mass overlap with first group of negative ions (sequential CO loss).

From the structure of $HFeCo_3(CO)_{12}$ it is presumed that the $[M - Co(CO)_4]^-$ negative ion is formed by removing one Co and four CO ligands (two terminal and two bridging) associated with Co, and all remaining anions in this category formed by sequential removal of CO from $[M - Co(CO)_4]^-$. The experimentally measured appearance energies, calculated thermochemical thresholds, negative ion yield curve peak maxima and their intensities for second group of negative ions are shown in Table 5.1. Although the formation of $[M - Co(CO)_4]^-$ is exothermic by 1.76 eV, the most intense negative ion fragment observed in this category was $[M - Co(CO)_5]^-$ and

the least intense fragment was $[M - Co(CO)_{10}]^-$. In the negative ion yield curves, the structures observed below 2 eV are most likely associated with single particle shape resonances and the structures observed above 2 eV are likely associated with core excited resonances associated with excitation of one or more electrons to the unoccupied MO.

Third group: formation of $[Fe(CO)_n]^-$

Negative ions formed in the third group consist of $[Fe(CO)_n]^-$, where n = 2 to 4. Negative ion yields corresponding to the formation of these negative ions are shown in Fig. 5.8b. The most prominent dissociation channel observed in this category was the formation of $[Fe(CO)_4]^-$, which is the second most intense negative ion fragment observed in electron attachment dissociation of $HFeCo_3(CO)_{12}$. From the quantum chemical analysis of the LUMO of $HFeCo_3(CO)_{12}$ (see Fig. 5.2), it is clear that the LUMO has anti-bonding character between the Fe apex and basal Co plane. Therefore, it is most likely that the intense contribution of $[Fe(CO)_4]^-$ formation is due to the occupation of an extra electron in the LUMO of $HFeCo_3(CO)_{12}$. In a study by Lomont *et al* [159] it is found that, when $Co_4(CO)_{12}$ is irradiated with 267 and 400 nm photons, the apical-basal cobalt bonds break and a new CO bridging intermediate forms. Similar reactions take place for $HFeCo_3(CO)_{12}$ during the formation of $[Fe(CO)_4]^-$.

The negative ion yield curve for $[Fe(CO)_4]^-$ shows a maximum contribution at 0 eV, which most likely a Feshbach resonance. Then it decays asymmetrically up to ~1.8 eV. The ion yield curve for $[Fe(CO)_3]^-$ shows an intense contribution at 1.3 eV and a broad minor contribution at 3.6 eV. The contribution at 1.3 eV may be shape resonance associated with the extra electron residing in a π^*(Fe-CO) MO. The ion yield curve for $[Fe(CO)_2]^-$ shows only one resonance structure with a maximum contribution at 4.2 eV. As discussed previously, the resonance structure at 3.6 and 4.2 eV are attributed to core excited resonances. The measured AE, calculated thermochemical thresholds, energy positions of ion yield maxima and their intensities are given in Table 5.1.

Electron impact ionization of $HFeCo_3(CO)_{12}$

The positive ion mass spectrum of $HFeCo_3(CO)_{12}$ was recorded with electron impact energy of 70 eV and is shown in Fig. 5.9. The observation of the parent cation in the mass spectrum confirms the presence of the non-dissociated parent molecule in the collision chamber. As expected, the most intense fragment in the positive mass scan was CO^+. Fragments corresponding to loss of CO ligands (from one CO ligands to all available CO ligands) are observed in the mass scan and the strongest signal associated with removal of CO ligands was for $[M - 5(CO)]^+$ formation. All the peaks marked with * originate from Toluene (C_7H_8), which was used in the initial step of the $HFeCo_3(CO)_{12}$ synthesis. There is no prior report about positive ion mass spectra of $HFeCo_3(CO)_{12}$. However, an electron impact mass scan of $Co_4(CO)_{12}$ is reported in Ref. [160]. The relative intensities of fragments formed with removal of different CO ligands from electron impact ionization of $Co_4(CO)_{12}$ exhibit similar behavior as that of $HFeCo_3(CO)_{12}$.

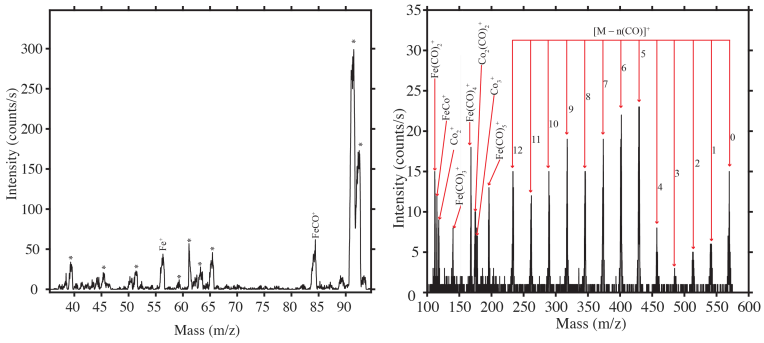

Figure 5.9. Positive ion mass scan of $HFeCo_3(CO)_{12}$ recorded at an electron impact energy of 70 eV. The left panel shows the mass scan in the m/z range of 35 to 95 and right panel shows in the m/z range of 100 to 580.

In order to get an impression of the extent of CO ligand loss through DEA and DI of $HFeCo_3(CO)_{12}$, the average number of CO ligands lost/molecule are calculated from the observed fragmentation channels by using the equation

$$COlost/molecule = \frac{\sum[N_{CO} \times I_{ch}]}{I_{tot}} \tag{5.4}$$

For DEA,
I_{ch} is the integrated intensity of negative ion yield curve for each DEA channel and N_{CO} is the number of CO lost through that particular DEA channel, I_{tot} is the sum of intensity of all DEA channel observed.

For DI,
I_{ch} is the peak intensity of each positive ion fragment observed in the positive ion mass spectrum and N_{CO} is the number of CO lost associated with that fragment, I_{tot} is the sum of intensity of all positive ion fragments observed in the mass spec.

These estimations are not perfect because the information regarding the neutral dissociation is unknown. Therefore, for both DEA and DI, an upper limit and a lower limit for the number of CO ligands lost per incident is calculated. The upper limit for DEA is estimated by assuming further fragmentations from the neutral species produced in the DEA channel. The extend of neutral species fragmentations are determined based on the available energy. The lower limit of DEA is estimated by assuming that the neutral counter parts are intact. In the case of DI, the upper limit is estimated by complete fragmentations from the neutral counter parts. For the lower limit, no fragmentation from the neutral counterparts is assumed. From these estimations, the calculated average number of CO ligands lost/incident for DEA to $HFeCo_3(CO)_{12}$ is 2 - 3, while for DI the calculated value is 4 - 9 CO ligands.

5.1.1.3 Conclusions

In the gas phase study of $HFeCo_3(CO)_{12}$, mainly DEA and DI of $HFeCo_3(CO)_{12}$ was discussed. Electron attachment to $HFeCo_3(CO)_{12}$ produced three groups of negative ions along with its parent anion. The first group of negative ions consists of $[M - n(CO)]^-$, where n = 1 - 12. The negative ion yields corresponding to the sequential

loss of CO ligands (i.e. for $[M - n(CO)]^-$ formation) show an interesting feature; i.e. resonant-like structures up to 11 eV above the IE of $HFeCo_3(CO)_{12}$ (i.e. at 20 eV). This is very unusual in DEA. This unusual behavior is attributed to the polynuclear structure of $HFeCo_3(CO)_{12}$ and the high number of bridging and terminal CO ligands. The polynuclear nature of $HFeCo_3(CO)_{12}$ and high number of associated CO ligands results in a high density of occupied/unoccupied molecular orbitals close to the HOMO-LUMO gap. The high density of molecular orbitals allows for multiple electronic excitations and quasi-continuous electron attachment from about 1 eV to about 20 eV. The electron attachment to $HFeCo_3(CO)_{12}$ at higher energies and the formation of a stable TNI leads to sequential CO loss that at sufficiently high energies results in removal of all available CO ligands, i.e., metastable decay of the initially formed parent anion. The second group of negative ions includes $[M - Co(CO)n]^-$, where n = 4 - 10. It is formed by sequential loss of COs from $[M - Co(CO)_4]^-$ and was comparatively less efficient. The third group of negative ions are $[Fe(CO)_n]^-$ where n = 2 - 4. These ions are formed by attaching an electron into the LUMO of $HFeCo_3(CO)_{12}$, which has antibonding character between the apical iron and basal cobalts. The negative ion fragments $[Fe(CO)_3]^-$ and $[Fe(CO)_2]^-$ are formed through loss of COs from $[Fe(CO)_4]^-$. The thermochemical thresholds for the formation of all observed negative ions were calculated at the PBE0/ma-def2-TZVP level of theory and compared with our measured AE values. In the case of the first group negative ions (i.e. sequential loss of all CO ligands) the threshold values are also calculated at the BP86/def2-TZVP level of theory. However in comparison with the measured AEs, they show significant deviations, especially for the losses of higher number of CO ligands.

DI of $HFeCo_3(CO)_{12}$ was characterized by rich fragmentations. Main fragments observed are fragments formed by sequential CO loss and iron containing fragments ($[Fe(CO)_n]^+$ with n = 1 - 5). These are similar fragments as observed in DEA to $HFeCo_3(CO)_{12}$, however, the branching ratios are considerably different.

5.1.2 Surface study of $HFeCo_3(CO)_{12}$

5.1.2.1 Introduction and motivation for the study

The property of $HFeCo_3(CO)_{12}$ in FEBID and the importance of understanding low energy electron interactions with $HFeCo_3(CO)_{12}$ was discussed in the previous section. The gas phase study is not sufficient to understand the FEBID reactions of $HFeCo_3(CO)_{12}$, mainly because the gas phase study is performed under single electron/molecule collision conditions, however the FEBID reaction takes place on a surface. This can be addressed with a surface study of $HFeCo_3(CO)_{12}$. The surface study cannot be performed directly in FEBID because of the higher background pressure and continued supply of precursor gas. Therefore, the surface study was performed in a separate UHV chamber. In this surface study, nanometer thick films of $HFeCo_3(CO)_{12}$ were adsorbed onto a clean and cold (153 K) gold substrate and irradiated with electrons from a flood gun at an electron energy of ~500 eV. During electron irradiation, the electron induced changes in the $HFeCo_3(CO)_{12}$ film are monitored using XPS and MS (more experimental details are in section 4.3). The capability of UHV surface science approach to monitor electron induced surface reactions are demonstrated for number of

FEBID precursor molecules like $MeCpPtMe_3$ [40], $Au(acac)Me_2$ [68], $Pt(PF_3)_4$ [69], $W(CO)_6$ [30], $Co(CO)_3NO$ [31], $(\eta^3\text{-}C_3H_5)Ru(CO)_3Br$ [73] and cis-$Pt(CO)_2$ [74]. From these previous surface studies, it is found that in general the electron induced decomposition of precursor molecules proceeds in two steps. In the first step, electron induced decomposition of precursor molecule results to the desorption of some ligands; forming a metal containing intermediate that remains bound to the substrate. If the metal containing intermediate undergoes further electron irradiation, the remaining ligands undergo electron induced decomposition rather than desorption. This is believed to be the major reason for organic impurities in FEBID. In the actual FEBID experiment, thermal reactions can also play a role. In that case, the remaining ligands may further desorb, leading to a higher metal content.

The main motivation behind the surface study of $HFeCo_3(CO)_{12}$ was the use of $HFeCo_3(CO)_{12}$ as the first bimetallic precursor molecule in FEBID as well as its relatively high performance in FEBID and exceptional behavior in DEA. The surface study of $HFeCo_3(CO)_{12}$ allows one to follow the fate of dissimilar atoms simultaneously (using XPS) during the electron induced deposition process.

5.1.2.2 Results and discussions

The changes in C(1s), O(1s), Fe(2p) and Co(2p) XPS regions that occur during the electron irradiation of nanometer thick $HFeCo_3(CO)_{12}$ film adsorbed onto gold substrate are shown in Fig. 5.10. The X-ray exposure to the adsorbed $HFeCo_3(CO)_{12}$ film induces similar changes as that produce by 500 eV electrons. The sensitivity of the $HFeCo_3(CO)_{12}$ film towards SEs produced by the interaction of X-ray irradiation on Au substrates is determined through a separate, controlled experiment. Analysis of the rate of decrease of the O(1s) area by the effect of X-ray irradiation reveals that the time taken for one XPS scan of the C(1s), O(1s), Fe(2p) and Co(2p) regions, as shown in Fig. 5.10, corresponds to an electron irradiation dose of 9.25 x 10^{14} e^-/cm^2. The effect of X-ray irradiation is incorporated into the electron dose reported in the surface study of $HFeCo_3(CO)_{12}$. In practice, the effect of X-ray irradiation is significant only for electron doses $< \approx 2$ x 10^{15} e^-/cm^2

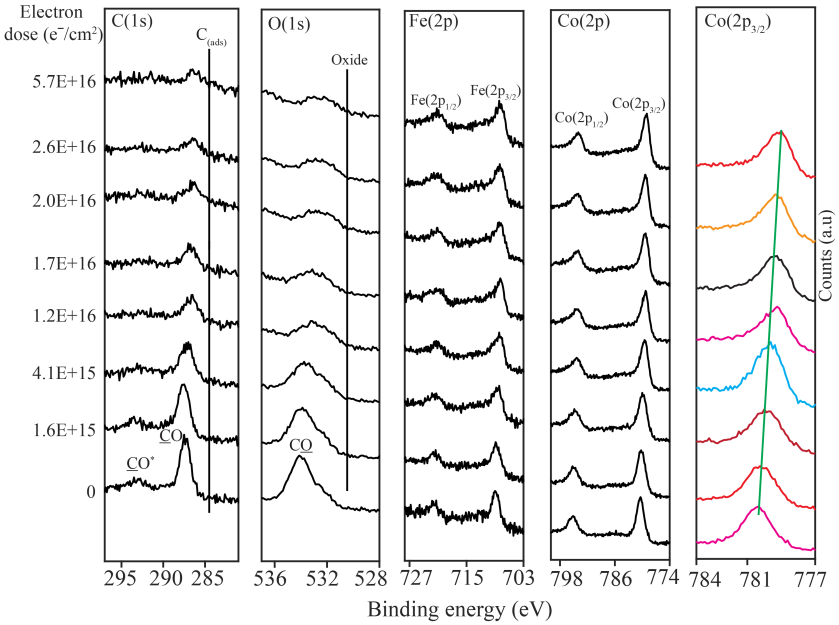

Figure 5.10. Evolution of the C(1s), O(1s), Fe(2p), Co(2p) and Co($2p_{3/2}$) XPS regions of nanometer thick $HFeCo_3(CO)_{12}$ films exposed to electron doses of $<\approx 5.7 \times 10^{16}$ e^-/cm^2. The C(1s), O(1s), Fe(2p) and Co(2p) spectra shown were measured with a pass energy of 22.36 eV; the RHS Co($2p_{3/2}$) region was followed with a pass energy of 11.2 eV. Adapted from ref. [49].

From Fig. 5.10 it is clear that prior to electron irradiation the C(1s) XPS region consists of two peaks centered at 287.6 and 293.2 eV; both indicative of adsorbed CO groups [161, 162]. The lower binding energy peak is assigned as the C(1s) peak of associated CO species, while the higher binding energy peak is a shake-up feature originating from the $\pi - \pi^*$ transitions that accompany the ejection of C(1s) electrons in metal carbonyls [161, 162]. Similar to the C(1s) XPS region, the O(1s) XPS region also consists of two peaks; an asymmetric peak centered at 534.1 eV associated with the O(1s) peak of CO ligands and a weaker $\pi - \pi^*$ shake-up peak centered at ~540 eV (not shown) [161, 162]. Prior to electron irradiation, the Fe(2p) XPS region shows two peaks centered at 709 and 722 eV, corresponding to the Fe($2p_{3/2}$) and Fe($2p_{1/2}$) transitions respectively. Similarly, the two peaks in Co(2p) XPS region are centered at 780.4 and 795.1 eV, which correspond to Co($2p_{3/2}$) and Co($2p_{1/2}$) transitions, respectively. From the analysis of XPS data recorded prior to electron irradiation, it should be noted that the nanometer thick film created for electron irradiation has molecular $HFeCo_3(CO)_{12}$ character. For e.g. the XPS spectral features in the C(1s) and O(1s) regions are due to the presence of carbonyl group and the estimated Co:Fe ratio is 3.19 which is close to the stoichiometric 3:1 ratio of the compound.

From Fig. 5.10 it is obvious that for electron doses $< \approx 5.7$ x 10^{16} e^-/cm^2, the most dominant change is the decrease in C(1s) and O(1s) XPS peak areas. The C(1s) and O(1s) peak positions shift to lower binding energy values with increasing electron doses,

but the shapes of the peaks remain relatively unchanged and there is no appearance of any additional peaks. The fractional coverage of both C(1s) and O(1s) decreases by ~75% and the C:O ratio remains constant. In the case of Fe(2p) and Co(2p), the integrated area of the XPS peaks remains almost constant (changing by <10%), which indicates the absence of any measurable metal desorption. Although the integrated areas remain constant with increasing the electron dose, the Fe(2p) peak slightly broadens and shifts towards higher binding energy (total shift ~0.23 eV). The changes in the Co(2p) XPS region are monitored by recording high energy resolution scan (shown in the right-hand side of Fig. 5.10. It indicates that with increasing electron dose, there is a measurable change in the Co(2p) peak position (total shift~1.3 eV) and furthermore, the peak shape become increasingly asymmetric. The change in the Co(2p) peak position is closely correlated with the fractional change in C(1s) and O(1s) (see insert of Fig. 12b).

Fig. 5.11 demonstrates the change in the C(1s), O(1s), Fe(2p) and Co(2p) XPS regions for significantly larger electron doses (> 2 x 10^{17} e^-/cm^2). XPS data of the $HFeCo_3(CO)_{12}$ film prior to electron irradiation is also shown for comparison (bottom most spectra in Fig. 5.11). Although the integrated area of the C(1s) and O(1s) XPS peaks in Fig. 5.11 remains constant, the spectral profile changes. The carbonyl peak centered at 287.6 eV systematically decreases and a new peak centered at 284.5 eV starts appearing. This can be ascribed to graphitic carbon [163]. From Fig. 5.11 one can see that after an electron dose of 1.8 x 10^{18} e^-/cm^2, the C(1s) region dominates the spectral intensity from graphitic carbon and the C(1s) signal from remaining CO is disappeared. For O(1s), the XPS peak gets broader and shifts to lower binding energy with a peak at ~530.5 eV becoming increasingly prevalent. The new O(1s) peak can be ascribed to formation of an oxide. The Fe(2p) peak also gets broader and shows the indication of iron oxides. In contrast, there is no significant change in the Co(2p) XPS region. Fig. 5.12 shows the fractional change in the C(1s), O(1s) and Co(2p) peak positions as a function of electron doses.

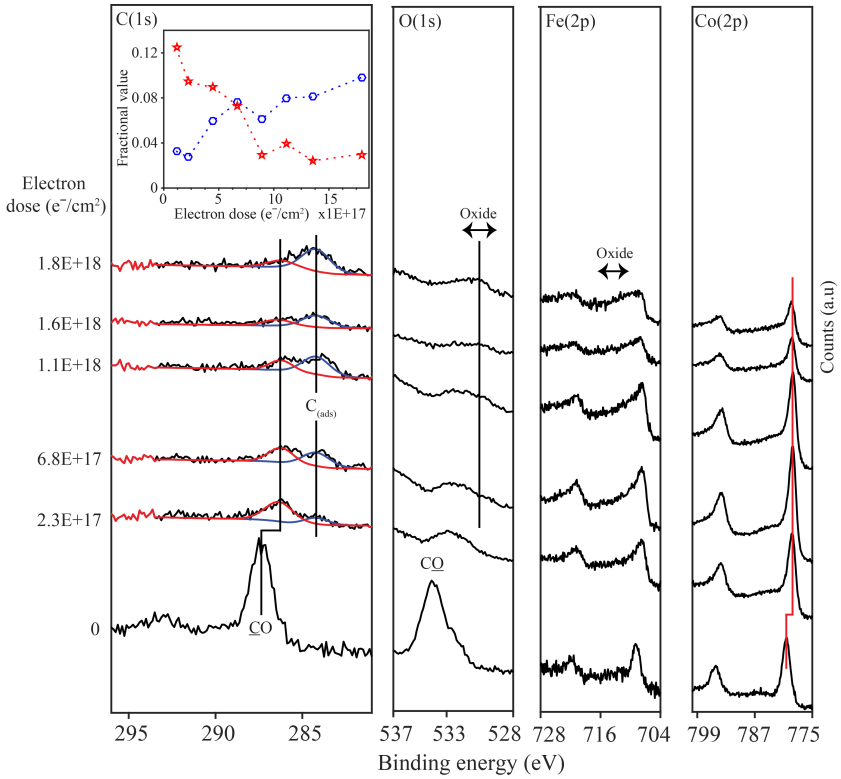

Figure 5.11. Evolution of the C(1s), O(1s), Fe(2p) and Co(2p) XPS regions of nanometer thick $HFeCo_3(CO)_{12}$ films, exposed to electron dose > 2×10^{17} e^-/cm^2. The insert in the C(1s) region shows the fractional change in the coverage of carbonyl (red stars) and graphitic carbon atoms (open blue circles) for these larger electron doses; carbon areas have been normalized to the XPS signal initially observed in the C(1s) region prior to any electron irradiation. Adapted from ref. [164].

The mass spectra recorded from gas phase $HFeCo_3(CO)_{12}$ (top) and during the electron irradiation of surface adsorbed $HFeCo_3(CO)_{12}$ (bottom) is shown in Fig. 5.13. The most intense peak observed in the gas phase mass spec of $HFeCo_3(CO)_{12}$ were CO (28 amu), C (12 amu) and O (16 amu), along with smaller peaks corresponding to Fe (56 amu), FeCO (84 amu) and residual water vapor in UHV chamber. All the peaks marked with star (*) originate from toluene used in the synthesis of $HFeCo_3(CO)_{12}$. The peaks observed during the electron irradiation of the $HFeCo_3(CO)_{12}$ film was associated with CO (28, 12 and 16 amu), along with a small contribution of residual water vapor.

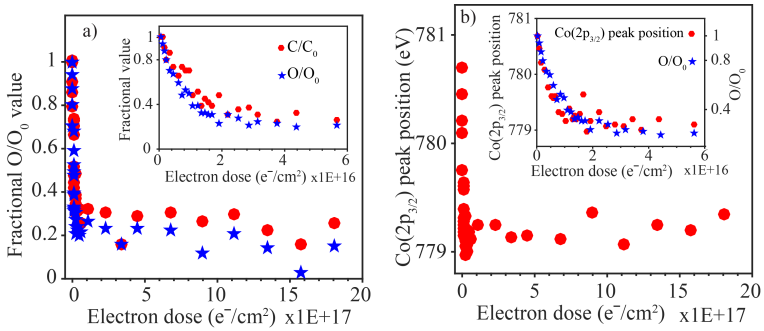

Figure 5.12. Change in (a) fractional coverage of carbon and oxygen atoms and (b) $Co(2p_{3/2})$ peak position for nanometer thick $HFeCo_3(CO)_{12}$ films, as a function of electron dose. The insets in (a) and (b) show the corresponding changes to the fractional coverage of carbon and oxygen atoms as well as the $Co(2p_{3/2})$ peak position for the comparatively small electron doses (<6 × 10^{16} e^-/cm^2) shown in Figure 5.10. Adapted from ref. [164].

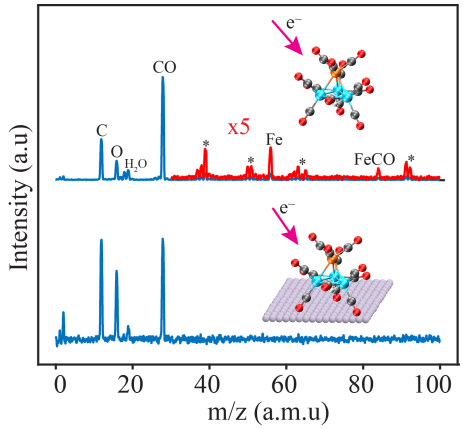

Figure 5.13. Mass spectrum (0 - 100 amu) of (top) gas phase $HFeCo_3(CO)_{12}$ and (bottom) during the electron irradiation of an $HFeCo_3(CO)_{12}$ film. No fragments were observed between 100 - 200 amu., adapted from ref. [164].

Fig. 5.14 shows the CO desorption kinetics observed during the electron irradiation of the adsorbed $HFeCo_3(CO)_{12}$ film using two different currents 5 and 30 μA. The rate of CO desorption is highest at the onset of electron irradiation and decreases to background level once an electron dose of ≈3 x 10^{16} e^-/cm^2 is reached. The CO desorption kinetics for 5 and 30 μA seem to be very similar. Fig. 5.14 also shows that the CO desorption kinetics monitored with the MS is closely correlated with the fractional decrease in carbon atoms (oxygen atoms follow the same trend) as observed by XPS.

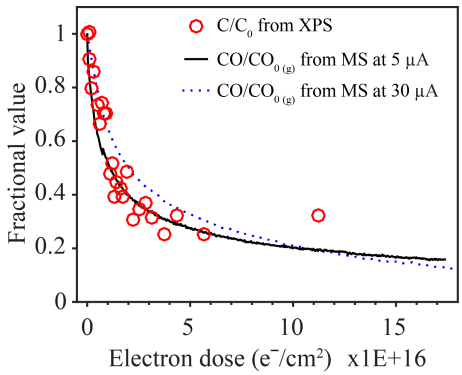

Figure 5.14. Kinetics of CO desorption observed during irradiation of a nanometer thick $HFeCo_3(CO)_{12}$ film (monitored at m/z = 12 (C)), plotted as a function of electron dose at a target current of 5 µA (black solid line) and 30 µA (blue dotted line). Also shown is the fractional coverage of carbon atoms, determined by XPS data from Fig. 5.10 (red circles). Adapted from ref. [164].

Fig. 5.15 shows the change in the C(1s), O(1s), Fe(2p) and Co(2p) XPS regions when a $HFeCo_3(CO)_{12}$ film adsorbed at 213 K is initially irradiated with an electron dose of 2.0 x 10^{16} e^-/cm^2 and then annealed to RT (298 K). The electron dose of 2.0 x 10^{16} e^-/cm^2 corresponds to the smallest electron dose required to cause electron induced CO desorption from all of the adsorbed $HFeCo_3(CO)_{12}$ film (Fig. 5.10). The changes in XPS peaks after electron irradiation of dose 2.0 x 10^{16} e^-/cm^2 are similar to those presented in Fig. 5.10. The upper most spectra in Fig. 5.15 show the change that occurs during the annealing of the electron irradiated $HFeCo_3(CO)_{12}$ film. All of the residual intensity in the C(1s) and O(1s) regions disappears, but the signal intensity in the Fe(2p) and CO(2p) regions remains.

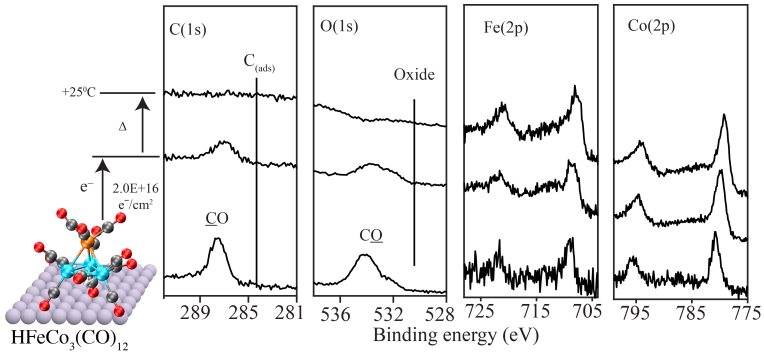

Figure 5.15. Changes in the C(1s), O(1s), Fe(2p) and Co(2p) XPS regions when a nanometer thick $HFeCo_3(CO)_{12}$ film was exposed to an electron dose of 2.0 × 10^{16} e^-/cm^2 (middle set of spectra) and then subsequently heated to room temperature (25 ^0C) (uppermost set of spectra), adapted from ref. [164].

Discussions

Based on the analysis of the XPS and MS data, the electron induced surface reactions of $HFeCo_3(CO)_{12}$ can be separated into two stages.

First stage: Electron stimulated CO desorption/precursor decomposition: The initial electron induced CO desorption and decomposition of $HFeCo_3(CO)_{12}$ is schematically represented in Fig. 5.16

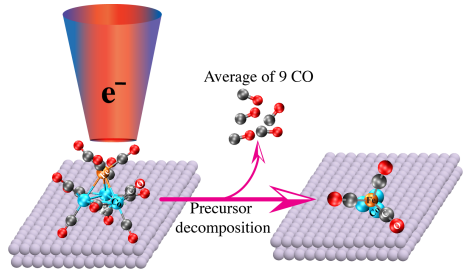

Figure 5.16. Schematic for electron induced dissociation of adsorbed $HFeCo_3(CO)_{12}$, adapted from ref. [164].

The initial electron induced CO desorption is directly evident from the mass spectrum (see Fig. 5.13) and the decrease in intensity of the C(1s) and O(1s) XPS peaks as shown in Fig. 5.10. The CO desorption evident from the XPS is coincident with the rate of CO desorption determined from MS (see Fig. 5.14). The analysis of the C(1s) and O(1s) XPS peaks during the initial stage does not show any evidence of the CO decomposition, indicating that CO desorption from $HFeCo_3(CO)_{12}$ occurs in the absence of CO decomposition. The extent of CO desorption can be determined from the fractional change in the C(1s) and O(1s) XPS peaks and the kinetics of CO desorption observed in MS. These analyses show that both carbon and oxygen signals decrease to ~25% of their initial values. Based on the stoichiometry of $HFeCo_3(CO)_{12}$, this means that on average each precursor molecule loses 9 of its 12 CO ligands.

The CO desorption during the initial electron induced precursor decomposition transforms the adsorbed $HFeCo_3(CO)_{12}$ molecules into partially decarbonylated species with an average stoichiometry of $HFeCo_3(CO)_3$, as shown in Fig. 5.16. This transformation is reflected in the increasing asymmetry of the Co ($2p_{3/2}$) peak shape and the decrease in binding energy from 780.4 to 779.1 eV (see Fig. 5.10), which is closer to the asymmetric peak shape and binding energy of metallic cobalt (metallic Co ($2p_{3/2}$) binding energy ~778.3 eV).

In relation to FEBID, when an electron interacts with $HFeCo_3(CO)_{12}$, it decomposes the precursor molecules and creates non-volatile partially decarbonylated intermediates and the CO ligands lost will be pumped away. This first step is analogous to the initial electron induced decomposition of previously studied FEBID precursor molecules like $Co(CO)_3NO$ [31] and $W(CO)_6$ [30], characterized by the initial desorption of CO ligands. It is interesting to note that in the initial electron induced decomposition, $HFeCo_3(CO)_{12}$ removes on average 75% of its CO ligands, but for $Co(CO)_3NO$ and $W(CO)_6$ no more than 50% of the CO ligands are removed [30, 31].

In UHV surface science experiments, the electron induced dissociation of $HFeCo_3(CO)_{12}$ ends in the "precursor limited regime" because there is no supply of precursor molecules during the electron irradiation. From Fig. 5.14 it is clear that the electron induced decomposition of $HFeCo_3(CO)_{12}$ and desorption of CO ligands depends only on electron dose and is invariant to electron flux. This indicates that the initial electron induced decomposition reaction of $HFeCo_3(CO)_{12}$ is a single electron process.

From the gas phase study of $HFeCo_3(CO)_{12}$ we saw that an average of 2 - 3 CO ligands are removed through DEA to $HFeCo_3(CO)_{12}$ while an average of 4 - 9 CO ligands are removed through DI. From the UHV surface science experiments of $HFeCo_3(CO)_{12}$ it is clear that there is no metal fragment desorption, therefore, from the comparison of observations made in gas phase and the surface study, it is most likely that the initial electron induced decomposition of $HFeCo_3(CO)_{12}$ proceeds through DI rather than DEA. Similar comparison for other previously studied FEBID precursor molecules like $MeCpPtMe_3$ [40] and $Pt(PF_3)_4$ [69] indicates that the initial electron induced decomposition proceeds through DEA, however, for some other FEBID precursor molecules like $W(CO)_6$ [30] and $Co(CO)_3NO$ [31] the extent of the initial electron induced reactions can only be described with the combination of DEA and DI process. One should note that the extent of neutral dissociation for these FEBID precursor molecules is unknown and also the surface induced dissociation of initially formed intermediates may occur in some cases, which would compromise the direct comparison between surface and gas phase studies.

In the gas phase study of $HFeCo_3(CO)_{12}$, the metal-metal bond cleavage is significant in the case of DI to $HFeCo_3(CO)_{12}$ and the total branching ratio for metal-metal bond rupture is about 0.5 with $[Fe(CO)_n]^+$ (n = 0 - 5) as the most intense fragments. In the UHV surface study of $HFeCo_3(CO)_{12}$, if we assume that the initial electron induced decomposition of $HFeCo_3(CO)_{12}$ proceeds through DI, then we observe a statistical process where the adsorbate created after initial electron induced decomposition will be a mixture of partially decarbonylated species such as $HFeCo_3(CO)_2$, $HFeCo_3(CO)_3$, $HFeCo_3(CO)_4$, $HFeCo_3(CO)_5$, etc., producing a film with an average stoichiometry of $HFeCo_3(CO)_3$. However, one should note that these partially decarbonylated intermediate could also include species with metal-metal bond cleavage which may occur during electron induced decomposition of $HFeCo_3(CO)_{12}$.

Second stage:

a) Electron stimulated CO decomposition: Following the initial electron induced decomposition of $HFeCo_3(CO)_{12}$ which is completed at an electron dose of $\approx$5.7 x 10^{16} e^-/cm^2, on average 9 of their 12 CO ligands are lost and partially decarbonylated intermediates of the form $HFeCo_3(CO)_3$ are formed. At further increases in electron dose (> 5.7 x 10^{16} e^-/cm^2), it is clear from the XPS data (see Fig. 5.11) that liberated CO ligands undergo electron stimulated decomposition via the reaction:

$$CO_{(ads)} + e^- \rightarrow C_{(ads)} + O^{2-}_{(ads)} \tag{5.5}$$

At electron dose of $\approx$1.8 x 10^{18} e^-/cm^2, we can see from Fig. 5.11 that the C(1s) region of the CO ligands diminishes until the signal is barely distinguishable and the C(1s) peak for Cads becomes dominating in the spectrum. This represents

the conclusion of electron stimulated CO decomposition reactions. The conversion of oxygen into oxide and formation of oxide species is most clearly evidenced by the observation of iron oxide in Fig. 5.11. In the case of cobalt, there is no change in the Co(2p) XPS peak profile which indicates that the oxidation exclusively effects iron. From the area analysis of the O(1s) XPS peak at higher electron doses, it is clear that the area remains constant and that indicates that the iron oxidation is exclusively due to CO ligand decomposition and not the reaction between iron atom and residual oxygen containing species such as water in the UHV chamber. The overall reaction process that occurs during the electron stimulated CO decomposition can be represent by the equation

$$HFeCo_3(CO)_{3(ads)} + e^- \rightarrow HFe^{x+}O_yCo_{3(ads)} + C_{ads} \tag{5.6}$$

This is schematically shown in fig. 5.17.
The exclusive iron oxidation that occurs during the electron stimulated CO decomposition, suggests that the CO ligands in the partially decarbonylated intermediates are bound exclusively to the Fe atom. Therefore, in all the schematics used to represent the electron induced reaction of $HFeCo_3(CO)_{12}$, the partially decarbonylated intermediates have CO ligands connected exclusively to the Fe atom.

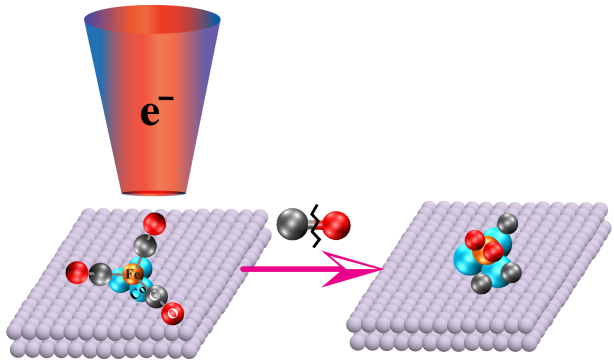

Figure 5.17. Schematic showing the electron stimulated CO decomposition of a partially decarbonylated $HFeCo_3(CO)_{12}$ intermediate., adapted from ref. [164].

b) Thermal reactions: The main objective of the surface study of $HFeCo_3(CO)_{12}$ was to get a good understanding of its electron induced bond breaking reactions in FEBID. In FEBID, the initial reaction must involve electron induced decomposition of precursor molecules. However, after the initial electron induced precursor decomposition, the intermediate formed could be subject to either further electron stimulated reactions (part (a) above), or thermally driven reactions. In the UHV surface study of $HFeCo_3(CO)_{12}$, the partially decarbonylated intermediates are formed at a substrate temperature of 213 K, however the actual FEBID reactions takes place at room temperature (RT). Therefore, the effect of temperature, which may trigger some thermal reactions to partially decarbonylated intermediates is addressed by first irradiating the nanometer thick $HFeCo_3(CO)_{12}$ film with electron doses just sufficient to complete the first stage

of reaction and then by subsequent annealing of the electron irradiated film to RT. The XPS data obtained from these studies (see Fig. 5.15) demonstrate that almost all of the CO ligands in the partially decarbonylated intermediate desorb upon annealing the electron irradiated film to RT, leaving behind only the Co and Fe atoms from the precursor molecule. The overall process derived in this experiment is schematically shown in Fig. 5.18 and can be represented by the equation

$$HFeCo_3(CO)_{3(ads)} + \Delta \rightarrow HFeCo_{3(ads)} + 3CO_{(g)} \tag{5.7}$$

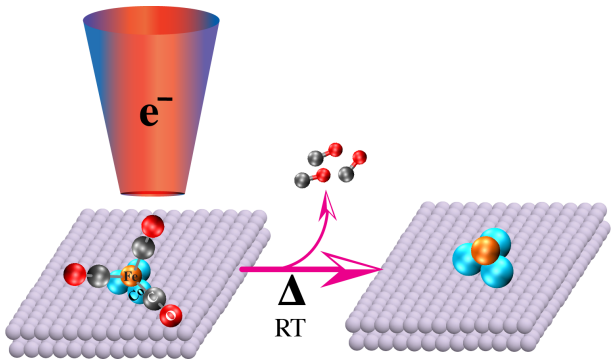

Figure 5.18. Effect of annealing a partially decarbonylated $HFeCo_3(CO)_{12}$ intermediate to room temperature (RT), showing the resultant CO desorption., adapted from ref. [164].

Overall relationship between UHV surface science data and FEBID

The initial event that occurs during FEBID of $HFeCo_3(CO)_{12}$ is the adsorption of $HFeCo_3(CO)_{12}$ onto a surface

$$HFeCo_3(CO)_{12} \leftrightarrow HFeCo_3(CO)_{12(ads)} \tag{5.8}$$

After adsorption, the precursor molecules decompose by electron beam. This is identical to the first stage (see Fig. 5.16) observed in the surface study of $HFeCo_3(CO)_{12}$, i.e. extensive CO desorption and formation of adsorbed, partially decarbonylated intermediates, most likely through DI of $HFeCo_3(CO)_{12}$. Thus

$$HFeCo_3(CO)_{12(ads)} + e^- \rightarrow HFeCo_3(CO)_{3(ads)} + 9CO_{(g)} \tag{5.9}$$

At this stage, the partially decarbonylated intermediates either undergo electron stimulated reactions; particularly CO ligand decomposition (see Figs. 5.11 and 5.17);

$$HFeCo_3(CO)_{3(ads)} + e^- \rightarrow HFe^{x+}O_yCo_{3(ads)} + C_{ads} \tag{5.10}$$

or reactions triggered by thermal effect lead to further desorption of CO ligands as shown in Fig. 5.15 and schematically represented in Fig. 5.18.

$$HFeCo_3(CO)_{3(ads)} + \Delta \rightarrow HFeCo_{3(ads)} + 3CO_{(g)} \tag{5.11}$$

The initial electron induced decomposition of $HFeCo_3(CO)_{12}$ and the ongoing competition between electron stimulated CO decomposition and thermally driven CO desorption of partially decarbonylated intermediates is schematically shown in Fig. 5.19.

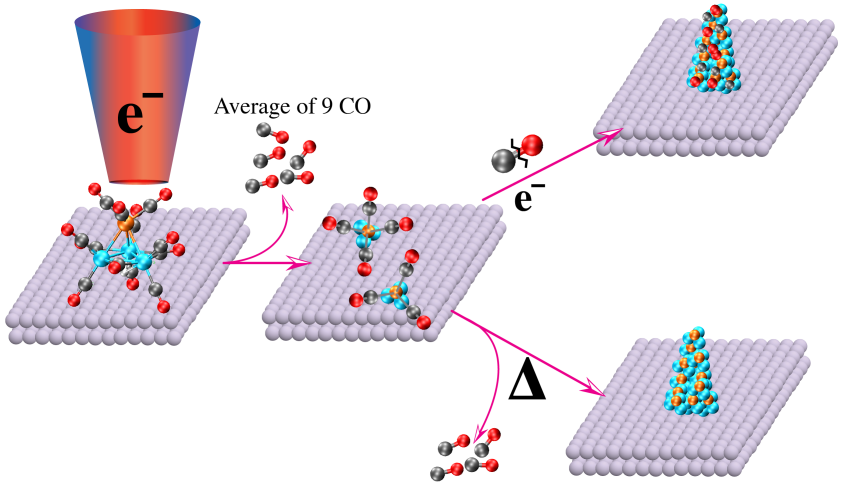

Figure 5.19. Schematic showing the electron induced decomposition of $HFeCo_3(CO)_{12}$ and the competition between electron stimulated decomposition or thermal desorption of CO ligands from the partially decarbonylated intermediates produced by precursor decomposition, adapted from ref. [164].

From Figs. 5.10 and 5.11, it is apparent that the electron stimulated CO ligand decomposition reaction of $HFeCo_3(CO)_{12}$ that occurs during the second stage is inefficient compared to the CO desorption process that occurs in the initial stage of electron induced decomposition. This suggests that during FEBID, thermal reactions have the most important role in determining the fate of the partially decarbonylated intermediates. Under these circumstances the overall reactivity of $HFeCo_3(CO)_{12}$ during FEBID will be dominated by the following sequence of reaction steps (shown schematically by the lower reaction pathway in Fig. 5.19).

$$HFeCo_3(CO)_{12(ads)} + e^- \rightarrow HFeCo_3(CO)_{3(ads)} + 9CO_{(g)} \tag{5.12}$$

$$HFeCo_3(CO)_{3(ads)} + \Delta \rightarrow HFeCo_{3(ads)} + 3CO_{(g)} \tag{5.13}$$

These reactions are in qualitative agreement with the performance of $HFeCo_3(CO)_{12}$ in FEBID i.e. the deposit obtained from $HFeCo_3(CO)_{12}$ shows metal content of >80% in FEBID. This indicates that after the initial electron induced decomposition of $HFeCo_3(CO)_{12}$, further reactions of intermediate species are dominated by thermally driven CO desorption as opposed to electron stimulated CO decomposition. More detailed discussion on the surface study of $HFeCo_3(CO)_{12}$ can be found in article 3.

5.1.2.3 Conclusions

The initial electron induced reactions of surface adsorbed $HFeCo_3(CO)_{12}$ lead to extensive CO ligand losses with an average of 9 CO ligands/molecule. The removal of CO ligands converts the surface adsorbed $HFeCo_3(CO)_{12}$ to a partially decarbonylated intermediate of the form $HFeCo_3(CO)_3$. The comparison of this CO desorption with the gas phase study of $HFeCo_3(CO)_{12}$ indicates that the initial electron induced reaction proceeds through DI rather than DEA. The extent of CO desorption observed in $HFeCo_3(CO)_{12}$ is significantly higher than the observed for previously studied CO containing FEBID precursor molecules like $Co(CO)_3NO$ and $W(CO)_6$. When the partially decarbonylated intermediate is exposed to further electron irradiation, the remaining CO ligands in the intermediate decompose into adsorbed carbon and oxides. The oxide formation was clearly evidenced in the formation of iron oxides; the Fe atoms were exclusively oxidized and not Co. This suggests that the CO ligands present in the intermediate are primarily attached to Fe and not to Co atoms. This also suggests that the CO ligands desorbed by the electron induced reactions are most likely the CO ligands attached to the Co atom. In order to address the different thermal conditions of UHV surface experiments and FEBID experiments, annealing experiments were performed, where an electron irradiated $HFeCo_3(CO)_{12}$ film was annealed to RT. In the annealing experiments, complete CO desorption occurs leaving behind Co and Fe atoms. This observation is in line with the high metal content of the deposit created from $HFeCo_3(CO)_{12}$ in FEBID. From this data, we propose that the overall FEBID reactions of $HFeCo_3(CO)_{12}$ can be written as an extensive initial electron induced CO desorption ($HFeCo_3(CO)_{12}(ads) + e^- \rightarrow HFeCo_3(CO)_3(ads) + 9CO(_g)$, followed by thermal desorption of CO ligands from the partially decarbonylated intermediates ($FeCo_3(CO)_3(ads) + \Delta \rightarrow FeCo_3(ads) + 3CO(_g)$).

5.2 $H_2FeRu_3(CO)_{13}$

5.2.1 Gas phase study of $H_2FeRu_3(CO)_{13}$

5.2.1.1 Introduction and motivation for the study

$H_2FeRu_3(CO)_{13}$ is a heterometallic precursor molecule and its synthesis was first reported in 1968 [165, 166]. This precursor molecule has been used in CVD to fabricate $FeRu_3$ alloy thin films [46]. Similar to $HFeCo_3(CO)_{12}$, this precursor molecule was also used in FEBID very recently [49]. The advantage of using heteronuclear precursor molecules in FEBID is discussed in section 5.1.1.1. Fabrication of magnetic metal alloy nanostructures has many applications (mostly discussed in section 5.1.1.1), for example it can be used for studying magnetism at nanoscale, fundamental applications in data storage, and spintronics.

The structure of $H_2FeRu_3(CO)_{13}$ is shown in Fig. 5.20. It has a similar structure as $HFeCo_3(CO)_{12}$, however the $H_2FeRu_3(CO)_{13}$ structure has a less symmetric arrangement with 13 carbonyls (four terminal CO attached to Fe and three terminal carbonyls for each Ru where two COs are bridging with Ru) and two bridging hydrogen atoms. The bond lengths between the Fe apex and the basal Ru atoms are in the range of 2.655

- 2.705 Å [49].

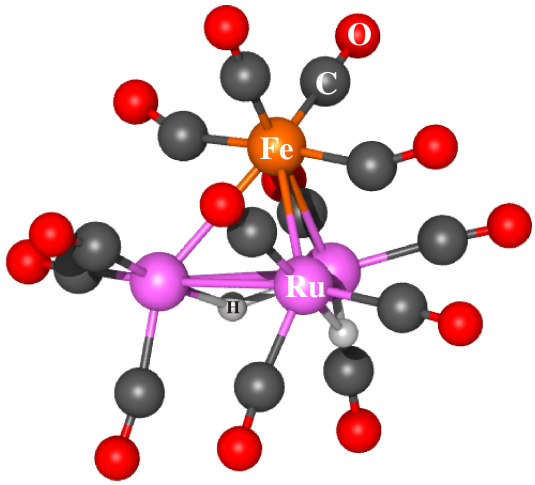

Figure 5.20. Ground state optimized geometry of neutral $H_2FeRu_3(CO)_{13}$

The performance of $H_2FeRu_3(CO)_{13}$ in FEBID was found to be very poor compared to the performance of $HFeCo_3(CO)_{12}$. In FEBID, $H_2FeRu_3(CO)_{13}$ showed only <30% of metal content, bad reproducibility and the Ru:Fe ratio was found to be 3.5:1, indicates partial iron loss [49].

The motivation behind the gas phase study of $H_2FeRu_3(CO)_{13}$ was the different performance of this precursor molecule in FEBID compared to that of the structurally similar heteronuclear precursor molecule $HFeCo_3(CO)_{12}$. The gas phase study of $H_2FeRu_3(CO)_{13}$ helps to identify the different low energy electron induced dissociation channels of $H_2FeRu_3(CO)_{13}$ which allows comparison with $HFeCo_3(CO)_{12}$.

5.2.1.2 Results and discussions

Dissociative electron attachment to $H_2FeRu_3(CO)_{13}$: DEA to $H_2FeRu_3(CO)_{13}$ is characterized by rich fragmentations. The negative ion yield curves are recorded by scanning over the electron energy range while keeping the settings on the quadrupole mass spectrometer constant for a single m/z ratio. However, the mass resolution was kept low to achieve a sufficiently intense ion signal. The isotope distribution of $H_2FeRu_3(CO)_{13}$ spans about 30 amu. This complicates the assignment of fragments just based on its mass. The Fe atom is isobar with the mass of two CO. This even further complicates the assignment of fragments based on their m/z ratio. In order to account for the complications of assigning fragments based on their m/z, the thermochemical threshold for individual fragments is calculated at the PBE0/ma-def2-TZVP level of theory. Thus, in many cases, the fragments are assigned based on the calculated thermochemical threshold along with the energy dependence of their negative ion yield curves.

There are mainly two fragmentation pathways observed in DEA to $H_2FeRu_3(CO)_{13}$; the apex loss and the loss of $Ru(CO)_n$. A minor fragmentation channel leading to the formation of $[Ru_2(CO)_n]^-$ (n = 4 - 7) is also observed [49]. In the apex loss with a

charge retention on the Fe atom, the most intense signal was $[Fe(CO)_4]^-$ and the low intense fragments were $[Fe(CO)_3]^-$ and $[Fe(CO)_2]^-$ (see Fig. 5.21a). The apex loss also leads to the formation of the complimentary fragments $[M - Fe(CO)_4]^-$, $[M - Fe(CO)_3]^-$ and $[M - Fe(CO)_2]^-$ with an intense signal from the $[M - Fe(CO)_3]^-$ fragment. This fragmentation continues with the charge retention on the $Ru_3(CO)_n$ base plane moiety and is observed up to the loss of 11 CO ligands in total (see Fig. 5.22). From the threshold calculations, these fragmentations are attributed to the loss of a neutral $Fe(CO)_4$ and an additional loss of up to 7 CO ligands. The calculated threshold values for the corresponding fragmentation channels are displayed in the respective panel of Fig. 5.22. In the threshold calculations, it is assumed that neutral $Fe(CO)_n$ losses proceed up to n = 4 and are followed by subsequent CO ligand losses whilst the hydrogens are retained on the respective ruthenium base plane fragments. From the m/z ratios, these fragments could also be assigned to $[M - (n+2)CO]^-$, where n = 2 - 11. However, the calculated threshold values for such fragmentations are generally about 3 - 9 eV above the onset of the observed negative ion yield curves. The comparison of the calculated thresholds and the observed AE values for these fragmentations are shown in Table. 5.2. The regression and nature of the negative ion yield curves shown in Fig. 5.22 are similar to the negative ion yield curves observed for sequential CO loss from $HFeCo_3(CO)_{12}$ (see Fig. 5.5). Therefore, the explanations used for $HFeCo_3(CO)_{12}$ can also apply to $H_2FeRu_3(CO)_{13}$. This behavior of regressions in the negative ion yield curves are typical for sequential metastable loss, where $[M - nCO]^-$ is the precursor for $[M - (n+1)CO]^-$. These regressions in the negative ion yield curves, however, require a quasi-continuous electron attachment over the energy range from a few eV up to above 20 eV. Such electron attachment to $HFeCo_3(CO)_{12}$ is discussed in section 5.1.1.2. A similar discussion can apply for $H_2FeRu_3(CO)_{13}$ because the MO energy diagrams for these compounds look very similar (shown in Fig. 5.23). In both cases the MO energy diagram shows a dense "band" of occupied/unoccupied molecular orbitals at the HOMO/LUMO gap. The dense band of occupied/unoccupied molecular orbitals supports the attachment of electrons at higher energies through multiple electronic excitations associated with the attachment process, i.e. the formation of "multi-particle-multi-hole resonances". The HOMO/LUMO of these molecules are spaced by about 3 eV, which allows for more than 6 electronic transitions at incident energy of around 20 eV.

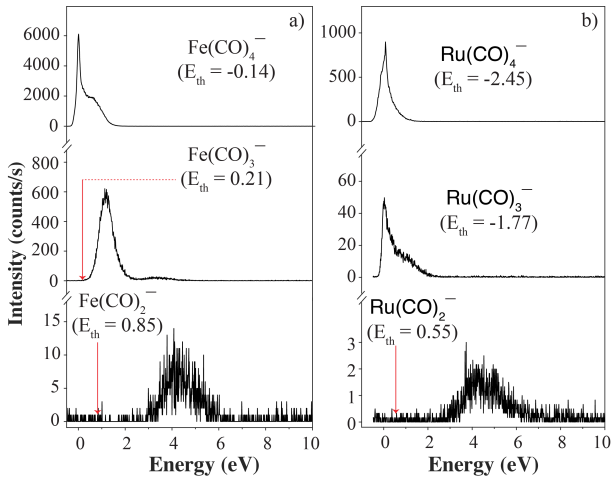

Figure 5.21. Negative ion yield curves for the formation of a) $[Fe(CO)_n]^-$ and b) $[Ru(CO)_n]^-$, where n = 2 - 4 by electron attachment dissociation of $H_2FeRu_3(CO)_{13}$. The thermochemical thresholds for the respective channels calculated at the PBE0/ma-def2 TZVP level of theory are given in parenthesis and indicated by red arrows, adapted from ref. [49].

Fragmentations though the apex loss by DEA to $H_2FeRu_3(CO)_{13}$ can be represented by the equations:

$$[H_2FeRu_3(CO)_{13}]^- \rightarrow [Fe(CO)_n]^- + H_2Ru_3(CO)_{13-n} (n = 2-4) \tag{5.14}$$

$$[H_2FeRu_3(CO)_{13}]^- \rightarrow [H_2Ru_3(CO)_{9-n}]^- + Fe(CO)_4 + nCO (n = 1-7) \tag{5.15}$$

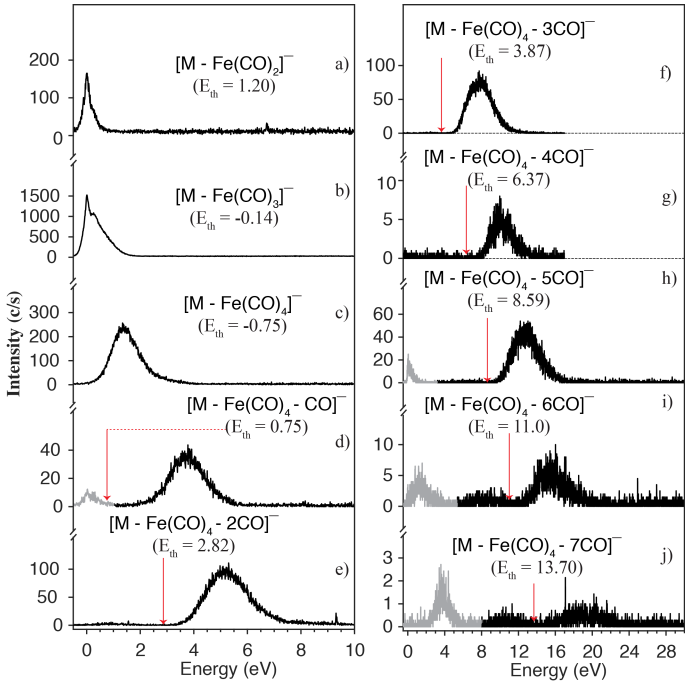

Figure 5.22. Loss of $Fe(CO)_2$ (panel a), $Fe(CO)_3$ (panel b), $Fe(CO)_4$ (panel c) and additional loss of up to 7 COs (from panel d to panel j) through DEA to $H_2FeRu_3(CO)_{13}$. The thermochemical thresholds for the respective channels calculated at the PBE0/ma-def2 TZVP level of theory are given in parenthesis and indicated by red arrows, adapted from ref. [49].

Similar to the apex loss, the formation of $[Ru(CO)_4]^-$, $[Ru(CO)_3]^-$ and $[Ru(CO)_2]^-$ are observed with ion yield characteristics similar to that of $[Fe(CO)_n]^-$ and shown in Fig. 5.21b [49]. From Fig. 5.21b, one can see that $[Ru(CO)_4]^-$ is the most intense signal; the formation of $[Ru(CO)_3]^-$ and $[Ru(CO)_2]^-$ is comparatively less intense. The complimentary ions $[M - Ru(CO)_3]^-$ and $[M - Ru(CO)_4]^-$, and further sequential CO ligand loss up to about 11 CO units from the charge retaining $FeRu_2$ containing moiety, is also observed. From the threshold calculations, similar to the apex loss, these fragmentations are attributed to loss of a neutral $Ru(CO)_4$ unit and an additional loss of up to 7 CO ligands from the charge retaining moiety. The ion yield curves correspond to these fragmentations are shown in Fig. 5.24.

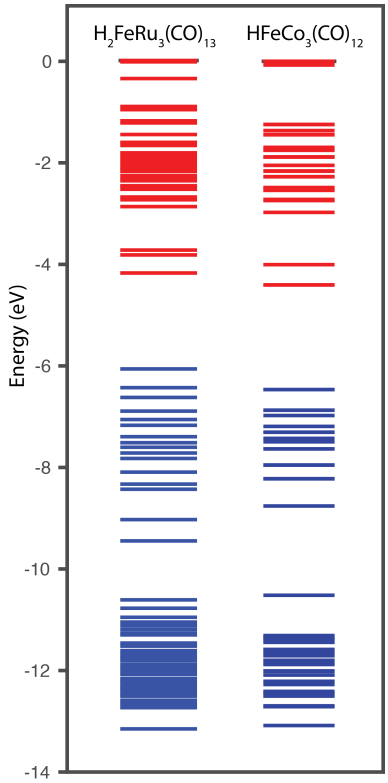

Figure 5.23. Calculated MO diagram of $H_2FeRu_3(CO)_{13}$ and $HFeCo_3(CO)_{12}$, red line represents the unocupied molecular orbitals and blue line represents the occupied molecular orbitals, adapted from ref. [49].

Table 5.2. Calculated threshold (E_{th}) values for the formation of negative ions [M − Fe(CO)$_2$]$^-$, [M − Fe(CO)$_3$]$^-$, [M − Fe(CO)$_4$]$^-$, and [M − Fe(CO)$_4$ − nCO]$^-$ (n = 1 - 7) through electron attachment dissociation of $H_2FeRu_3(CO)_{13}$. These threshold values are compared with corresponding isobar fragments [M − nCO]$^-$, where n = 4 - 13. Threshold values are estimated from the single point energy calculation at the PBE0/ma-def2-TZVP level of theory, geometry optimizations are carried out at the BP86/def2-TZVP level of theory. ZPE corrections and thermal corrections are included in the calculated threshold values. Appearance energy (AE) values are estimated from the rising part of the corresponding ion yield curves. All values are in eV.

Fragment	E_{th} at PBE0/ma-def2-TZVP	Fragment	E_{th} at PBE0/ma-def2-TZVP	AE
[M − 4CO]$^-$	1.69	[M − Fe(CO)$_2$]$^-$	1.20	0
[M − 5CO]$^-$	3.42	[M − Fe(CO)$_3$]$^-$	-0.14	0
[M − 6CO]$^-$	5.02	[M − Fe(CO)$_4$]$^-$	-0.75	0.5±0.1
[M − 7CO]$^-$	7.66	[M − Fe(CO)$_4$ − CO]$^-$	0.75	1.8±0.2
[M − 8CO]$^-$	8.56	[M − Fe(CO)$_4$ − 2CO]$^-$	2.82	3.2±0.2
[M − 9CO]$^-$	12.62	[M − Fe(CO)$_4$ − 3CO]$^-$	3.87	4.4±0.2
[M − 10CO]$^-$	16.30	[M − Fe(CO)$_4$ − 4CO]$^-$	6.37	7.4±0.2
[M − 11CO]$^-$	15.94	[M − Fe(CO)$_4$ − 5CO]$^-$	8.59	9±0.2
[M − 12CO]$^-$	19.00	[M − Fe(CO)$_4$ − 6CO]$^-$	11.00	11.9±0.2
[M − 13CO]$^-$	22.82	[M − Fe(CO)$_4$ − 7CO]$^-$	13.70	14.6±0.2

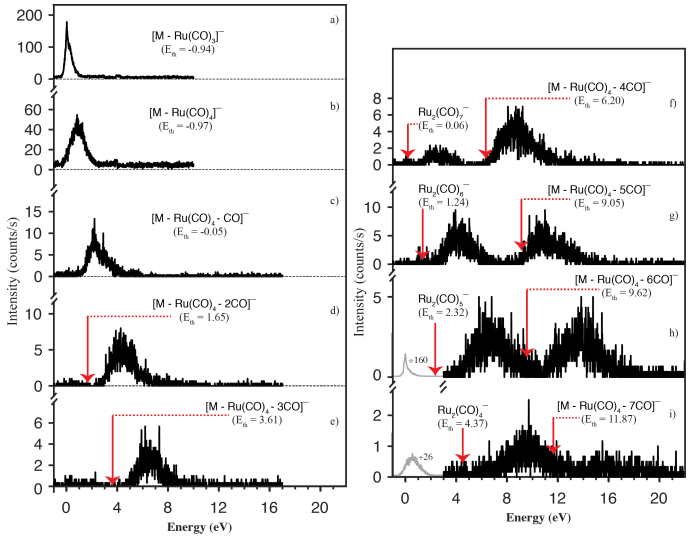

Figure 5.24. Negative ion yield curves for the loss of $Ru(CO)_3$ (panel a), $Ru(CO)_4$ (panel b) and further loss of up to 7 COs (panel c to i) by DEA to $H_2FeRu_3(CO)_{13}$. Also, the ion yield curves for $[Ru_2(CO)_n]^-$ with n = 7 - 4 appear in panels f)-i) respectively, due to the overlap of the isotope distribution of these fragments with that of the respective $[M - Ru(CO)_4 - nCO]^-$ (n = 4 - 7) fragments. The thermochemical thresholds for the respective channels calculated at the PBE0/ma-def2 TZVP level of theory are given in parenthesis and indicated by red arrows, adapted from ref. [49].

The geometrical change that occurs when an electron attaches to $H_2FeRu_3(CO)_{13}$ is quite different from $HFeCo_3(CO)_{12}$. Although the HOMO of $H_2FeRu_3(CO)_{13}$ doesn't show strong bonding character between Fe and Ru, it does show a bonding character along the bridging CO ligands. The HOMO and LUMO of $H_2FeRu_3(CO)_{13}$ is shown in Fig. 5.25. When an electron attaches to $H_2FeRu_3(CO)_{13}$, there is no significant weakening of metal-metal bonding between the apex Fe and Ru base plane but rather a moderate weakening of the bonding within the Ru basal plane, and between the Ru and Fe apex, i.e from 2.934 to 3.037 Å between the hydrogen bridged Ru atoms and from 2.687 to 2.781 Å between the Ru and Fe apex. All other geometrical changes were negligible. In the case of $HFeCo_3(CO)_{12}$ the weakening of metal-metal bonding between the apex and the base plane was very clear. Spin density of the ground state anion of $HFeCo_3(CO)_{12}$ in both the constrained geometry of the neutral (vertical transition) and the relaxed geometry is shown in Fig. 5.26. If we compare the spin density of the $HFeCo_3(CO)_{12}$ anion (see Fig. 5.3) and the $H_2FeRu_3(CO)_{13}$ anion one can see that for $HFeCo_3(CO)_{12}$ the spin density is more localized on the Fe apex, which is in line with the charge retention observed in the apex loss from $HFeCo_3(CO)_{12}$. On the other hand, the spin density of the relaxed anion geometry of $H_2FeRu_3(CO)_{13}$ is in line with the observation of fragments with considerable fraction of charge retention on the Ru base plane [49].

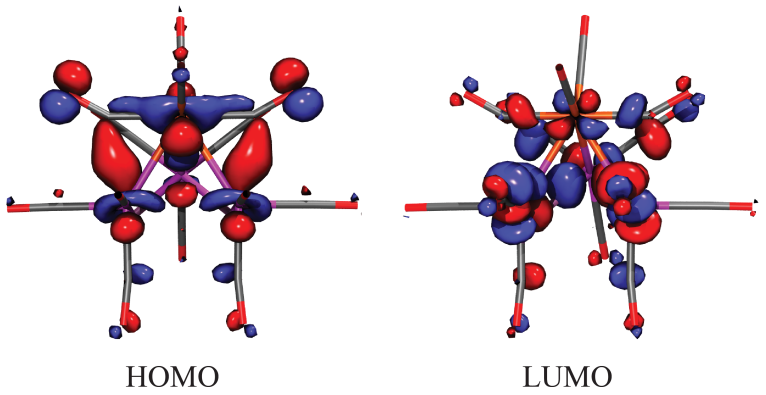

Figure 5.25. The highest occupied molecular orbital (HOMO) and lowest unoccupied molecular orbital (LUMO) of $H_2FeRu_3(CO)_{13}$.

Fragmentation of the basal plane leading to the formation of the fragments $[Ru_2(CO)_n]^-$ (n = 4 - 7) with fairly low intensity is also observed in electron attachment dissociation of $H_2FeRu_3(CO)_{13}$. The m/z ratio for the isotope distribution of these fragments overlap significantly with that of fragments $[M - Ru(CO)_4 - nCO]^-$ with n = 7 - 4. The negative ion yield curves shown in panels (f)-(i) of Fig. 5.24, contain both of these fragments. The assignment of these fragments is based on the calculated thermochemical thresholds, which are displayed in the respective panels.

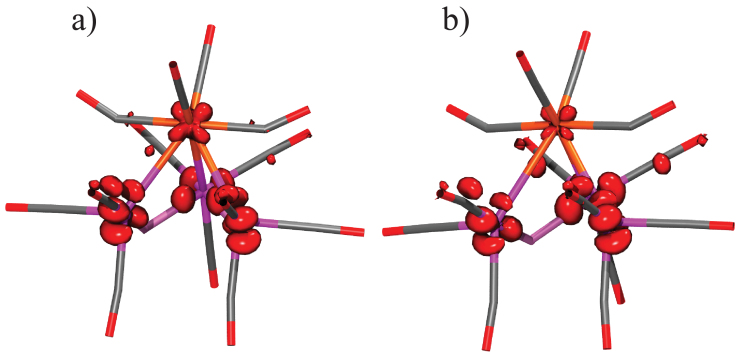

Figure 5.26. Calculated spin density of the $[H_2FeRu_3(CO)_{13}]^-$ anion; a) in the constrained geometry of neutral $H_2FeRu_3(CO)_{13}$ (vertical transition) b) in the relaxed ground state geometry of the anion, adapted from ref. [49].

Based on the observed negative ion yield curves (see Fig. 5.22) and the thermochemical threshold calculations for the possible fragmentation (see Table 5.6), it is obvious that the sequential loss of CO ligands from $H_2FeRu_3(CO)_{13}$ with the remaining metal core intact, is absent. This is clearly different from the electron attachment

fragmentation of $HFeCo_3(CO)_{12}$. While the formation of $[Fe(CO)_n]^-$ (n=4 - 2) through apex loss is similar for both $H_2FeRu_3(CO)_{13}$ and $HFeCo_3(CO)_{12}$.

Dissociative ionization of $H_2FeRu_3(CO)_{13}$

The dissociative ionization spectra/electron impact mass spectra of $H_2FeRu_3(CO)_{13}$ recorded with electron impact energy of 70 eV is shown in Fig. 5.27. Panel (a) in Fig. 5.27 shows the m/z range from 50 to 315 amu and panel b) shows the m/z range from 280 to 670 amu. As we can see from Fig. 5.27, the fragmentation through electron impact ionization of $H_2FeRu_3(CO)_{13}$ is very rich and characterized by broad contributions and significant m/z overlap due to the wide isotope distribution of Ru. As discussed before, the mass of Fe is the same as twice the mass of CO, which further complicates the assignment of fragments observed in the mass spectra. Furthermore, in the lower mass range, doubly charged fragments are formed through multiple ionization. From panel (a) it is obvious that for the m/z range up to about 300 amu, the dominant regression is the formation of $[Fe(CO)_n]^+$ with n = 0 - 5. The mass spectrum in the higher mass range (panel (b)) is mainly characterized by two regressions. The first regression can be assigned to $[M - nCO]^+$ with n = 3 - 13, but it can also be assigned to $[M - Fe - (n\text{-}2)CO]^+$. The second regression can be assigned to $[M - Ru - nCO]^+$ with n = 6 - 11, which can also be attributed to $[M - Ru - Fe - (n\text{-}2)CO]^+$. In the higher mass range, other significant contributions observed are $[M - 2Ru - 6CO]^+$ and $[M - 2Ru - 7CO]^+$. Again, these contributions may also be from $[M - 2Ru - Fe - 4CO]^+$ and $[M - 2Ru - Fe - 5CO]^+$ [49].

The number of CO ligands lost/incident is calculated for both DEA and DI of $H_2FeRu_3(CO)_{13}$. The procedure is the same as discussed at the end of section 5.1.1.2. For estimating the lower limit of DI in $H_2FeRu_3(CO)_{13}$, it is assumed that the higher m/z regression is associated with neutral iron loss as $Fe(CO)_4$. i.e. the loss of apex iron with 4 CO ligands connected to Fe. For the $[Fe(CO)_n]^+$ regression it is assumed that the neutral counterparts formed in DI stay intact. For estimating the higher limit of DI, it is assumed that the higher m/z regression is not associated with Fe loss (i.e. no formation of $[M - Fe - (n\text{-}2)CO]^+$, $[M - Ru - Fe - (n\text{-}2)CO]^+$, $[M - 2Ru - Fe - 4CO]^+$ and $[M - 2Ru - Fe - 5CO]^+$) and in the $[Fe(CO)_n]^+$ regression it is assumed that the neutral counterparts fragment through complete CO loss. In the case of DEA, the upper limit is estimated by assuming additional CO loss from the neutral counterparts produced in the respective DEA channel. The additional CO loss through the fragmentation of neutral counterparts is estimated based on the available excess energy known from the thermochemical threshold calculations. The lower limit for DEA is calculated by assuming neutral Fe and Ru carbonyls (mainly tetracarbonyls) intact without further fragmentations. From these estimations, the calculated average number of CO ligands lost/incident for DEA to $H_2FeRu_3(CO)_{13}$ is 0.5 to 3, while for DI the calculated value is 3 - 9 CO ligands. In DEA, all fragmentations are associated with metal-metal bond rupture, but for DI, this value is somewhere about 50 - 100% depending on how large a fraction of $[M - nCO]^+$ is actually due to the formation of $[M - Fe - (n\text{-}2)CO]^+$. Detailed discussion on gas phase study of $H_2FeRu_3(CO)_{13}$ can be found in article 4

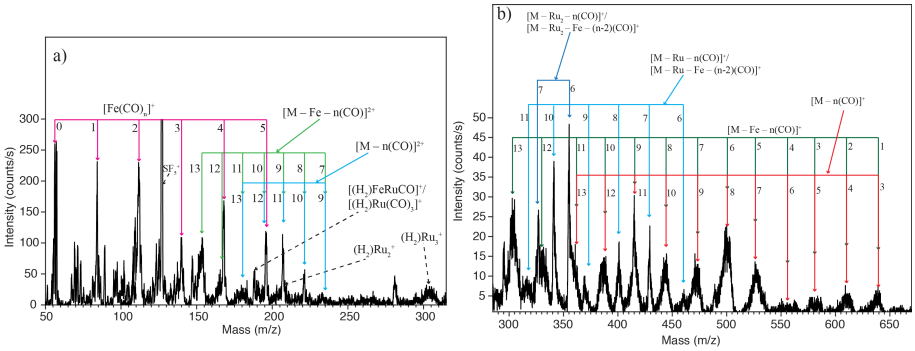

Figure 5.27. Electron impact ionization spectra of $H_2FeRu_3(CO)_{13}$ recorded at electron energy of 70 eV, left panel shows the positive ion fragments formed in the mass range 50 to 315 amu and the right panel shows positive ion fragments in the mass range 280 to 670 amu, adapted from ref. [49].

Conclusions

DEA and DI of $H_2FeRu_3(CO)_{13}$ are characterized by rich fragmentations. Because of the wide isotope distribution of $H_2FeRu_3(CO)_{13}$ (which spans about 30 amu), thermochemical threshold calculations at the PBE0/ma-def2-TZVP level of theory and the onset of negative ion yield curves are used to assign the fragments observed in DEA. In DEA, the dominant fragmentation pathways observed are apex loss and the loss of $Ru(CO)_n$. The apex loss consists of fragments $[Fe(CO)_n]^-$ (n = 2 - 4) with charge retention on the Fe moiety, its complimentary fragments $[M - Fe(CO)_2]^-$, $[M - Fe(CO)_3]^-$, $[M - Fe(CO)_4]^-$ and its continuation as $[M - Fe(CO)_4 - n(CO)]^-$ (n = 1 - 7). From the m/z ratio of the later fragments, it can also be assigned to $[M - (n+2)CO]^-$ (with n = 2 - 11), however, the calculated thresholds for these fragmentations are 3 - 9 eV above the onset of the observed negative ion yield curves which clearly rule out the possibility of $[M - (n+2)CO]^-$ formation. The observations of resonance like structure in the higher energy range (10 - 20 eV) for $H_2FeRu_3(CO)_{13}$ is similar to that of $HFeCo_3(CO)_{12}$, and are typical for metastable sequential loss where $[M - nCO]^-$ is the precursor for $[M - (n+1)CO]^-$. These metastable decays are achieved through quasi-continuous electron attachment (over the energy range few eV to about 20 eV) enabled by the dense band of occupied/unoccupied molecular orbitals close to the HOMO-LUMO gap of $H_2FeRu_3(CO)_{13}$. The fragments formed through loss of $Ru(CO)_n$ consists of $[M - Ru(CO)_3]^-$, $[M - Ru(CO)_4]^-$ and $[M - Ru(CO)_4 - n(CO)]^-$ (n = 1 - 7). A set of fragments, $[Ru(CO)_n]^-$ (n = 2 - 4), are formed with similar ion yield characteristics as $[Fe(CO)_n]^-$. In addition to these fragments, the fragmentation of the basal plane and the formation of $[Ru_2(CO)_n]^-$ (with n = 4 - 7) are also observed in DEA to $H_2FeRu_3(CO)_{13}$, but with fairly low intensities.

The dominant fragments formed in the lower m/z range (below 300 amu) due to DI are $[Fe(CO)_n]^+$ (n = 0 - 5). In the higher m/z range (>300 amu) mainly two regressions are formed due to DI. The first regression can be assigned as $[M - n(CO)]^+$ (n = 3 - 13), but it can also be assigned as $[M - Fe - (n-2)(CO)]^+$. The second regression can be assigned as $[M - Ru - n(CO)]^+$ (n = 6 - 11), it can also be attributed to $[M - Ru -$

$Fe - (n\text{-}2)CO]^+$.

Based on the fragmentations observed in DEA and DI of $H_2FeRu_3(CO)_{13}$, the calculated average number of CO ligands lost/incident for DEA is 0.5 to 3. In the case of DI, the average number of CO ligands lost/incident is calculated to be 3 - 9. All fragmentations observed in DEA are associated with metal-metal bond rupture, but for DI, it is somewhere about 50 - 100%.

5.2.2 Surface study of $H_2FeRu_3(CO)_{13}$

5.2.2.1 Introduction and motivation for the study

The details of the heteronuclear bimetallic precursor molecule $H_2FeRu_3(CO)_{13}$, its uses and its applications are discussed in section 5.2.1.1. The performance of $H_2FeRu_3(CO)_{13}$ in FEBID is poor compared to the structurally similar bimetallic FEBID precursor molecule $HFeCo_3(CO)_{12}$.

From a fundamental point of view, it is important to understand why the performance of $H_2FeRu_3(CO)_{13}$ is very different from the structurally related $HFeCo_3(CO)_{12}$. This is the motivation behind the surface study of $H_2FeRu_3(CO)_{13}$. The gas phase study of $H_2FeRu_3(CO)_{13}$ is discussed in the section 5.2.1. However, the gas phase study alone is not sufficient to understand the electron induced reactions of $H_2FeRu_3(CO)_{13}$ in FEBID because therein, the electron induced reactions occur on a surface. As stated before, this can be addressed with the UHV surface science approach. The UHV surface study of $H_2FeRu_3(CO)_{13}$ is performed similar to $HFeCo_3(CO)_{12}$ and experimental details can be found in section 4.3.

5.2.2.2 Results and discussions

The evolution of the C(1s), O(1s), Fe(2p) and Ru(3d)/C(1s) XPS regions of a nanometer thick $H_2FeRu_3(CO)_{13}$ film (adsorbed onto a gold substrate at 213 K) exposed to different electron doses at 500 eV, is shown in Fig. 5.28. The area analyses of the XPS data recorded prior to electron irradiation reveal that the O:Ru and O:Fe ratios are ~4.8 and ~14.5, respectively. Also there is no sign of CO decomposition, which indicates that the molecule in the deposited film is molecularly intact prior to electron irradiation.

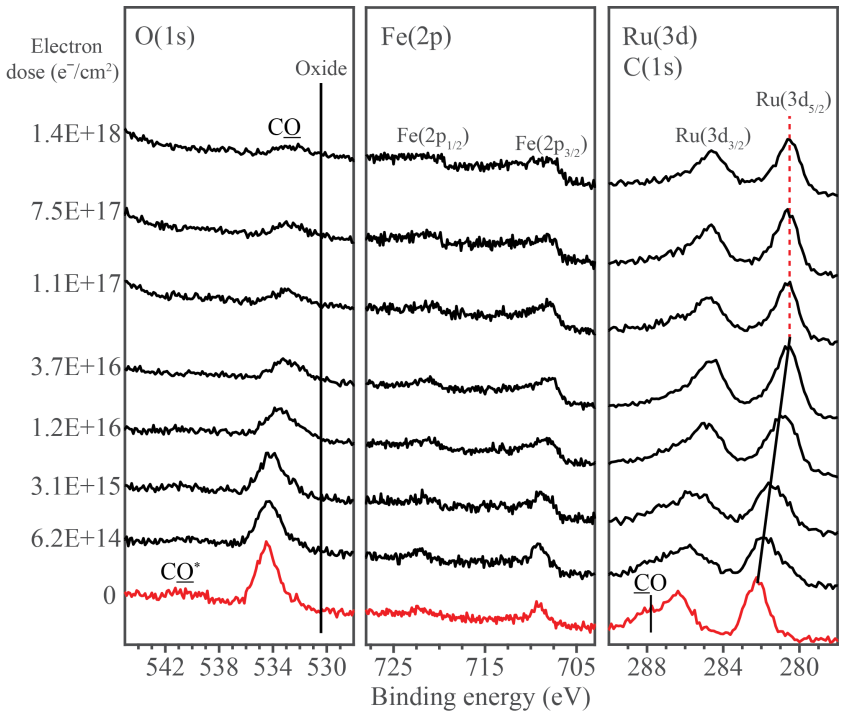

Figure 5.28. Evolution of O(1s), Fe(2p) and Ru(3d)/C(1s) XPS regions of a $H_2FeRu_3(CO)_{13}$ film exposed to electron doses up to 1.4×10^{18} e^-/cm^2 at 500 eV incident energy, adapted from ref. [49].

The O(1s) XPS region of $H_2FeRu_3(CO)_{13}$ prior to electron irradiation consist of two peaks centered at 534.5 and 540.6 eV. The lower binding energy peak can be ascribed to the O(1s) peak of CO ligands and the higher binding energy peak can be ascribed to a $\pi - \pi^*$ shake up feature associated with the CO ligands [161, 162]. The intensity of the O(1s) XPS peak decreases significantly for electron doses $<\approx 5\text{x}10^{16}$ e^-/cm^2. However, after this dose the O(1s) XPS peak remains constant in intensity and peak position. During the entire period of electron irradiation there was no sign of oxide formation, which would be expected to produce an asymmetric XPS peak centered at about 530.5 eV [164].

In the Fe(2p) XPS region, prior to electron irradiation, there are two visible peaks centered at 709.1 and 722.3 eV that corresponds to $Fe(2p_{3/2})$ and $Fe(2p_{1/2})$ transitions in $H_2FeRu_3(CO)_{13}$, respectively. There was only a minor change observed in the Fe(2p) XPS region during electron irradiation except the small shift in Fe(2p) peak position (~0.6 eV) accompanied by a small amount of peak broadening.

The Ru(3d)/C(1s) XPS region can be fitted with three peaks prior to electron irradiation. The fitting of these regions is shown in Fig. 5.29, the fitted region at 286.2 and 282.2 eV corresponds to the $Ru(3d_{3/2})$ and $Ru(3d_{5/2})$ transitions, respectively. Another small peak centered at 287.7 eV, which appeared as a shoulder on the higher binding energy side of the $Ru(3d_{3/2})$ peak can be ascribed to the C(1s) peak of the CO

ligands [163]. The shake up feature of the C(1s) associated with the CO ligands, which is expected at ~293.2 eV is not visible because of its low intensity. During the electron irradiation, the peak positions, corresponding to Ru($3d_{3/2}$) and Ru($3d_{5/2}$), decrease noticeably towards lower binding energies. The qualitative decrease in the intensity of the XPS peak corresponding to CO ligands is also visible. From the spectral fitting of the Ru(3d)/C(1s) XPS region measured after an electron dose of $1.4x10^{18}$ e^-/cm^2 (which is shown in Fig. 5.29) it is clear that there is no graphitic carbon formed (peak expected at 284.5 eV), even with increased electron irradiation.

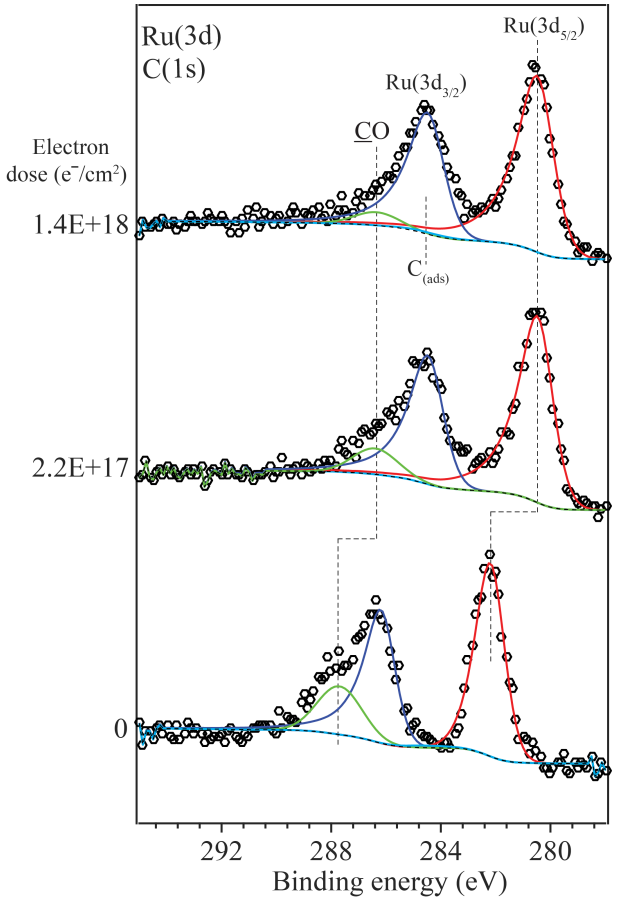

Figure 5.29. Fitting of the Ru(3d)/C(1s) XPS region prior to electron irradiation and with electron dose of 2.2×10^{17} e^-/cm^2 and 1.4×10^{18} e^-/cm^2 at 500 eV, The XPS regions are fitted using CASA XPS program.

As discussed for $HFeCo_3(CO)_{12}$ in section 5.1.2.2, the SEs produced by the effect of X-rays can induce some changes to the $H_2FeRu_3(CO)_{13}$ film. These effects are studied in a separate control experiment. Results from these experiments reveal that the X-rays can produce similar changes as electron irradiation produces to nanometer thick

film of $H_2FeRu_3(CO)_{13}$ but at a much slower rate. Based on the area analysis of the O(1s) XPS peak it is estimated that the time required to acquire an XPS scan of O(1s), Fe(2p) and C(1s)/Ru(3d) is equal to an electron dose of $\approx 6.3 \times 10^{14}$ e^-/cm^2. This value indicates that the effect of X-ray irradiation during the measurement shown in Fig. 5.28 is minimal except for the shorter electron doses, where the measured dose based on the electron irradiation is accordingly slightly underrepresented.

The fractional change in oxygen estimated from the area analysis of the O(1s) XPS peak and the change in the Ru(3d) XPS peak position with increasing electron irradiation is shown in Fig. 5.30. From Fig. 5.30, one can see that the fractional change in oxygen atom and the Ru(3d) XPS peak position follow similar dependencies on electron irradiation and decrease significantly for electron doses $<\approx 6 \times 10^{16}$ e^-/cm^2, but remain almost constant thereafter. The binding energy of the $Ru(3d_{5/2})$ peak decreases systematically from an initial value of 282.2 eV to 280.6 eV (this value is closer to the Ru metal binding energy of 280.1 eV [163]) after an electron dose of $\approx 6 \times 10^{16}$ e^-/cm^2, which indicates partial reduction of ruthenium during the decomposition process. Over the electron irradiation, with same electron doses, the fractional decrease in oxygen coverage indicates reduction of the oxygen content by 70% of its initial value.

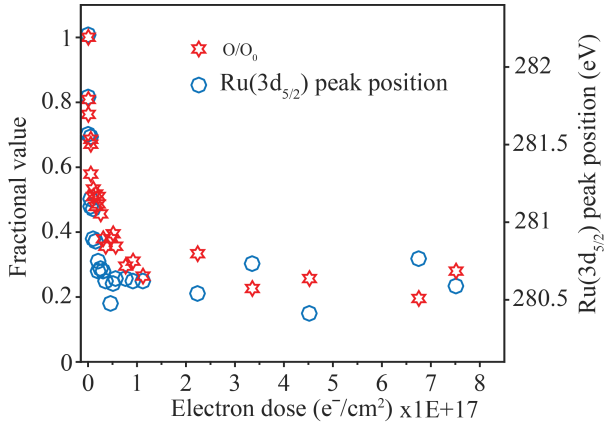

Figure 5.30. Change in fractional coverage of oxygen atoms (red stars) and, $Ru(3d_{5/2})$ peak position (blue open circle) for $H_2FeRu_3(CO)_{13}$ films, all plotted as a function of electron dose, adapted from ref. [49].

The mass spectrum of species coming off from the adsorbed film of $H_2FeRu_3(CO)_{13}$ during electron irradiation is shown in Fig. 5.31. The only species observed in the mass spectrum were CO ligand species (m/z = 28 (CO), 12 (C), 16 (O)), along with some hydrogen and water residual species present in the UHV chamber.

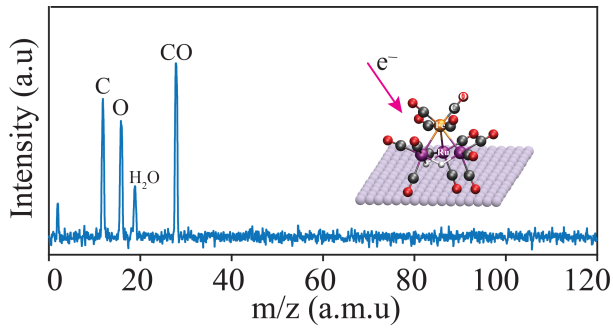

Figure 5.31. Mass spectrum of gas phase species desorbed from the $H_2FeRu_3(CO)_{13}$ film during the course of an electron dose ~1.2×10^{17} e^-/cm^2, adapted from ref. [49].

Figure 5.32 shows the change in O(1s), Fe(2p) and Ru(3d)/C(1s) XPS regions when nanometer thick film of $H_2FeRu_3(CO)_{13}$ (bottom set of spectra) first irradiated with electron dose of 1.3x10^{17} e^-/cm^2 and then annealed to RT (topmost spectra). For the electron irradiation, an electron dose of 1.3x10^{17} e^-/cm^2 was chosen because this is the minimum dose required to complete the initial stage of the electron induced reaction in terms of CO desorption (see Fig. 5.28). The evolution of the O(1s), Fe(2p) and Ru(3d)/C(1s) signal with electron irradiation of dose 1.3x10^{17} e^-/cm^2 shown in Fig. 5.32 is similar to that shown in Fig. 5.28 with the dominant change being the reduction of O(1s) signal intensity (~70% of its initial value) and a decrease in binding energy of Ru(3d) (decreased by about 1.6 eV). Upon annealing, the electron irradiated $H_2FeRu_3(CO)_{13}$ film to RT, the O(1s) intensity further decreased by only 8%. Moreover, a small shoulder on the higher binding energy side of the $Ru(3d_{3/2})$ peak was still visible, which indicates the presence of CO ligands. There was no change in the peak position of Ru(3d) observed, however a slight broadening in the Fe(2p) XPS peak was noticed.

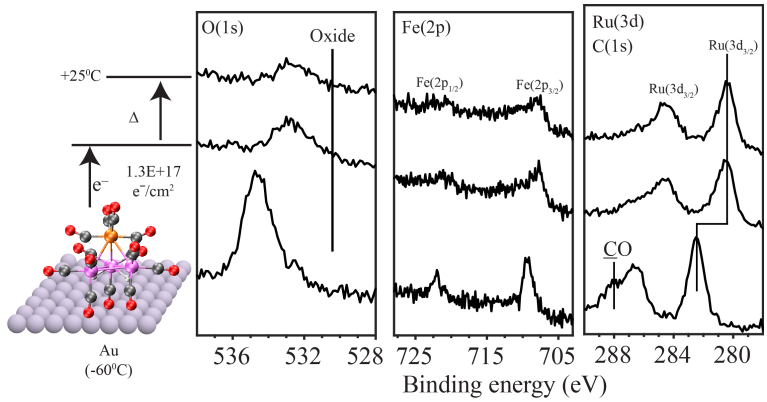

Figure 5.32. Changes in the O(1s), Fe(2p) and Ru(3d)/C(1s) XPS regions when an $H_2FeRu_3(CO)_{13}$ film was exposed to an electron dose of 1.3×10^{17} e^-/cm^2 (middle set of spectra) and then subsequently heated to room temperature (298 K) (uppermost set of spectra), adapted from ref. [49].

Discussion of results obtained in the surface study of $H_2FeRu_3(CO)_{13}$
From the previous surface study of $HFeCo_3(CO)_{12}$ it was found that the initial step in the electron induced reaction of FEBID precursor molecules involves decomposition of precursor molecules accompanied by ligand desorption. In the case of $H_2FeRu_3(CO)_{13}$, from Fig. 5.30 it is clear that this initial electron induced reaction is completed at electron doses on the order of $1.0x10^{17}$ e^-/cm^2, where the CO ligands present in the $H_2FeRu_3(CO)_{13}$ film are reduced to ~30% of their initial value. The removal of CO ligands from the $H_2FeRu_3(CO)_{13}$ film is evidenced by a decrease in the O(1s) XPS peak area (see Fig. 5.28) and the evolution of CO detected by MS (see Fig. 5.31). The electron induced decomposition of $H_2FeRu_3(CO)_{13}$ also causes reduction in the binding energy of Fe(2p) (from 709.1 to 708.5 eV) and Ru(3d) (from 282.2 to 280.6 eV). The reduced binding energy of Ru(3d) (280.6 eV) is closer to the binding energy of metallic ruthenium (280.1 eV), which suggest an extensive CO desorption from the Ru atoms.

From the analysis of Fig. 30 it is clear that 65 - 70% of the CO ligands present in the $H_2FeRu_3(CO)_{13}$ film desorb during their initial electron induced decomposition. Based on the stoichiometry of $H_2FeRu_3(CO)_{13}$ one can therefore estimate that on average 8 - 9 of the 13 CO ligands present in $H_2FeRu_3(CO)_{13}$ desorb following the initial electron induced decomposition. From the gas phase experiments of $H_2FeRu_3(CO)_{13}$ which were discussed in section 5.2.1.2, it is estimated that on average of 3 - 9 CO ligands were removed from $H_2FeRu_3(CO)_{13}$ through DI of $H_2FeRu_3(CO)_{13}$, while only ~0.5 - 3 CO ligands are removed through DEA of $H_2FeRu_3(CO)_{13}$. The contribution of ND for removing CO ligands from $H_2FeRu_3(CO)_{13}$ cannot be determined using the current gas phase experiments described in this thesis. However, from the nature of ND discussed in section 3.1.2.1, it is expected that $H_2FeRu_3(CO)_{13}$ decomposition is as similar to the decomposition through DEA rather than DI. Therefore, from the comparison of gas phase and surface data, it is reasonable to assume that the initial electron induced decomposition of $H_2FeRu_3(CO)_{13}$ proceeds through DI rather than DEA. The same trend is observed for $HFeCo_3(CO)_{12}$ as well (see section 5.1.2.2).

The analysis of Fig. 5.28 shows no oxide formation (does not present any appearance of lower binding energy peaks in the O(1s) XPS region). As a result, one can conclude that the parent molecule is initially converted to a partially decarbonylated surface bound intermediate as shown in Fig. 5.33. In Fig. 5.33 it is also shown that the initial electron induced decomposition of $H_2FeRu_3(CO)_{13}$ proceeds through DI, rather than DEA. The formation of single partially decarbonylated intermediate is not expected, but rather the formation of a mixture of partially decarbonylated intermediates such as $H_2FeRu_3(CO)_x$(x=4,5). Due to the lack of sensitivity of XPS towards hydrogen, it was not possible to gain any insight into the fate of hydrogen atoms present in the precursor molecule.

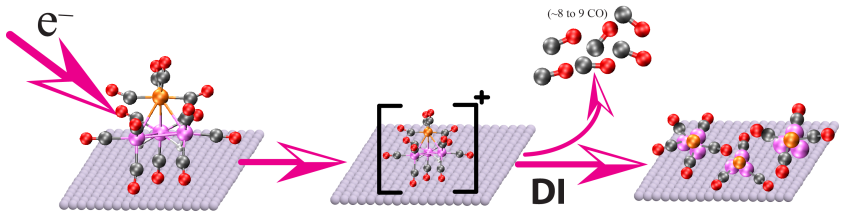

Figure 5.33. Initial decomposition/deposition of a surface adsorbed $H_2FeRu_3(CO)_{13}$ precursor, mediated by DI. The mixture of partially decarbonylated intermediates shown on the right side represents the statistical nature of DI, each generated by the loss of a different number of CO groups from the parent molecule, adapted from ref. [49].

Fate of the partially decarbonylated intermediate:
In typical FEBID experiments, electron induced reactions take place at RT under steady state conditions. In that case, the partially decarbonylated intermediate formed will be subject to either the effects of further electron irradiation or undergo thermally triggered reactions. Using surface science experiments, one can independently probe the fate of partially decarbonylated intermediates towards increased electron irradiation or thermal effect.

Stability towards further electron irradiation:
After an electron irradiation dose of $\approx$1.0x10^{17} e$^-$/cm^2, the adsorbed $H_2FeRu_3(CO)_{13}$ molecule converts into a partially decarbonylated intermediate as shown in Fig. 5.33 with average stoichiometry of $H_2FeRu_3(CO)_{4.5}$. The effect of further electron irradiation (electron dose $>\approx$1.0x10^{17} e$^-$/cm^2) to partially decarbonylated intermediates can be found in Figs. 5.28 and 5.30. Analysis of XPS data shown in Figs. 5.28 and 5.30 for electron doses $>\approx$1.0x10^{17} e$^-$/cm^2 reveals no noticeable changes in the O(1s), Fe(2p) and Ru(3d)/C(1s) XPS regions. This indicates that the CO ligands that remained in the partially decarbonylated intermediates are relatively stable towards increased electron irradiation. This behavior is quite different from the previously studied CO containing FEBID precursor molecules, where the decomposition of CO ligands and formation of graphitic carbon and metal oxides is commonly observed [30, 31]. Why the CO ligands in the $H_2FeRu_3(CO)_{13}$ intermediate stable towards extended electron irradiation is not very clear thus further investigation is required.

Thermal stability:
Typical FEBID experiments are performed at room temperature. However, the UHV surface study of $H_2FeRu_3(CO)_{13}$ was performed at 213 K. In order to check the effect of temperature, a separate experiment conducted with $H_2FeRu_3(CO)_{13}$ in which the adsorbed $H_2FeRu_3(CO)_{13}$ film was first irradiated with a dose sufficient to create partially decarbonylated intermediates and then these partially decarbonylated intermediate were annealed to RT (shown in Fig. 5.32). Analysis of Fig. 5.32 reveals that after annealing to RT there is relatively small reduction in the O(1s) intensity (O(1s) area reduced by ~22%) but most of the CO ligands still remain in the partially decarbonylated intermediate with average stoichiometry of $H_2FeRu_3(CO)_{3.5}$

From the FEBID experiments, the metal content of the deposits created from $H_2FeRu_3(CO)_{13}$ are reported to be <30at%. From the surface science results discussed for $H_2FeRu_3(CO)_{13}$ it is clear that the partially decarbonylated intermediate ($H_2FeRu_3(CO)_x$) created by electron induced decomposition of $H_2FeRu_3(CO)_{13}$ will not change significantly whether it is subjected to increased electron irradiation (see Fig. 5.28) or thermal processing (see Fig. 5.32). As a result, the carbon and oxygen contained in the partially decarbonylated intermediates will be incorporated into the deposit created from $H_2FeRu_3(CO)_{13}$ in FEBID. Therefore, the overall electron induced reactions of $H_2FeRu_3(CO)_{13}$ experience during its FEBID can be represented as:

$$H_2FeRu_3(CO)_{13(physisorbed)} + e^- \rightarrow H_2FeRu_3(CO)_x (x = 4,5)(chemisorbed) + 8.5(CO)\uparrow(g) \quad (5.16)$$

$$H_2FeRu_3(CO)_x (x = 4,5)(chemisorbed) + e^-/\Delta \rightarrow most \quad CO \quad ligands \quad are \quad retained \quad (5.17)$$

This overall process is also shown schematically in Fig. 5.34, where the partially decarbonylated intermediates are co-deposited in the growing deposit. From the stoichiometry of the partially decarbonylated intermediate formed after irradiation and annealing of $H_2FeRu_3(CO)_{13}$, one can estimate the metal content remained in the partially decarbonylated intermediate, the estimated metal content is <31%. These values are matching well with the values found in the FEBID experiment of $H_2FeRu_3(CO)_{13}$ (i.e. metal content <30%).

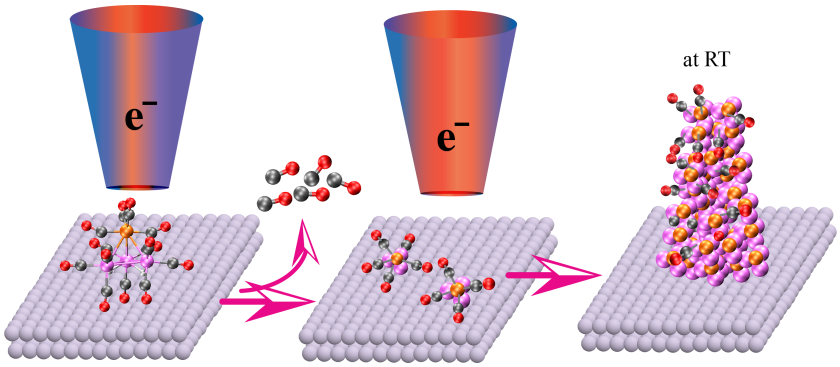

Figure 5.34. Schematic showing the incorporation of partially decarbonylated intermediates of $H_2FeRu_3(CO)_{13}$ into the deposit in FEBID, adapted from ref. [49].

5.2.2.3 Conclusions

In the initial electron induced reactions of surface adsorbed $H_2FeRu_3(CO)_{13}$, 70% of the CO ligands were removed and a partially decarbonylated intermediate was formed with an average stoichiometry of $H_2FeRu_3(CO)_{4.5}$. Compared to previously studied CO containing FEBID precursor molecules like $Co(CO)_3NO$ and $W(CO)_6$, the bimetallic precursor molecule $H_2FeRu_3(CO)_{13}$ shows extensive CO desorption (i.e.

~70%). However, the extent of the initial CO desorption for $H_2FeRu_3(CO)_{13}$ is similar to that of the bimetallic precursor molecule $HFeCo_3(CO)_{12}$. When comparing the extent of CO desorption with the gas phase results of $H_2FeRu_3(CO)_{13}$, it is most likely that the initial electron induced surface reactions of $H_2FeRu_3(CO)_{13}$ proceed through DI rather than DEA. With further electron irradiation to the partially decarbonylated intermediate $H_2FeRu_3(CO)_x$ (x = 4.5), no significant changes were observed, which is quite different from the previously studied CO containing FEBID precursor molecules where CO decomposition and oxidation occurred. In the annealing experiment which was conducted to mimic the thermal conditions of the FEBID experiment, the O(1s) intensity of CO ligands in the partially decarbonylated intermediate reduced only slightly, thus CO ligands in the intermediate still remained with an average stoichiometry of $H_2FeRu_3(CO)_{3.5}$. The stability of CO ligands in the intermediate $H_2FeRu_3(CO)$x (x = 4.5) towards further electron irradiation and thermally triggered desorption are in line with the metal content of deposits created from $H_2FeRu_3(CO)_{13}$ in FEBID.

5.3 FEBID of dichlorosilacyclohexane, silacyclohexane and trisilacyclohexane

5.3.1 Role of DEA and DI in the electron beam induced deposition of dichlorosilacyclohexane and silacyclohexane

5.3.1.1 Introduction and motivation for the study

Secondary electron generation during the FEBID process, its interactions with FEBID precursor molecule and different dissociation mechanisms that are active in the SE energy ranges are discussed in previous sections (see sections 2.2.2 and 2.2.3). For the last few years there have been significant efforts put into de-convoluting the effects of different dissociation mechanisms and to better understand the chemistry and physics behind these dissociation mechanisms in FEBID. Ultimately this may aid the design of suitable precursors for FEBID. In this context, there have been many gas phase studies conducted mainly regarding DEA and DI of different organometallic precursor molecules (see the introduction section of chapter 3). Many surface studies intended to link the gas phase observations to the actual conditions in FEBID have also been conducted. These are also discussed in chapter 3.

Although these gas phase and surface studies provide a better insight into DEA and DI and in some cases the most probable dissociation mechanism responsible for the initial electron induced decomposition of FEBID precursor molecules, they do not provide direct comparison between the role of DEA and DI in the deposition and its influence on deposit formation in FEBID. Using two kinds of precursor molecules, one that is active towards both DEA and DI processes and another that is inert to DEA and active towards DI, is an approach to directly compare the role of DEA and DI in the electron induced deposition and deposit formation in FEBID.

The recent gas phase study of the silicon containing precursor molecules dichlorosilacyclohexane (DCSCH) and silacyclohexane (SCH) show that SCH is active with respect to DI but completely inert with respect to DEA (within the sensitivity of the

instrument used). DCSC, on the other hand, is active with respect to both DEA and DI. The structures of DCSCH and SCH are shown in Fig. 5.35. Different sensitivities of DCSCH and SCH towards fragmentation induced by DEA motivated the FEBID experiments conducted with these precursor molecules in the current thesis. In the FEBID experiment, the different sensitivities of DCSCH and SCH towards DEA effects on the growth dynamics of deposits created from these precursor molecules were investigated. Another motivation to perform EBID experiments with DCSCH and SCH is that these precursors can be used as a potential precursor for silicon oxide, SiO_2 depositions, especially in presence of oxidizing agents such as water or oxygen. Silicon oxide depositions have many optical applications, e.g. use for the deposition of transparent nano-optics, [92, 167, 168] SiO_2 deposition can e.g. be used for repairing Deep Ultraviolet (DUV) mask [169].

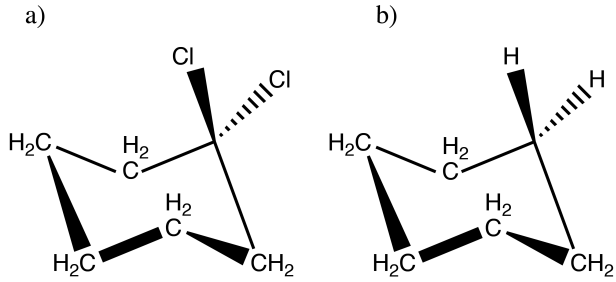

Figure 5.35. Molecular structure of a) dichlorosilacyclohexane (DCSCH), b) silacyclohexane (SCH).

5.3.1.2 Results and discussions

There has been no report of depositions created from DCSCH and SCH in FEBID. So, this is the first EBID experiment of DCSCH and SCH. In the EBID experiment, both DCSC and SCH successfully produced deposits on top of a silicon substrate. Pillars created from DCSCH and SCH are shown in Fig. 5.36. Both have typical pillar characteristics i.e. a cylindrical lower part and a conical upper part. In order to characterize the growth dynamics of both precursors, a series of pillars were deposited with varying electron beam exposure times, but all the other parameters such as precursor pressure, beam energy, beam current are kept constant. The changes in pillar base diameter for varying beam exposure time for DCSCH and SCH are shown in the plot in Fig. 5.37a. In the initial stage of pillar growth, the base diameter increases abruptly, but after 300 s the pillar base diameter starts saturating. The highest initial lateral growth measured for DCSH is 12 nm/s (measured at 300 ms) and that for SCH is 8 nm/s (measured at 600 ms). The lateral growth rate decreases significantly after 300 s and the saturated pillar base diameter is ~90 nm for DCSCH and ~70 nm for SCH. From Fig. 5.37a it is clear that the saturated pillar base diameters of DCSCH are larger than for SCH for the entire range of deposition time. The change in pillar height of these precursor molecules for varying beam exposure time is shown in Fig. 5.37b. Both precursor molecules show a linear increase in the pillar height with beam exposure time but slight decreases in the vertical growth rate at higher electron beam exposure time.

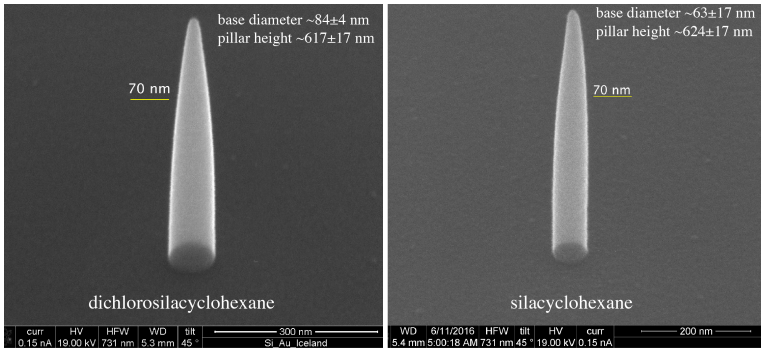

Figure 5.36. SEM image of pillars deposited from DCSCH (left panel) and SCH (right panel). The precursor pressure was 3×10^{-5} mbar and the total deposition time was 180 s for both DCSCH and SCH. Electron beam energy of 20 keV and a current of 150 pA were used for the deposition. The base diameters and heights are given in the respective images, adapted with permission from ref. [170].

An energy dispersive X-ray (EDX) analysis was employed to find out the composition of the deposit. All the depositions for EDX measurements were performed on a gold substrate to distinguish the deposit elements from the substrate elements. From the EDX analysis it is found that DCSCH has a Si/O/C/Cl ratio of 1.0/2.4/5.8/0.2, and SCH has a Si/O/C ratio of 1.0/1.1/6.0. In both cases the Si/C ratio was close to that of the precursor molecules (1/5), and the additional carbon content in the deposition most likely originates from background gases. The Si/O ratio estimated for DCSCH is almost twice that for SCH, which is most likely due to the hydrolysis of the Si-Cl bond in presence of residual water in the FEBID chamber.

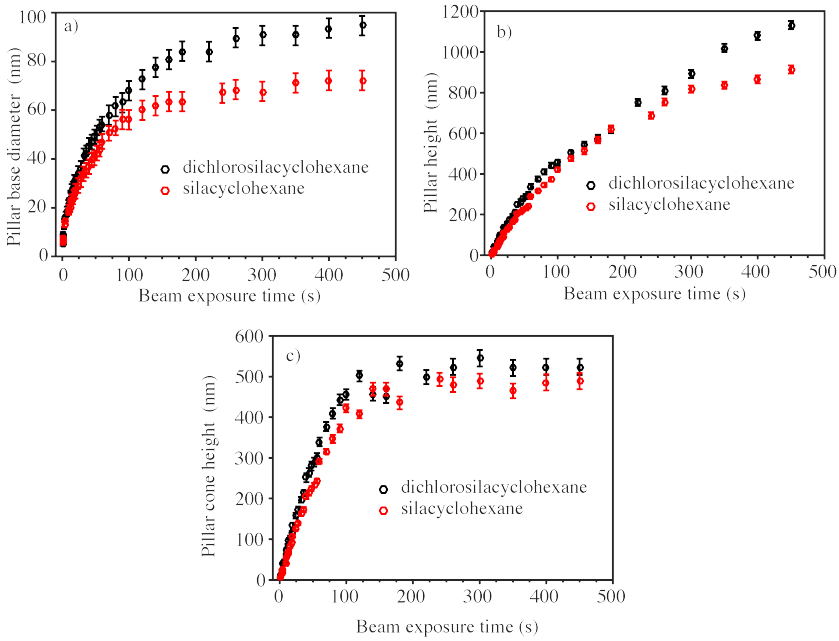

Figure 5.37. (a) Measured pillar base diameter, (b) pillar height and (c) heights of the cone shaped section of the upper part of the pillars as a function of electron beam exposure time for DCSCH and SCH as black and red circles, respectively. The experimental parameters like precursor pressure, electron beam energy, current are kept constant during the experiment, adapted with permission from ref. [170].

In a typical EBID pillar growth, one can distinguish three growth regime, nucleation stage, fast growth stage and a saturation stage [20, 171]. Nucleation stage is the initial growth stage, where a dot like structure will form, mostly due to the scattered electrons from the substrate. In the fast growth stage, a conical shape starts appearing with maximum lateral and vertical growth rate. In the fast growth stage, the growth will enhance by forward and backscattered electrons (FSE and BSE) generated in the growing deposit, as well as SEs created by the FSEs and BSEs from both the substrate and the deposit [171]. The morphology of cone growth mostly depends upon the primary electron beam interaction volume and it is material dependent [171]. When the interaction volume of the primary electrons is confined to the pillar volume, the lateral growth stops. At this point the cone will no longer change its shape, but a cylindrical structure will start growing under the conical part. The cone angles of the pillars were measured from the tilted SEM images of the pillars. In the beginning stage, the pillar cone angle for DCSCH is 71 and that for SCH is 74^0 respectively. The change in pillar tip cone height for DCSCH and SCH with varying beam exposure time is shown in Fig. 5.37c. From Fig. 5.37, it is obvious that for both DCSCH and SCH the pillar tip cone height saturates at about 500 nm. This value is significantly lower than the interaction volume of bulk silicon, the estimated interaction volume of Si for 20 keV PEs using Kanayana and Okayama equation [172] is ~4.7 μm. However, the interaction volume

of pillar geometry is not necessarily the same as the interaction volume of bulk. For e.g. the Monte Carlo simulated penetration depth of 20 keV electrons in a flat aluminum substrate is 3200 nm, while the simulate 20 keV electron penetration depth in a pillar geometry with a 10^0 cone angle is only 240 nm [173]. Similarly in the case of bulk SiO_2, the calculated interaction volume for 20 keV electrons is ~3 μm, while for cylindrical geometry it is only 500 nm [174]. If we assume the pillars deposited from DCSCH and SCH are SiO_2, then the interaction volume of 20 keV electrons on 80 nm pillar geometry might be <500 nm, which is in agreement with the observation made from Fig. 5.37c. After 180 s of electron beam exposure time, the lower part of the pillar grows as cylindrical and at this point the pillar base diameter and cone height saturates. Therefore, one can define the pillar growth at 180 s as the saturation point, after this, the lateral growth diminishes but the pillar height keeps increasing.

The evolution of pillar volume as a function of electron beam exposure time is shown in Fig. 5.38a. From Fig. 5.38a one can see that the pillar volume is larger for DCSCH compared to SCH. The difference in volume growth for DCSCH and SCH is better visible in the volume growth rate curve, which is shown in Fig. 5.38b, where the volume growth rate is larger for DCSCH compared to SCH.

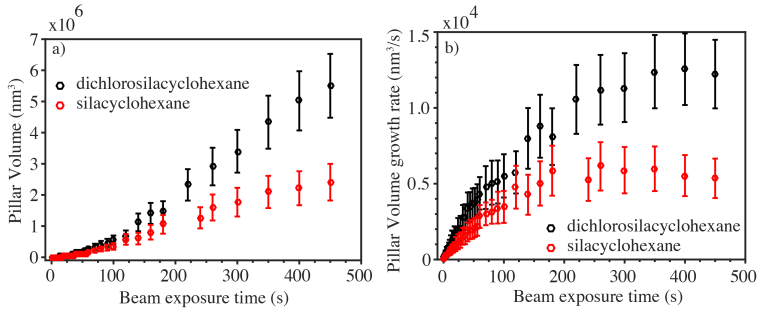

Figure 5.38. (a) pillar volume determined from the measured pillar diameter, pillar height, tip cone height and cone angle, versus exposure time for DCSCH and SCH. (b) the pillar volume growth rate versus exposure time for DCSCH and CSH., adapted with permision from ref. [170].

When comparing the lateral growth of DCSCH and SCH pillars below 180 s, it is obvious from Fig. 5.37 that DCSCH pillars have larger base diameter compared to that of SCH pillars. In the beginning of pillar growth, the difference in pillar base diameter is ~1.3 nm and it gradually increase with beam exposure time. At 180 s the difference in pillar base diameter is close to 20 nm. The analysis of Fig. 5.38b shows that the pillar volume growth rate for DCSCH is twice that of SCH, in the early growth stage and the same enhancement in growth rate for DCSCH is maintained even at higher beam exposure time. (i.e. DCSCH volume growth rate is ~2 times that of SCH). As the SEs have significant influence on the lateral growth of pillars, one should expect smaller base diameter for pillars deposited when DEA channels are not available if the DI and ND cross sections are similar, as is the case for SCH.

If we inspect the DEA results of DCSCH in ref [140] one can see that DEA to

DCSCH is mainly active below 2 eV and in the range from 6 - 9 eV with similar integral cross sections for both of these energy ranges. This means that the inert behavior of SCH compared to DCSCH only matter for electrons of energy < 2 eV and in the range of 6 - 9 eV. The effective dissociation yield of DEA during EBID not only depends upon the DEA cross section but also on the available electrons within the respective energy ranges. From the secondary electron emission spectra of Si irradiated by 1 keV [175], the estimated integrated contribution of electrons with energy < 2 eV and in the range 6 - 9 eV is ~50% of the total emitted SEs below 20 eV and extrapolation of the SE yield to 100 eV would bring this value a bit down. Since we do not have an estimate of DEA and DI cross section of DCSCH and SCH, it is difficult to know how much is the actual contribution of DEA to deposition compared to DI. In the earlier stage of pillar growth, the difference in pillar base diameter for DCSCH and SCH is small, but at a later stage the difference increases and shows a maximum value at the saturation point i.e. at 180 s. At this saturation point the SE yield will be at its maxima as is shown in ref [66, 171] hence the difference in diameter observed at this point might be attributed to the <2 eV and 6 - 9 eV electrons.

In summary, although DCSCH shows clearly higher lateral growth compared to SCH and DEA would cause this additional lateral growth, the evidence obtained is insufficient to ascribe the additional lateral growth fully to the effect of DEA. The electron scattering in the deposit created from these precursors may be different which will result in different electron yields and the absolute cross sections for the individual dissociation processes are not known.

In order to further study the effect of low energy SEs in the deposition process of DCSCH and SCH, experiments were also conducted where deposits are grown in close proximity of each other and the broadening through the proximity effect is observed.

Proximity effect comparison between DCSCH and SCH

When a pillar is deposited in close proximity to a previously-deposited pillar, SEs, BSEs and FSEs emitted from the newly-deposited pillar may induce deposition on the previously-deposited pillar. This is called the proximity effect. The proximity effect may be most visible during the deposition of an array of dots and the broadening of the diameter of deposited dots (due to the proximity effect) will depend upon the order in which they are deposited. An array of dots was deposited for both DCSCH and SCH in two different geometries. The two different geometries are shown schematically in Fig. 5.39. The schematic in Fig. 5.39a corresponds to a circular arrangement of dots, shown in blue. The first pillar is deposited in the center of the circle and the other 8 pillars are deposited surrounding the central pillar; the order of deposition is marked in the figure. The expected additional broadening of the deposit due to proximity effect is shown in the figure with red filled circles. The red arrows indicate the pillars causing the additional broadening. If the proximity effect was absent, all the dots would be expected to have the same diameter after deposition. The schematic in Fig. 5.39b corresponds to a square arrangement of dots. The blue filled circle represents the diameter of dots if there was no proximity effect, the red and green circle represent the additional deposition due to the proximity effect and the red and green arrows indicate the origin of the additional deposition.

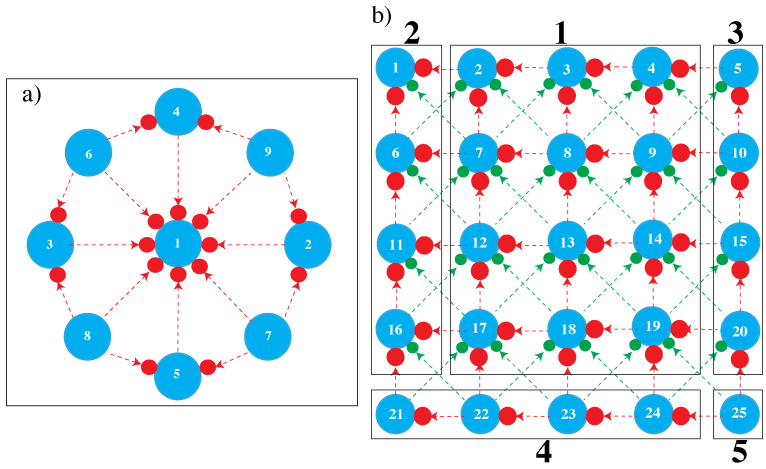

Figure 5.39. a) Schematic showing the order of pillar deposition in a circular array around a central dot. b) Schematic showing the order of pillar deposition in a square array. Blue filled circles represent the diameter of the pillars with no proximity effect, red filled circles represent the lateral broadening induced by the deposition of pillars in close proximity (nearest neighbours) and green filled circles represent the lateral broadening induced by the deposition of pillars that are not as close, but still capable of inducing additional deposition. In the circular configuration these were not indicated, and in the square configuration these are the next diagonal neighbours. The bold numbers, shown for the square configuration, represent the areas with the same expected pillar diameters. adapted with permission from ref. [170].

From the schematic shown in Fig. 5.39a, one can see that the largest dot in the presence of the proximity effect after the deposition process will be dot 1, the second largest dots should be 2 - 5 and the smallest dots should be 6 - 9. In the case of the square arrangement shown in Fig. 5.39b, the areas where similar diameters are expected are grouped and indicated by the areas numbered 1 - 5. The largest diameter dots will belong to area 1, then the second largest will be in area 2 and the smallest diameter dot will be the last one, i.e. the 25^{th} dot.

Two sets of circular arranged pillars deposited from DCSCH are shown in Fig. 5.40a. both top-down image and 45^0 tilted images are shown in the figure. Fig. 5.40b shows a similar circular arrangement of pillars deposited from SCH, wherein all parameters were kept the same as for DCSCH. The proximity effect is clearly visible in both Fig. 5.40a and Fig. 5.40b. The dots 2 - 5 and 6 - 9 expected to have same diameters, indeed have almost the same diameters and the order from large to small is as described in Fig. 5.39a.

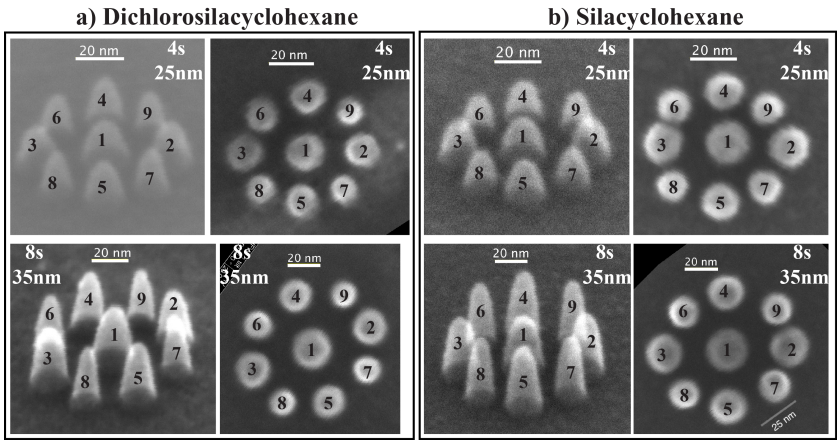

Figure 5.40. 45^0 tilted (left) and head-on view (right) of two sets of 9 closely spaced pillars deposited in a circular arrangement, (a) deposited with DCSCH and (b) deposited with SCH. The beam exposure time and the distance between nearby pillars are marked in the corner of each image, adapted with prmission from ref. [170].

The first pillar of DCSCH deposited with a beam exposure time of 4 s in the circular arrangement has a diameter of 17.9 $\pm$ 3 nm. The average diameter of pillars 2 - 5, deposited with same beam exposure time is 15 $\pm$ 1 nm and, for pillars 6 - 9, the average diameter is 12.4 $\pm$ 1 nm. Similar analysis for SCH shows a diameter of 18.8 $\pm$ 3 nm for the first deposited pillar, an average diameter of 16.0 $\pm$ 1 nm for pillars 2 - 5 and an average diameter of 13.8 $\pm$ 1 nm for pillars 6 - 9. The relative broadening due to the proximity effect can be calculated by subtracting the average diameter of pillars 6 - 9 from the diameter of first deposited pillar. The observed relative broadening for DCSCH is 5.5 $\pm$ 1 nm and that for SCH is 5.0 $\pm$ 1 nm. For the 8 s exposure time, the same analysis results in a relative broadening of 8.0 $\pm$ 1 nm for DCSCH and 7.7 $\pm$ 1 nm for SCH.

Two sets of a square arrangement of deposited pillars from DCSCH and SCHS are shown in Fig. 5.41. In the first set, seen in the top row of Fig. 5.41, the parameters used are a beam exposure time of 2 s and a distance between pillars of 15 nm. In the second set, seen in the bottom row of Fig. 5.41, the parameters used are a beam exposure time of 4 s and a distance between pillars of 20 nm. The order of depositions is same as shown in the schematic of Fig. 5.39b, the first and last deposited pillars is marked in Fig. 5.41.

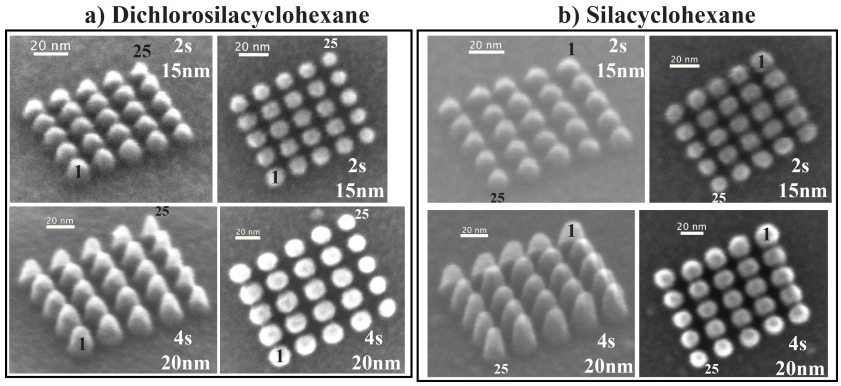

Figure 5.41. Square arrays of pillars deposited with beam exposure time and neighbouring pillar distance as indicated for (a) DCSCH and (b) SCH. The first (1) and last (25) pillars are indicated and the order of deposition is as shown in Fig. 5.39b, adapted with permission from ref. [170].

The proximity effect is clearly visible for the array of pillars deposited in Fig 5.41. For the beam exposure time of 2 s shown in Fig. 5.41a, the average diameter of DCSCH pillars deposited in area 1 is 12.1 $\pm$ 1 nm, that in area 2 is 12.4 $\pm$ 2 nm and that in area 3 is 11.7 $\pm$ 1 nm. In the second smallest area (area 4), the average diameter is 10.4 $\pm$ 1 nm, and the smallest deposited pillar has a diameter of 9.6 $\pm$ 2 nm. A similar square arrangement of deposited pillars from SCH is shown in Fig. 5.41b. For the beam exposure time of 2 s and pillar distance of 15 nm, the average diameter of SCH pillars deposited in area 1 is 12.5 $\pm$ 1 nm, in area 2 the average diameter is 13.1 $\pm$ 2 nm and similarly in area 3 and 4 the average pillar diameters are 11.9 $\pm$ 1 nm and 11.2 $\pm$ 1 nm, respectively. The diameter of the last-deposited pillar (i.e. area 5) is 10.6 $\pm$ 2 nm. The relative broadening due to the proximity effect in the array of pillar deposition can be calculated by taking the difference between the average diameter of pillars deposited in area 1 and the diameter of the last-deposited pillar. In the case of DCSCH pillars deposited with a beam exposure time of 2 s and a pillar distance of 15 nm, the calculated relative broadening is 2.5 $\pm$ 0.5 nm. Similar calculation for the DCSCH pillars deposited with a beam exposure time of 4 s and distance between pillars of 20 nm gives a relative broadening of 3.8 $\pm$ 0.5 nm. For pillars deposited from SCH, these numbers are 1.9 $\pm$ 0.5 nm and 2.2 $\pm$ 0.5 nm, respectively. It is thus clear that pillars deposited from both DCSCH and SCH show considerable broadening through the proximity effect. However, with considering the estimated errors, the difference observed for DCSCH and SCH are not significant.

As discussed in the above sections, the difference in DEA to DCSCH is only significant for electrons with energy <2 eV and in the range 6 - 9 eV. In order to have contribution from DEA to the broadening of pillars through the proximity effect, the SEs with these energies should reach the neighboring pillars. To obtain a better estimate of the number of electrons with these energies emitted from the silicon pillars, a Monte Carlo simulation was carried out. The sample for the simulation was a flat silicon substrate with a 1 nm diameter Si half sphere on the top, which resembles a tiny silicon

deposit on a silicon substrate (see Fig. 5.42a).

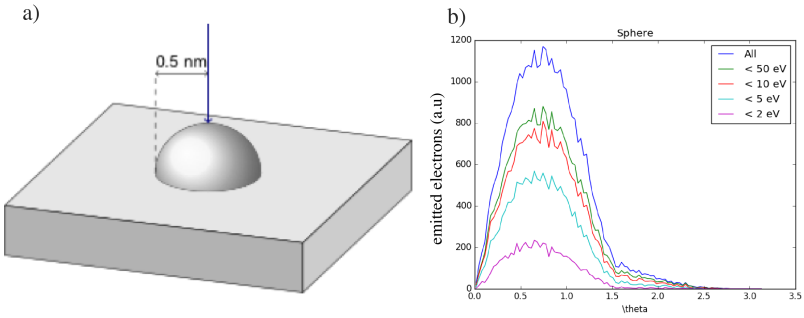

Figure 5.42. Monte Carlo simulation of the angular distribution of electrons emitted from (a) a flat Si substrate with a 1 nm diameter Si half sphere on top upon exposure with a zero-diameter 20 keV electron beam at the location of the top of the half sphere, shown as a dark blue arrow. b) Curves of emitted electrons with energy below the indicated values at a specific angle theta. Theta is the angle between the emitted electron direction and the direction of the incident beam, adapted with permission from ref. [170].

The simulated angular distribution of emitted electrons is shown in Fig. 5.42b. The top curve contains all possible emitted electrons up to 20 keV. Curves for electrons with maximum energies of less than 50 eV, less than 10 eV, less than 5 eV, and less than 2 eV can also be seen in Fig. 5.42b, indicated by color. The integrated intensity of emitted electrons with energy < 2e V and in the range 5 - 10 is about 50% of the total intensity of emitted electrons with energy < 20 keV.

Although a large number of SEs with energy relevant to DEA of DCSCH are available, the difference in relative broadening due to the proximity effect is insignificant for DCSCH and SCH. However, as previously discussed, the absolute cross-sections for DEA and DI of these precursor molecules are unknown. Furthermore, the deposits create from DCSCH and SCH are electrical insulators, therefore the SEs and BSEs emitted from the growing deposit may induce a negative charge in the neighboring pillars. The trajectory of low energy electrons reaching the neighboring pillars will be significantly affected by such induced charges. Detailed discussions on the EBID of DCSCH and SCH, as well as the potential roles of DEA and DI in the deposition process of these precursor molecules, can be found in article 5.

5.3.1.3 Conclusions

The first EBID experiment on the deposition of silicon from DCSCH and SCH is presented and growth dynamics of pillars deposited from these two precursors using FEBID are characterized by growing a series of pillars with varying beam exposure time. The growth dynamics of pillars deposited from DCSCH and SCH are compared in context to their different sensitivity towards DEA.

The lateral growth rate of DCSCH is noticeably higher than that of SCH. Additionally, the saturated pillar base diameter for DCSCH (~90 nm) is significantly larger than that of SCH (~70 nm). The volume growth rate of DCSCH over the entire beam expo-

sure period is twice that of SCH. These observations show the trend that sensitivity of a precursor molecule toward DEA may cause additional lateral growth and an increased volume growth rate. However, due to the lack of sufficient data for the absolute DEA, DI and ND cross-sections of these precursor molecules and the potential effect by the different physical and chemical properties of the deposit, a conclusive statement is not possible.

Compositional analysis using EDX of the deposited pillars shows a Si/C ratio close to the stoichiometric Si/C ratio for pillars deposited from both DCSCH and SCH. However, the Si/O ratio observed for pillars deposited from DCSCH is twice that of pillars deposited from SCH. This we attribute to the efficient hydrolysis of the Si-Cl bonds through residual water present in the chamber.

The proximity effects for pillars deposited from DCSCH and SCH are clearly visible and the effect is consistently larger for those deposited from DCSCH: however, when considering the estimated errors, it is difficult to assign the lesser proximity effect of pillars deposited from SCH to its inert behavior to DEA. Although 50% of secondary electrons below 20 keV are available to induce DEA in DCSCH, DI is clearly important for both DCSCH and SCH and thus the absence or presence of DEA in FEBID of these molecules does not necessarily have a clear effect.

5.3.2 Gas phase study and FEBID of trisilacyclohexane

5.3.2.1 Introduction and motivation for the study

As discussed in 5.3.1.1, Si, SiC and SiO_2 based nanostructures are used for nano-optics and photolithography mask repair applications. Different silicon-based precursor molecules used in FEBID thus far are SiH_4 [176], Si_2H_6 [177], tetraethoxysilane (TEOS, $Si(OCH_2CH_3)_4$) [178], tetramethoxysilane (TMOS, $Si(OCH_3)_4$) [178], tetramethylsilane (TMS, $Si(CH_3)_4$ [178], triphenylsilanol [179].

Although there are reports of silicate deposition in 1960 [180], the first detailed study of silica deposition from triphenylsilanol due to electron induced-dissociation was carried out by Woodman *et al* in 1965 [179]. Silica deposition from electron-induced dissociation of surface-adsorbed tetramethylsilane and deposit characterization was carried out by Faber *et al* in 1969 [181]. An electron beam assisted SiO_2 deposition from silane (SiH_4) was reported in 1983 [182]. The first FEBID of pure SiO_2 in an ultrahigh-vacuum SEM was reported by Nakano *et al* in 1996 [183]. By monitoring the current flowing through the sample, Bret *et al* [184] performed a controlled FEBID of SiO_2 from TEOS. Using room temperature FEBID, Perentes *et al* [178] fabricated contamination-free transparent silicon-based nanostructures from precursor molecules such as TEOS, TMOS and TMS in the presence of a controlled O_2 flow. From this study, they also found that TMS has many advantages over TEOS and TMOS in fabricating denser silicon material. The complications of introducing a silicon precursor and O_2 into a FEBID system through different gas injection needles to fabricate pure SiO_2 was addressed in a recent study of Riazanova *et al* [185] by intermixing a silicon precursor (TEOS) and O_2 in a single gas injection system. Since SiO_2 is an insulating material, deposition of SiO_2 in FEBID may create some issues with regards to accumulation of charges; De Boer *et al* [186] studied the charging effect of depositing SiO_2 material

in FEBID using the precursor molecule 2,4,6,8,10-pentamethyl-cyclopenta-siloxane (PMCPS).

Most of the precursor molecules mentioned above behaved quite well in FEBID and were capable of creating contamination-free silicon-based nanostructures; however, there is still a need for new silicon-based FEBID precursor molecules, which may give qualitatively and quantitatively good deposition, which may ultimately be applicable for nanophotonics, nanoplasmonics and many other applications.

The gas phase study and electron beam-induced deposition of the silicon-based precursor molecule 1,3,5-trisilacyclohexane (TSCH) will be presented in this section. In order to study the electron induced growth dynamics of TSCH and to understand the growth behaviour with relatively low and high energy PE beam we choose three electron beam energies 1, 5 and 20 keV. TSCH is an intermediate compound between cyclohexane and cyclohexasilane with a Si/C stoichiometric ratio of 1:1 (the molecular structure of TSCH is shown in Fig. 5.43). Compared to other commonly used organic silicon precursor molecules like SiH_4, Si_2H_6, TEOS, TMOS, TMS, and triphenylsilanol, the precursor TSCH has a higher Si:C ratio. This might be an advantage of using TSCH as a silicon-based precursor in FEBID. TSCH is a liquid at room temperature and is sufficiently volatile under these conditions to use as a FEBID precursor. There have been two patents filed for fabricating silicon carbide from TSCH using plasma-enhanced CVD and plasma-enhanced ALD [187, 188].

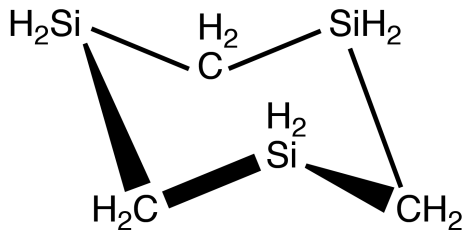

Figure 5.43. Molecular structure of 1,3,5-trisilacyclohexane.

5.3.2.2 Results and discussions

Gas phase study of TSCH

Both negative and positive ion mass scans of TSCH were performed using a quadrupole mass spectrometer. As discussed in the chapter 3, the most efficient mechanism to form a negative ion fragment is DEA, the other relatively inefficient mechanism is DD. No fragments were detected in the negative ion mass scan of TSCH, meaning that TSCH is inert to DEA and DD. Although neutral dissociation of TSCH cannot be measured in this study, based on the inert behavior of TSCH towards DEA we expect that TSCH is inert to secondary electrons in the energy range of 0 to about 6 eV. This may be an advantage of using TSCH in FEBID, as low energy SEs have been found to cause lateral broadening of deposited structures and co-deposition of impurities (see chapter 2).

The positive ion mass spectrum of TSCH recorded at an incident electron energy of 70 eV is shown in Fig. 5.44. The most intense fragment observed in the positive ion mass spectrum of TSCH is Si^+ (28), the peak at m/z of 28 shown in the Fig. 5.44

however has contribution (30%) from N_2 (28). The fragments $[SiCH_n]^+$ (m/z = 40 - 44) are also observed with significant contribution. Other fragments identified along with molecular ion $[Si_3C_3H_{12}]^+$ (m/z of 132) are $[SiC_2H_n]^+/[Si_2H_n]^+$ (m/z = 55 - 60), $[Si_2CH_n]^+$ (m/z = 69 - 74), $[Si_2C_2H_n]^+$ (m/z = 83 - 88) and $[Si_2C_3H_n]^+$ (m/z = 99 - 103). By looking into positive ion mass spectra of TSCH, it is most likely that the deposit created from TSCH in FEBID is most likely silicon carbide.

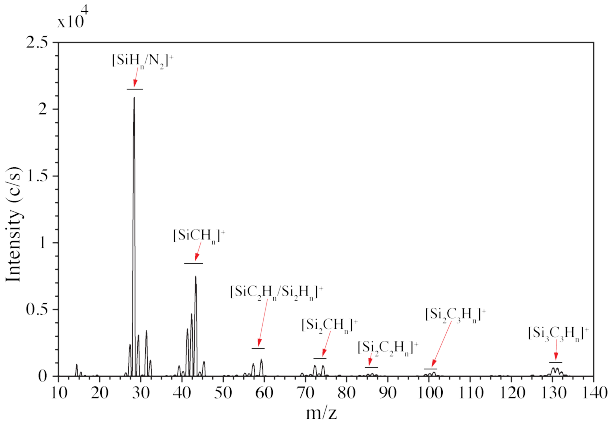

Figure 5.44. Positive ion mass spectrum of TSCH recorded with electron impact energy of 70 eV.

Nanopillar formation from TSCH

Pillars deposited from TSCH using focused electron beams of 1, 5 and 20 keV in FEBID are shown in Fig. 5.45. Each pillar shown in Fig. 5.45 was deposited with a total beam exposure time of 16 s and the pillar deposition was achieved using spot exposure mode. I have not been able to analyse the composition of the deposits, however I assume that the deposit will most likely silicon carbide. The pillars deposited in FEBID are generally characterized by their base diameter, height and volume of deposited material. The estimated values for these parameters are shown in Fig. 5.45 (how the values are estimated is described in section 4.4). As we can see from Fig. 5.45, the diameters of pillars deposited with 1 keV (~53.1 nm) is larger than those deposited with 5 keV (~46.6 nm) and 20 keV (~40.0 nm). The diameter of TSCH pillars deposited with varying beam exposure times for 1, 5 and 20 keV are shown in Fig. 5.46. From the SEM images, it was difficult to measure the dimensions of pillars deposited with beam exposure time of < 300 ms, therefore these are not included in Fig. 5.46. Series of pillar depositions are achieved by incrementally increasing the beam exposure time from 300 ms to 300 s.

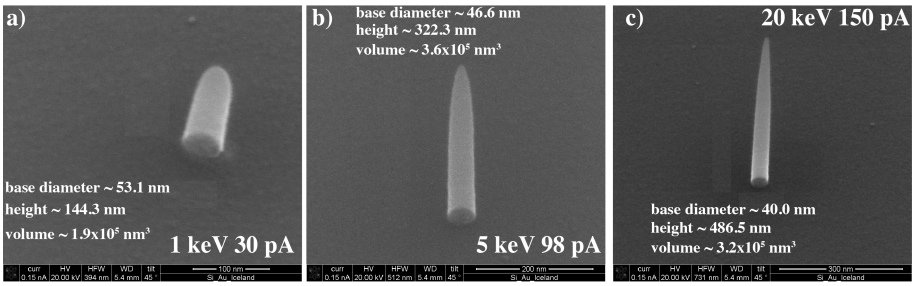

Figure 5.45. Nanopillars fabricated from TSCH precursor using focused electron beams of (a) 1 keV, 30 pA, (b) 5 keV, 98 pA and (c) 20 keV, 150 pA. All pillars were deposited with beam exposure time of 16 s.

As discussed in section 5.3.1.2, typical pillar growth in FEBID consists of three stages: nucleation, fast growth and saturation. The manner in which pillars grow in each of these stages is discussed in section 5.3.1.2. The nucleation stage of TSCH pillar growth can be seen as the starting point of the curve in Fig. 5.46a, i.e. ~300 ms or below. The fast growth stage of TSCH pillars occurs between 300 ms and 24 s and is quite visible in Fig. 5.46a for all 3 beam energies (i.e. 1, 5 and 20 keV). Although there should not be further lateral growth after the fast growth regime has finished, we could clearly see some increase in lateral growth after this point for TSCH as shown in Fig. 5.46a. This lateral growth most likely originates from deposition produced by forward scattered electrons (FSEs). Although the three regimes are the same for TSCH pillars deposited with 1, 5 and 20 keV, the pillar base diameters are different. The difference in pillar diameter can be mainly attributed to the different penetration depth of 1, 5 and 20 keV primary electrons. Electrons with energy of 20 keV can penetrate deeper into a substrate compared to those with energies of 5 and 1 keV, as a result SE yield on the surface will be lesser for 20 keV, which reduces the spatial distribution of SEs for 20 keV. This means that the lateral broadening due to SEs emitted by the impact of 20 keV electrons will be comparatively smaller than by 5 or 1 keV electrons. At 24 s, where the fast growth regime ends, the pillar base diameter for 20 keV is ~43 nm, that for 5 keV is 47 nm and for 1 keV is 54 nm. From the pillar base diameter vs beam exposure time plot of TSCH (shown in Fig. 5.46a) we can estimate the lateral growth rate by dividing the pillar base diameter with corresponding beam exposure time. The lateral growth rate of TSCH pillars measured at the nucleation stage (i.e. at ~300 ms) for 1 keV is 35 nm/s, that for 5 keV is 33 nm/s and that for 20 keV is 30 nm/s respectively.

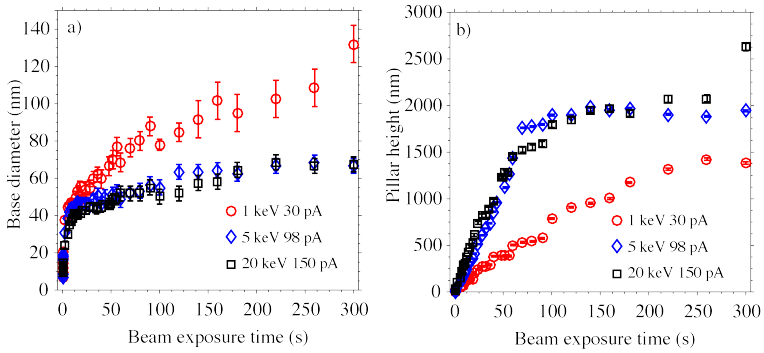

Figure 5.46. Evolution of a) base diameter and b) height with respect to electron beam exposure time for TSCH pillars fabricated with 1 keV, 30 pA; 5 keV, 98 pA and 20 keV, 150 pA electron beams. Pillar diameter and heights are measured from the SEM images of the pillars (see chapter 4).

The vertical growth of TSCH pillars is shown in Fig. 5.46b in terms of pillar height and beam exposure time. A linear relation between pillar height and beam exposure time is observed for 1 keV over the beam exposure time of 300 ms to 260 s, similar behaviour is observed for 5 and 20 keV over the beam exposure time of 300 ms to 90 s. After about 90 s, the pillar height remains almost constant for 5 and 20 keV, which is most likely due to the change in regime from the current-limited regime to the precursor-limited regime. In the precursor-limited regime, the number of precursor molecules in the area of deposition will be significantly less and thus a slower growth rate with beam exposure time will be observed. During the FEBID process, the supply of precursor molecules is replenished by surface diffusion of adsorbed precursor molecules to the area of the primary electron beam [189]. With the increase in pillar height, the number of precursor molecules diffusing to the top of the pillar is reduced, leading to conversion of the regime to the precursor-limited regime. At 100 s, the height of pillars deposited with 5 and 20 keV is $> 1.8\ \mu$m; at this height, significantly fewer precursor molecules will be available on the pillar tip. Further, at increased pillar height, the electron dose (i.e. number of primary electrons interacting/unit area on the surface) on the pillar tip will be reduced due to defocusing of the primary electron beam. This will also slow down vertical growth. In the case of the TSCH pillars deposited with 1 keV, the electron-molecule interaction regime remains current-limited regime even after 100 s because the pillar height is comparatively smaller. From the measured pillar heights, we can calculate the vertical growth rate by dividing the pillar height with corresponding beam exposure time and averaging it. the average vertical growth rate calculated over the beam exposure time of 300 ms to 300 s for 1 keV is 10.8 nm/s, that for 5 keV is 19.3 nm/s and that for 20 keV is 25.4 nm/s.

From the discussions in section 5.3.1.2 and SEM images of the pillars, it is clear that initial pillar growth is conical, and with continuing electron irradiation a cylindrical section grows under the conical region. Therefore, from the SEM images of pillars deposited with TSCH, we can calculate the deposited volume by assuming the deposited pillar as a combination of conical and cylindrical shapes (also see section 4.4). Fig.

5.47a shows the volume of TSCH pillars deposited with varying beam exposure times for 1, 5 and 20 keV electron beams. From the pillar volume vs beam exposure time plot we can estimate the volume growth rate by dividing the pillar volume with corresponding beam exposure time. The TSCH volume growth rate for 1, 5 and 20 keV are shown in Fig. 5.47b. The TSCH pillar volume growth rate with change in beam exposure time show similar profile for 5 and 20 keV, in both cases the volume growth rate increases up to about 80 s and then decreases. The decrease in pillar volume growth rate is most likely due to change in growth regime from current limited regime to precursor limited regime. As I mentioned before, in precursor limited regime the growth rate will be slower with beam exposure time. In the case of 1 keV, volume growth rate increases for the entire beam exposure time (i.e 300 ms to 300 s), which indicates that for 1 keV the pillar growth over the beam exposure time 300 ms to 300 s is in current limited regime.

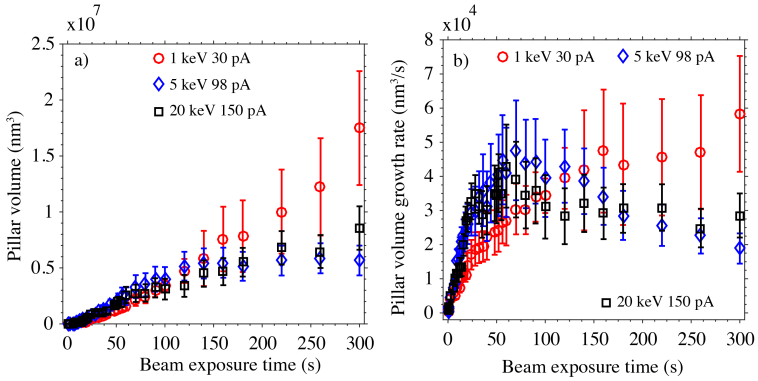

Figure 5.47. Change in (a) deposited volume and (b) volume growth rate with respect to beam exposure time for pillars fabricated from TSCH with 1 keV, 30 pA; 5 keV, 98 pA and 20 keV, 150 pA incident electron beams. The deposited volume is measured from the SEM image of the pillars (see more details in chapter 4).

It is obvious from Fig. 5.48, that the tip of the TSCH pillar deposited with 5 keV has a round bulged shape. However, it is absent for 1 and 20 keV. This bulged shape in the TSCH pillar for 5 keV starts to appear at an electron beam exposure time of ~70 s. The volume of the bulged shape then increases with increased electron beam exposure time. The evolution of the bulged structure with increased electron beam exposure is shown in Fig. 5.49. As we can see from Fig. 5.49, in the initial stage the bulged structure has an elliptical shape; however, with increasing electron beam exposure, it becomes more spherical in shape. At 70 s, the calculated volume of the bulged structure is ~2.5x10^4 nm^3, and at 300 s it has increased to 1.3x10^5 nm^3.

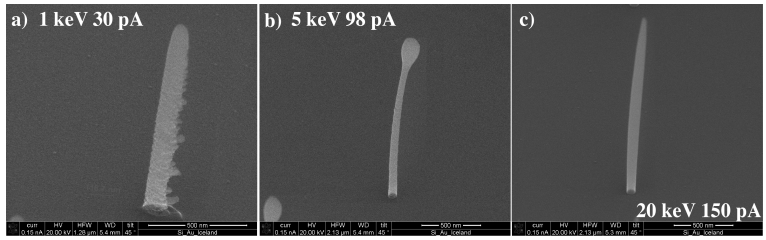

Figure 5.48. Pillars deposited from TSCH with a) 1 keV 30 pA, b) 5 keV 98 pA and c) 20 keV 150 pA, only the pillar deposited with 5 keV shows the bulged structure in the tip of pillar. All pillars are deposited with electron beam exposure time of 220 s.

The bulged shape on the TSCH pillar tip may be formed due to the effect of electron induced heating on the pillar tip. When primary electrons (PEs) interact with material, some amount of PE energy can deposit into the material and convert to thermal energy. The dissipation of thermal energy in the material depends upon the material's thermal conductivity. The thermal effect has significant influence in high aspect ratio nanopillars, because the primary electron energy is localized on the tip of pillars. Using the Monte Carlo electron-solid interaction model, Randolph *et al* [190] studied the effect of electron beam-induced heating in FEBID. In the model, they calculated the thermal energy distribution profile of bulk and SiO_2 nanostructures. In the case of pillar geometry, their model suggests that the pillar tip temperature increases sharply with pillar height; therefore, the temperature will be maximized for taller pillars. Their model also suggests that the tip temperature is slightly higher for 5 keV (~5% higher) incident electron beams compared to 20 keV incident electron beams. For a pillar with a height of 2 μm, 5 keV electrons can create electron-induced heating with temperatures in the range of 150 to 200 ^{0}C [190]. At these temperatures, TSCH may thermally decompose and contribute some deposition in addition to electron-induced deposition. This may lead to increased deposition on the pillar tip for taller pillars. It is most likely the reason for the appearance of the bulged structure on the taller TSCH pillars deposited with a 5 keV incident electron beam.

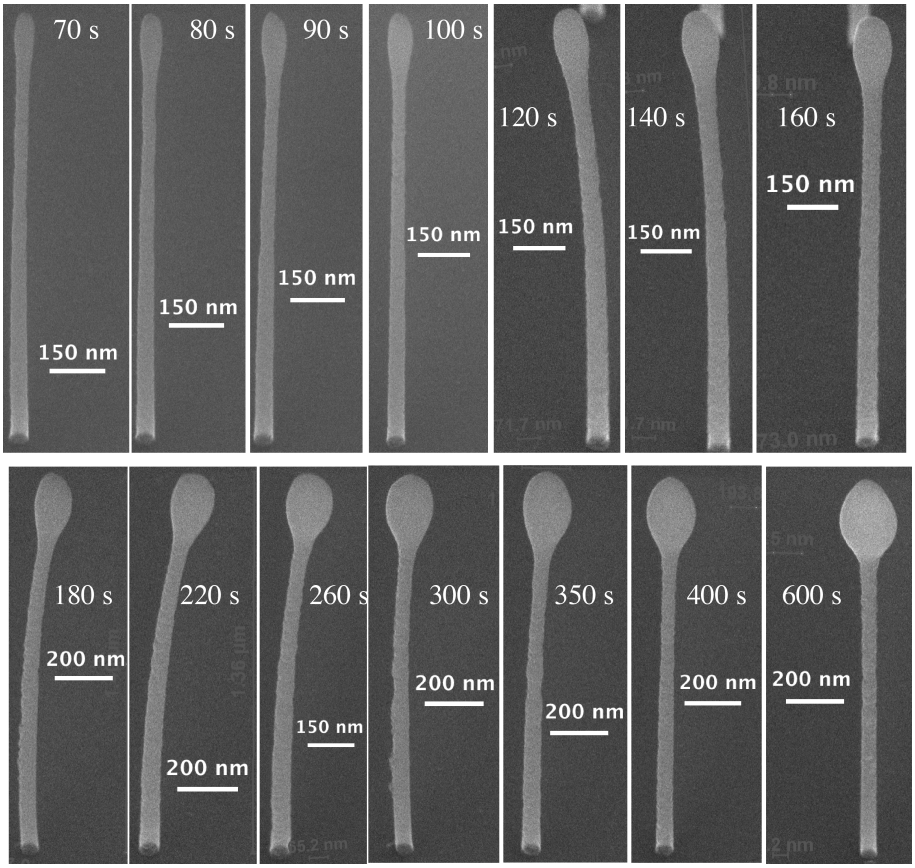

Figure 5.49. Pillars deposited from TSCH with a 5 keV, 98 pA primary electron beam. The beam exposure time used for depositing each pillar is shown on the top side of each image.

Since TSCH is inert to low energy (0 - 6 eV) SEs, we compared the effect of SEs during the deposition of very close pillars for 1, 5 and 20 keV incident electron beams. As previously discussed, when a pillar is deposited in close proximity to a previously deposited pillar, the SEs produced during deposition of the new pillar will induce additional deposition on the previously deposited pillar. This effect is called proximity effect (discussed in section 5.3.1.2 for DCSCH and SCH). Fig. 5.50 compares the proximity effect of depositing very close TSCH pillars (distance between neighbouring pillars are marked in the figure) for 1, 5 and 20 keV incident electron beams. From the measured base diameter of the first and last deposited pillar, we can calculate the relative broadening. The calculated relative broadening for deposition with a 1 keV primary electron beam is ~20 nm, that for 5 keV is ~10 nm and that for 20 keV is ~2 nm. The relative broadening for 20 keV in TSCH is similar to that of SCH (relative broadening is ~4 nm)

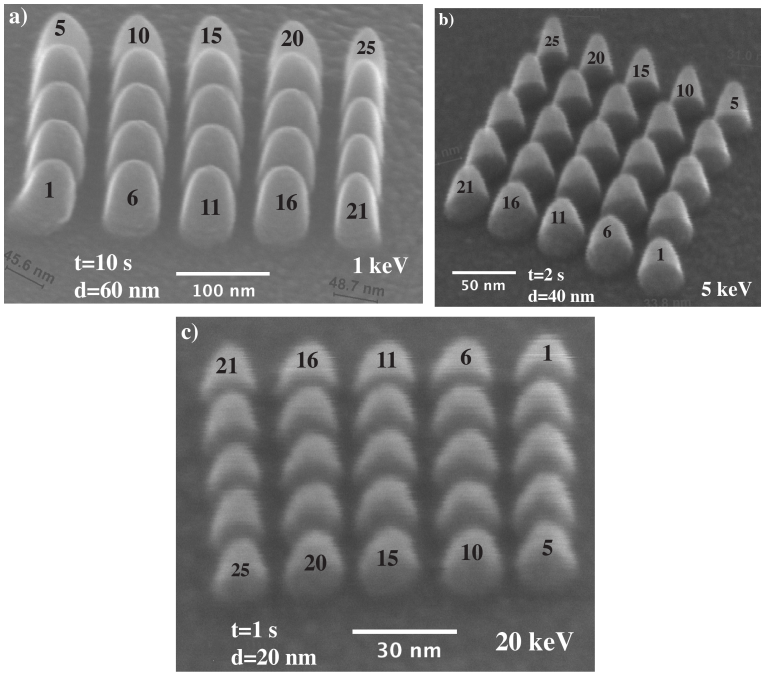

Figure 5.50. Array of closely spaced pillars deposited from TSCH with (a) 1 keV, 30 pA; (b) 5 keV, 98 pA and (c) 20 keV, 150 pA incident electron beams. The beam exposure time (t), distance between adjacent pillars (d) and order of depositions (1 - 25) are marked in the image.

5.3.2.3 Conclusions

A study of the gas phase electron-induced decomposition and electron beam-induced deposition of the silicon-based precursor molecule TSCH has been discussed here. In the gas phase study of TSCH, no negative ion fragments were detected from the mass spectrum of TSCH. In the positive ion mass spectrum of TSCH, relatively intense fragments Si^+ (28) and $[SiCH_n]^+$ (m/z = 40 - 44) are observed along with molecular ion $[Si_3C_3H_{12}]^+$ (m/z of 132).

The growth dynamics of TSCH in FEBID were characterized by measuring the base diameter, height and deposited volume of a series of pillars deposited with varying incident electron beam energies and exposure times. Three different primary electron beam energies: 1, 5 and 20 keV, were used to deposit pillars from TSCH, the pillars were subsequently characterized. The observed TSCH pillar diameter (for entire beam exposure time) was higher for 1 keV compared to 5 and 20 keV, this we attributed to different penetration depth and spatial distribution of emitted SEs of 1, 5 and 20 keV primary electron beams. The fast growth regime of TSCH ends at 24 s and the TSCH pillar base diameter estimated at that point is ~43 nm for the 20 keV, ~47 nm for 5 keV and ~54 nm for 1 keV. The initial lateral growth (at 300 ms) of TSCH pillars is higher for 1 keV primary electron beam (35 nm/s) compared to 20 keV (30 nm/s) and 5 keV (33 nm/s). The vertical growth of TSCH pillars shows linear behavior with respect

to deposition time for the 1 keV primary electron beam; however, for 5 and 20 keV, the linear behavior is observed only for beam exposure times of < 90 s. Above 90 s, the pillar height remains constant, which we attributed to the change in growth regime from current-limited to precursor-limited. The deposited volume of TSCH pillars was estimated from the SEM image of pillars and subsequently the volume growth rate was estimated. Compared to DCSCH and SCH, TSCH have significantly higher vertical growth rate.

The TSCH pillars deposited with a 5 keV incident electron beam shows an interesting feature at higher electron beam exposure time (> 70 s). The tips of the TSCH pillars deposited with electron beam exposure time of > 70 s have a bulged shape, however this bulged shape is absent for pillars deposited using 1 and 20 keV primary electron beams. We attributed this to the effect of electron beam-induced heating.

The proximity effect when growing close TSCH pillars was also investigated for 1, 5 and 20 keV primary electron beams. In the proximity effect, the relative broadening is higher for the 1 keV primary electron beam (~20 nm) compared to 20 keV (~2 nm) and 5 keV (~2 nm).

6 Summary and outlook

This thesis mainly discussed low energy electron interactions with the bimetallic FEBID precursor molecules $HFeCo_3(CO)_{12}$ and $H_2FeRu_3(CO)_{13}$ and the silicon-based FEBID precursor molecules DCSCH, SCH and TSCH. For the bimetallic FEBID precursor molecules, both gas phase and UHV surface study results are presented. In the case of silicon-containing FEBID precursor molecules, the gas phase study of TSCH are discussed and the growth dynamics of DCSCH, SCH and TSCH in FEBID are also discussed.

In FEBID, $HFeCo_3(CO)_{12}$ shows a metal content of > 80% and the Fe:Co ratio is 1:3, which is the stoichiometric ratio of the precursor molecule. Conversely, $H_2FeRu_3(CO)_{13}$ shows a metal content of < 30% and the Fe:Ru ratio is 1:3.5, which means there is some Fe loss in the deposit. The gas phase and surface studies of $HFeCo_3(CO)_{12}$ and $H_2FeRu_3(CO)_{13}$ were mainly focused to understand why these two structurally similar precursors produce such different metal contents and stoichiometry under FEBID conditions.

In the gas phase study of $HFeCo_3(CO)_{12}$, electron attachment to $HFeCo_3(CO)_{12}$ shows three main fragmentation pathways: sequential loss of COs (formation of $[M - n(CO)]^-$ ions), apex loss (formation of $[Fe(CO)_n]^-$ ions) and breaking of the Co_3 base plane (formation of $[M - Co(CO)_n]^-$ ions). In addition to these fragmentation pathways, formation of the molecular anion by electron attachment to $HFeCo_3(CO)_{12}$ is observed at 0 eV. Electron impact ionization of $HFeCo_3(CO)_{12}$ leads to the formation of $[Fe(CO)_n]^+$ and $[M - n(CO)]^+$, along with the parent molecular cation $[HFeCo_3(CO)_{12}]^+$. Although the fragments observed in DI of $HFeCo_3(CO)_{12}$ are similar to the fragments observed in DEA, the relative intensities are significantly different.

In the initial electron-induced reactions of surface-adsorbed $HFeCo_3(CO)_{12}$ under UHV conditions, extensive desorption of CO ligands (75% of the initial value) is observed, which results in the formation of a partially decarbonylated intermediate with an average stoichiometry of $HFeCo_3(CO)_3$. With further electron irradiation of the partially decarbonylated intermediate, CO ligands present in the intermediate decompose into adsorbed carbon (C_{ads}) and oxide. The effect of thermally triggered reactions to partially decarbonylated intermediate is studied by annealing the electron-irradiated $HFeCo_3(CO)_{12}$ film to room temperature, showing complete CO ligand desorption from the partially decarbonylated intermediate and leaving behind Co and Fe.

Electron attachment to $H_2FeRu_3(CO)_{13}$ results to the fragmentations with mainly apex loss and $Ru(CO)_n$ loss. A minor fragmentation channel leading to the formation of $[Ru_2(CO)_n]^-$ is also observed in the DEA of $H_2FeRu_3(CO)_{13}$. Electron impact ionization of $H_2FeRu_3(CO)_{13}$ leads to the formation of $[Fe(CO)_n]^+$ fragments in the

m/z range < 300 amu and two regressions ($[M - n(CO)]^+/[M - Fe - (n\text{-}2)(CO)]^+$ and $[M - Ru - n(CO)]^+/[M - Ru - Fe - (n\text{-}2)(CO)]^+$ in the m/z range > 300 amu.

The electron-induced reactions of surface-adsorbed $H_2FeRu_3(CO)_{13}$ are initiated by extensive CO desorption (70% of CO ligands desorb initially), which produces a partially decarbonylated intermediate with average stoichiometry of $H_2FeRu_3(CO)_{4.5}$. Further electron irradiation or annealing does not bring significant changes to the partially decarbonylated intermediate, but a slight reduction in the O(1s) intensity is observed and thus the average stoichiometry of the partially decarbonylated intermediate becomes $FeRu_3(CO)_{3.5}$.

From the summarized gas phase and surface study observations of $HFeCo_3(CO)_{12}$ and $H_2FeRu_3(CO)_{13}$, we can make a comparison between these two bimetallic precursor molecules. The comparison clearly shows that the initial electron-induced decomposition of these precursor molecules proceeds through DI and the extension of initial CO desorption is similar for $HFeCo_3(CO)_{12}$ and $H_2FeRu_3(CO)_{13}$. However, increased electron irradiation results in decomposition of CO ligands in the partially decarbonylated intermediate of $HFeCo_3(CO)_{12}$ but not in $H_2FeRu_3(CO)_{13}$. Also, thermally-driven reactions lead to the complete removal of CO ligands from the partially decarbonylated intermediate of $HFeCo_3(CO)_{12}$, but only a negligible amount of CO ligands are removed from the partially decarbonylated intermediate of $H_2FeRu_3(CO)_{13}$. This observation might explain why $HFeCo_3(CO)_{12}$ and $H_2FeRu_3(CO)_{13}$ behave so differently in FEBID. The combined gas phase and surface study of $HFeCo_3(CO)_{12}$ and $H_2FeRu_3(CO)_{13}$ presented in this thesis clearly show the potential capability of thos approach to understand the electron induced reaction of precursor molecules in FEBID. Similarly, different quantum chemical calculations applied in this thesis to find the energetics of negative ion formation and to explain the interesting negative ion yield feature appeared well above the IE of $HFeCo_3(CO)_{12}$ and $H_2FeRu_3(CO)_{13}$ clearly shows the necessity of choosing and applying the right quantum chemical calculations in the DEA to heteronuclear transition metal complexes.

The growth dynamics of the silicon-containing FEBID precursor molecules DCSCH, SCH and TSCH, which have different DEA and DI characteristics were studied by growing pillars with varying beam exposure time. Although the lateral growth, volume growth rate and proximity effect of SCH was lower compared to DCSCH and it may be originated from the inert behaviour of SCH to DEA, it is difficult to make a conclusive statement due to insufficient data. But when comparing the growth dynamics of DCSCH and SCH presented in this thesis, one thing is clear that designing precursor molecules with inert behaviour towards DEA alone doesn't bring significant changes.

From the growth dynamic study of TSCH presented in this thesis, one thing is obvious that TSCH have higher vertical growth rate compared to previously reported silicon centered FEBID precursor molecules. This will be very promising to use TSCH as a potential FEBID precursor.

Although the comparison of gas phase and surface studies between $HFeCo_3(CO)_{12}$ and $H_2FeRu_3(CO)_{13}$ gives a deeper insight into its different performance in FEBID, a more fundamental study is required to understand why the partially decarbonylated intermediate of $HFeCo_3(CO)_{12}$ and $H_2FeRu_3(CO)_{13}$ show different thermally triggered reactions. We cannot separate the effect of further electron irradiation and temperature during an actual FEBID experiment, because they act simultaneously during the FEBID

process, however the effect of temperature and further electron irradiation were studied separately in the UHV surface science experiments. Therefore, a new approach is needed to introduce to address this issue. Further, the independent roles of DEA and DI in the FEBID is still not clear. New experiments must be designed in order to accomplish this goal.

Bibliography

[1] Richard P Feynman. There's plenty of room at the bottom. *Engineering and science*, 23(5):22–36, 1960.

[2] Norio Taniguchi. On the basic concept of nanotechnology. In *International Conference on Production Engineering*, pages 18–23, 1974.

[3] 1990.

[4] Christopher R Moon, Laila S Mattos, Brian K Foster, Gabriel Zeltzer, and Hari C Manoharan. Quantum holographic encoding in a two-dimensional electron gas. *Nature Nanotechnology*, 4(3):167–172, 2009.

[5] Bharat Bhushan. *Springer handbook of nanotechnology*. Springer Science & Business Media, 2010.

[6] Kellar Autumn, Metin Sitti, Yiching A Liang, Anne M Peattie, Wendy R Hansen, Simon Sponberg, Thomas W Kenny, Ronald Fearing, Jacob N Israelachvili, and Robert J Full. Evidence for van der waals adhesion in gecko setae. *Proceedings of the National Academy of Sciences*, 99(19):12252–12256, 2002.

[7] Kellar Autumn, Yiching A Liang, S Tonia Hsieh, and Wolfgang Zesch. Adhesive force of a single gecko foot-hair. *Nature*, 405(6787):681, 2000.

[8] Ampere A Tseng, Kuan Chen, Chii D Chen, and Kung J Ma. Electron beam lithography in nanoscale fabrication: recent development. *IEEE Transactions on Electronics Packaging Manufacturing*, 26(2):141–149, 2003.

[9] F Watt, AA Bettiol, JA Van Kan, EJ Teo, and MBH Breese. Ion beam lithography and nanofabrication: a review. *International Journal of Nanoscience*, 4(03):269–286, 2005.

[10] Banqiu Wu and Ajay Kumar. Extreme ultraviolet lithography: a review. *Journal of Vacuum Science & Technology B: Microelectronics and Nanometer Structures Processing, Measurement, and Phenomena*, 25(6):1743–1761, 2007.

[11] Massimo Tormen, Gianluca Grenci, Benedetta Marmiroli, and Filippo Romanato. X-ray lithography. *Nano-Lithography*, pages 1–86, 2013.

[12] Jerome P Silverman. Challenges and progress in x-ray lithography. *Journal of Vacuum Science & Technology B: Microelectronics and Nanometer Structures Processing, Measurement, and Phenomena*, 16(6):3137–3141, 1998.

[13] Vivek Bakshi. *EUV lithography*, volume 178. Spie Press, 2009.

[14] Gilbert J Chin. A dry year. *science*, 301(5638):1291–1291, 2003.

[15] Jeroen A van Kan and Andrew A Bettiol. *Proton beam writing: a new 3D nanolithographic technique*, pages 297–310. Springer, 2009.

[16] Burn J Lin. Optical lithography: present and future challenges. *Comptes Rendus Physique*, 7(8):858–874, 2006.

[17] Yifang Chen. Nanofabrication by electron beam lithography and its applications: A review. *Microelectronic Engineering*, 135:57–72, 2015.

[18] Ivo Utke, Patrik Hoffmann, and John Melngailis. Gas-assisted focused electron beam and ion beam processing and fabrication. *Journal of Vacuum Science & Technology B*, 26(4):1197–1276, 2008.

[19] WF Van Dorp and CW Hagen. A critical literature review of focused electron beam induced deposition. *Journal of Applied Physics*, 104(8):081301, 2008.

[20] N Silvis-Cividjian, CW Hagen, LHA Leunissen, and P Kruit. The role of secondary electrons in electron-beam-induced-deposition spatial resolution. *Microelectronic Engineering*, 61:693–699, 2002.

[21] N Silvis-Cividjian, CW Hagen, and P Kruit. Spatial resolution limits in electron-beam-induced deposition. *Journal of Applied Physics*, 98(8):084905, 2005.

[22] Zhi-Quan Liu, Kazutaka Mitsuishi, and Kazuo Furuya. A dynamic monte carlo study of the in situ growth of a substance deposited using electron-beam-induced deposition. *Nanotechnology*, 17(15):3832, 2006.

[23] ZQ Liu, K Mitsuishi, and K Furuya. Nanofabrication of tungsten supertip by electron-beam-induced deposition. *Physica E: Low-dimensional Systems and Nanostructures*, 29(3):702–706, 2005.

[24] ZQ Liu, K Mitsuishi, and K Furuya. The growth behavior of self-standing tungsten tips fabricated by electron-beam-induced deposition using 200 keV electrons. *Journal of Applied Physics*, 96(7):3983–3986, 2004.

[25] Sarah Engmann, Michal Stano, Štefan Matejčík, and Oddur Ingólfsson. The role of dissociative electron attachment in focused electron beam induced processing: a case study on cobalt tricarbonyl nitrosyl. *Angewandte Chemie International Edition*, 50(40):9475–9477, 2011.

[26] Sarah Engmann, Michal Stano, Štefan Matejčík, and Oddur Ingólfsson. Gas phase low energy electron induced decomposition of the focused electron beam induced deposition (febid) precursor trimethyl (methylcyclopentadienyl) platinum (iv)($MeCpPtMe_3$). *Physical Chemistry Chemical Physics*, 14(42):14611–14618, 2012.

[27] K Wnorowski, M Stano, C Matias, S Denifl, W Barszczewska, and Š Matejčík. Low-energy electron interactions with tungsten hexacarbonyl–$W(CO)_6$. *Rapid Communications in Mass Spectrometry*, 26(17):2093–2098, 2012.

[28] Sarah Engmann, Benedikt Ómarsson, Michal Lacko, Michal Stano, Štefan Matejčík, and Oddur Ingólfsson. Dissociative electron attachment to hexafluoroacetylacetone and its bidentate metal complexes M(hfac) 2; M= Cu, Pd. *The Journal of Chemical Physics*, 138(23):234309, 2013.

[29] Sarah Engmann, Michal Stano, Peter Papp, Michael J Brunger, Štefan Matejčík, and Oddur Ingólfsson. Absolute cross sections for dissociative electron attachment and dissociative ionization of cobalt tricarbonyl nitrosyl in the energy range from 0 ev to 140 ev. *The Journal of Chemical Physics*, 138(4):044305, 2013.

[30] Samantha G Rosenberg, Michael Barclay, and D Howard Fairbrother. Electron induced reactions of surface adsorbed tungsten hexacarbonyl ($W(CO)_6$). *Physical Chemistry Chemical Physics*, 15(11):4002–4015, 2013.

[31] Samantha G Rosenberg, Michael Barclay, and D Howard Fairbrother. Electron beam induced reactions of adsorbed cobalt tricarbonyl nitrosyl ($Co(CO)_3NO$) molecules. *The Journal of Physical Chemistry C*, 117(31):16053–16064, 2013.

[32] Rachel M Thorman, T P Ragesh Kumar, D Howard Fairbrother, and Oddur Ingólfsson. The role of low-energy electrons in focused electron beam induced deposition: four case studies of representative precursors. *Beilstein journal of nanotechnology*, 6:1904, 2015.

[33] Oddur Ingólfsson, Fritz Weik, and Eugen Illenberger. The reactivity of slow electrons with molecules at different degrees of aggregation: gas phase, clusters and condensed phase. *International Journal of Mass Spectrometry and Ion Processes*, 155(1-2):1–68, 1996.

[34] Ilko Bald, Judith Langer, Petra Tegeder, and Oddur Ingólfsson. From isolated molecules through clusters and condensates to the building blocks of life. *International Journal of Mass Spectrometry*, 277(1):4–25, 2008.

[35] Christopher R Arumainayagam, Hsiao-Lu Lee, Rachel B Nelson, David R Haines, and Richard P Gunawardane. Low-energy electron-induced reactions in condensed matter. *Surface Science Reports*, 65(1):1–44, 2010.

[36] Esther Böhler, Jonas Warneke, and Petra Swiderek. Control of chemical reactions and synthesis by low-energy electrons. *Chemical Society Reviews*, 42(24):9219–9231, 2013.

[37] O Yavas, C Ochiai, M Takai, A Hosono, and S Okuda. Maskless fabrication of field-emitter array by focused ion and electron beam. *Applied Physics Letters*, 76(22):3319–3321, 2000.

[38] O Yavas, C Ochiai, M Takai, YK Park, C Lehrer, S Lipp, L Frey, H Ryssel, A Hosono, and S Okuda. Field emitter array fabricated using focused ion and

electron beam induced reaction. *Journal of Vacuum Science & Technology B: Microelectronics and Nanometer Structures Processing, Measurement, and Phenomena*, 18(2):976–979, 2000.

[39] A Botman, M Hesselberth, and JJL Mulders. Improving the conductivity of platinum-containing nano-structures created by electron-beam-induced deposition. *Microelectronic Engineering*, 85(5):1139–1142, 2008.

[40] Joshua D Wnuk, Justin M Gorham, Samantha G Rosenberg, Willem F van Dorp, Theodore E Madey, Cornelis W Hagen, and D Howard Fairbrother. Electron induced surface reactions of the organometallic precursor trimethyl (methylcyclopentadienyl) platinum (iv). *The Journal of Physical Chemistry C*, 113(6):2487–2496, 2009.

[41] HWP Koops, A Kaya, and M Weber. Fabrication and characterization of platinum nanocrystalline material grown by electron-beam induced deposition. *Journal of Vacuum Science & Technology B: Microelectronics and Nanometer Structures Processing, Measurement, and Phenomena*, 13(6):2400–2403, 1995.

[42] RC Che, M Takeguchi, M Shimojo, W Zhang, and K Furuya. Fabrication and electron holography characterization of FePt alloy nanorods. *Applied Physics Letters*, 87(22):223109, 2005.

[43] F Porrati, E Begun, M Winhold, Ch H Schwalb, R Sachser, AS Frangakis, and M Huth. Room temperature L10 phase transformation in binary CoPt nanostructures prepared by focused-electron-beam-induced deposition. *Nanotechnology*, 23(18):185702, 2012.

[44] F Porrati, B Kämpken, A Terfort, and M Huth. Fabrication and electrical transport properties of binary Co-Si nanostructures prepared by focused electron beam-induced deposition. *Journal of Applied Physics*, 113(5):053707, 2013.

[45] F Porrati, M Pohlit, J Müller, S Barth, F Biegger, C Gspan, H Plank, and M Huth. Direct writing of cofe alloy nanostructures by focused electron beam induced deposition from a heteronuclear precursor. *Nanotechnology*, 26(47):475701, 2015.

[46] Edwin P Boyd, Douglas R Ketchum, Haibin Deng, and Sheldon G Shore. Chemical vapor deposition of metallic thin films using homonuclear and heteronuclear metal carbonyls. *Chemistry of Materials*, 9(5):1154–1158, 1997.

[47] JM De Teresa, A Fernández-Pacheco, R Córdoba, L Serrano-Ramón, S Sangiao, and MR Ibarra. Review of magnetic nanostructures grown by focused electron beam induced deposition (febid). *Journal of Physics D: Applied Physics*, 49(24):243003, 2016.

[48] Amalio Fernández-Pacheco, Robert Streubel, Olivier Fruchart, Riccardo Hertel, Peter Fischer, and Russell P Cowburn. Three-dimensional nanomagnetism. *Nature Communications*, 8:15756, 2017.

[49] Ragesh Kumar T P P, Paul Weirich, Lukas Hrachowina, Marc Hanefeld, Ragnar Bjornsson, Helgi Rafn Hrodmarsson, Sven Barth, D. Howard Fairbrother, Michael Huth, and Oddur Ingólfsson. Electron interactions with the heteronuclear carbonyl precursor ($H_2FeRu_3(CO)_{13}$): from fundamental gas phase and surface science studies to focused electron beam induced deposition. *Manuscript submitted*, 2017.

[50] R Lariviere Stewart. Insulating films formed under electron and ion bombardment. *Physical review*, 45(7):488, 1934.

[51] John HL Watson. An effect of electron bombardment upon carbon black. *Journal of Applied Physics*, 18(2):153–161, 1947.

[52] VE Cosslett. Particle“growth”in the electron microscope. *Journal of Applied Physics*, 18(9):844–845, 1947.

[53] James Hillier. On the investigation of specimen contamination in the electron microscope. *Journal of Applied Physics*, 19(3):226–230, 1948.

[54] AE Ennos. The origin of specimen contamination in the electron microscope. *British Journal of Applied Physics*, 4(4):101, 1953.

[55] Robert W Christy. Formation of thin polymer films by electron bombardment. *Journal of applied physics*, 31(9):1680–1683, 1960.

[56] Allen G Baker and William C Morris. Deposition of metallic films by electron impact decomposition of organometallic vapors. *Review of Scientific Instruments*, 32(4):458–458, 1961.

[57] A Broers. High-resolution systems for microfabrication. 32:38–45, 01 1979.

[58] AN Broers, WW Molzen, JJ Cuomo, and ND Wittels. Electron-beam fabrication of 80-å metal structures. *Applied Physics Letters*, 29(9):596–598, 1976.

[59] Willem F Van Dorp, Bob Van Someren, Cornelis W Hagen, Pieter Kruit, and Peter A Crozier. Approaching the resolution limit of nanometer-scale electron beam-induced deposition. *Nano letters*, 5(7):1303–1307, 2005.

[60] RB Jackman and JS Foord. Electron beam stimulated chemical vapor deposition of patterned tungsten films on Si (100). *Applied physics letters*, 49(4):196–198, 1986.

[61] B Hübner, HWP Koops, H Pagnia, N Sotnik, J Urban, and M Weber. Tips for scanning tunneling microscopy produced by electron-beam-induced deposition. *Ultramicroscopy*, 42:1519–1525, 1992.

[62] Hiroji Morimoto, Takehisa Kishimoto, Mikio Takai, Shinsuke Yura, Akihiko Hosono, Soichiro Okuda, Stephan Lipp, Lothar Frey, and Heiner Ryssel. Electron-beam-induced deposition of pt for field emitter arrays. *Japanese Journal of Applied Physics*, 35(12S):6623, 1996.

[63] Hongyu Ximen and Phillip E Russell. Microfabrication of afm tips using focused ion and electron beam techniques. *Ultramicroscopy*, 42:1526–1532, 1992.

[64] KT Kohlmann, L-M Buchmann, and WH Brünger. Repair of open stencil masks for ion projection lithography by e-beam induced metal deposition. *Microelectronic Engineering*, 17(1-4):427–430, 1992.

[65] Y Ito, AL Bleloch, and LM Brown. Nanofabrication of solid-state fresnel lenses for electron optics. *Nature*, 394(6688):49, 1998.

[66] DA Smith, JD Fowlkes, and PD Rack. A nanoscale three-dimensional monte carlo simulation of electron-beam-induced deposition with gas dynamics. *Nanotechnology*, 18(26):265308, 2007.

[67] CW Hagen, N Silvis-Cividjian, and P Kruit. Resolution limit for electron beam-induced deposition on thick substrates. *Scanning*, 28(4):204–211, 2006.

[68] Joshua D Wnuk, Justin M Gorham, Samantha G Rosenberg, Willem F van Dorp, Theodore E Madey, Cornelis W Hagen, and D Howard Fairbrother. Electron beam irradiation of dimethyl-(acetylacetonate) gold (iii) adsorbed onto solid substrates. *Journal of Applied Physics*, 107(5):054301, 2010.

[69] Kees Landheer, Samantha G Rosenberg, Laurent Bernau, Petra Swiderek, Ivo Utke, Cornelis W Hagen, and D Howard Fairbrother. Low-energy electron-induced decomposition and reactions of adsorbed tetrakis (trifluorophosphine) platinum [$Pt(PF_3)_4$]. *The Journal of Physical Chemistry C*, 115(35):17452–17463, 2011.

[70] JD Wnuk, SG Rosenberg, JM Gorham, WF Van Dorp, CW Hagen, and DH Fairbrother. Electron beam deposition for nanofabrication: insights from surface science. *Surface Science*, 605(3):257–266, 2011.

[71] Samantha G Rosenberg, Michael Barclay, and D Howard Fairbrother. Electron induced surface reactions of organometallic Metal$(hfac)_2$ precursors and deposit purification. *ACS applied materials & interfaces*, 6(11):8590–8601, 2014.

[72] Julie A Spencer, Samantha G Rosenberg, Michael Barclay, Yung-Chien Wu, Lisa McElwee-White, and D Howard Fairbrother. Understanding the electron-stimulated surface reactions of organometallic complexes to enable design of precursors for electron beam-induced deposition. *Applied Physics A*, 117(4):1631–1644, 2014.

[73] Julie A Spencer, Joseph A Brannaka, Michael Barclay, Lisa McElwee-White, and D Howard Fairbrother. Electron-induced surface reactions of η3-allyl ruthenium tricarbonyl bromide [(η3-C_3h_5) $Ru(CO)_3Br$]: Contrasting the behavior of different ligands. *The Journal of Physical Chemistry C*, 119(27):15349–15359, 2015.

[74] Julie A Spencer, Yung-Chien Wu, Lisa McElwee-White, and D Howard Fairbrother. Electron induced surface reactions of cis-$Pt(CO)_2cl_2$: A route to focused

electron beam induced deposition of pure pt nanostructures. *Journal of the American Chemical Society*, 138(29):9172–9182, 2016.

[75] Florian Vollnhals, Martin Drost, Fan Tu, Esther Carrasco, Andreas Späth, Rainer H Fink, Hans-Peter Steinrück, and Hubertus Marbach. Electron-beam induced deposition and autocatalytic decomposition of $Co(CO)_3NO$. *Beilstein Journal of Nanotechnology*, 5:1175, 2014.

[76] MN Hedhili, JH Bredehöft, and P Swiderek. Electron-induced reactions of $MeCpPtMe_3$ investigated by hreels. *The Journal of Physical Chemistry C*, 113(30):13282–13286, 2009.

[77] Jonas Warneke, Willem F Van Dorp, Petra Rudolf, Michal Stano, Peter Papp, Štefan Matejčík, Tobias Borrmann, and Petra Swiderek. Acetone and the precursor ligand acetylacetone: distinctly different electron beam induced decomposition? *Physical Chemistry Chemical Physics*, 17(2):1204–1216, 2014.

[78] Kaliappan Muthukumar, Ingo Opahle, Juan Shen, Harald O Jeschke, and Roser Valentí. Interaction of $W(CO)_6$ with SiO_2 surfaces: a density functional study. *Physical Review B*, 84(20):205442, 2011.

[79] SJ Randolph, JD Fowlkes, and PD Rack. Focused, nanoscale electron-beam-induced deposition and etching. *Critical Reviews in Solid state and Materials Sciences*, 31(3):55–89, 2006.

[80] Michael Huth, Fabrizio Porrati, Christian Schwalb, Marcel Winhold, Roland Sachser, Maja Dukic, Jonathan Adams, and Georg Fantner. Focused electron beam induced deposition: A perspective. *Beilstein Journal of Nanotechnology*, 3:597, 2012.

[81] Kirsten Ingolf Schiffmann. Investigation of fabrication parameters for the electron-beam-induced deposition of contamination tips used in atomic force microscopy. *Nanotechnology*, 4(3):163, 1993.

[82] D Beaulieu, Yong Ding, ZL Wang, and WJ Lackey. Influence of process variables on electron beam chemical vapor deposition of platinum. *Journal of Vacuum Science & Technology B: Microelectronics and Nanometer Structures Processing, Measurement, and Phenomena*, 23(5):2151–2159, 2005.

[83] JJL Mulders, LM Belova, and Anastasiia Riazanova. Electron beam induced deposition at elevated temperatures: compositional changes and purity improvement. *Nanotechnology*, 22(5):055302, 2010.

[84] Klaus Edinger, Hans Becht, Johannes Bihr, Volker Boegli, Michael Budach, Thorsten Hofmann, Hans WP Koops, Peter Kuschnerus, Jens Oster, and Petra Spies. Electron-beam-based photomask repair. *Journal of Vacuum Science & Technology B: Microelectronics and Nanometer Structures Processing, Measurement, and Phenomena*, 22(6):2902–2906, 2004.

[85] Ted Liang, Eric Frendberg, Barry Lieberman, and Alan Stivers. Advanced photolithographic mask repair using electron beams. *Journal of Vacuum Science & Technology B: Microelectronics and Nanometer Structures Processing, Measurement, and Phenomena*, 23(6):3101–3105, 2005.

[86] Ted Liang and Alan R Stivers. Damage-free mask repair using electron-beam-induced chemical reactions. In *SPIE's 27th Annual International Symposium on Microlithography*, pages 375–384. International Society for Optics and Photonics.

[87] Vidyut Gopal, Velimir R Radmilovic, Chiara Daraio, Sungho Jin, Peidong Yang, and Eric A Stach. Rapid prototyping of site-specific nanocontacts by electron and ion beam assisted direct-write nanolithography. *Nano Letters*, 4(11):2059–2063, 2004.

[88] Wolfgang Fritzsche, Konrad Böhm, Eberhard Unger, and J Michael Köhler. Making electrical contact to single molecules. *Nanotechnology*, 9(3):177, 1998.

[89] Wolfgang Fritzsche, J Michael Köhler, Konrad J Böhm, Eberhard Unger, Thomas Wagner, Remo Kirsch, Michael Mertig, and Wolfgang Pompe. Wiring of metallized microtubules by electron beam-induced structuring. *Nanotechnology*, 10(3):331, 1999.

[90] Jan Richter, Michael Mertig, Wolfgang Pompe, Ingolf Mönch, and Hans K Schackert. Construction of highly conductive nanowires on a dna template. *Applied Physics Letters*, 78(4):536–538, 2001.

[91] S Graells, R Alcubilla, G Badenes, and R Quidant. Growth of plasmonic gold nanostructures by electron beam induced deposition. *Applied Physics Letters*, 91(12):121112, 2007.

[92] HWP Koops, OE Hoinkis, MEW Honsberg, R Schmidt, R Blum, G Böttger, A Kuligk, C Liguda, and M Eich. Two-dimensional photonic crystals produced by additive nanolithography with electron beam-induced deposition act as filters in the infrared. *Microelectronic Engineering*, 57:995–1001, 2001.

[93] A Weber-Bargioni, A Schwartzberg, M Schmidt, B Harteneck, DF Ogletree, PJ Schuck, and S Cabrini. Functional plasmonic antenna scanning probes fabricated by induced-deposition mask lithography. *Nanotechnology*, 21(6):065306, 2010.

[94] Jason Brown, Paul Kocher, Chandra S Ramanujan, David N Sharp, Keiichi Torimitsu, and John F Ryan. Electrically conducting, ultra-sharp, high aspect-ratio probes for AFM fabricated by electron-beam-induced deposition of platinum. *Ultramicroscopy*, 133:62–66, 2013.

[95] I-Chen Chen, Li-Han Chen, Xiang-Rong Ye, Chiara Daraio, Sungho Jin, Christine A Orme, Arjan Quist, and Ratnesh Lal. Extremely sharp carbon nanocone probes for atomic force microscopy imaging. *Applied Physics Letters*, 88(15):153102, 2006.

[96] Gemma Rius. Technology basis and perspectives on focused electron beam induced deposition and focused ion beam induced deposition. *Nuclear Instruments and Methods in Physics Research Section B: Beam Interactions with Materials and Atoms*, 341:37–43, 2014.

[97] Olivier May, Dušan Kubala, and Michael Allan. Dissociative electron attachment to $Pt(PF_3)_4$: a precursor for focused electron beam induced processing (FEBIP). *Physical Chemistry Chemical Physics*, 14(9):2979–2982, 2012.

[98] YM Lau, PC Chee, JTL Thong, and V Ng. Properties and applications of cobalt-based material produced by electron-beam-induced deposition. *Journal of Vacuum Science & Technology A: Vacuum, Surfaces, and Films*, 20(4):1295–1302, 2002.

[99] C Schößler, A Kaya, J Kretz, M Weber, and HWP Koops. Electrical and field emission properties of nanocrystalline materials fabricated by electron-beam induced deposition. *Microelectronic Engineering*, 30(1-4):471–474, 1996.

[100] L Rotkina, J-F Lin, and JP Bird. Nonlinear current-voltage characteristics of Pt nanowires and nanowire transistors fabricated by electron-beam deposition. *Applied Physics Letters*, 83(21):4426–4428, 2003.

[101] A Fernández-Pacheco, JM De Teresa, R Córdoba, and MR Ibarra. Magnetotransport properties of high-quality cobalt nanowires grown by focused-electron-beam-induced deposition. *Journal of Physics D: Applied Physics*, 42(5):055005, 2009.

[102] E Slot, MJ Wieland, G De Boer, P Kruit, GF Ten Berge, AMC Houkes, R Jager, T Van De Peut, JJM Peijster, and SWHK Steenbrink. Mapper: high throughput maskless lithography. In *Proc. SPIE*, volume 6921, page 69211P.

[103] Drouin Dominique, Couture Alexandre, Real, Gauvin Raynald, Hovington Pierre, Homy Paula, and Hendrix Demers. Casino version 3.2.0.4.

[104] L. Reimer. *Scanning Electron Microscopy*. Springer-Verlag, Berlin, 1998.

[105] Michael Allan. Electron scattering in $pt(pf_3)_4$: Elastic scattering, vibrational, and electronic excitation. *The Journal of Chemical Physics*, 134(20):204309, 2011.

[106] Matija Zlatar, Michael Allan, and Juraj Fedor. Excited states of $Pt(PF_3)_4$ and their role in focused electron beam nanofabrication. *The Journal of Physical Chemistry C*, 120(19):10667–10674, 2016.

[107] L. G. Christophoru. *Electron-Molecule Interactions and their Applications*, volume ; Vol. 1. Academic Press, Orlando, Florida, 1984.

[108] Jyoti Rajput, Lutz Lammich, and Lars H Andersen. Measured lifetime of sf 6-. *Physical Review Letters*, 100(15):153001, 2008.

[109] Ragesh Kumar T P, Benedikt Ómarsson, Stefán Þ Kristinsson, and Oddur Ingólfsson. Dissociative electron attachment to bromotrifluoromethane. *International Journal of Mass Spectrometry*, 387:78–82, 2015.

[110] T P Ragesh Kumar, B Brynjarsson, Benedikt Ómarsson, D Jones, M Hoshino, H Tanaka, P Limão-Vieira, Brunger M J, and Oddur Ingólfsson. Negative ion formation through dissociative electron attachment to the group iv tetrachlorides: Carbon tetrachloride, silicon tetrachloride and germanium tetrachloride. *International Journal of Mass Spectrometry, submitted*, 2017.

[111] George J Schulz. Resonances in electron impact on diatomic molecules. *Reviews of Modern Physics*, 45(3):423, 1973.

[112] George J Schulz. Resonances in electron impact on atoms. *Reviews of Modern Physics*, 45(3):378, 1973.

[113] A Schramm, II Fabrikant, JM Weber, E Leber, MW Ruf, and H Hotop. Vibrational resonance and threshold effects in inelastic electron collisions with methyl iodide molecules. *Journal of Physics B: Atomic, Molecular and Optical Physics*, 32(9):2153, 1999.

[114] Kenneth D Jordan and Paul D Burrow. Studies of the temporary anion states of unsaturated hydrocarbons by electron transmission spectroscopy. *Accounts of Chemical Research*, 11(9):341–348, 1978.

[115] Michael A Morrison. The physics of low-energy electron-molecule collisions: a guide for the perplexed and the uninitiated. *Australian journal of physics*, 36(3):239–286, 1983.

[116] Michael Allan. Study of triplet states and short-lived negative ions by means of electron impact spectroscopy. *Journal of Electron Spectroscopy and Related Phenomena*, 48(2):219–351, 1989.

[117] Thomas Jaffke, Eugen Illenberger, Mathias Lezius, Stefan Matejcik, David Smith, and Tilmann D Märk. Formation of C_{60}^- and C_{70}^- by free electron capture. activation energy and effect of the internal energy on lifetime. *Chemical physics letters*, 226(1-2):213–218, 1994.

[118] Oddur Ingólfsson and Eugen Illenberger. Effective intermolecular relaxation in $(C_6F_6)_n^-$ clusters: mechanism of $C_6F_6^-$ formation on low energy electron impact. *International journal of mass spectrometry and ion processes*, 149:79–86, 1995.

[119] Robert Send, Michael Kühn, and Filipp Furche. Assessing excited state methods by adiabatic excitation energies. *Journal of Chemical Theory and Computation*, 7(8):2376–2386, 2011.

[120] Yu-Ran Luo. *Comprehensive handbook of chemical bond energies*. CRC press, 2007.

[121] J Országh, M Danko, A Ribar, and Š Matejčík. Nitrogen second positive system studied by electron induced fluorescence. *Nuclear Instruments and Methods in Physics Research Section B: Beam Interactions with Materials and Atoms*, 279:76–79, 2012.

[122] Anita Ribar, Marián Danko, Juraj Országh, Filipe Ferreira da Silva, Ivo Utke, and Štefan Matejčík. Dissociative excitation study of iron pentacarbonyl molecule. *The European Physical Journal D*, 69(4):117, 2015.

[123] Sylvain Massey, Andrew D Bass, and Léon Sanche. Role of low-energy electrons (< 35 ev) in the degradation of $Fe(CO)_5$ for focused electron beam induced deposition applications: Study by electron stimulated desorption of negative and positive ions. *Journal of Physical Chemistry C*, 119:12708–12719, 2015.

[124] Leon Sanche. Low-energy electron scattering from molecules on surfaces. *Journal of Physics B: Atomic, Molecular and Optical Physics*, 23(10):1597, 1990.

[125] Hubertus Marbach. Electron beam induced surface activation: a method for the lithographic fabrication of nanostructures via catalytic processes. *Applied Physics A*, 117(3):987–995, 2014.

[126] L Sanche. Dissociative attachment in electron scattering from condensed O_2 and CO. *Physical review letters*, 53(17):1638, 1984.

[127] Donald Rapp and Donald D Briglia. Total cross sections for ionization and attachment in gases by electron impact. ii. negative-ion formation. *The Journal of Chemical Physics*, 43(5):1480–1489, 1965.

[128] A Stamatovic and GJ Schulz. Dissociative attachment in CO and formation of C^-. *The Journal of Chemical Physics*, 53(7):2663–2667, 1970.

[129] Go Jo Schulz. Cross sections and electron affinity for o^- ions from O_2, CO, and CO_2 by electron impact. *Physical review*, 128(1):178, 1962.

[130] Douglas R Hartree. The wave mechanics of an atom with a non-coulomb central field. part i. theory and methods. In *Mathematical Proceedings of the Cambridge Philosophical Society*, volume 24, pages 89–110. Cambridge University Press, 1928.

[131] Vladimir Fock. Näherungsmethode zur lösung des quantenmechanischen mehrkörperproblems. *Zeitschrift für Physik A Hadrons and Nuclei*, 61(1):126–148, 1930.

[132] John C Slater. Atomic shielding constants. *Physical Review*, 36(1):57, 1930.

[133] Pierre Hohenberg and Walter Kohn. Inhomogeneous electron gas. *Physical Review*, 136(3B):B864, 1964.

[134] Walter Kohn and Lu Jeu Sham. Self-consistent equations including exchange and correlation effects. *Physical Review*, 140(4A):A1133, 1965.

[135] Axel D Becke. Density-functional exchange-energy approximation with correct asymptotic behavior. *Physical Review A*, 38(6):3098, 1988.

[136] John P Perdew. Density-functional approximation for the correlation energy of the inhomogeneous electron gas. *Physical Review B*, 33(12):8822, 1986.

[137] John P Perdew, Kieron Burke, and Matthias Ernzerhof. Generalized gradient approximation made simple. *Physical Review Letters*, 77(18):3865, 1996.

[138] Carlo Adamo and Vincenzo Barone. Toward reliable density functional methods without adjustable parameters: The PBE0 model. *The Journal of Chemical Physics*, 110(13):6158–6170, 1999.

[139] Frank Neese. The orca program system. *Wiley Interdisciplinary Reviews: Computational Molecular Science*, 2(1):73–78, 2012.

[140] Elías H Bjarnason, Benedikt Ómarsson, Nanna Rut Jónsdóttir, Ingvar Árnason, and Oddur Ingólfsson. Dissociative electron attachment and dissociative ionization of 1, 1-dichloro-1-silacyclohexane and silacyclohexane. *International Journal of Mass Spectrometry*, 370:39–43, 2014.

[141] D Klar, M-W Ruf, and H Hotop. Attachment of electrons to molecules at submillielectronvolt resolution. *Chemical Physics Letters*, 189(4-5):448–454, 1992.

[142] B Gstir, S Denifl, G Hanel, M Rümmele, T Fiegele, P Cicman, M Stano, S Matejcik, P Scheier, K Becker, et al. Electron impact multiple ionization of neon, argon and xenon atoms close to threshold: appearance energies and wannier exponents. *Journal of Physics B: Atomic, Molecular and Optical Physics*, 35(13):2993, 2002.

[143] S Denifl, B Gstir, G Hanel, L Feketeova, S Matejcik, K Becker, A Stamatovic, P Scheier, and TD Märk. Multiple ionization of helium and krypton by electron impact close to threshold: appearance energies and wannier exponents. *Journal of Physics B: Atomic, Molecular and Optical Physics*, 35(22):4685, 2002.

[144] Ragesh Kumar T P, Sven Barth, Ragnar Bjornsson, and Oddur Ingólfsson. Structure and energetics in dissociative electron attachment to $HFeCo_3(CO)_{12}$. *The European Physical Journal D*, 70(8):163, 2016.

[145] Caroline A Schneider, Wayne S Rasband, and Kevin W Eliceiri. Nih image to imagej: 25 years of image analysis. *Nat Methods*, 9(7):671–675, 2012.

[146] Florian Weigend and Reinhart Ahlrichs. Balanced basis sets of split valence, triple zeta valence and quadruple zeta valence quality for H to Rn: Design and assessment of accuracy. *Physical Chemistry Chemical Physics*, 7(18):3297–3305, 2005.

[147] Jingjing Zheng, Xuefei Xu, and Donald G Truhlar. Minimally augmented karlsruhe basis sets. *Theoretical Chemistry Accounts*, 128(3):295–305, 2011.

[148] William Humphrey, Andrew Dalke, and Klaus Schulten. Vmd: visual molecular dynamics. *Journal of Molecular Graphics*, 14(1):33–38, 1996.

[149] P Chini, L Colli, and M Peraldo. Preparazione a proprietá dellídrocarbonile $HFeCo_3(CO)_{12}$ e di alcuni composti derivati dallánione $FeCo_3(CO)_{12}$. *Gazz. Chim. Ital*, 90:1005–1020, 1960.

[150] David K Liu, Angela L Lai, and Roger J Chin. Photochemical vapor deposition of mixed-metal thin films from organometallic precursors containing heteronuclear metal-metal bonds. *Materials Letters*, 10(7-8):318–322, 1991.

[151] David B Lambrick, N Mason, Steve R Hoon, M Kilner, and JN Chapman. The preparation of co/fe alloy fine particles from $HFeCo_3(CO)_{12}$. *IEEE Transactions on Magnetics*, 24(2):1644–1646, 1988.

[152] F Gazeau, C Baravian, J-C Bacri, R Perzynski, and M I Shliomis. Energy conversion in ferrofluids: Magnetic nanoparticles as motors or generators. *Physical Review E*, 56(1):614, 1997.

[153] Andreas S Lübbe, Christoph Alexiou, and Christian Bergemann. Clinical applications of magnetic drug targeting. *Journal of Surgical Research*, 95(2):200–206, 2001.

[154] Jeffrey R Childress and Robert E Fontana. Magnetic recording read head sensor technology. *Comptes Rendus Physique*, 6(9):997–1012, 2005.

[155] Raymond G Teller, Robert D Wilson, Richard K McMullan, Thomas F Koetzle, and Robert Bau. A neutron diffraction study of $HFeCo_3(CO)_9(P(OCH_3)_3)_3$, a metal cluster complex with a triply bridging hydride ligand. *Journal of the American Chemical Society*, 100(10):3071–3077, 1978.

[156] Richard E Sullivan, Michael S Lupin, and Robert W Kiser. Negative parent ion in the mass spectrum of hexacarbonylvanadium. *Journal of the Chemical Society D: Chemical Communications*, (12):655a–655a, 1969.

[157] Gary F Holland, Donald E Ellis, David R Tyler, Harry B Gray, and William C Trogler. Theoretical, spectroscopic, and electrochemical studies of tetracobalt, tetrarhodium, and tetrairidium dodecacarbonyl and tris (diphenylphosphino) methane-substituted derivatives. *Journal of the American Chemical Society*, 109(14):4276–4281, 1987.

[158] Ragesh Kumar T P, Ragnar Bjornsson, Sven Barth, and Oddur Ingólfsson. Formation and decay of negative ion states up to 11 ev above the ionization energy of the nanofabrication precursor $HFeCo_3(CO)_{12}$. *Chemical Science*, 8(9):5949–5952, 2017.

[159] Justin P Lomont, Son C Nguyen, and Charles B Harris. Ultrafast trir and dft studies of the photochemical dynamics of $Co_4(CO)_{12}$ in solution. *Organometallics*, 31(10):4031–4038, 2012.

[160] Nist mass spec data center, s.e. stein, director, "mass spectra" in nist chemistry webbook, nist standard reference database number 69, eds. p.j. linstrom and w.g. mallard, national institute of standards and technology, gaithersburg md, 20899, doi:10.18434/t4d303, (retrieved september 19, 2017).

[161] EW Plummer, WR Salaneck, and Joel Steven Miller. Photoelectron spectra of transition-metal carbonyl complexes: comparison with the spectra of adsorbed co. *Physical Review B*, 18(4):1673, 1978.

[162] M Barber, JA Connor, MF Guest, MB Hall, IH Hillier, and WNE Meredith. High energy photoelectron spectroscopy of transition metal complexes. part 1; bonding in substituted and unsubstituted first row carbonyls. *Faraday Discussions of the Chemical Society*, 54:219–226, 1972.

[163] J. F Moulder. *Handbook of X-Ray Photoelectron Spectroscopy*. Chanhassen, 1995.

[164] T P Ragesh Kumar, Ilyas Unlu, Sven Barth, Oddur Ingólfsson, and D Howard Fairbrother. Electron induced surface reactions of $HFeCo_3(CO)_{12}$, a bimetallic precursor for focused electron beam induced deposition (febid). *Submitted to The Journal of Physical Chemistry C*, 2017.

[165] DBW Yawney and FGA Stone. Ruthenium–iron carbonyls. *Chemical Communications (London)*, (11):619–620, 1968.

[166] J Knight and M J Mays. *Chem. and Ind,.*, 9:115, 1968.

[167] A Perentes, A Bachmann, M Leutenegger, I Utke, C Sandu, and P Hoffmann. Focused electron beam induced deposition of a periodic transparent nano-optic pattern. *Microelectronic Engineering*, 73:412–416, 2004.

[168] S Babin, M Weber, and HWP Koops. Fabrication of a refractive microlens integrated onto the monomode fiber. *Journal of Vacuum Science & Technology B: Microelectronics and Nanometer Structures Processing, Measurement, and Phenomena*, 14(6):4076–4079, 1996.

[169] Alexandre Perentes, Patrik Hoffmann, and Frans Munnik. Focused electron beam induced deposition of pure SIO_2. In *Proc. SPIE 6533, 23rd European Mask and Lithography Conference*, page 65331Q.

[170] T P Ragesh Kumar, Sangeetha Hari, Krishna K Damodaran, Oddur Ingólfsson, and Cornelis W. Hagen. Electron beam induced deposition of silacyclohexane and dichlorosilacyclohexane; the role of dissociative ionization and dissociative electron attachment in the deposition process. *Accepted for publication*, 2017.

[171] Daryl A Smith, Jason D Fowlkes, and Philip D Rack. Understanding the kinetics and nanoscale morphology of electron-beam-induced deposition via a three-dimensional monte carlo simulation: The effects of the precursor molecule and the deposited material. *Small*, 4(9):1382–1389, 2008.

[172] K_ Kanaya and S Okayama. Penetration and energy-loss theory of electrons in solid targets. *Journal of Physics D: Applied Physics*, 5(1):43, 1972.

[173] Markus Weber. Scattering of non-relativistic electrons in tip structures. *Journal of Physics D: Applied Physics*, 27(7):1363, 1994.

[174] Uwe Hübner, R Plontke, M Blume, A Reinhardt, and HWP Koops. On-line nanolithography using electron beam-induced deposition technique. *Microelectronic Engineering*, 57:953–958, 2001.

[175] Maurizio Dapor. A monte carlo investigation of secondary electron emission from solid targets: Spherical symmetry versus momentum conservation within the classical binary collision model. *Nuclear Instruments and Methods in Physics Research Section B: Beam Interactions with Materials and Atoms*, 267(18):3055–3058, 2009.

[176] Tetsuya Sato, Minoru Mitsui, Junji Yamanaka, Kiyokazu Nakagawa, Yutaka Aoki, Shouji Sato, and Chiharu Miyata. Formation of microcrystalline silicon and sin x films by electron-beam-induced-chemical vapor deposition at ultra low temperature. *Thin Solid Films*, 508(1):61–64, 2006.

[177] F Bozso and Ph Avouris. Electron induced chemical vapor deposition by reactions induced in adsorbed molecular layers. *Applied Physics Letters*, 53(12):1095–1097, 1988.

[178] Alexandre Perentes and Patrik Hoffmann. Focused electron beam induced deposition of si-based materials from SiOxCy to stoichiometric SiO_2: Chemical compositions, chemical-etch rates, and deep ultraviolet optical transmissions. *Chemical Vapor Deposition*, 13(4):176–184, 2007.

[179] T P Woodman. The formation of thin films of silica by the electron bombardment of triphenylsilanol. *British Journal of Applied Physics*, 16(3):359, 1965.

[180] K R Shoulders. *Stanford Res. Inst. Rept., p. 124*, 1960.

[181] E S Faber, R N Tauber, and Barret Broyde. Deposition of silicon by electron irradiation of tetramethylsilane. *Journal of Applied Physics*, 40(7):2958–2964, 1969.

[182] L R Thompson, J J Rocca, K Emery, P K Boyer, and G J Collins. Electron beam assisted chemical vapor deposition of SiO_2. *Applied Physics Letters*, 43(8):777–779, 1983.

[183] Koji Nakano, Tetsuhiro Horie, and Hitoshi Sakamoto. Low-temperature growth of SiO_2 films by electron-induced ultrahigh vacuum chemical vapor deposition. *Japanese Journal of Applied Physics*, 35(12S):6570, 1996.

[184] T Bret, I Utke, A Bachmann, and P Hoffmann. In situ control of the focused-electron-beam-induced deposition process. *Applied Physics Letters*, 83(19):4005–4007, 2003.

[185] Anastasia V Riazanova, BN Costanzi, A Aristov, YGM Rikers, V Ström, JJL Mulders, AV Kabashin, E Dan Dahlberg, and LM Belova. Gas-assisted electron-beam-induced nanopatterning of high-quality Si-based insulator. *Nanotechnology*, 25(15):155301, 2014.

[186] Sanne K De Boer, Willem F van Dorp, and Jeff Th M De Hosson. Charging effects during focused electron beam induced deposition of silicon oxide. *Journal of Vacuum Science & Technology B, Nanotechnology and Microelectronics: Materials, Processing, Measurement, and Phenomena*, 29(6):06FD01, 2011.

[187] Timothy W Weidman and Todd Schroeder. Methods for deposition of silicon carbide and silicon carbonitride films, May 14 2013. US Patent 8,440,571.

[188] Robert P Mandal. Very low dielectric constant plasma-enhanced CVD films, April 1 2003. US Patent 6,541,367.

[189] L Reimer and M Wächter. Contribution to the contamination problem in transmission electron microscopy. *Ultramicroscopy*, 3:169–174, 1978.

[190] SJ Randolph, JD Fowlkes, and PD Rack. Effects of heat generation during electron-beam-induced deposition of nanostructures. *Journal of Applied Physics*, 97(12):124312, 2005.

Article I

Structure and energetics in dissociative electron attachment to $HFeCo_3(CO)_{12}$

Ragesh Kumar T P, Sven Barth, Ragnar Bjornsson and Oddur Ingólfsson.
The European Physical Journal D, **70** 163 (2016)

Ragesh Kumar T P carried out all the experiments and computations and analysed the data, he wrote the first draft of the paper and contributed to editing until publication.

Eur. Phys. J. D (2016) 70: 163
DOI: 10.1140/epjd/e2016-70164-y

THE EUROPEAN PHYSICAL JOURNAL D

Regular Article

Structure and energetics in dissociative electron attachment to $HFeCo_3(CO)_{12}$[⋆,⋆⋆]

Ragesh Kumar T P[1], Sven Barth[2], Ragnar Bjornsson[1,a], and Oddur Ingólfsson[1,b]

[1] Science Institute and Department of Chemistry, University of Iceland, Dunhagi 3, 107 Reykjavík, Iceland
[2] Vienna University of Technology, Institute of Materials Chemistry, Getreidemarkt 9/BC/02, 1060 Vienna, Austria

Received 4 March 2016 / Received in final form 9 June 2016
Published online 30 August 2016 –

Abstract. Here we report structural parameters on the heteronuclear transition metal complex $HFeCo_3(CO)_{12}$ and its anion formed upon electron attachment, as well as the thermochemical thresholds for sequential CO loss and the loss of the apical group (as $Fe(CO)_3^-$ and $Fe(CO)_4^-$). Geometrical parameters from single crystal X-ray diffraction are compared with calculated values from density functional theory calculations, for the neutral and anionic ground state of this transition metal cluster. Further, experimental appearance energies for sequential CO loss and the formation of $Fe(CO)_3^-$ and $Fe(CO)_4^-$ are compared to the respective calculated threshold values. Geometry optimizations were performed at the BP86/def2-TZVP level of theory while the threshold energies were calculated at the PBE0/ma-def2-TZVP level of theory. The SOMO of the anion is found to have a clear Fe-Co anti-bonding character resulting in elongation of the Fe-Co bonds and the transformation of one of the terminal Co-CO groups to a bridging Co-CO-Fe group upon electron attachment. The thermochemical threshold PBE0 calculations are concordant with the observed appearance energies and structural parameters from single crystal X-ray diffraction for the neutral molecule are well reproduced at the BP86/def2-TZVP level of theory.

1 Introduction

Due to their large diversity in electronic and structural properties, and thus their tuneable chemical reactivity and selectivity, transition metal clusters hold a promise of numerous applications in homogeneous and heterogeneous catalysis [1]. From a fundamental aspect, these entities are not any less interesting, as they may be seen as a bridge between single atom properties and these of the corresponding bulk material [2]. Furthermore, heteronuclear transition metal complexes offer an interesting route for composition control in thin film deposition and the deposition of functional nanostructures. In this context $HFeCo_3(CO)_{12}$ has been used in chemical vapour deposition (CVD) [3] for controlled deposition of mixed Fe/Co films and the corresponding metal oxide films. More recently $HFeCo_3(CO)_{12}$ has been used in focused electron beam induced deposition (FEBID) [4] for the fabrication of functional nanostructures. In that study, FEBID with $HFeCo_3(CO)_{12}$ as a precursor was used to fabricate ferromagnetic nano-wires and nano-bars and was found to produce high metal content Fe/Co (>80%) alloy structures with good reproducibility. Hence in FEBID, heteronuclear transition metal complexes may open up a new avenue for the fabrication of mixed-metal nanostructures of well-defined composition as an alternative route to co-deposition of homonuclear complexes in a binary gas beam setup [5–7].

It is well recognized that low energy electron induced processes i.e., dissociative electron attachment (DEA), dissociative ionization (DI), neutral dissociation (ND; upon electron excitation) and eventually dipolar dissociation (DD) play a determining role in FEBID [8–10]. Thus, to better understand the deposition process in FEBID, it is important to characterize the relative role of these processes, their electron energy dependence and individual fragment formation. For this purpose a number of gas phase studies on low energy electron interaction with potential organometallic FEBID precursors have been conducted in recent years; see for example references [11–20]. However, these studies exclusively consider mono-nuclear transition metal complexes and to our knowledge no such studies have been conducted on heterometallic compounds such as $HFeCo_3(CO)_{12}$.

⋆ Contribution to the Topical Issue "Advances in Positron and Electron Scattering", edited by Paulo Limao-Vieira, Gustavo Garcia, E. Krishnakumar, James Sullivan, Hajime Tanuma and Zoran Petrovic.
⋆⋆ Supplementary material in the form of one pdf file available from the Journal web page at
http://dx.doi.org/10.1140/epjd/e2016-70164-y

[a] e-mail: ragnarbj@hi.is
[b] e-mail: odduring@hi.is

Motivated by the promising results obtained in FEBID with the heteronuclear transition metal complex $HFeCo_3(CO)_{12}$ [4] and the lack of data on its interaction with low energy electrons, we have set out to characterize its properties with regards to the interaction with electrons in the energy range from about 0 to 100 eV. In the current contribution the focus is on the thresholds for fragment formation upon dissociative electron attachment, the structure of the neutral precursor molecules and its transient negative ion (TNI; formed upon electron attachment), as well as the structure of the fragments formed in DEA. For completeness, experimental threshold values and structural parameters are compared to and extended by DFT calculations.

$HFeCo_3(CO)_{12}$ is a tetranuclear transition metal complex first synthesized by Chini et al. [21]. The details of the synthesis and some improvements can be found in [4]. It belongs to the C_{3v} point group, containing one C_3 principle axes and three σ_v planes of symmetry. The general structure of $HFeCo_3(CO)_{12}$ was initially assigned by Guglielminotti et al. [22] through analogy with the similar complex $HFeCo_3(CO)_9(P(OMe_3)_3)_3$ [23] and later confirmed through X-ray diffraction by Porrati et al. [4]. In this compound the metal atoms are arranged in a tetrahedral geometry with Fe forming the apex and the hydrogen is centred below the Co_3 basal plane and is coordinated to all three Co atoms. Of the 12 CO ligands, 3 are terminally bound to the apical Fe atom, 6 are terminally bound to the Co atoms (two to each) and the remaining 3 CO ligands each bridge two neighbouring Co atoms. The experimentally determined structure of $HFeCo_3(CO)_{12}$ is shown in Figure 1 and the main structural parameters are given in Tables 1 and 2, where they are compared with the calculated parameters for both the neutral and anionic ground state of $HFeCo_3(CO)_{12}$. The Cartesian coordinates for the neutral and anionic molecule can be found in the supplementary information file SI1_Geometrical-parameters.pdf. An extensive table where individual angles from the X-ray diffraction data are compared with the calculated parameters for both the neutral and anionic ground state can be found in the supplementary information file SI2_Individual-angles.pdf.

Photo-fragmentation and electronic absorption spectra of $HFeCo_3(CO)_{12}$ in solution were reported by Geoffroy and Epstein in the late 80's [24] and compared with the same for $HCCo_3(CO)_9$ and $H_3CCo_3(CO)_9$. The spectra were recorded at room temperature and at 77 K. At 300 K, $HFeCo_3(CO)_{12}$ shows a broad absorption in the visible range with a maximum at 528 nm and shoulders on the UV slope at 380, 324 and 280 nm. At 77 K the visible contribution splits up in two with maxima at 591 and 525 nm and distinct peaks are observed in the UV region at 377 and 324 nm. Photo-fragmentation at 350 nm was, however, found to be slow. For $HCCo_3(CO)_9$ and $H_3CCo_3(CO)_9$, the authors did not observe any distinct change in the UV/VIS absorption upon changing the apical group, leading them to the conclusion that the transitions observed are primarily located at the basal Co_3 unit. This is further supported by ESR spectra of the one-electron reduction

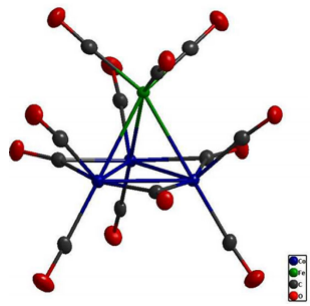

Fig. 1. Structure of $HFeCo_3(CO)_{12}$ determined from X-ray crystallography (reproduced from Ref. [4]).

products from $YCCo_3(CO)_9$ (with Y being e.g. halogen, alkyl- or an aryl group) [25,26] indicating that the added electron occupies an orbital delocalized on the three basal cobalt atoms, with little spin density on the apical carbon. Furthermore, based on molecular orbital analysis on $YCCo_3(CO)_9$ with Y = S and Se [27] these transitions are inferred to be from non-bonding to anti-bonding metal-metal orbitals located at the Co_3 base. Based on similarities between the UV/VIS spectra of $HFeCo_3(CO)_{12}$ and $HCCo_3(CO)_9$ and $H_3CCo_3(CO)_9$ the authors [24] infer that the situation is similar for $HFeCo_3(CO)_{12}$. According to our data this analogy does not hold, which in fact is not surprising considering the fundamentally different nature of the apical groups when proceeding from a carbon to a transition metal (see discussion in the following sections).

With the aid of electronic absorption spectra, photoelectron spectroscopy and SCF-Xα-DV calculations Holland et al. [28,29] and Trogler [30] explored the molecular orbital energy levels and assigned the lowest lying transitions observed in their UV/VIS spectra for $M_4(CO)_{12}$ with M = Co, Rh and Ir. From these, the first two are of C_{3v} symmetry and their electronic configuration is predicted to be $\ldots 21e^2$, $17a_1^2$, $22e^2 \ldots 6a_2^2$, $25e^2$, $19a_1^2$, $20a_1^2$, $26e^2$ and the first two LUMOs to be 27e, $7a_2$. Similar to $HFeCo_3(CO)_{12}$ they observed transitions in the visible range at 660, 540 and 460 nm and in the UV range at 375 and 340 nm. The former of the UV transitions (375 nm) is attributed to a metal-metal $\sigma \rightarrow \sigma*$ transition and tentatively assigned as an excitation from 22e to 27e, which is calculated to take place at 393 nm (3.15 eV). These orbitals were both found to contain significant d-character at both the apical and the basal cobalts, thus contributing to bonding along the tetrahedral faces. The analog transition in $HFeCo_3(CO)_{12}$ should thus be expected to weaken the metal-metal bonding of the apical-basal Fe-Co bond. Furthermore, recently Lomont et al. [31] conducted a combined theoretical and experimental, time-resolved study on the photo-fragmentation dynamics

Table 1. Bond lengths (Å) of $HFeCo_3(CO)_{12}$ from single crystal X-ray diffraction (XRD) and BP86/def2-TZVP geometry optimizations of the ground state neutral molecule and its anion. Standard deviations are in parentheses and difference between the calculated and the measured values for the neutral are given in percentages.

Bond length	Neutral (calc.)	Neutral (XRD)	% deviation	Anion (calc.)
Co1-Co2	2.508	2.491	0.682	2.494
Co1-Co3	2.509	2.483	1.047	2.491
Co2-Co3	2.509	2.50	0.360	2.554
Average		2.492 (0.009)	0.696	
Fe4-Co1	2.54	2.538	0.079	2.609
Fe4-Co2	2.54	2.558	0.704	2.879
Fe4-Co3	2.54	2.553	0.470	2.868
Average		2.550 (0.01)	0.418	
Fe4-CO_{bridge} (between Fe4 and Co1)	2.866			2.124
Fe4-C22	1.777	1.799	1.223	1.782
Fe4-C23	1.777	1.813	1.986	1.782
Fe4-C24	1.777	1.813	1.986	1.772
Average		1.808 (0.008)	1.732	
Co1-C16	1.959	1.981	1.111	1.939
Co2-C21	1.959	1.961	0.102	1.937
Co3-C19	1.958	1.981	1.161	1.965
Average		1.974 (0.012)	0.791	
Co1-C15	1.761	1.761	0	1.832
Co2-C20	1.761	1.789	1.565	1.772
Co3-C17	1.761	1.785	1.345	1.772
Average		1.778 (0.015)	0.970	
Co1-C28	1.788	1.808	1.051	1.745
Co2-C26	1.789	1.870	4.385	1.774
Co3-C18	1.788	1.840	2.826	1.773
Average		1.839 (0.031)	2.754	
Co1-H25	1.718			1.763
Co2-H25	1.717			1.696
Co3-H25	1.716			1.695
Average	1.717	1.734[a]		
H25-Co plane	0.964	0.978[a]		0.909

[a] Neutron diffraction study of $HFeCo_3(CO)_9(OCH_3)_3$ [23].

of $Co_4(CO)_{12}$. In this study irradiation of $Co_4(CO)_{12}$ at 267 and at 400 nm was found to result primarily in cleavage of the apical-basal Co-Co bond and the formation of new, CO bridged intermediates. These observations are very much in line with our calculations and are also reflected in the experimental data as we will discuss below.

2 Methods

2.1 X-ray diffraction measurements

Single crystal X-ray diffraction experiments were performed at low temperature (100 K) on a BrukerAxs Smart Apex II diffractometer with a CCD area detector using graphite-monochromated Mo-K_α radiation ($\lambda = 71.073$ pm). Data were collected with ω and φ-scans and 0.5° frame width. Data was corrected for polarisation and Lorentz effects, and an empirical absorption correction (Sadabs) was applied. The cell dimensions were refined with all unique reflections. The structures were solved with direct methods (Shelxs97) [32] and refinement to convergence was carried out with the full-matrix least squares method based on F^2 (Shelxl97) with anisotropic structure parameters for all non-hydrogen atoms. $HFeCo_3(CO)_{12}$ crystallizes in the monoclinic space group C2/c and isotropic refinement converged to $R = 0.030$ and $R_w = 0.079$. Strong disorder is observed for the crystals with the metal tetrahedral tilted by 180°. The disorder was solved for one set of molecules with a 50:50 split and the other position was characterized by only 3% of the molecules occupying the second position. Due to the small population density, no CO could be refined for this position. The structural data are extracted from the position of the molecule with 97% population density containing metal atoms labeled Co1, Co2, Co3 and Fe4.

The CIF file for the results of the single crystal structure determination was not deposited in a database due to the uncertainty of assigning Fe and Co to specific positions using XRD, however, the three equivalent positions should be occupied by Co atoms, which is in line with data on substituted derivatives of this compound [23]. The CIF

Table 2. Selected bond angles (degrees) of $HFeCo_3(CO)_{12}$ from single crystal X-ray diffraction (XRD) and BP86/def2-TZVP geometry optimizations of the ground state neutral molecule and its anion. Standard deviations are in parentheses and difference between the calculated and the measured values for the neutral are given in percentages. Where there is no significant change in the individual bond angles, only the average values are shown (for the full set of angles see the supplementary information file 'SI2_Individual-angles.pdf').

Bond angles	Neutral (calc.)	Neutral (XRD)	% deviation	Anion (calc.)
Co-Co-Co (avg.)	60.0	60.0	0.0	60.0
Co-Fe4-Co (avg.)	59.2	58.5	1.20	53.5
Co1-Co2/3-Fe4 (avg.)	60.4	60.4	0.0	57.7
Co3/2-Co1-Fe4 (avg.)	60.4	61.4	1.55	68.6
Co2/3-Co3/2-Fe4 (avg.)	60.4	60.7	0.49	63.6
Fe4-Co1-C15	81.4	82.0	0.73	53.8
Fe4-Co2-C20	81.4	78.3	3.96	79.7
Fe4-Co3-C17	81.3	81.3	0.00	79.3
Co1-Fe4-C22/23 (avg.)	101.3	101.2	0.10	111.0
Co2/3-Fe4-C22/23 (avg.)	101.3	101.0	0.35	101.5
Co2/3-Fe4-C24 (avg.)	101.4	99.6	1.81	90.5
Co1-Co2/3-C20/17 (avg.)	128.9	129.2	0.19	127.1
Co2/3-Co1-C15	129.0	127.2	1.42	114.2
Co2-Co3-C17	128.9	128.8	0.08	128.9
Co3-Co2-C20	129.1	130.8	1.30	129.1
Co-C_{bridge}-Co (avg.)	79.7	78.5	1.44	80.0
C15-Co1-C28	100.1	95.9	4.38	100.3
C20-Co2-C26	100.2	97.8	2.45	102.1
C17-Co3-C18	100.2	97.4	2.87	102.0
C23-Fe4-C24	94.3	96.6	2.38	93.3
C22-Fe4-C24	94.3	95.8	1.57	93.0
C23-Fe4-C22	94.3	95.3	1.05	104.1
C22-Fe4-C21	73.6	76.8	4.17	80.3
C23-Fe4-C16	73.7	77.5	4.90	80.6
C24-Fe4-C19	73.7	77.2	4.53	64.9
Fe4-C19-O9	132.9	132.9	0.00	131.6
Fe4-C16-O6	132.9	134.3	1.04	128.6
Fe4-C21-O11	133.0	132.7	0.23	128.8
C18-Co3-H25	90.9			90.1
C26-Co2-H25	90.8			90.0
C28-Co1-H25	90.8			109.8

file is included here as the supplementary information file SI3_IronCobaltCarbonylHydrid_a.cif.

2.2 Appearance energy measurements

Dissociative electron attachment experiments were carried out with a crossed electron/molecule beam setup under single collision condition. Details of the experimental setup can be found in reference [33], so we only give a brief description here. An electron beam with about 110 meV energy distribution (FWHM) is generated with a trochoidal electron monochromator and crossed with an effusive beam of the target gas generated by sublimation of the solid $HFeCo_3(CO)_{12}$ sample into the interaction zone through a capillary tube. In order to get a sufficient working pressure of about 4×10^{-7} mbar, the inlet system is maintained at 348–353 K and to prevent sticking of the compound on the monochromator and extraction lenses, the chamber is maintained at about 393 K. Negative ions formed in the interaction region are extracted with a weak electric field and analysed with a quadrupole mass spectrometer. The electron beam energy was calibrated based on the SF_6^-/SF_6 yield at 0 eV and the energy resolution of the electron beam was determined from the FWHM of the SF_6^- signal. In lack of any physically meaningful approach for the determination of appearance energies in DEA, these are estimated by fitting a line to the rising side of the ion yield and extrapolation to the base line as shown in Figure 2 for the loss of 4, 8 and 12 CO. These fragments are chosen to reflect the validity of this approach over the whole signal to noise ratio for the current measurements. For the loss of up to 11 CO the upper limit of the threshold is determined by fitting

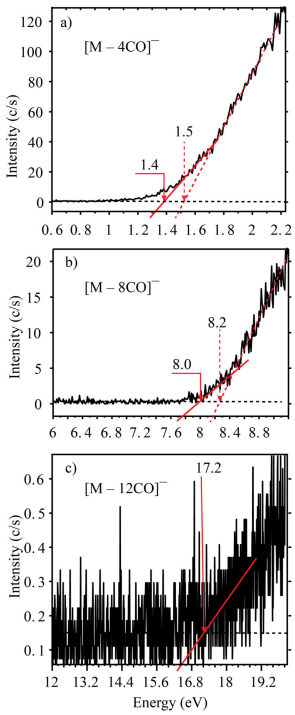

Fig. 2. Examples of linear fits for the estimation of the appearance energy (AE). The fits to the negative ion yield curves for the loss of 4 CO (a), 8 CO (b) and 12 CO (c) are shown to reflect the whole signal to noise ratio. The interception of the solid red line with the base line is taken as the AE, while that of the dashed line is taken as the upper limit of the uncertainty (applies for the loss of (0–11 CO). The uncertainty for the AE for the loss of 0–11 CO is estimated to be about 0.2 eV, while that for the loss of all 12 CO is estimated to be about 0.5 eV.

an extended section of the rising side as shown by dashed lines in Figure 2 and the lower limit is estimated from the base line. From visual inspection and the variation between data sets we estimate these values to be accurate within ±0.2 eV for loss of up to 11 CO, but for the loss of 12 CO the signal to noise level is comparatively low and we estimate the uncertainty to be about ±0.5 eV.

2.3 Quantum chemical calculations

All quantum chemical calculations were performed using the ORCA computational chemistry software [34]. The geometry optimizations for the neutral molecule, its anion and all fragments were carried out with density functional theory using the functional BP86 [35,36] and the polarized triple-zeta basis set def2-TZVP [37]. Following geometry optimization, single point energies were calculated with the hybrid DFT functional PBE0 [38,39] and the minimally augmented polarized triple zeta basis set ma-def2-TZVP [37,40]. All BP86 and PBE0 calculations additionally included the D3(BJ) dispersion correction [41,42] to account for weak vdW interactions that standard density functionals do not describe well. The calculated threshold values were not found to be very basis-set dependent. The threshold values, however showed significant improvement when going from a GGA functional (BP86) to a hybrid-GGA (PBE0), as shown in Table 3. The RIJCOSX approximation [43] was used for faster evaluation of the Coulomb and Exchange terms in the PBE0 calculations. Zero-point energy (ZPE) contributions were included for all intermediates from harmonic vibrational frequencies calculated at the BP86/def2-TZVP level. Threshold calculations with and without ZPE contribution for all species are shown in Table 3. We deduced the threshold by subtracting minimum energy of all the fragments from the minimum energy of the parent molecule. For the fragments $[M\text{-}CO]^-$ and $[M\text{-}2CO]^-$ different isomers were explored but the energies were usually similar. In each calculation, the electronic structure was explored by analysis of both canonical and localized molecular orbitals as well as spin densities. The dissociative electron attachment experiments were carried out at about 353 K, and in order to account for this experimental condition; we included in the calculations, the thermal energy of the parent molecule from harmonic vibrational normal mode calculations (including rotational and translational contributions as well). Note that this is the temperature of the inlet system while the monochromator and at least a part of the inlet capillary leading to the reaction region is maintained at about 390 K. The thermal energy of the neutral molecule at 353 K, which corresponds to about 1.2 eV is thus a conservative estimate (would be about 1.4 eV at 390 K). The thermally corrected threshold value was obtained by adding the thermal energy to the total energy of parent molecule. All the optimized geometries and the molecular orbitals were plotted using VMD [44].

3 Results and discussion

3.1 Geometrical and electronic properties of the relaxed neutral and anionic ground state of $HFeCo_3(CO)_{12}$

Figure 1 shows the experimentally determined structure for $HFeCo_3(CO)_{12}$ constructed from the X-ray diffraction data, while Figure 3 shows the calculated structure for the relaxed ground state geometry of the neutral and

Table 3. Calculated adiabatic and vertical attachment energies as well as threshold energies for sequential CO loss and the loss of the apical Fe group ($Fe(CO)_3^-$ and $Fe(CO)_4^-$) through electron attachment dissociation of $HFeCo_3(CO)_{12}$. Only the lowest energy fragments are included in the table. Single point electronic energies using PBE0/ma-def2-TZVP are calculated on geometries optimized with BP86/def2-TZVP. Included ZPE energies are calculated with BP86/def2-TZVP. The final E_{th} values are thermally corrected values, obtained by adding the BP86/def2-TZVP calculated thermal energy at 353 K to the total energy of the neutral molecule (1.2 eV, corresponding temperature of the inlet system). All values are in eV.

Fragment	BP86/def2-TZVP (without ZPE)	PBE0/ma-def2-TZVP (without ZPE)	PBE0/ma-def2-TZVP (ZPE correction included)	E_{th} (included ZPE and thermal correction)	AE
$M^-_{adiabatic}$	−3.07	−2.73	−2.77		0
$M^-_{vertical}$	−2.48	−2.49			
$[M\text{-}CO]^-$ (from Fe)	−1.67	−1.81	−1.94	−3.13	0
$[M\text{-}CO]^-$ (bridging Co and Fe)	−1.79	−1.70	−1.79	−2.90	0
$[M\text{-}CO]^-$ (terminal above Co plane)	−1.51	−1.29	−1.31	−2.49	0
$[M\text{-}CO]^-$ (terminal below Co plane)	−1.79	−1.67	−1.68	−2.87	0
$[M\text{-}CO]^-$ (bridging two Co)	−1.49	−1.36	−1.31	−2.56	0
$[M\text{-}2CO]^-$	0.33	−0.29	−0.55	−1.74	0
$[M\text{-}3CO]^-$	2.19	0.96	0.65	−0.54	0
$[M\text{-}4CO]^-$	4.07	2.92	2.47	1.28	1.4 ± 0.1
$[M\text{-}5CO]^-$	6.37	4.27	3.68	2.49	3.1 ± 0.2
$[M\text{-}6CO]^-$	8.40	5.39	4.72	3.52	4.5 ± 0.2
$[M\text{-}7CO]^-$	10.70	7.33	6.56	5.36	6.4 ± 0.2
$[M\text{-}8CO]^-$	13.08	9.36	8.52	7.32	8.0 ± 0.2
$[M\text{-}9CO]^-$	15.91	11.95	10.97	9.77	10.1 ± 0.2
$[M\text{-}10CO]^-$	17.49	13.37	12.34	11.14	12.4 ± 0.2
$[M\text{–}11CO]^-$	20.32	14.73	13.59	12.39	14.4 ± 0.2
$[M\text{-}12CO]^-$	22.91	17.44	16.25	15.05	17.2 ± 0.5
$Fe(CO)_4^-$	0.62	0.50	0.42	−0.78	0
$Fe(CO)_3^-$	1.68	1.65	1.49	0.29	0.70 ± 0.2

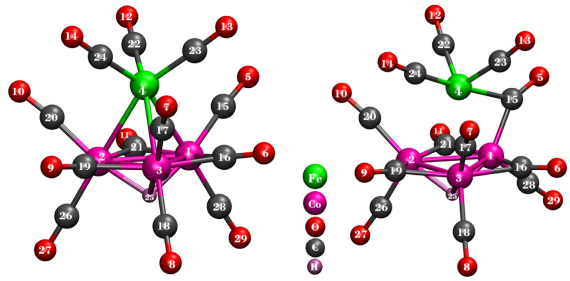

(a) Neutral (b) Anion

Fig. 3. (a) Optimized geometry of neutral $HFeCo_3(CO)_{12}$ in its ground state using the DFT functional BP86 and the basis set def2-TZVP. (b) Optimized geometry of $[HFeCo_3(CO)_{12}]^-$ in its ground state using the same functional and basis set.

Eur. Phys. J. D (2016) 70: 163

the anionic molecule. The X-ray diffraction CIF file and the Cartesian coordinates for the calculated neutral and anionic structure can be found in the supplementary information files; SI3_IronCobaltCarbonylHydrid_a.cif and SI1_Geometrical-parameters.pdf, respectively. In Table 1 the experimentally determined bond lengths for the neutral molecule are compared to the calculated ones and the corresponding parameters for the relaxed structure of the anionic ground state. In Table 2 the same comparison is presented for selected angles. Where there is no significant difference between individual angles describing the same or similar geometrical aspect their average is shown in Table 2. A detailed account on individual angles is tabulated in the supplementary information file SI2_Individual-angles.pdf.

$HFeCo_3(CO)_{12}$ belongs to the C_{3v} point group with a tetrahedral metal core composed of a Co_3 base and an Fe apex. As already mentioned above, three of the 12 CO ligands are terminally bound to the Fe apex, two are terminally bound to each Co atom and the remaining three form each a bridge between two neighbouring Co atoms. The average experimental Co-Co and Co-Fe bond lengths are 2.492 and 2.550 Å respectively, which agrees well with the calculated values of 2.509 and 2.540 Å, respectively (<1% deviation). The average experimental values for the terminal CO groups; Fe-CO, Co-CO_{above} (above the Co_3 plane) and Co-CO_{below} (below the Co_3 plane) are 1.808, 1.778 and 1.839 Å, respectively. The calculated values for these bond lengths are all slightly lower than the experimental ones, with the deviation being about 1.7, 1.0 and 2.8% respectively. Finally, the experimental value for the Co-CO-Co bridging bond is found to be 1.974 Å, which is essentially the same as the calculated value (1.959 Å). We cannot resolve the positions of the hydrogen atom in the X-ray diffraction patterns, but our calculations place it 0.964 Å below the Co_3 basal plane and correspondingly the H-Co bond length is 1.717 Å for this three centred hydrogen. This is in good agreement with neutron diffraction data for $HFeCo_3(CO)_9(OCH_3)_3$ where the hydrogen is found to be 0.978 Å below the Co_3 basal plane and the average H-Co bond length is found to be 1.734 Å [23].

The most noticeable changes when proceeding from the relaxed neutral ground state geometry to the relaxed anionic ground state geometry is the weakening of the bonding of the Fe apex to the basal Co_3 unit. This is manifested in the elongation of two of the three Fe-Co bonds (Co2 and Co3 in Fig. 3 and Tab. 1) from 2.540 Å in the neutral to 2.879 Å (Co2) and 2.868 Å (Co3) in the anion. The bond length Fe-Co1, on the other hand, only changes from 2.540 Å in the neutral to 2.609 Å in the anion, but at the same time the originally terminal C15(O) group at Co1 is converted to a Co1-C15(O)-Fe bridging ligand. Correspondingly the distance from Fe to C15 is reduced from 2.866 Å in the neutral (where this CO is not bound to the apical Fe) to 2.124 Å in the Fe4-C15(O)-Co bridged anion.

The most significant changes in angles, when proceeding from the neutral to the anion, are these that describe the position of the apical $Fe(CO)_3$ group relative to the Co_3 base. Correspondingly, the C24-Fe4-C19 angle changes from 73.7° in the neutral to 64.9° in the optimized anion geometry. The matching C22-Fe4-C21 and C23-Fe4-C16 angles change from 73.6° and 73.7° in the neutral geometry to 80.3° and 80.6° respectively in the relaxed anion geometry. Most noticeable, however, is the change in the Fe4-Co1-C15 angle, which is narrowed from 81.4° in the terminal Co1-C15(O) configuration of the neutral to 53.8° in the Fe-C15(O)-Co1 bridged anionic configuration.

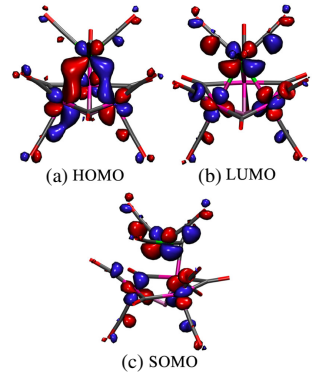

Fig. 4. (a) The highest occupied molecular orbital (HOMO) and (b) the lowest unoccupied molecular orbital (LUMO) of $HFeCo_3(CO)_{12}$. (c) The singly occupied molecular orbital (SOMO) of the ground state anion; $[HFeCo_3(CO)_{12}]^-$ in its relaxed geometry.

This picture of significant weakening of the bonds between the apical Fe and the Co_3 base and the transformation of one of the terminal Co-CO groups to a Fe-C(O)-Co bridging ligand is in good agreement with our DEA experiments. In fact, the second most pronounced dissociation channel is the formation of $Fe(CO)_4^-$, which appears at 0 eV electron energy (see further the discussion in Sect. 3.2). This is also consistent with analysis of the HOMO, LUMO and SOMO of $HFeCo_3(CO)_{12}$ shown as isosurfaces in Figure 4 and the spin density of the anion, shown in Figure 5 for the constrained and relaxed anionic geometry. From Figure 4 it is apparent that the HOMO has metal-metal bonding character along the tetrahedral faces separating the Fe apex from the Co_3 base while the LUMO has a distinct anti-bonding Co-Fe metal-metal character. Furthermore, the SOMO is to a large extent located at the apical Fe (Fig. 4), and the same is true for the spin density for both the constrained and the relaxed geometry (Fig. 5). Hence, the excess charge is to a large extent located on the Fe apex.

In their electronic absorption, photoelectron and SCF-Xα-DV studies on $M_4(CO)_{12}$, (M = Co, Rh and Ir)

 Eur. Phys. J. D (2016) 70: 163

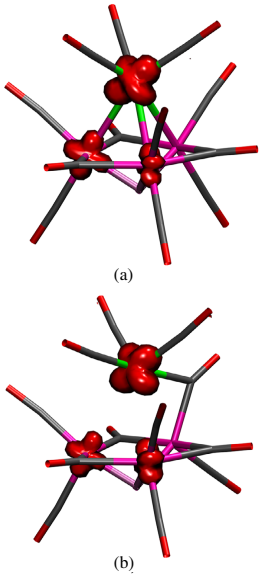

Fig. 5. (a) Spin density of the anion; $[HFeCo_3(CO)_{12}]^-$ in the constrained geometry of the neutral (vertical transition) and (b) spin density of the anion; $[HFeCo_3(CO)_{12}]^-$ in its relaxed ground state geometry.

Holland et al. [28,29] assigned the lowest lying transitions observed for $Co_4(CO)_{12}$ in the visible range to a metal to ligand charge transfer transition. From the two distinct UV transitions they observed at 375 and 340 nm, they tentatively assigned the former to a metal-metal $\sigma \rightarrow \sigma^*$ transition from a relatively low-lying valence orbital of e symmetry (22e) to the LUMO (27e). These orbitals are found to have metal-metal bonding and anti-bonding character, respectively, between both the apical and basal cobalt atoms. This agrees well with our calculations as well as our experimental observations in DEA. Furthermore, in many aspects DEA may be compared to photofragmentation. In the former case, the excess electron occupies a previously unoccupied molecular orbital, generally anti-bonding in nature, while in the latter case an occupation of the same MO may result from an electronic excitation from a lower lying MO (in the case of core excited resonances in DEA the electron attachment may also be associated with an concomitant electron excitation; see for example Ref. [45]). In fact, in a combined theoretical and experimental time-resolved photo-fragmentation study, Lomont et al. [31] found that irradiation of $Co_4(CO)_{12}$ at 267 and at 400 nm results primarily in cleavage of the apical-basal Co-Co bonds and the formation of new CO-bridged intermediates. These observations are very much in line with our calculations and are also reflected in our DEA data. Finally, we note that although the early photo-fragmentation study of Geoffroy and Epstein [24] showed only slow degradation of $HFeCo_3(CO)_{12}$, at 350 nm, the main products were $Co_4(CO)_{12}$ (degassed solution) and $Co_2(CO)_8$ (under hydrogen). Though these products are obviously the result of more complex chemistry than simple photo-induced loss of the apical Fe group, both of these products are concomitant with that being the first step.

3.2 Threshold and appearance energies for sequential CO loss and the loss of $Fe(CO)_3^-$ and $Fe(CO)_4^-$ from $HFeCo_3(CO)_{12}$ upon electron attachment

Dissociative electron attachment to $HFeCo_3(CO)_{12}$ is mainly characterized by two channels; sequential CO loss and loss of the apical iron group. While, the loss of one and two CO are exothermic and appear through a maximum at about 0 eV incident electron energy, further CO loss proceeds through rather broad contributions progressively shifted by about 2 eV to higher energy with the maximum for the loss of 12 CO groups being close to about 20 eV. The loss of the apical iron is mainly observed through the formation of $Fe(CO)_4^-$ close to 0 eV, but to lesser extent also the formation of $Fe(CO)_3^-$ and $Fe(CO)_2^-$ is observed. The most significant channels are the loss of two CO and the formation of $Fe(CO)_4^-$ (about 4:1), with the former being 2–3% of the SF_6^- calibration signal intensity (normalized with regards to the pressure).

If we consider the CO ligands in $HFeCo_3(CO)_{12}$ to be grouped into 4 groups composed of three equivalent CO each, and we presume that the nature of the individual CO ligands does not change when other CO ligands are removed, then there are more than 40 000 ways to remove all 12 ligands from a rigid core. Hence, there are more than 40 000 possible reaction pathways for the loss of all CO ligands from $HFeCo_3(CO)_{12}$ assuming that the reaction proceeds from the rigid core of the C_{3v} neutral geometry, without CO removal influencing the remaining ligands. The real situation, where structural relaxation, vibrational and electronic dynamics and even rearrangement reactions accompany each step from the initial TNI formation to the loss of the last CO ligand, is even more complex. It is thus clear that a rigorous mapping of the entire reaction path through optimization of all possible sequences of CO loss is not practical.

In the current approach, the initial loss of one CO was calculated from both the constrained (neutral) configuration of the anion and the relaxed anionic ground state (see Fig. 3). All geometry optimizations were carried out at the BP86 level of theory with single point energy calculations at the PBE0 level of theory. The optimizations systematically explored removal of a terminal CO ligand from the Fe apex and from above and below the Co_3 plane, as well

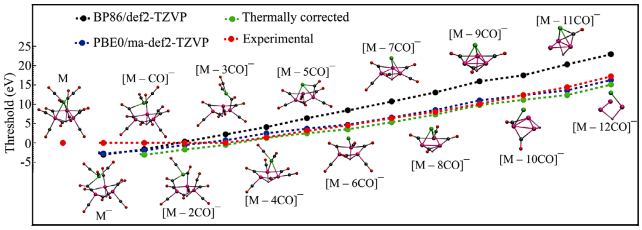

Fig. 6. Calculated threshold values from Table 3 and the optimized geometries of the corresponding anions. The threshold energy in eV is shown on the y-axis. Details on the thermally corrected threshold calculation and estimation of appearance energies are in the text and in Table 3.

Table 4. Calculated (PBE0/ma-def2-TZVP) CO bond dissociation energies (eV) from different positions at the neutral and anionic $HFeCo_3(CO)_{12}$ as well as the adiabatic electron affinity of the charge retaining fragment (from the anion).

Bond	BDE (Neutral)	BDE (anion)	Electron affinity
Fe-CO	2.046	0.92	3.85
Co-CO_{above}	2.382	1.44	3.67
Co-CO_{below}	1.726	1.05	3.39
Co-$CO_{bridged}$	2.29	1.36	3.65

as removal of one of the Co-Co bridging CO ligands. For the relaxed anionic geometry as a starting point, optimization after removal of the Fe-Co bridging ligand were also carried out. These optimizations result in different local minima and the reaction energies are shown in Table 3. It is, however, clear that the CO loss from the molecular anion is an exothermic process in all cases and that the CO loss is most favourable from the Fe apex. Conversely, single CO loss from the anion is least favourable from the terminal CO above the Co_3 plane and from the Co-Co bridging CO ligands. For the carbonyls at the Co_3 base, the threshold values correspond well with the calculated bond dissociation energies (BDEs) for the anionic as well as the neutral molecule, which are shown in Table 4 for comparison. The apical Fe-CO bonds, on the other hand, are apparently considerably destabilized in the anionic ground state as compared to the neutral one. This is very apparent when comparing the BDEs given for the neutral and the anion in Table 4, but is also clear from the threshold values given in Table 3. In this context it is noted, that for a single bond rupture upon electron attachment, the thermochemical threshold is given by the respective BDE for the neutral parent less the electron affinity of the charge-retaining fragment (also shown in Tab. 4).

A similar systematic approach as for single CO loss, was taken for all other fragments, except for $[M - nCO]^-$ with $n = 2$–5, where the preceding minimum energy structure $[M - (n - 1)\ CO]^-$ was additionally used as initial geometry for the optimization. For $n = 1$–4, optimizations from the relaxed anionic ground state resulted in the lowest energy geometry while for all other fragments the lowest energy geometry resulted from optimizations from the rigid (neutral) geometry of the anion. The energy difference, however, was generally insignificant (50–100 meV) and the resulting structures were similar. The lowest energy structures derived in this way are depicted in Figure 6 along with the threshold energies for the individual processes calculated at the BP86/def2-TZVP and PBE0/ma-def2-TZVP level of theory. Also shown are the thermally corrected values at the PBE0 level of theory and the experimental appearance energies (AEs). These values are also listed in Table 3 along with the ZPE contributions calculated from the harmonic vibrational frequencies at the BP86 level of theory. Also shown in Table 3 are threshold values for the loss of the Fe apex as $Fe(CO)_3^-$ and $Fe(CO)_4^-$. Note that DEA is a resonant process that is generally characterized by the initial formation of a TNI through a vertical transition within the Franck-Condon (FC) region between the ground state neutral and the anionic state formed [45]. Thus the energy dependency and consequently the AE is often defined by the FC-overlap rather than the thermochemical threshold for the respective process. The former is thus often observed at considerably higher energies than the expected thermochemical threshold. Accordingly, an underestimation of the AE by threshold calculations do not allow rigorous judgement of the performance of the theory applied. An overestimation on the other hand is a clear sign of a failure to reproduce the thermochemistry correctly.

For sequential CO loss, the threshold energies shown in Figure 6 and Table 3, are calculated from the difference between the total energy of the neutral parent molecule less the sum of the total energy of the neutral CO units lost, and the total energy of the geometrically optimized anionic fragment. In the case of the $Fe(CO)_3^-$ and $Fe(CO)_4^-$ formation, the remaining neutral core is optimized starting from the constrained (neutral) geometry of the anion and the threshold for this process is the difference of the total energy of the neutral precursor molecule less the sum of the total energy of the fragments.

From Table 3 it is clear that the AE for the loss of up 3 CO units from $HFeCo_3(CO)_{12}$ is around 0 eV, indicating that these processes are exothermic. However, even when considering the thermal and the ZPE corrections, the BP86 threshold for the loss of 3 CO units is about 0.7 eV above the observed AE. Furthermore, this overestimation of the thresholds at the BP86 level of theory increases steadily with the number of CO units removed and for the loss of 9 CO the calculated threshold is more than 3.5 eV above the observed appearance energies. The threshold values calculated at the PBE0 level of theory (PBE0 being a hybrid DFT method), on the other hand, are all in accordance with the observed appearance energies, i.e., below or very close to these. The increasing overestimation of the threshold energies with increasing CO loss at the BP86 level of theory as compared to the PBE0 level is also very apparent in the divergence of these with increasing CO loss in Figure 6. Interestingly, BP86 predicts a lower reaction energy for the formation of the relaxed molecular anion than PBE0 i.e., −3.07 vs. −2.73 eV respectively. Including the ZPE leads to the corresponding adiabatic electron affinity values of 3.11 and 2.77 eV, respectively. The vertical attachment energy on the other hand, is virtually the same for both methods. This is also the case for the formation of $Fe(CO)_3^-$ and the threshold for formation of $Fe(CO)_4^-$ differs only by about 0.1 eV for the two levels of theory (Tab. 3). Hence, where no metal-CO bonds are broken the threshold values predicted at these levels of theory are very close. The considerable overestimation of the threshold values for the CO loss at the BP86 level of theory is thus likely to be either due to overestimation of the metal CO interaction or underestimation of the triple-bond component in the stabilization of CO.

4 Conclusions

We have compared structural parameters for $HFeCo_3(CO)_{12}$ derived from single crystal X-ray diffraction with the corresponding values, calculated at the BP86 level of theory for the neutral and the anionic ground state of this heteronuclear organometallic complex. The agreement of the calculated parameters for the neutral ground state with the X-ray diffraction data is excellent and from the calculations for the relaxed ground state geometry of the anion we can infer a consistent model of the electron attachment process and the dynamics of the following relaxation of the TNI formed. Hence, we find the LUMO of the neutral to be antibonding along the tetrahedral faces connecting the Co_3 base of the metal core with the Fe atom at the apex and the location of the SOMO of the anion and its spin density is to a large extent located at the apical Fe. Accordingly the computed structure of the anionic ground state shows a substantial elongation of two of the three Fe-Co bonds while the above plane, terminal CO group at the remaining Co is transformed into a bridging ligand between this basal Co and the apical Fe atom. Hence, the incoming electron occupies a LUMO, that is antibonding along the Co-Fe bonds and this leads to a relaxed anionic structure with substantially weakened Fe-Co bonds, sizable spin density on the apical Fe, and a new Fe-C(O)-Co bridging bond. This is consistent with our DEA experiments, where $Fe(CO)_4^-$, which is the most logical low-threshold fragment within this picture, is found to be the second most abundant fragment at 0 eV incident energy. Furthermore, these dynamics also agree well with an earlier, time-resolved photo-fragmentation study on the irradiation of $Co_4(CO)_{12}$ at 267 nm and at 400 nm which was found to result primarily in cleavage of the apical-basal Co-Co bond and the formation of new, CO-bridged intermediates [31].

In a second section we presented calculations for the reaction energy for the formation of the molecular anion, the sequential loss of all CO ligands and the loss of the apical Fe as $Fe(CO)_3^-$ and $Fe(CO)_4^-$, and we compare these with the corresponding experimentally determined AEs. In all calculations the geometry optimizations were carried out at the BP86/def2-TZVP level of theory and single point calculations were carried out with the hybrid functional PBE0 and the ma-def2-TZVP basis set. The reaction energies are found to be similar at both levels of theory for the formation of the molecular anion and the formation of $Fe(CO)_3^-$ and $Fe(CO)_4^-$, and to be in accordance with the experimental appearance energies for these processes. However, BP86/def2-TZVP clearly overestimates the reaction energies for the sequential loss of the carbonyl group upon electron attachment. For the loss of 3 CO units from the molecular anion the reaction energy predicted at the BP86 level is already 0.7 eV above the experimental AE and about 1.2 eV above the PBE0 value. For the loss of 6 CO the BP86 value is about 2.0 eV above the AE and 3.0 eV above the PBE0 value and for the loss of 12 CO about 3.3 eV above the AE and about 5.5 eV above the PBE0 value. It is thus evident that the BP86 functional systematically overestimates the reaction energy for the CO loss from the anionic ground state of this compound and also that this effect is cumulative. Hence, either this approach overestimates the metal CO interaction or underestimates the triple-bond component in the stabilization of CO. PBE0 does not suffer from this problem and appears to describe the thermochemistry well. It would be interesting to expand this comparison to other transition metal carbonyls and also to dissociative ionization i.e., to CO loss from a positively charged parent molecule.

It is an honour to have the opportunity to contribute to this special issue in honour of Michael Allan and Steve Buckman, both scientists which extensive work has been defining for their closely related fields of expertise, i.e., electron-molecule and positron-molecule interaction, respectively. Their contribution to the electron and positron community is significant and has taught us that science can be thorough and ambitious but social and good fun at the same time. OI extends his thanks to both Michael Allan and Steve Buckman for their hospitality during his visits at their research groups. This work was supported by the Icelandic Center of Research (RANNIS) Grant No. 13049305(1-3) and the University of Iceland Research

Fund, and was conducted within the framework of the COST Action CM1301; Chemistry for ELectron-Induced NAnofabrication (CELINA). RKTP acknowledges a doctoral grant from the University of Iceland Research Fund and financial support from the COST Action CM1301; CELINA, for short term scientific mission (STSM). RB acknowledges support from the Icelandic Research Fund, Grant No. 141218051. The authors thank F. Biegger for the determination of the crystal structure.

References

1. B.C. Gates, L. Guczi, H. Knözinger, *Metal clusters in catalysis* (Elsevier, Amsterdam, 1986)
2. M. Moskovits, Ann. Rev. Phys. Chem. **42**, 465 (1991)
3. C.L. Czekaj-Korn, G.L. Geoffroy, Transformation of Organometallics into Common and Exotic Materials: Design and Activation **141**, 157 (1988)
4. F. Porrati, M. Pohlit, J. Müller, S. Barth, F. Biegger, C. Gspan, H. Plank, M. Huth, Nanotechnology **26**, 475701 (2015)
5. M. Winhold, C.H. Schwalb, F. Porrati, R. Sachser, A.S. Frangakis, B. Kämpken, A. Terfort, N. Auner, M. Huth, ACS nano **5**, 9675 (2011)
6. F. Porrati, E. Begun, M. Winhold, C.H. Schwalb, R. Sachser, A. Frangakis, M. Huth, Nanotechnology **23**, 185702 (2012)
7. F. Porrati, B. Kämpken, A. Terfort, M. Huth, J. Appl. Phys. **113**, 053707 (2013)
8. R.M. Thorman, R. Kumar T P, D.H. Fairbrother, O. Ingólfsson, Beilstein J. Nanotechnol. **6**, 1904 (2015)
9. N. Silvis-Cividjian, C. Hagen, L. Leunissen, P. Kruit, Microelectron. Eng. **61**, 693 (2002)
10. A. Botman, D. De Winter, J. Mulders, J. Vacuum Sci. Technol. B **26**, 2008 (2008)
11. S. Engmann, M. Stano, Š. Matejčík, O. Ingólfsson, Angew. Chem. Int. Ed. **50**, 9475 (2011)
12. M. Allan, J. Chem. Phys. **134**, 204309 (2011)
13. O. May, D. Kubala, M. Allan, Phys. Chem. Chem. Phys. **14**, 2979 (2012)
14. S. Engmann, M. Stano, Š. Matejčík, O. Ingólfsson, Phys. Chem. Chem. Phys. **14**, 14611 (2012)
15. K. Wnorowski, M. Stano, C. Matias, S. Denifl, W. Barszczewska, Š. Matejčík, Rapid Commun. Mass Spectrom. **26**, 2093 (2012)
16. K. Wnorowski, M. Stano, W. Barszczewska, A. Jówko, Š. Matejčík, Int. J. Mass Spectrom. **314**, 42 (2012)
17. S. Engmann, B. Ómarsson, M. Lacko, M. Stano, Š. Matejčík, O. Ingólfsson, J. Chem. Phys. **138**, 234309 (2013)
18. S. Engmann, M. Stano, P. Papp, M.J. Brunger, Š. Matejčík, O. Ingólfsson, J. Chem. Phys. **138**, 044305 (2013)
19. P. Papp, S. Engmann, M. Kučera, M. Stano, Š. Matejčík, O. Ingólfsson, Int. J. Mass Spectrom. **356**, 24 (2013)
20. M. Lacko, P. Papp, K. Wnorowski, Š. Matejčík, Eur. Phys. J. D **69**, 84 (2015)
21. P. Chini, L. Colli, M. Peraldo, Gazz. Chim. Ital. **90**, 1005 (1960)
22. E. Guglielminotti, D. Osella, P. Stanghellini, J. Organomet. Chem. **281**, 291 (1985)
23. R.G. Teller, R.D. Wilson, R.K. McMullan, T.F. Koetzle, R. Bau, J. Am. Chem. Soc. **100**, 3071 (1978)
24. G.L. Geoffroy, R.A. Epstein, Inorganic Chem. **16**, 2795 (1977)
25. J.C. Kotz, J.V. Petersen, R.C. Reed, J. Organomet. Chem. **120**, 433 (1976)
26. B.M. Peake, B.H. Robinson, J. Simpson, D.J. Watson, Inorganic Chem. **16**, 405 (1977)
27. C.E. Strouse, L.F. Dahl, J. Am. Chem. Soc. **93**, 6032 (1971)
28. G.F. Holland, D.E. Ellis, W.C. Trogler, J. Am. Chem. Soc. **108**, 1884 (1986)
29. G.F. Holland, D.E. Ellis, D.R. Tyler, H.B. Gray, W.C. Trogler, J. Am. Chem. Soc. **109**, 4276 (1987)
30. W.C. Trogler, Acc. Chem. Res. **23**, 239 (1990)
31. J.P. Lomont, S.C. Nguyen, C.B. Harris, Organometallics **31**, 4031 (2012)
32. G.M. Sheldrick, SHELXS-97, Program for Crystal Structure Determination, University of Göttingen, Göttingen (1997)
33. E.H. Bjarnason, B. Ómarsson, S. Engmann, F.H. Ómarsson, O. Ingólfsson, Eur. Phys. J. D **68**, 121 (2014)
34. F. Neese, Wiley Interdiscip. Rev.: Comput. Mol. Sci. **2**, 73 (2012)
35. A.D. Becke, Phys. Rev. A **38**, 3098 (1988)
36. J.P. Perdew, Phys. Rev. B **33**, 8822 (1986)
37. F. Weigend, R. Ahlrichs, Phys. Chem. Chem. Phys. **7**, 3297 (2005)
38. J.P. Perdew, K. Burke, M. Ernzerhof, Phys. Rev. Lett. **77**, 3865 (1996)
39. C. Adamo, V. Barone, J. Chem. Phys. **110**, 6158 (1999)
40. J. Zheng, X. Xu, D.G. Truhlar, Theoret. Chem. Acc. **128**, 295 (2011)
41. S. Grimme, J. Antony, S. Ehrlich, H. Krieg, J. Chem. Phys. **132**, 154104 (2010)
42. S. Grimme, S. Ehrlich, L. Goerigk, J. Comput. Chem. **32**, 1456 (2011)
43. F. Neese, F. Wennmohs, A. Hansen, U. Becker, Chem. Phys. **356**, 98 (2009)
44. W. Humphrey, A. Dalke, K. Schulten, J. Mol. Graphics **14**, 33 (1996)
45. I. Bald, J. Langer, P. Tegeder, O. Ingólfsson, Int. J. Mass Spectrom. **277**, 4 (2008)
46. R. Kumar T P, S. Barth, R. Bjornsson, O. Ingólfsson (2016) (In preparation)

Article II

Formation and decay of negative ion states up to 11 eV above the ionization energy of the nanofabrication precursor $HFeCo_3(CO)_{12}$

Ragesh Kumar T P, Ragnar Bjornsson, Sven Barth and Oddur Ingólfsson.

Chemical Science, **8** 5949-5952 (2017)

Ragesh Kumar T P carried out all the experiments and computations and analysed the data, he wrote the first draft of the paper and contributed to editing until publication.

Chemical Science

EDGE ARTICLE

View Article Online
View Journal | View Issue

Check for updates

Cite this: *Chem. Sci.*, 2017, **8**, 5949

Formation and decay of negative ion states up to 11 eV above the ionization energy of the nanofabrication precursor $HFeCo_3(CO)_{12}$†

Ragesh Kumar T P,[a] Ragnar Bjornsson,[a] Sven Barth[b] and Oddur Ingólfsson*[a]

Received 29th April 2017
Accepted 20th June 2017

DOI: 10.1039/c7sc01927k

rsc.li/chemical-science

In single electron collisions with the heteronuclear metal carbonyl compound $HFeCo_3(CO)_{12}$ we observe the formation of long-lived negative ion states up to about 20 eV, 11 eV above its ionization energy. These transient negative ions (TNIs) relax through dissociation (dissociative electron attachment, DEA), losing up to all 12 CO ligands, demonstrating their resilience towards reemission of the captured electron – even at such very high energies. This is unique in DEA and we hypothesize that this phenomenon is rooted in the orbital structure enabling a scaffold of multi-particle, electronically excited resonances. We support this with calculated MO-diagrams revealing dense bands of energy levels near the HOMO–LUMO gap. $HFeCo_3(CO)_{12}$ is a promising focused electron beam induced deposition (FEBID) precursor and we argue that its unusual DEA behavior relates to its exceptional performance in FEBID. This may be general to a class of molecules with high potential for nano-fabrication by FEBID.

Introduction

The understanding of low energy electron interaction with molecules of different constellation is fundamental to a broad spectrum of processes. These include industrially relevant areas such as plasma physics[1] and nanofabrication[2–4] as well as natural phenomena in atmospheric and astro-chemistry[5,6] and in radiation damage to biologically relevant molecules.[7–9] The formation of transient negative ions (TNIs) through electron capture and their subsequent relaxation through fragmentation, *i.e.*, dissociative electron attachment (DEA),[10,11] is an important aspect of such low energy electron-induced chemistry. This is a resonant process, where electron capture can generally be understood as a vertical transition from the initial neutral molecular state to the resulting negative ion state. The TNI formed may constitute a single particle resonance or a two-particle, core-excited resonance, where the attachment process is concomitant with an electronic excitation within the molecule, *i.e.*, a two-particle-one-hole resonance with two electrons occupying previously vacant orbitals and a single electron vacancy in a lower lying orbital. A relaxation of such a resonance to the neutral ground state through electron emission (autodetachment, AD) is a two-particle process and thus inefficient. Furthermore, when the electronically excited parent state of the neutral is energetically above the TNI state formed, AD leading to the electronically excited parent state cannot proceed without additional energy in the respective AD coordinate. Such resonances, referred to as Feshbach or closed-channel resonances, may thus have comparatively long lifetimes with regards to AD, favoring their relaxation through dissociation, *i.e.*, DEA.

Focused electron beam induced deposition (FEBID)[12,13] is a direct-write nano-fabrication approach where high resolution metal structures may be achieved through a continuous supply of organometallic precursor molecules at a surface being exposed to a tightly focused high energy electron beam. Ideally such precursors fully decompose under the electron beam, leaving a pure metal deposit while the ligands are pumped away. However, incomplete decomposition and deposit broadening is the rule rather than the exception[2,12] and it is generally recognized that the dominant decomposition processes are induced through the interaction of the precursor molecules with low energy secondary electrons produced through the interaction of the high energy beam with the solid substrate, rather than through interaction with the primary beam.[3] Along with dissociative ionization (DI), neutral dissociation (ND) upon electron excitation and dipolar dissociation (DD),[14,15] DEA is an important mechanism of such low energy secondary electron induced decomposition and can proceed with very high cross-sections.[16–18]

$HFeCo_3(CO)_{12}$, a heteronuclear carbonyl-cluster compound, is an emerging FEBID precursor, allowing high purity deposits (>80%) of a Fe/Co metal alloy with potential for controllable magnetic properties.[19] It is thus a very promising candidate for the fabrication of well-defined functional nanostructures.

[a]*Science Institute, University of Iceland, Dunhagi 3, 107 Reykjavik, Iceland. E-mail: oddur@hi.is*

[b]*Institute of Materials Chemistry, Vienna University of Technology, Getreidemarkt 9/BC/02, 1060 Vienna, Austria*

† Electronic supplementary information (ESI) available: Experimental and computational details. See DOI: 10.1039/c7sc01927k

In this context, we have studied low energy electron interaction with this precursor, and we find that with regards to DEA it shows extraordinary behavior, for which we offer an explanation and we argue that this phenomenon should be general for a class of molecules with potential as high performing FEBID precursors.

Results and discussion

Fig. 1 displays the negative ion yield curves for the molecular anion and the loss of 1 and 2 CO ligands from $HFeCo_3(CO)_{12}$ at around 0 eV incident electron energy, while Fig. 2 combines the ion yield curves for sequential loss of 3–12 CO ligands upon electron attachment in the energy range from 0 to about 27 eV. In principle, negative ion fragments may also arise from DD, however, the threshold for the respective DD processes is shifted to higher energies by the ionization energy (IE) of the neutral counterpart in the DEA process. Hence, in the current case, DD should appear about 14 eV (IE of CO) above the respective DEA processes.

As electron attachment is most efficient at very low incident energies, *i.e.* close to 0 eV,[20] it is not surprising that the most efficient channel, the loss of 2 CO, is observed at this energy. In this context, it is important to keep in mind the detection window of the current instrument. Here the extraction time from the ionization region is around 10 μs and the flight time through the quadrupole mass filter about 50 μs. Negative ions that fragment during the flight through the mass filter will not maintain stable trajectories and will not be detected. Thus, we only observe ions that are formed within the first 10 μs after electron capture, but are stable against further fragmentation during their flight through the mass filter. This is reflected in the low yield of the molecular ion and $[M - 1CO]^-$ at 0 eV as compared to $[M - 2CO]^-$. The adiabatic electron affinity of $HFeCo_3(CO)_{12}$ calculated at the PBE0 level of theory is 2.77 eV.[21] This excess energy has to be efficiently distributed within the respective molecular anions for them to be detected in the current experiment. Further, the loss of 1 CO is exothermic by 3.13 eV and the loss of 2 CO by 1.74 eV. This is reflected in the dominating loss of the second CO, as the 3.13 eV available after the loss of one CO result in further dissociation. The 1.74 eV excess energy remaining after the second CO loss is probably lower or close to the threshold for further CO loss and may be distributed as internal and kinetic energy of the departing fragments, increasing the survival probability of $[M - 2CO]^-$ (this fragment has 69 vibrational degrees of freedom).

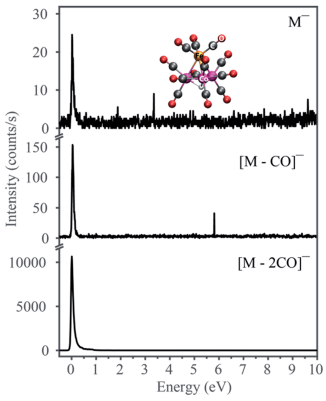

Fig. 1 Negative ion yield curves for the formation of the molecular anion M^- and the fragments $[M - CO]^-$ and $[M - 2CO]^-$. Here M is the neutral molecule $HFeCo_3(CO)_{12}$. The DFT-optimized structure is shown in the top panel.

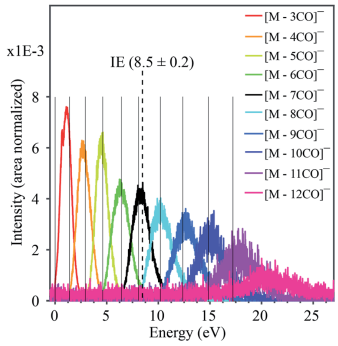

Fig. 2 Combined negative ion yield curves for $[M - nCO]^-$ ($n = 3–12$) formed by DEA to $HFeCo_3(CO)_{12}$ in the energy range 0–27 eV. Solid vertical lines represent the appearance energies of negative ions, *i.e.* the onset of the respective channels. The dotted vertical line shows the molecular ionization energy (IE).[21]

This reflection of the formation probability of the TNI and its decay probability in the ion yields is general to DEA experiments, and readily explainable. However, the further progression of CO loss from the initially formed TNI is extraordinary for four main reasons:

(i) it requires the formation of the TNI more than 11 eV above the ionization limit of the molecule (8.5 eV (ref. 21)),

(ii) the respective TNI must be sufficiently stable with respect to AD to survive the time it takes for dissociation of up to 12 CO units. This is especially intriguing as the energy dependency of the CO loss channels substantiates that this is sequential loss as is discussed here below,

(iii) each fragment shows a distinct energy dependence appearing through a "resonant-like" structure shifted by about 2 eV to higher energy for every CO lost, and

(iv) the attachment of a single electron can trigger the complete decomposition of the ligand structure through loss of all 12 CO.

The formation of negative ion resonances above the ionization limit of the respective molecule is not unheard of, but such resonances are usually only few eV above their IE, and may be explained by inner-shell excitations and high-lying Rydberg states.[17] An exceptional case is the fullerene C_{60}, where the intact TNI is observed up to 14 eV.[22] This is ascribed to electronically excited Feshbach resonances associated with π to π^* transitions and plasmon excitations. For the current molecule, however, the observed ion yields would require a series of two-particle-one-hole resonances extending from the lowest lying HOMO–LUMO transitions up to inner shell excitations extending up to about 20 eV. Furthermore, a close look at the apparent "resonant-like" structure of the ion yields for the individual fragments reveals that the maximum intensity of each fragment, $[M - nCO]^-$, coincides with the onset of the next CO loss, $[M - (n+1)CO]^-$. This is typical for sequential loss, where $[M - nCO]^-$ is the precursor of $[M - (n+1)CO]^-$. This is further substantiated by the approximate 2 eV spacing between the respective contributions, reflecting the expected bond dissociation energy of the CO units.[21] This picture, however, requires a quasi-continuous electron attachment extending from few eV up to about 20 eV. Moreover, the corresponding TNIs formed must be sufficiently stable with regards to AD to allow time for sequential loss of up to 12 CO units, and we emphasize that this is at about 11 eV above the ionization limit of this molecule.

With this in mind we expect that there is a large density of fairly long-lived excited states involved in the initial formation of the TNIs. Direct *ab initio* calculations of the anionic excited states would be ideal to explore these. However, this is impractical, as a proper theoretical description to account for anion states, formed *via* multiple orbital excitations of the neutral molecule, requires a multiconfigurational wave function treatment, which is not currently feasible for such large molecules. Furthermore, calculations of metastable states require inclusion of coupling to the free electron continuum.[23] Instead, we present molecular orbital diagrams from DFT calculations of the neutral $HFeCo_3(CO)_{12}$ at the BP86 level of theory. Though these do not reveal the actual anionic state densities, they do present the molecular orbital structure available to support TNI states in the relevant energy range. For comparison we have calculated MO energy diagrams for the $HFeCo_3$ metal core along with those for the metal carbonyls $Fe(CO)_5$, $W(CO)_6$ and $Co_2(CO)_8$, and the hypothetical, linear carbonyl compound $Co_4(CO)_{12}$ (6 bridging COs). The linear form of $Co_4(CO)_{12}$ was calculated instead of the real cluster form in order to compare to a molecule of similar size as $HFeCo_3(CO)_{12}$ but without metal–metal bonding and featuring more bridging carbonyls. Fig. 3 shows the respective MO energy level diagrams. It is clear that $HFeCo_3(CO)_{12}$ shows dense "bands" of occupied/unoccupied molecular orbitals close to the HOMO–LUMO gap, while the MO structure of $Fe(CO)_5$ and $W(CO)_6$ is much more discrete in this region. $Co_2(CO)_8$, on the other hand, already shows increased density of occupied/unoccupied molecular orbitals close to the HOMO–LUMO gap

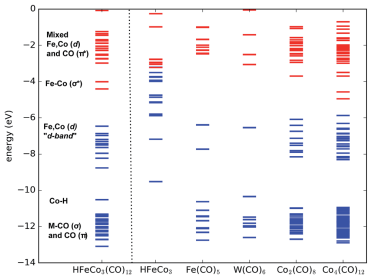

Fig. 3 Molecular (valence) orbital diagram of $HFeCo_3(CO)_{12}$ (left) compared to the $HFeCo_3$ metal core and simpler carbonyl complexes and the hypothetical linear $Co_4(CO)_{12}$. Occupied orbitals are in blue and unoccupied orbitals red. Orbital labels refer to $HFeCo_3(CO)_{12}$.

and the MO diagram for the hypothetical, linear $Co_4(CO)_{12}$ is very similar to that of $HFeCo_3(CO)_{12}$. The metal core alone shows what can be interpreted as an emerging metallic structure with increased density of occupied valence orbitals in close proximity to an emerging "conduction band".

In $HFeCo_3(CO)_{12}$ the highest occupied MOs are mostly metal-based σ-bonding d-orbitals and d-orbitals with some ligand mixing due to metal–carbonyl back-bonding. Below this band there is the bonding Co–H orbital, the metal–carbonyl σ orbitals and the π orbitals within the CO ligands. The unoccupied orbitals include the metal–metal σ^* d-orbitals followed by a dense "band" of ligand CO π^* orbitals. We note that the covalency in the compound results in considerable mixing of the metal d-orbitals and ligand CO π^* orbitals, making orbital excitations between them likely to occur. Further, the polynuclear nature of this compound gives rise to a dense constellation of occupied metal d-orbitals, a "d-band" at the HOMO–LUMO gap. This is absent in the mono-nuclear carbonyls $Fe(CO)_5$ and $W(CO)_6$, but starts emerging in the di-nuclear $Co_2(CO)_8$ and is fully fledged in the hypothetical linear $Co_4(CO)_{12}$. We further note that $HFeCo_3(CO)_{12}$, $Co_4(CO)_{12}$ and $Co_2(CO)_8$ contain 3, 6 and 2 bridging carbonyls, favorably contributing to the mixing of the metal d-orbitals and ligand π^* orbitals.

We note in this context that $Co_2(CO)_8$ has shown good performance in FEBID and Co deposits of purity higher than 90% have been achieved with this precursor[24] (see also ref. 25 and references therein). Similarly, depositions of 75–80 at% in Fe have been achieved with $Fe_2(CO)_9$,[26] a precursor with 3 bridging and 6 terminal carbonyls.

Turning back to Fig. 1 and 2, it is clear that the loss of 1 and 2 CO proceeds through a single particle 0 eV resonance. This is also the case for the low energy side of the $[M - 3CO]^-$ yield, apparent through the double structure of the ion yield curve (see ESI S1†). Below the transition energy between the "d-band" and the dense metal–ligand π^* orbitals, single-particle shape

resonances are likely to dominate (loss of 3 and 4 CO). At higher energies, *i.e.*, above about 3–4 eV, core-excited resonances constituting transitions between the "d-band" and the dense metal–ligand π^* orbitals are bound to play an increasing role. Moreover, these may include multiple electron excitations already at around 7 eV and such multi-particle-multi-hole resonances will dominate at higher energies. At an electron incident energy of about 20 eV, the excess energy is sufficient to induce the transition of 5–6 electrons.

Conclusions

In conclusion, we attribute the unusual DEA behavior of $HFeCo_3(CO)_{12}$ to the combination of the poly-nuclear structure of this organometallic compound and the high number and different nature of carbonyl ligands (bridging and terminal). The former gives rise to a high density of metal-based HOMOs, while the latter gives rise to a high density of unoccupied ligand CO π^* orbitals close to the HOMO–LUMO gap. This and the substantial mixing of these orbitals allows for multiple electronic excitations in conjunction with the electron attachment process, giving rise to long-lived multi-particle-multi-hole resonances at high energies. In conjunction with sub-excitation single-particle resonances at low energies and two-particle-one-hole resonances at intermediate energies, this allows for a quasi-continuous electron attachment from about 1 eV up to about 20 eV – *i.e.*, about 11 eV above the IE of this molecule. This in turn provides sufficient energy for sequential loss of all 12 CO ligands upon attachment of a single electron. Considering the exceptional performance of $HFeCo_3(CO)_{12}$ in FEBID,[19] we argue that its molecular structure and the resulting MO constellation may offer guidance for the design of FEBID precursors allowing high purity metal deposition.

Acknowledgements

This work was supported by the Icelandic Center of Research (RANNIS) Grant No. 13049305(1-3) and the University of Iceland Research Fund. RKTP acknowledges a doctoral grant from the University of Iceland Research Fund and financial support from the COST Action CM1301; CELINA, for short term scientific missions (STSMs). R. B. acknowledges support from the Icelandic Research Fund, Grant No. 141218051.

References

1 L. G. Christophoru, *Electron-Molecule Interactions and their Applications*, Academic Press, Orlando, Florida, 1984.
2 R. M. Thorman, R. K. T P, D. H. Fairbrother and O. Ingólfsson, *Beilstein J. Nanotechnol.*, 2015, **6**, 1904–1926.
3 N. Silvis-Cividjian, C. Hagen, L. Leunissen and P. Kruit, *Microelectron. Eng.*, 2002, **61**, 693–699.
4 S. Bhattarai, A. R. Neureuther and P. P. Naulleau, Advances in Patterning Materials and Processes XXXIII, *Proc. SPIE*, 2016, **9779**, 97790B–97791B.
5 Q.-B. Lu, *Phys. Rep.*, 2010, **487**, 141–167.
6 F. Carelli, M. Satta, T. Grassi and F. Gianturco, *Astrophys. J.*, 2013, **774**, 97.
7 B. Boudaïffa, P. Cloutier, D. Hunting, M. A. Huels and L. Sanche, *Science*, 2000, **287**, 1658–1660.
8 I. Baccarelli, I. Bald, F. A. Gianturco, E. Illenberger and J. Kopyra, *Phys. Rep.*, 2011, **508**, 1–44.
9 L. Sanche, *Eur. Phys. J. D*, 2005, **35**, 367–390.
10 I. Bald, J. Langer, P. Tegeder and O. Ingólfsson, *Int. J. Mater. Sci.*, 2008, **277**, 4–25.
11 O. Ingólfsson, F. Weik and E. Illenberger, *Int. J. Mass Spectrom. Ion Processes*, 1996, **155**, 1–68.
12 I. Utke, P. Hoffmann and J. Melngailis, *J. Vac. Sci. Technol., B: Microelectron. Nanometer Struct.–Process., Meas., Phenom.*, 2008, **26**, 1197–1276.
13 W. Van Dorp and C. Hagen, *J. Appl. Phys.*, 2008, **104**, 081301.
14 E. Böhler, J. Warneke and P. Swiderek, *Chem. Soc. Rev.*, 2013, **42**, 9219–9231.
15 C. R. Arumainayagam, H.-L. Lee, R. B. Nelson, D. R. Haines and R. P. Gunawardane, *Surf. Sci. Rep.*, 2010, **65**, 1–44.
16 S. Engmann, M. Stano, Š. Matejčík and O. Ingólfsson, *Angew. Chem., Int. Ed.*, 2011, **50**, 9475–9477.
17 O. May, D. Kubala and M. Allan, *Phys. Chem. Chem. Phys.*, 2012, **14**, 2979–2982.
18 K. Wnorowski, M. Stano, C. Matias, S. Denifl, W. Barszczewska and Š. Matejčík, *Rapid Commun. Mass Spectrom.*, 2012, **26**, 2093–2098.
19 F. Porrati, M. Pohlit, J. Müller, S. Barth, F. Biegger, C. Gspan, H. Plank and M. Huth, *Nanotechnology*, 2015, **26**, 475701.
20 E. P. Wigner, *Phys. Rev.*, 1948, **73**, 1002.
21 R. K. T P, S. Barth, R. Bjornsson and O. Ingólfsson, *Eur. Phys. J. D*, 2016, **70**, 163.
22 M. Lezius, P. Scheier and T. Märk, *Chem. Phys. Lett.*, 1993, **203**, 232–236.
23 I. I. Fabrikant, S. Eden, N. J. Mason and J. Fedor, in *Advances In Atomic, Molecular, and Optical Physics*, ed. C. C. L. Ennio Arimondo and F. Y. Susanne, Academic Press, 2017, vol. 66, pp. 545–657.
24 L. Serrano-Ramón, R. Córdoba, L. A. Rodríguez, C. s. Magén, E. Snoeck, C. Gatel, I. s. Serrano, M. R. Ibarra and J. M. De Teresa, *ACS Nano*, 2011, **5**, 7781–7787.
25 E. Begun, O. V. Dobrovolskiy, M. Kompaniiets, R. Sachser, C. Gspan, H. Plank and M. Huth, *Nanotechnology*, 2015, **26**, 075301.
26 R. Córdoba, D.-S. Han and B. Koopmans, *Microelectron. Eng.*, 2016, **153**, 60–65.

Article III

Electron Induced Surface Reactions of $HFeCo_3(CO)_{12}$, a Bimetallic Precursor for Focused Electron Beam Induced Deposition (FEBID)

Ragesh Kumar T P, Ilyas Unlu, Sven Barth, Oddur Ingólfsson and D. Howard Fairbrother.

Submitted to The Journal of Physical Chemistry C, 2017

Ragesh Kumar T P carried out all the experiments and contributed for analysing the data, he wrote the first draft of the paper and contributed to editing until submission.

THE JOURNAL OF PHYSICAL CHEMISTRY C

Electron Induced Surface Reactions of $HFeCo_3(CO)_{12}$, a Bimetallic Precursor for Focused Electron Beam Induced Deposition (FEBID)

Ragesh Kumar T P[1], Ilyas Unlu[2], Sven Barth[3], Oddur Ingólfsson[1] and D. Howard Fairbrother[*2]

[1] Science Institute and Department of Chemistry, University of Iceland, Dunhagi 3, 107 Reykjavík, Iceland
[2] Department of Chemistry, Johns Hopkins University, Baltimore, Maryland 21218, United States

[3]TU Wien, Inst. of Materials Chemistry, Getreidemarkt 9/BC/02, A-1060 Wien, Austria.

Corresponding Author: D. Howard Fairbrother howardf@jhu.edu

Abstract

The use of bimetallic precursors in focused electron beam induced deposition (FEBID) allows mixed metal nanostructures with well-defined metal ratios to be generated in a single step process. $HFeCo_3(CO)_{12}$ is an example of one such bimetallic precursor which has previously been shown to form deposits with unusually high metal content (> 80%) as compared to typical FEBID deposits (< 30% metal content). To better understand the elementary bond breaking steps involved in FEBID of $HFeCo_3(CO)_{12}$ we have employed a UHV surface science approach to study the effect of electron irradiation on nanometer thick films of $HFeCo_3(CO)_{12}$ molecules. Using a combination of *in situ* X-ray photoelectron spectroscopy and mass spectrometry we observed that the initial step of electron induced $HFeCo_3(CO)_{12}$ dissociation is accompanied by desorption of ≈75% of the CO ligands from the precursor. A comparison with recent gas phase studies of $HFeCo_3(CO)_{12}$ indicates that this process is consistent with a dissociative ionization process, mediated by the secondary electrons produced by interaction of the primary beam with the substrate. The loss of CO ligands from $HFeCo_3(CO)_{12}$ in the initial dissociation step creates partially decarbonylated intermediates, $HFeCo_3(CO)_x$ ($x_{avg.} \approx 3$). During a typical FEBID process further electron exposure or thermal reactions can further transform these intermediates. In our UHV surface science approach the effect of these two processes can be studied in isolation and identified. Under the influence of further electron irradiation XPS data reveals that the remaining CO ligands in the partially decarbonylated intermediates decompose to form residual carbon and iron oxides, suggesting that those CO ligands which desorbed in the initial step are lost predominantly from the Co atoms. However, annealing experiments demonstrate that CO ligands in the partially decarbonylated intermediates desorb under vacuum conditions at room temperature, leaving behind films that are free of almost any carbon or oxygen contaminants. This combination of efficient CO desorption during the initial dissociation step, followed by thermal CO desorption from the partially decarbonylated $HFeCo_3(CO)_x$ ($x_{avg.} \approx 3$) intermediates provide a rationale for the high metal contents observed in FEBID nanostructures created from $HFeCo_3(CO)_{12}$.

Introduction

Focused electron beam induced deposition (FEBID) [1-2] is a predominantly vacuum-based, direct-write, three dimensional nanofabrication technique based on electron induced dissociation of volatile precursor molecules. In FEBID, a high-energy electron beam is focused onto a substrate and dissociates precursor molecules, transiently adsorbed on the substrate surface, into volatile and nonvolatile fragments. The volatile fragments can be pumped away, while the nonvolatile fragments becoming incorporated into a growing deposit. For metal deposits, volatile organometallics are the most commonly used precursors. Compared to other vacuum based nanofabrication technique like electron beam lithography (EBL), extreme ultraviolet- and ultraviolet lithography (EUVL and UVL, respectively) [3-4], FEBID has several useful advantages. For example, it can directly write an almost unlimited array of free-standing 3-D nanostructures on any substrate, irrespective of its geometry. Moreover, FEBID does not need any resist layer or solvent for deposition[1] and has been successfully used in a number of technological and scientific applications, where conventional lithography is not suitable. For example, using the popular Pt precursor $MeCpPtMe_3$, FEBID has been used to repair photolithography masks [5-7], while $W(CO)_6$, $Co_2(CO)_8$, $MeCpPtMe_3$ precursors have been used to produce custom tips for scanning tunneling [8-9] and atomic force microscopes[10-11], and FEBID of $Me_2Au(acac)$, $W(CO)_6$ and tetra-ethyl-ortho-silicate $Si(OC_2H_5)_4$ precursors has provided a route to fabricate and modify nanophotonic and nanoplasmonic devices [12-14].

In the FEBID applications mentioned above, nanostructures are fabricated using homometallic precursors. Typical homonuclear organometallic precursor used in FEBID include $MeCpPtMe_3$, $Au(acac)Me_2$, $Pt(PF_3)_4$, $W(CO)_6$ and $Co(CO)_3NO$ [1]. However for some FEBID applications such as magnetic data storage, nanoelectronics and information technology it is desirable to fabricate bimetallic alloy nanostructures. The fabrication of bimetallic nanostructures using FEBID is a relatively recent development [15] which has been accomplished principally by co-depositing different metals simultaneously from separate homonuclear precursors using dual or multichannel precursor gas injection systems [16-18]. However, in this approach it is difficult to exert good control over the composition of the deposit and the reproducibility is generally poor [18]. To overcome these limitations, F. Porrati *et al* [19] have, for the first time, used a bimetallic precursor; $HFeCo_3(CO)_{12}$. This volatile organometallic precursor was first synthesized by Chini *et al* [20], and has been used in chemical vapor deposition (CVD)[21] and photochemical vapor deposition (PCVD)[22] to fabricate FeCo thin films. $HFeCo_3(CO)_{12}$ has also been used to prepare magnetic ferrofluids which have applications in magnetically controlled drug targeting[23] as well as building nanoscale devices like nanomotors, nanogenerators and nanopumps [24]. In FEBID, $HFeCo_3(CO)_{12}$ was used to fabricate FeCo magnetic alloy nanostructures with a well-defined metal ratio, matching the stoichiometry of the precursor [19]. Hall magnetometric measurements on 50 nm x 250 nm FeCo nanobars demonstrated that the fabricated FeCo structure was ferromagnetic [19], an important property for building magnetic data storage devices. A potential application for these magnetic data storage devices could be as building blocks in the creation of nano-sized magnetic recordings read/write heads; [25] the current read/write speed of hard disk drive heads is ≈200 Gbit/in^2 and by decreasing the read/write head size to sub 20 nm, the read/write speed could increase to 1000 Gbit/in^2 [25]. Moreover; fundamental investigations on 3D geometries that are not accessible by current crystallisation or other template based techniques can be facilitated by FEBID, opening up the possibility to study the physics of 3D nanomagnets as well as their potential applications [26].

Although FEBID has many attractive features as a direct write strategy for nanofabrication, it has not yet attained its full potential, in large part due to issues such as lateral broadening of deposited structures [27]

and the presence of unacceptable levels of organic impurities in the deposits [1, 28]. With respect to the issue of contamination, several important properties of FEBID deposits such as conductivity [29-31], magnetic behaviour [32] and catalytic activity [29] are adversely affected by the unwanted co-deposition of organic impurities (commonly carbon and oxygen) in the FEBID deposits. The major cause of impurities in the FEBID deposits arises from incomplete removal of ligands during the electron-stimulated deposition of the precursor molecules, although secondary reactions involving residual water and/or hydrocarbons in the deposition chamber also contribute. To date, almost all FEBID precursors were initially designed for CVD, which works on the basis of thermal as opposed to electron induced dissociation [33]. This in turns leaves significant potential for performance improvement in targeted precursors design specifically for electron-induced decomposition in FEBID.

An important step in the design of new precursors specifically tailored for FEBID is to develop a more fundamental understanding of how their electron induced decomposition proceeds. Studies to-date indicate that precursor dissociation is mediated mainly by low energy secondary electrons generated by the interaction of the primary electrons with the substrate/deposit, rather than through direct interaction of precursor molecules with the primary beam [34-36]. These low energy electrons (< ≈100 eV) can cause decomposition of adsorbed precursor molecules through four distinct processes; dissociative electron attachment (DEA), dissociative ionization (DI) and neutral or dipolar dissociation upon electron excitation (ND and DD, respectively) [36-42]. In DEA, a free electron is resonantly captured by the respective molecule to form a transient negative ion (TNI), which then relaxes, either by re-emission of the electron (autodetachment) or by dissociation forming a negative ion and one or more neutral species. DEA is most efficient at very low energies, i.e., around 0 eV [36]. DI, on the other hand, is a non-resonant process with an onset at or above the ionization energy of the molecule and generally reaches a maximum efficiency somewhere between 50 and 100 eV [36]. In DI, the fragments are a positive ion (fragment) and one or more neutrals. ND is also a non-resonant process that sets in at the threshold of the first molecular electronic excitation, producing two or more neutral, mainly radical fragments [36]. However, due to the difficulty in detecting neutral fragments, no direct experimental data on ND of FEBID precursors is currently available. Finally, DD is an inefficient dissociation process initiated by electron excitation(s) within the parent molecules and results in a positive and a negative fragment being formed [36].

The susceptibility of FEBID precursors to these processes can be best studied in the gas phase under single collision conditions, where charged fragments generated from the interaction of electrons with precursor molecules can be identified and their yields determined as a function of the incident electron energy. Importantly, such gas phase studies can differentiate between the individual low energy induced processes and may offer a basis to evaluate their relative efficiency and their branching ratios [36]. Recent gas phase studies on $HFeCo_3(CO)_{12}$ [43-45] have revealed an exceptional behaviour of this compound with regards to DEA, showing a wide range of fragments and attachment cross sections up to energies 11 eV above its ionization energy, where the loss of all 12 CO ligands was observed. However, despite the extensive fragmentation observed in DEA, DI is the more efficient process with regards to the average number of CO molecules lost during $HFeCo_3(CO)_{12}$ fragmentation; in DEA it is 2-3, while in DI it ranges from 4-9 [46].

In the current contribution, we employ a surface science approach under ultra-high vacuum (UHV) conditions to study electron induced surface reactions in nanometer thin films of $HFeCo_3(CO)_{12}$ precursor molecules. The principle techniques used for this study are X-ray photoelectron spectroscopy (XPS) and mass spectrometry (MS), used to monitor changes in the composition and bonding within the film as well as identify neutral gas phase species generated when thin films of $HFeCo_3(CO)_{12}$ are exposed to electrons with incident energies of 500 eV. Compared to gas phase studies, they offer a platform to study the deposition and decomposition of this precursor under condensed phase conditions closer to those in FEBID.

Moreover, the UHV surface science experiments are conducted under cryogenic temperatures (-60 °C) where the evolution of a pre-deposited precursor film can be followed as the electron dose is increased while in FEBID experiments are conducted at room temperature under steady-state conditions with continuous precursor supply. As a result, the UHV surface science approach is better suited to identifying the sequence of elementary reaction steps experienced by precursor molecules during FEBID, including the identification of volatile fragments produced during the deposition process and the concomitant changes to the composition and bonding within the adsorbed precursor molecules. Compared to gas phase studies, surface science studies do not allow differentiation between individual processes such as DEA, DI and DD, because precursor molecules are exposed to simultaneously to secondary electrons with a range of energies. In conjunction with data from gas phase studies, however, these surface science studies have the potential to identify the initial electron induced mechanism of precursor dissociation in FEBID based on the initial step observed in the surface science studies as compared to the different fragments and their relative intensities observed in the gas phase[36].

Previously we have used this UHV surface science approach to study electron reactions (and thermal reactions of intermediate species) of a wide variety of homonuclear organometallic complexes including $MeCpPtMe_3$ [47], $Au(acac)Me_2$ [48], $Pt(PF_3)_4$ [49], $W(CO)_6$ [50], $Co(CO)_3NO$ [51], $(\eta^3\text{-}C_3H_5)Ru(CO)_3Br$ [52] and $cis\text{-}Pt(CO)_2Cl_2$ [53]. In general we have found that electron induced dissociation of precursor molecules proceeds in two steps. In the first step, electron stimulated decomposition of the precursor molecule leads to desorption of some ligands from the adsorbed precursor molecule, leaving behind a metal-containing intermediate bound to the substrate. If this intermediate is subject to further electron irradiation, remaining ligands typically undergo decomposition rather than desorption, and we believe that it is this process, which is the primary cause of organic impurities in FEBID deposits. In some instances, however, these intermediates are susceptible to thermal reactions, which generally leads to further ligand desorption and a concomitant improvement in the metal content. It should be noted that these studies are conducted at low substrate temperatures (typically < - 120°C) and on inert substrates (typically Au and a:C) so that any substrate effects are eliminated/minimized. In support of this assertion we have routinely observed the same electron stimulated processes to occur, independent of the substrate.

The present study of $HFeCo_3(CO)_{12}$ was motivated in part by its use as the first bimetallic FEBID precursor and its exceptional behavior with regards to DEA [19, 44], but also because it offers the ability to follow the fate of two dissimilar metal atoms simultaneously (using XPS) during the elementary reaction steps that underpin FEBID. FEBID deposits created from $HFeCo_3(CO)_{12}$ have also been shown to exhibit metal contents > 80%, much higher than typically observed for homonuclear FEBID precursors [1]. In contrast, FEBID nanostructures created from a similar bimetallic precursor $H_2FeRu_3(CO)_{13}$, in common with most FEBID precursors, exhibit significantly lower metal contents (< 30%) [46]. Consequently, fundamental studies on the elementary reactions of $HFeCo_3(CO)_{12}$ in FEBID may help to shed light on the structural aspects of organometallic precursors that promote efficient and complete ligand desorption and the creation of deposits with higher metal contents.

Experimental

Precursor molecule: The synthesis of $HFeCo_3(CO)_{12}$ was carried out using a procedure slightly modified from the one described by Chini *et al.* [20] All handling and synthesis procedures were carried out under an inert atmosphere using Schlenk and glove box techniques to prevent oxidation. $Co_2(CO)_8$, $Fe(CO)_5$, HCl, DCl, D_2O and acetone were purchased from Sigma Aldrich. Solvents were degassed before use.

In a typical synthesis procedure, 0.50 g (2.6 mmol) $Fe(CO)_5$ and 1.51 g (4.4 mmol) $Co_2(CO)_8$ were combined in a three-neck flask and 4.8 ml acetone was added dropwise. After stirring this dark solution at 40 °C for 2 h the temperature was increased to 60 °C for 12 h. All volatile components were removed under reduced pressure (2 x 10^{-2} mbar; 25 °C) and collected in a cooling trap (liquid N_2). The dark solid residue was dissolved in 10 ml degassed water and filtered in 15 ml HCl conc. (37%), although the yield could be increased by using 5 ml degassed water to transfer most of the complex to the hydrochloric acid. The mixture of the precipitated raw product and HCl was stirred for 1 h at room temperature before the dark purple raw product was separated from the acidic solution via filtration and dried overnight under reduced pressure. Dark purple needles of $HFeCo_3(CO)_{12}$ were obtained after recrystallization from toluene. The products were then kept under dynamic vacuum (~10^{-3} mbar; 25 °C) for 2 h to remove toluene.

Surface Experiments: Electron induced surface reactions were studied by exposing nanometer thick films of $HFeCo_3(CO)_{12}$ under UHV conditions to electrons with a flood gun as the electron source. The electron induced surface reactions were monitored using XPS while gas phase species were identified by MS. More details of the UHV chamber and its capabilities can be found in previous publications [47-48].

Sample handling: To minimize any decomposition of the precursor caused by oxidation the precursor molecules were loaded into a glass finger inside a N_2 glove box, and attached to a UHV compatible leak valve. The leak valve/glass finger assembly was then attached to the UHV chamber containing the XPS and MS. Due to the low volatility of $HFeCo_3(CO)_{12}$ (it volatilizes above 70 °C to provide a chamber pressure in the 10^{-7} Torr regime) we were able to evacuate the glass finger by directly pumping through the UHV leak valve with the compound at room temperature.

Substrate: All XPS and MS experiments were conducted on a polycrystalline gold substrate. Gold was chosen as the substrate because it is chemically inert and none of its XPS peaks overlap with those of the precursor (Fe, Co, C or O). Prior to each experiment, the Au substrate was cleaned by sputtering with 4 keV Ar^+ ions and the substrate surface cleanliness was verified by XPS scans of the C(1s) and O(1s) regions.

Creating $HFeCo_3(CO)_{12}$ films: To volatilize $HFeCo_3(CO)_{12}$, we heated the glass finger to ≈75 ^{0}C. This caused the chamber pressure to increase from ≈7 × 10^{-9} Torr to ≈8 × 10^{-7} Torr. Nanometer thick films of $HFeCo_3(CO)_{12}$ were created by depositing $HFeCo_3(CO)_{12}$ precursor molecules onto sputter cleaned gold substrates at low temperatures (-120 ^{0}C). Depositing $HFeCo_3(CO)_{12}$ films at -120 ^{0}C as opposed to the lowest substrate temperatures that could be attained (-160 ^{0}C) minimized the chance of adsorption from residual water in the UHV chamber and any toluene residual from the synthesis of $HFeCo_3(CO)_{12}$. To create sufficiently thick $HFeCo_3(CO)_{12}$ films, as judged by XPS it was necessary to dose the precursor molecules continuously for 2 h. The thickness of the films were estimated by measuring the signal attenuation from the substrate Au (4f) XPS peak, using an inelastic mean free path of 2 nm for Au (4f) photoelectrons [54]. Typical $HFeCo_3(CO)_{12}$ film thickness ranged from ≈ 1.4 nm to ≈ 1.6 nm. Based on the effective size of the molecule (determined from the computed structure of the molecule [45]) this corresponds to an average coverage of between 1-2 monolayers. Although films were deposited using a substrate temperature of -120 ^{0}C, we increased the substrate temperature from -120 ^{0}C to -60 ^{0}C prior to electron irradiation to ensure that any co-adsorbed water had desorbed prior to electron irradiation.

Electron source: A commercial flood gun (Spec FG 15/40) was used to irradiate the adsorbed precursor molecules. The electron flux was measured by recording the target current on the sample. During any one experiment we maintained a constant electron flux on the surface/film by keeping the target current constant. Electron exposures were reported in terms of the electron dose (electron dose = target current x electron exposure). For electron dose of up to 5.6 × 10^{16} e^-/cm^2, we typically used a target current of 5 μA, while for larger electron doses we used a target current of 30 μA. For all experiments, we used an incident

electron energy of 500 eV. This represents the sum of the electron energy from the flood gun (+480 V) and a positive bias (+20 V), which was applied to prevent the escape of secondary electrons generated by the primary electrons.

X-ray photoelectron spectroscopy: All XPS data was measured by PHI 5400 XPS using Mg Kα X-rays ($h\nu$ = 1253.6 eV). Spectra were deconvoluted using a commercial software (CASA XPS). The binding energies for C(1s), O(1s), Fe(2p) and Co(2p) peaks were calibrated by aligning the Au ($4f_{7/2}$) peak to 84.0 eV. Unless noted all XPS data were acquired at a pass energy of Pass energy of 22.36 eV, 0.125eV/step and 50msec/step.

Mass spectrometry: Gas phase species were monitored with a quadrupole mass spectrometer (Balzers Prisma QMS, 0-200 amu) located ≈ 5 cm from the sample and operating in electron ionization mode (electron energy 70eV)

Results

Figure 1 and Figure 2 show the changes in the C(1s), O(1s), Fe(2p) and Co(2p) XPS regions that occur during the electron irradiation of nanometer thick films of $HFeCo_3(CO)_{12}$. Figure S1 shows that the X-ray irradiation of adsorbed $HFeCo_3(CO)_{12}$ films (needed for XPS analysis) produces a similar change to the C(1s) and O(1s) regions as that produced by 500 eV electrons. This similarity supports the idea that the dissociation of adsorbed $HFeCo_3(CO)_{12}$ precursor molecules is mediated by secondary electrons, in this case produced by X-ray irradiation of the Au substrate. The sensitivity of the $HFeCo_3(CO)_{12}$ film towards secondary electrons produced by the exposed X-rays was determined in a separate control experiments. Analysis of the rate of decrease in O(1s) signal intensity produced by X-ray irradiation (Figure S2) reveals that the time taken for one XPS scan of the C(1s), O(1s), Fe(2p) and Co(2p) regions as shown in Figure 1 corresponds to an electron dose of 9.25×10^{14} e$^-$/cm^2. To reflect this, the electron dose reported in this paper reflects the effective electron dose delivered by the electron gun and the X-ray irradiation. In practice, the effect of X-ray irradiation is only significant for cumulative electron doses $< \approx 2 \times 10^{15}$ e$^-$/cm^2.

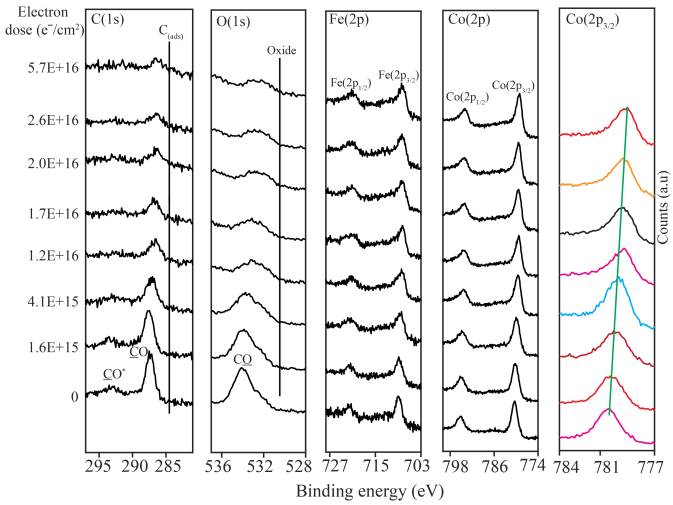

Figure 1. Evolution of the C(1s), O(1s), Fe(2p), Co(2p) and Co($2p_{3/2}$) XPS regions of 1.4 - 1.6 nm thick $HFeCo_3(CO)_{12}$ films exposed to electron doses of $< \approx 5.7 \times 10^{16}$ e⁻/cm². The C(1s), O(1s), Fe(2p) and Co(2p) spectra shown were measured with a pass energy of 22.36 eV; the RHS Co$2p_{3/2}$ region was followed with a pass energy of 11.2 eV.

Prior to electron irradiation, Figure 1 shows that the C(1s) XPS region consists of two peaks centered at 287.6 and 293.2 eV, both indicative of adsorbed carbonyl groups [55-56]. The lower binding energy peak can be assigned to the C(1s) peak of CO species while the higher binding energy peak is a shake up feature caused by a π-π* transition that can accompany the ejection of C(1s) electrons in metal carbonyls [55-56]. The O(1s) region also initially consists of two peaks; an asymmetric peak centered at 534.1 eV associated with the O(1s) peak of CO ligands and a weaker π-π* shake up peak centered at ≈540 eV (not shown) [55-56]. The two peaks initially present within the Fe region at 709 and 722 eV correspond to Fe$2p_{3/2}$ and Fe$2p_{1/2}$ transitions, respectively. Similarly, the two peaks in the Co XPS region centered at 780.4 and 795.1 eV correspond to Co$2p_{3/2}$ and Co$2p_{1/2}$ transitions, respectively. It should also be noted that the C(1s), O(1s), Fe(2p) and Co(2p) XPS spectra shown in Figure 1 prior to electron exposure are consistent with the deposition of molecular $HFeCo_3(CO)_{12}$; for example, the XPS spectral features in the C(1s) and O(1s) regions are due to the presence of carbonyl groups and the cobalt to iron ratio determined from analysis of the Co(2p) and Fe(2p) regions is 3.19, close to the stoichiometric 3:1 ratio of the compound.

For electron doses $< \approx 5.7 \times 10^{16}$ e⁻/cm², Figure 1 demonstrates that the dominant change is the significant decrease in the C(1s) and O(1s) peak areas. As a result, the π-π* shake up feature in the C(1s) region can no longer be detected for electron doses in excess of $\approx 2.6 \times 10^{16}$ e⁻/cm². The peak positions in

the C(1s) and O(1s) regions both shift to lower binding energy as the electron dose increases, although the shape of the peaks remains relatively unchanged. Furthermore, there is no sign of graphitic carbon or the formation of oxide species, evident by the absence of any graphitic carbon (C(1s) peak at ≈ 284.5 eV) or oxide species (peak at ≈ 530.5 eV). The fractional coverage of both carbon and oxygen atoms for electron dose of < 5.7×10^{16} e^-/cm^2 follow the same trend, both decreasing by ≈ 75% (shown as an inset to Figure 3a), while the C:O ratio remains constant. In contrast to the obvious changes in the C(1s) and O(1s) regions, the integrated areas of the peaks in the Fe(2p) and Co(2p) regions remain essentially constant (varying by less than 10%) as a result of electron irradiation, indicating absence of any measureable metal desorption. Although the Fe(2p) peaks remain relatively unaffected, there is a slight broadening and a shift towards higher binding energy with increasing electron dose (total shift is ≈0.23 eV). Due to the higher spectral intensity observed in the Co(2p) region it was possible to follow the changes in this region with a higher energy resolution using a lower pass energy. Results of these experiments, shown in the right-hand side plot of Figure 1, indicate that increasing the electron dose to about 5.7×10^{16} e^-/cm^2 leads to a small but measureable shift in the $Co(2p_{3/2})$ peak position (total shift ≈ 1.3 eV) and a peak shape that becomes increasingly asymmetric. The change in the Co(2p) peak position for these comparatively small electron doses, shown as the insert to Figure 3b is seen to be closely correlated with the decrease in oxygen atom coverage (and therefore by inference also the coverage of carbon atoms).

Figure 2 shows the evolution of the C(1s), O(1s), Fe(2p) and Co(2p) XPS regions for significantly larger electron doses (> 2×10^{17} e^-/cm^2) than those shown in Figure 1. For comparative purposes the spectra of a $HFeCo_3(CO)_{12}$ film prior to electron irradiation is shown as the bottom most spectra. In marked contrast to the behavior observed for smaller electron doses (Figure 1) the integrated areas in both the C(1s) and O(1s) regions remains invariant for electron dose >2×10^{17} e^-/cm^2, as shown in Figure 3(a). However, despite the lack of changes in area there are changes in the spectral profiles in both the C(1s) and O(1s) regions. For example, there is a slow, but systematic decrease in the carbonyl peak centered at 287.6 eV, accompanied by the concomitant appearance and subsequent increase in the intensity of a new peak centered at 284.5 eV, which can be ascribed to graphitic carbon (C_{ads}) [57]. Indeed, Figure 2 shows that after an electron dose of 1.8×10^{18} e^-/cm^2, the C(1s) region is dominated by spectral intensity from graphitic carbon, with almost no observable C signal from remaining CO. In the O(1s) region, these larger electron doses cause the peak to broaden and shift to lower binding energy with a peak at ≈ 530.5 eV becoming increasingly prevalent. This new lower binding energy peak is consistent with the formation of an oxide; this assertion is supported by the observation of the same peak when a $HFeCo_3(CO)_{12}$ film was exposed to an extremely large electron dose (2.1×10^{18} e^-/cm^2) in the presence of residual water vapor in the background (see Figure S3). The observation of oxide species in the O(1s) region is also coincident with a visible broadening of the Fe(2p) peak to higher binding energy, indicative of the formation of iron oxides. In contrast, there was no measurable changes in the Co(2p) XPS region, including the $Co(2p_{3/2})$ peak position (Figure 3(b)). Analysis of Figure 3 reveals that the changes to the C(1s), O(1s) and Fe(2p) regions observed in Figure 2 (1.8×10^{18} e^-/cm^2 < electron doses > 2×10^{17} e^-/cm^2) occur for electron doses that are at least an order of magnitude greater than those responsible for the changes in Figure 1 (electron doses < 5.7×10^{16} e^-/cm^2). Figure 3c shows that the fractional decrease in coverage of oxygen atoms seen for $HFeCo_3(CO)_{12}$ in this study is also very similar in magnitude and rate to the one observed for another recently studied bimetallic compound, $H_2FeRu_3(CO)_{13}$, [46] during electron exposure.

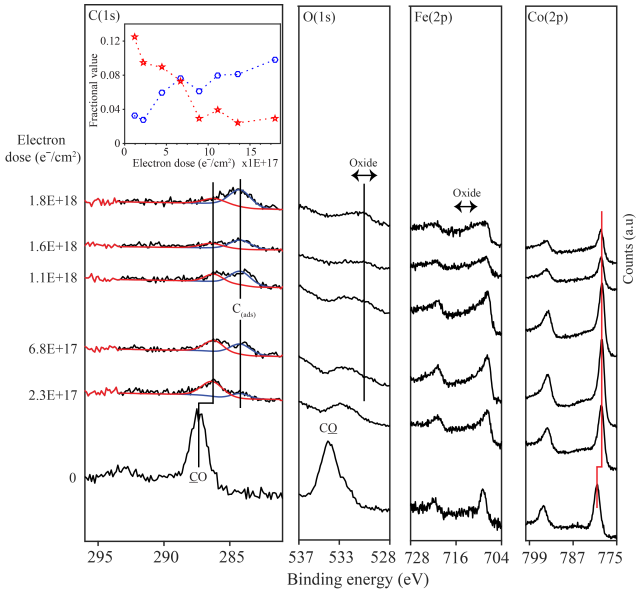

Figure 2. Evolution of the C(1s), O(1s), Fe(2p) and Co(2p) XPS regions of 1.4 - 1.6 nm thick $HFeCo_3(CO)_{12}$ films, exposed to electron dose > 2×10^{17} e^-/cm^2. The insert in the C(1s) region shows the fractional change in the coverage of carbonyl (red stars) and graphitic carbon atoms (open blue circles) for these larger electron doses; carbon areas have been normalized to the XPS signal initially observed in the C(1s) region prior to any electron irradiation.

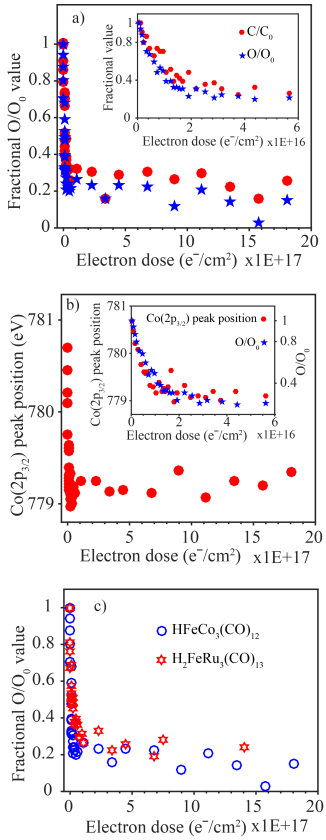

Figure 3. Change in (a) fractional coverage of carbon and oxygen atoms and (b) Co($2p_{3/2}$) peak position for 1.4 - 1.6 nm thick $HFeCo_3(CO)_{12}$ films, as a function of electron dose. The insets in (a) and (b) show the corresponding changes to the fractional coverage of carbon and oxygen atoms as well as the Co($2p_{3/2}$) peak position for the comparatively small electron doses (< 6×10^{16} e^-/cm^2) shown in Figure 1. Figure 3c) compares the change in fractional coverage of oxygen atoms for $HFeCo_3(CO)_{12}$ and $H_2FeRu_3(CO)_{13}$ films

exposed to 500 eV electrons, both plotted as a function of electron dose ($H_2FeRu_3(CO)_{13}$ data from ref. [46]).

Figure 4 compares mass spectra (0 – 100 amu) observed from (top) gas phase $HFeCo_3(CO)_{12}$ and (bottom) during the electron irradiation of adsorbed $HFeCo_3(CO)_{12}$ molecules. The most intense peaks observed in the mass spectrum of gas phase $HFeCo_3(CO)_{12}$ were CO (28), C (12) and O (16), along with smaller peaks at Fe (56), FeCO (84) and water vapor residual in the UHV chamber. Peaks marked with a star originate from toluene, used in the synthesis of $HFeCo_3(CO)_{12}$. During the electron beam irradiation of adsorbed $HFeCo_3(CO)_{12}$ films, the only peaks observed where associated with CO (28,12 and 16), along with a small contribution from residual water vapor. The absence of any discernible Fe or FeCO peaks supports the findings from the XPS (see Figure 1 and 2) that electron irradiation does not cause any desorption of metal-containing fragments from adsorbed $HFeCo_3(CO)_{12}$ molecules.

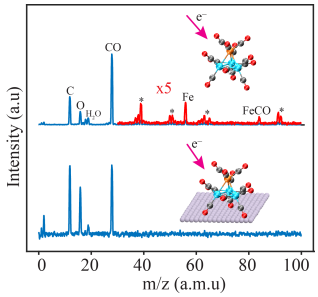

Figure 4. Mass spectrum (0 - 100 amu) of (top) gas phase $HFeCo_3(CO)_{12}$ and (bottom) during the electron irradiation of an $HFeCo_3(CO)_{12}$ film. No fragments were observed between 100-200 amu. The bottom spectra represent the average of five mass spectra recorded during an electron dose of 3.2×10^{16} e^-/cm^2.

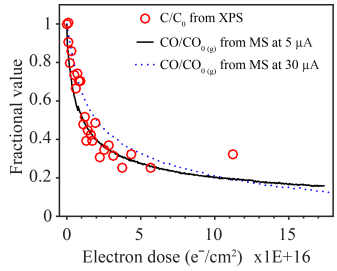

Figure 5. Kinetics of CO desorption observed during irradiation of 1.4 - 1.6 nm thick $HFeCo_3(CO)_{12}$ film (monitored at m/z = 12 (C)), plotted as a function of electron dose at a target current of 5 μA (black solid line) and 30 μA (blue dotted line). Also shown is the fractional coverage of carbon atoms, determined by XPS data from Figure 1 (red circles).

Figure 5 shows the normalized CO desorption kinetics observed during the electron irradiation of $HFeCo_3(CO)_{12}$ films using two different target currents (5 and 30 μA), plotted in terms of the total electron dose (electron dose = target current × time). The CO desorption kinetics were monitored by following changes in the signal at m/z = 12 (C) whose signal originates exclusively from CO. The rate of CO desorption from the film is observed to be greatest at the onset of irradiation and decreases to background levels once an electron dose of ≈ 3×10^{16} e^-/cm^2 is reached. Moreover, the CO desorption kinetics for the two target currents, when plotted in terms of the total electron dose, are seen to be very similar to one another. Figure 5 also shows that the rate of CO desorption from the film is closely correlated with the rate of loss of carbon atoms (and therefore by inference oxygen atoms) from the films observed by XPS.

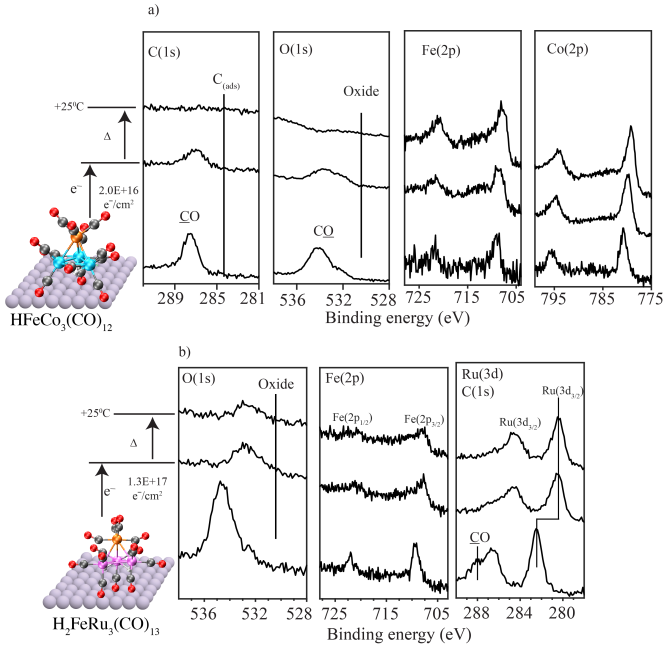

Figure 6. (a) Changes in the C(1s), O(1s), Fe(2p) and Co(2p) XPS regions when a 1.4 to 1.6 nm thick $HFeCo_3(CO)_{12}$ film was exposed to an electron dose of 2.0×10^{16} e^-/cm^2 (middle set of spectra) and then subsequently heated to room temperature (25 ^{0}C) (uppermost set of spectra), (b) Changes in O(1s), Fe(2p) and Ru(3d)/C(1s) region for a 1.1 to 1.4 nm thick $H_2FeRu_3(CO)_{13}$ film first irradiated to 1.3×10^{17} e^-/cm^2 (middle set of spectra) and then annealed to RT (uppermost set of spectra), adapted from ref. [46]. For both molecules the films were adsorbed on a gold surface.

Figure 6a shows the changes in the C(1s), O(1s), Fe(2p) and Co(2p) XPS regions that occur when a $HFeCo_3(CO)_{12}$ film initially adsorbed at -60 ^{0}C was exposed to an electron dose of 2.0×10^{16} e^-/cm^2 and then subsequently annealed to RT (25 ^{0}C). An electron dose of 2.0×10^{16} e^-/cm^2 was chosen because it corresponds to the smallest electron dose required to cause all of the electron induced desorption of carbon and oxygen atoms from $HFeCo_3(CO)_{12}$ films as determined by XPS (see Figure 3a). Changes in the C(1s) and O(1s) XPS regions after an electron dose of 2.0×10^{16} e^-/cm^2 are similar to those reported in Figure 1, with a significant decrease in the C(1s) and O(1s) XPS peak areas. The uppermost spectra in Figure 6a show that upon annealing this electron irradiated film, all of the residual intensity in the C(1s) and O(1s) regions disappears and only signal intensity in the metallic Co(2p) and Fe(2p) regions remains.

In Figure 6b we compare the experiment shown in Figure 6a with the recent results of an analogous experiment conducted using $H_2FeRu_3(CO)_{13}$[46]. In the case of $H_2FeRu_3(CO)_{13}$, an electron dose of 1.3×10^{17} e^-/cm^2 was found to be sufficient to complete the initial stage of reaction, where the O(1s) intensity was reduced by ≈70% of its initial value (see Figure 3c). As discussed previously this fractional decrease in the O(1s) signal is comparable to that observed in the present study of $HFeCo_3(CO)_{12}$. However, upon annealing the irradiated $H_2FeRu_3(CO)_{13}$ film to room temperature it retains measureable O(1s) intensity. This is in contrast to the loss of all O(1s) intensity for the irradiated $HFeCo_3(CO)_{12}$ film (compare the uppermost O(1s) spectra in Figure 6(a) and 6(b)).

Discussion

Based on our XPS and MS measurements, the electron induced surface reactions of $HFeCo_3(CO)_{12}$ can be partitioned into two stages. In the first stage, which occurs for electron doses of $< \approx 5.7 \times 10^{16}$ e^-/cm^2, the transformation is dominated by significant decreases in the C(1s) and O(1s) XPS peak areas accompanied by CO desorption. The second stage of the reaction occurs for electron dose $> \approx 5.7 \times 10^{16}$ e^-/cm^2. In this stage, the residual carbon and oxygen coverage remain almost constant, although changes do occur to the oxygen, carbon and iron containing species. In the following sections, we will discuss these two stages of the reaction and their relationship to the FEBID process in more detail

First step: Electron stimulated CO desorption / precursor deposition: The initial interaction of electrons with adsorbed $HFeCo_3(CO)_{12}$ molecules leads to significant CO desorption. Schematically we can represent this step as shown in Figure 7:

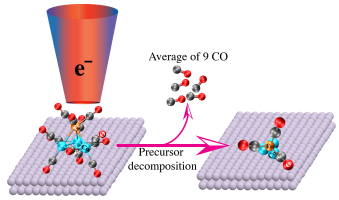

Figure 7. Schematic for electron induced dissociation of adsorbed $HFeCo_3(CO)_{12}$

The loss of CO is observed directly by mass spectrometry in Figure 5, and it is CO desorption which is responsible for the loss of intensity in the O(1s) and C(1s) peak areas shown in Figures 1 and 3. The loss of CO is further supported by the observation in XPS that although the peak areas decrease, the O:C ratio remains constant. Moreover, the loss of carbon and oxygen observed by XPS is coincident with the rate of CO desorption (Figure 5). Analysis of the C(1s) and O(1s) regions during this initial step also reveals an absence of any graphitic carbon or oxide species, indicating that CO desorption from the parent (precursor) occurs in the absence of CO decomposition. The extent of CO desorption can be determined by noting that during this initial stage of the reaction the carbon and oxygen signals both decrease to ≈ 25% of their initial values. Based on the stoichiometry of the precursor ($HFeCo_3(CO)_{12}$), this indicates that on average each precursor molecule loses 9 of its initial 12 CO ligands.

CO desorption from the precursor under the influence of electron irradiation would cause the adsorbed $HFeCo_3(CO)_{12}$ molecules to transform into partially decarbonylated species with an average stoichiometry of $HFeCo_3(CO)_3$ as shown in Figure 7. This loss of CO ligands as the precursor is transformed into a partially decarbonylated intermediate is reflected in the increasingly asymmetric peak shape and decrease in binding energy in the Co ($2p_{3/2}$) peak from 780.4 to 779.1 eV (Figure 1), which is closer to the binding energy and asymmetric peak shape associated with metallic Co ($2p_{3/2}$ binding energy of 778.3 eV)[57]. Consistent with this assertion, Figure 3 shows that the shift in the Co($2p_{3/2}$) peak position occurs concomitantly with the loss of C and O from the film. The significantly lower signal-to-noise (see Figure 1) prevented us from conducting the same detailed analysis in the Fe(2p) region.

In separate experiments, we studied $DFeCo_3(CO)_{12}$ in an attempt to probe the fate of the hydrogen atoms using mass spectrometry. However, the signal at mass 2 was dominated by contributions from residual H_2 in the UHV chamber and the mass 4 signal from D_2 was inconsistent. Consequently, we are not able to make a definitive statement as to the fate of the hydrogen atom in the precursor, although in gas phase experiments the hydrogen is found to stay attached to the metal atoms during electron exposure and fragmentation[46] and we therefore presume the same is the case here.

In relationship to FEBID, this initial interaction of electrons with adsorbed $HFeCo_3(CO)_{12}$ molecules corresponds to the event that will convert the molecular precursor into a nonvolatile, partially decarbonylated species while the CO ligands lost from the precursor will be pumped away. This first step is analogous to reactions we have observed with other FEBID precursors like $Co(CO)_3NO$ [51] and $W(CO)_6$ [50], characterized by partial ligand (CO) desorption. What is particularly noteworthy in this study is the

extent of CO desorption; our results indicate that $HFeCo_3(CO)_{12}$ loses on average 75% of its 12 CO ligands in the initial step. In contrast, no more than 50% of the CO groups in $W(CO)_6$ and $Co(CO)_3NO$ desorb when these FEBID precursors decompose under the influence of electron irradiation. In terms of the reaction cross-section we note that precursor decomposition is complete by $\approx 5 \times 10^{16} e^-/cm^2$. This is similar to values we have measured before for other carbonyl precursors. For example, CO desorption from $W(CO)_6$ and $Co(CO)_3NO$ was complete after an electron dose of $\approx 5 \times 10^{16}$ e^-/cm^2 and 6.2×10^{16} e^-/cm^2. Thus, results from the present study add to the body of data suggesting that although the nature and extent of ligand desorption is precursor dependent, the rate of electron stimulated precursor decomposition is relatively constant.

In the UHV surface science studies, electron induced precursor dissociation takes place under a pseudo precursor limited regime, since there is no supply of precursor molecules during electron irradiation. In this precursor-limited regime, Figure 5 shows that the rate of electron induced precursor decomposition that leads to CO desorption depends only on the electron dose and is invariant to electron flux. This indicates that the initial electron induced decomposition step for $HFeCo_3(CO)_3$ is, as expected a single(one) electron process.

The extent of CO desorption also provides a basis to identify the underlying mechanism responsible for the precursor's decomposition. In FEBID it is widely accepted that the precursor molecules react with the secondary electrons generated by the interaction of the primary beam with the substrate, rather than directly with the primary electron beam [34-35]. In surface science studies different electron stimulated decomposition mechanisms (e.g. DEA vs DI) cannot be differentiated because precursor molecules are exposed simultaneously to secondary electrons with a wide range of energies, predominantly in the regime between 0-100 eV. However, this limitation does not exist in gas phase studies where fragments are generated under single collision conditions when electrons of well-defined energies interact with precursor molecules. A recent gas phase study of the $HFeCo_3(CO)_{12}$ molecule [44-46] carried out using a crossed electron/molecule collision set up under single collision conditions has shown that an average of 2 to 3 CO ligands are lost from the molecule through DEA, while DI of $HFeCo_3(CO)_{12}$ molecules at 70 eV leads to 4 to 9 CO ligands desorbing [46]. In DI and DEA charged fragments are detected and the lower limit of CO loss for either process is calculated by assuming that the neutral fragment stays intact, while the upper limit presumes total CO loss from the neutral fragment. It is clear from the current surface experiments that metal containing fragments are not desorbing from the surface. Thus, through comparison of the average CO loss in DEA and DI of $HFeCo_3(CO)_{12}$ in the gas phase, with the initial CO loss observed here, it appears more likely that the initial electron induced dissociation of adsorbed $HFeCo_3(CO)_{12}$ molecules proceeds through DI rather than DEA. Comparisons of gas phase and surface experiments of other organometallic FEBID precursors has indicated that some precursors react predominantly through DEA ($MeCpPt^{IV}Me_3$ [47, 58], $Pt(PF_3)_4$ [49, 59]), while others appear to be best described as a combination of DEA and DI processes ($W(CO)_6$ [50, 60], $Co(CO)_3NO$ [51, 61]). In contrast, the bimetallic $HFeCo_3(CO)_{12}$ appears to decompose predominantly via DI. Similarly, another bimetallic precursor molecule $H_2FeRu_3(CO)_{13}$ also appears to decompose through DI [46]. We however note, that the extent of neutral dissociation is not known for these precursors. It should also be noted that in principle surface induced dissociation of initially formed intermediates may occur and this would compromise direct comparisons between gas phase and surface science studies [62].

Gas phase studies can also be analyzed to determine the potential significance of metal-metal bond rupture during the initial decomposition of the bimetallic precursor. Indeed, metal-metal bond cleavage is significant in DI of $HFeCo_3(CO)_{12}$ [46]. The total branching ratio for metal-metal bond ruptures is about 0.5, with $Fe(CO)_n^+$ (n = 0-5) being the most significant species. In the UHV surface science approach

employed in this study, MS and XPS data provide information on the average number of CO molecules desorbing and the resultant stoichiometric change in the $HFeCo_3(CO)_{12}$ film. If we assume that CO ligands are lost from $HFeCo_3(CO)_{12}$ via DI due to electronic excitation/ionization then we are observing a statistical process where the adsorbates present after initial electron induced dissociation of $HFeCo_3(CO)_{12}$ will be a mixture of partially decarbonylated species such as $HFeCo_3(CO)_2$, $HFeCo_3(CO)_3$, $HFeCo_3(CO)_4$ and $HFeCo_3(CO)_5$ etc., producing a film with an overall stoichiometry of $HFeCo_3(CO)_3$. Examples of these intermediates are shown in Figures 7 – 10. However, it should be noted that these intermediates could include species where metal-metal bond cleavage also occurred during precursor decomposition (e.g. $HFeCo_3(CO)_3$ could also include $HFe(CO)_3$ and 3Co).

Second step:

(a) Electron stimulated CO decomposition: When CO desorption is complete at an electron dose of ≈ $5.7 \times 10^{16} e^-/cm^2$, the precursor $HFeCo_3(CO)_{12}$ molecules have on average lost 9 of their 12 CO ligands and been converted into a partially decarbonylated intermediates with an average stoichiometry of $HFeCo_3(CO)_3$. Upon further increase in the electron dose (> $5.7 \times 10^{16} e^-/cm^2$), the XPS data in Figure 2 indicate that the residual CO groups undergo electron-stimulated decomposition thus:

$$CO_{(ads)} + e^- \rightarrow C_{(ads)} + O^{2-}{}_{(ads)} \quad (1)$$

This transformation is shown most clearly in the C(1s) region of Figure 2 where the decrease in the CO peak is accompanied by a concomitant increase in the coverage of C(ads) species. Once an electron dose of ≈$1.8 \times 10^{18} e^-/cm^2$ is reached, Figure 2 shows that the peak in the C(1s) region from the CO ligands has almost completely disappeared and the C_{ads} peak dominates; this represents the conclusion of the electron stimulated reactions. Consistent with equation (1) there is no change in the integrated areas within either the C(1s) or O(1s) regions during this phase of the reaction. The formation of oxide species is most clearly evidenced by the formation of iron oxides, shown in Figure 2. Interestingly there is no change in the Co(2p) peak profile, indicating that oxidation occurs exclusively to the iron atoms. The lack of any change in the O(1s) area in this second stage of the reaction also supports the idea that iron oxidation is exclusively a result of CO decomposition, and not a result of reactions between iron atoms and oxygen containing species in the vacuum chamber, a process which would be expected to increase the O(1s) signal intensity. Thus, the overall process of electron stimulated CO decomposition can be represented schematically by Figure 8 and by the reaction:

$$HFeCo_3(CO)_{3(ads)} + e^- \rightarrow HFe^{x+}O_yCo_{3(ads)} + C_{(ads)} \quad (2)$$

The exclusivity of iron oxidation despite the presence of three times more Co atoms in the precursor also suggests that the residual CO ligands in the partially decarbonylated intermediates are bound predominantly and potentially exclusively to the lone Fe atom.

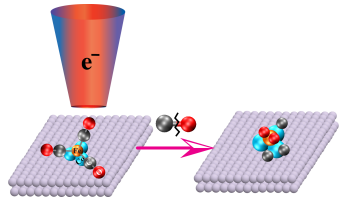

Figure 8. Schematic showing the electron stimulated CO decomposition of a partially decarbonylated $HFeCo_3(CO)_{12}$ intermediate.

(b) Thermal reactions: The overarching objective of this work is to better understand the elementary bond breaking reactions that occur during FEBID of the bimetallic precursor, $HFeCo_3(CO)_{12}$. In FEBID, the initial deposition event must be induced by electron-stimulated reactions with adsorbed precursor molecules, otherwise nanostructures could not be directly written by the incident electron beam. However, once precursor deposition has occurred (the first stage in the reaction) any intermediates formed during the deposition step could be subject either to further electron stimulated reactions (part (a) above) or thermal reactions. However, in the present UHV surface science study the partially decarbonylated intermediates are created at a substrate temperature of -60 ^{0}C, while typical FEBID occurs at ambient temperatures. The relative importance and impact of any thermal reactions was therefore addressed by first exposing $HFeCo_3(CO)_{12}$ molecules adsorbed at -60 ^{0}C to an electron dose just sufficient to complete the first stage of reaction and create partially decarbonylated intermediates on the surface, before annealing these species to room temperature in the absence of any further electron irradiation. Results from these studies, shown in Figure 6a, demonstrate that almost all of the CO ligands in the partially decarbonylated intermediate desorb when the substrate is annealed to room temperature, leaving behind only cobalt and iron atoms from the precursor molecule. The overall process is shown in Figure 9 and represented by the following equation:

$$HFeCo_3(CO)_{3(ads)} + \Delta \rightarrow HFeCo_{3(ads)} + 3CO_{(g)} \qquad (3)$$

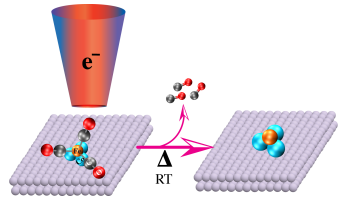

Figure 9. Effect of annealing a partially decarbonylated $HFeCo_3(CO)_{12}$ intermediate to room temperature (RT), showing the resultant CO desorption.

In this respect, the propensity for thermal desorption over thermal decomposition of the CO ligands in the partially decarbonylated intermediates is in accord with the low levels (2 – 5%) of residual carbon and oxygen observed in conformal deposits created by the thermal dissociation of $HFeCo_3(CO)_{12}$ at 200° C [21].

Overall relationship between UHV surface science data and FEBID:

In FEBID of $HFeCo_3(CO)_{12}$, the initial event is adsorption of precursor molecules onto the surface:

$$HFeCo_3(CO)_{12\ (g)} \leftrightarrow HFeCo_3(CO)_{12\ (ads)} \quad (4)$$

The next step involves precursor decomposition, analogous to the first step identified in the present study (see Figure 7), which we have shown involves a single electron process leading to extensive CO desorption and the formation of a surface bound, partially decarbonylated intermediate, most likely through dissociative ionization of the parent molecule, thus:

$$HFeCo_3(CO)_{12\ (ads)} + e^- \rightarrow HFeCo_3(CO)_{3\ (ads)} + 9CO_{\ (g)} \quad (5)$$

At this stage of FEBID, the partially decarbonylated intermediates thus formed can undergo one of two processes; further electron stimulated reactions, which can lead to decomposition of the residual CO ligands (see Figure 8):

$$HFeCo_3(CO)_{3\ (ads)} + e^- \rightarrow HFe^{x+}OyCo_{3\ (ads)} + C_{(ads)} \quad (6)$$

or thermal reactions initiating further CO desorption as shown in Figure 6a, and schematically in Figure 9:

$$HFeCo_3(CO)_{3\ (ads)} + \Delta \rightarrow HFeCo_{3(ads)} + 3CO_{(g)} \quad (7)$$

The initial decomposition step as well as the subsequent competition between electron stimulated decomposition or thermal desorption of residual CO groups in the partially decarbonylated intermediates is shown schematically in Figure 10.

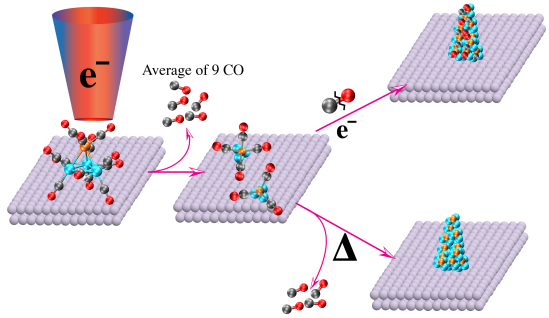

Figure 10. Schematic showing the electron induced decomposition of $HFeCo_3(CO)_{12}$ and the competition between electron stimulated decomposition or thermal desorption of CO ligands from the partially decarbonylated intermediates produced by precursor decomposition.

In a typical FEBID experiment deposition is occurring under steady state conditions in the presence of a constant flux of precursor molecules and electrons. Under these conditions the fate of the $HFeCo_3(CO)_3$ intermediates produced by the decomposition of the precursor will depend on the relative rates of the electron and thermally stimulated reactions (reactions (6) and (7) above). Although our UHV experiments

do not provide a direct measure of these relative rates we note that the rate of electron stimulated decomposition for the partially decarbonylated intermediates (step 2) is significantly slower than that of the initial electron stimulated decomposition of the parent $HFeCo_3(CO)_{12}$ molecule (step 1). Thus, step 1 requires an electron dose $\approx 6 \times 10^{16}$ e$^-$/cm^2, while the electron stimulated decomposition of the resultant decarbonylated intermediate is only complete after an electron dose of $> 1 \times 10^{18}$ e$^-$/cm^2. The relative inefficiency of electron stimulated decomposition of the $HFeCo_3(CO)_3$ (s) intermediates (step 2) is most clearly evidenced in Figure 2 where XPS analysis shows that after an electron dose of $\approx 5.7 \times 10^{16}$ e$^-$/cm^2 all of the precursor molecules have decomposed and yet the adsorbate layer shows no evidence of any CO decomposition, as evidenced by the lack of any C(ads) or oxide species. In contrast, if the rate of electron stimulated decomposition of the $HFeCo_3(CO)_3$(ads) intermediate was occurring at a similar rate to the electron stimulated decomposition of the $HFeCo_3(CO)_{12}$(ads) parent molecules, we would expect to see evidence of some C(ads) and oxide species at a point in the reaction co-ordinate where all of the parent molecules have decomposed. This relative inefficiency of the electron stimulated decomposition of the partially decarbonylated $HFeCo_3(CO)_3$(s) species (step 2) as compared to the initial precursor decomposition (step 1) suggests that once the partially decarbonylated intermediates are produced, thermal reactions are likely to play an important role in determining their ultimate fate. Under these conditions the overall reactivity of the $HFeCo_3(CO)_{12}$ precursor will be dominated by the following sequence of elementary reaction steps (shown schematically by the lower reaction pathway in Figure 7):

$$HFeCo_3(CO)_{12\ (ads)} + e^- \rightarrow HFeCo_3(CO)_{3\ (ads)} + 9CO_{(g)} \quad (5)$$

$$HFeCo_3(CO)_{3\ (ads)} + \Delta \rightarrow HFeCo_{3(ads)} + 3CO_{(g)} \quad (7)$$

In qualitative agreement with this mechanism of reaction, FEBID deposits created from $HFeCo_3(CO)_{12}$ have been shown to exhibit metal contents > 80%, indicative of a process where further reactions of intermediate species are dominated by thermal desorption of residual ligands as opposed to electron stimulated decomposition.

Another difference between the present study and typical FEBID experiments is the energy of the primary electrons. In the present study 500eV primary electrons are used while in FEBID the incident electron energies are typically > 10keV. It is widely accepted that the low energy secondary electrons (> 100eV) generated by the interaction of the primary beam with the substrate are responsible for the electron induced chemistry and changing the primary beam energy will alter the relative intensity and energy distribution of the secondary electrons. This in turn will alter the rates of electron stimulated reactions but will not change the fundamental bond breaking nature of the reactions themselves.

Contrasting $HFeCo_3(CO)_{12}$ with other FEBID Precursors:

In a recent publication we have discussed gas phase fragmentation, electron induced surface reactions and FEBID of the similar precursor $H_2FeRu_3(CO)_{13}$ [46]. Interestingly, the extent of CO desorption from $HFeCo_3(CO)_{12}$ and $H_2FeRu_3(CO)_{13}$ during the initial electron stimulated decomposition of these two bimetallic precursors is similar. For $H_2FeRu_3(CO)_{13}$, the fractional decrease in the O(1s) signal indicates that on average 8-9 of the 13 CO ligands desorb, supported by MS data as well as changes in both the O(1s) and C(1s) regions [46]. This is comparable to the average loss of 9 CO groups from $HFeCo_3(CO)_{12}$ during decomposition.

Despite this similarity, however, FEBID deposits made from $HFeCo_3(CO)_{12}$ have metal contents > 80% while FEBID deposits made from $H_2FeRu_3(CO)_{13}$ have metal contents < 30% [46]. The root cause for the

different performance of $HFeCo_3(CO)_{12}$ and $H_2FeRu_3(CO)_{13}$ in FEBID is clearly not a consequence of the efficiency of CO desorption in the initial electron induced dissociation process.

The difference in the behavior between these two precursors in FEBID appears to lie in the relative thermal stability of the CO groups within the partially decarbonylated intermediates created when the precursors decompose. Accordingly, Figure 6 demonstrates that while all of the CO groups in the $HFeCo_3(CO)_3$ intermediate are thermally unstable with respect to desorption at room temperature, a significant fraction of the CO groups in the $H_2FeRu_3(CO)_x$ ($x \approx 4,5$) intermediates are stable at room temperature and can therefore become incorporated into the deposit as it grows during FEBID [46]. This comparison supports our assertion that the second step, the thermal desorption of the intact CO groups from the initially created $HFeCo_3(CO)_x$ ($x_{avrg} \approx 3$) intermediates at room temperature is critical for the formation of the high metal content deposits achieved in FEBID with $HFeCo_3(CO)_{12}$.

The performance of $HFeCo_3(CO)_{12}$ as a FEBID precursor can also be compared with other CO containing precursors we have studied under UHV surface science conditions, notably $W(CO)_6$ [50] and $Co(CO)_3NO$ [51]. For $W(CO)_6$, the initial decomposition step is comparatively inefficient compared to $HFeCo_3(CO)_{12}$, with less than 50% of the CO groups desorbing. Moreover, the residual partially decarbonylated $W(CO)_x$ ($x \approx 4$) intermediates formed as a result of $W(CO)_6$ decomposition are stable at room temperature and undergo efficient electron stimulated decomposition ($W(CO)_x + e^- \rightarrow (W_xO_y)C$). Consequently, FEBID deposits produced from $W(CO)_6$ contain oxidized tungsten atoms encased in a carbonaceous matrix [50]. In the case of $Co(CO)_3NO$, initial decomposition leads to a desorption/loss of ≈ 50% of the CO groups, although the residual CO groups thermally desorb when the substrate has reached 25 °C [51]. Consequently, FEBID deposits made from $Co(CO)_3NO$ contain little or no carbon, but are compromised in terms of metal content by the decomposition of the NO ligand which occurs during electron stimulated decomposition of the precursor [63-64].

Results from the present study also show evidence of iron oxidation in the absence of any Co oxidation, suggesting that the residual CO ligands left over after the initial decomposition/deposition step are localized on the Fe and that the Co atoms are largely free of CO ligands. This would also be consistent with the importance of the apex ($Fe(CO)_4$) loss channel observed in the gas phase studies [43, 45] as well as the shift of the Co $2p_{3/2}$ peak position and shape in the UHV surface science studies to one that is more indicative of metallic Co. Indeed in a broader sense, if the results from the present study on $HFeCo_3(CO)_{12}$, where are considered alongside the previously reported behavior of $W(CO)_6$ [65-67], $Co(CO)_3NO$ [63-64, 68], $H_2FeRu_3(CO)_{13}$ [46] and the high metal contents often observed from deposits made from $Co_2(CO)_8$ [32, 69-70] the implication is that CO groups attached to cobalt atoms are efficiently removed in FEBID. The underlying reason for this apparent correlation is unclear and certainly worthy of further investigation. Another implication from this study and a comparison with other related studies, is that precursors which yield deposits with relatively high metal content in FEBID are those where > 50% of the native ligands desorb in the initial decomposition step to create intermediates whose ligands are themselves unstable with respect to thermal desorption. In this regard, a more detailed understanding including theoretical insights into the ligand bond strengths in FEBID intermediates, such as the partially decarbonylated intermediates implicated in the present study, would be invaluable in helping to rationalize our experimental observations and to provide predictive information for designing new FEBID precursors that yield deposits with high metal contents.

Conclusions

The reactions of electrons with physisorbed $HFeCo_3(CO)_{12}$ molecules causes extensive CO loss, with an average of 9 CO molecules desorbing per molecule. This one electron process converts the organometallic precursor into partially decarbonylated nonvolatile intermediates with an average stoichiometry of $HFeCo_3(CO)_3$. A comparison with related gas phase studies suggests that this initial electron induced CO desorption step is triggered by dissociative ionization of $HFeCo_3(CO)_{12}$, rather than dissociative electron attachment. Although the rate of electron stimulated decomposition is comparable to other CO-containing FEBID precursors which have been studied, e.g., $(W(CO)_6$ and $Co(CO)_3NO)$, the extent of CO desorption is significantly higher. Another recently studied bimetallic FEBID precursor ($H_2FeRu_3(CO)_{13}$[46]), however, shows similarly extensive CO desorption. Further electron irradiation of the partially decarbonylated intermediate formed by the initial electron stimulated fragmentation of $HFeCo_3(CO)_{12}$, causes decomposition of the residual CO ligands rather than further CO desorption, leading exclusively to Fe oxidation. This suggests that the CO groups in the partially decarbonylated intermediates are located primarily on the iron and not the Co atoms, further implying that the CO desorption observed during decomposition of the precursor is localized to the CO groups bound to the Co atoms. In contrast to the effect of electron irradiation, when the partially decarbonylated $HFeCo_3(CO)_3$ intermediates are annealed to room temperature, complete CO desorption occurs leaving behind only Fe and Co. These observations provide a means to rationalize the high metal contents observed when $HFeCo_3(CO)_{12}$ is used in FEBID, with an overall reaction sequence that involves extensive CO desorption in the initial deposition step ($HFeCo_3(CO)_{12}(ads) + e^- \rightarrow HFeCo_3(CO)_3(ads) + 9CO(g)$), followed by thermal desorption of CO ligands from the resultant partially decarbonylated intermediate ($FeCo_3(CO)_3(ads) + \Delta \rightarrow FeCo_3(ads) + 3CO(g)$).

Supporting Information File 1

File name: Supporting information

Title: Supporting information for Electron induced surface reactions of $HFeCo_3(CO)_{12}$, a Bimetallic Precursor for Focused Electron Beam Induced Processing (FEBIP)

Acknowledgements

The authors acknowledge the support provided by the COST Action CELINA CM1301. DHF thanks the National Science Foundation for support of this work through the linked collaborative grants CHE-1607621 and CHE-160754. OI acknowledges supported from the Icelandic Center of Research (RANNIS) Grant No. 13049305(1-3) and the University of Iceland Research Fund. RKTP acknowledges a doctoral grant from the University of Iceland Research Fund and financial support from the COST Action CM1301; CELINA, for short term scientific missions (STSMs) to enable this work.

References:

1. Utke, I.; Hoffmann, P.; Melngailis, J., Gas-assisted focused electron beam and ion beam processing and fabrication. *J. Vac. Sci. Technol. B* **2008,** *26* (4), 1197-1276.
2. Van Dorp, W.; Hagen, C., A critical literature review of focused electron beam induced deposition. *J. Appl. Phys* **2008,** *104* (8), 081301.
3. Lepore, A., *Electron-Beam ULSI Applications*. William Andrew Publishing: New York, 2001; p 670 755.
4. Bakshi, V., *EUV lithography*. Spie Press: 2009; Vol. 178.
5. Edinger, K.; Becht, H.; Bihr, J.; Boegli, V.; Budach, M.; Hofmann, T.; Koops, H. W.; Kuschnerus, P.; Oster, J.; Spies, P., Electron-beam-based photomask repair. *J. Vac. Sci. Tech. B* **2004,** *22* (6), 2902-2906.

6. Liang, T.; Frendberg, E.; Lieberman, B.; Stivers, A., Advanced photolithographic mask repair using electron beams. *J. Vac. Sci. Tech. B* **2005,** *23* (6), 3101-3105.
7. Liang, T.; Stivers, A. R. In *Damage-free mask repair using electron-beam-induced chemical reactions*, SPIE's 27th Annual International Symposium on Microlithography, International Society for Optics and Photonics, 2002; pp 375-384.
8. Hübner, B.; Koops, H.; Pagnia, H.; Sotnik, N.; Urban, J.; Weber, M., Tips for scanning tunneling microscopy produced by electron-beam-induced deposition. *Ultramicroscopy* **1992,** *42*, 1519-1525.
9. Liu, Z.; Mitsuishi, K.; Furuya, K., The growth behavior of self-standing tungsten tips fabricated by electron-beam-induced deposition using 200 keV electrons. *J. Appl. Phys* **2004,** *96* (7), 3983-3986.
10. Brown, J.; Kocher, P.; Ramanujan, C. S.; Sharp, D. N.; Torimitsu, K.; Ryan, J. F., Electrically conducting, ultra-sharp, high aspect-ratio probes for AFM fabricated by electron-beam-induced deposition of platinum. *Ultramicroscopy* **2013,** *133*, 62-66.
11. Chen, I.-C.; Chen, L.-H.; Ye, X.-R.; Daraio, C.; Jin, S.; Orme, C. A.; Quist, A.; Lal, R., Extremely sharp carbon nanocone probes for atomic force microscopy imaging. *Appl. Phys. Lett* **2006,** *88* (15), 153102.
12. Graells, S.; Alcubilla, R.; Badenes, G.; Quidant, R., Growth of plasmonic gold nanostructures by electron beam induced deposition. *Appl. Phys. Lett* **2007,** *91* (12), 121112.
13. Koops, H.; Hoinkis, O.; Honsberg, M.; Schmidt, R.; Blum, R.; Böttger, G.; Kuligk, A.; Liguda, C.; Eich, M., Two-dimensional photonic crystals produced by additive nanolithography with electron beam-induced deposition act as filters in the infrared. *Microelectron. Eng* **2001,** *57*, 995-1001.
14. Weber-Bargioni, A.; Schwartzberg, A.; Schmidt, M.; Harteneck, B.; Ogletree, D.; Schuck, P.; Cabrini, S., Functional plasmonic antenna scanning probes fabricated by induced-deposition mask lithography. *Nanotechnology* **2010,** *21* (6), 065306.
15. Che, R.; Takeguchi, M.; Shimojo, M.; Zhang, W.; Furuya, K., Fabrication and electron holography characterization of FePt alloy nanorods. *Appl. Phys. Lett* **2005,** *87* (22), 223109.
16. Winhold, M.; Schwalb, C. H.; Porrati, F.; Sachser, R.; Frangakis, A. S.; Kämpken, B.; Terfort, A.; Auner, N.; Huth, M., Binary Pt–Si nanostructures prepared by focused electron-beam-induced deposition. *ACS nano* **2011,** *5* (12), 9675-9681.
17. Porrati, F.; Begun, E.; Winhold, M.; Schwalb, C. H.; Sachser, R.; Frangakis, A.; Huth, M., Room temperature L10 phase transformation in binary CoPt nanostructures prepared by focused-electron-beam-induced deposition. *Nanotechnology* **2012,** *23* (18), 185702.
18. Porrati, F.; Kämpken, B.; Terfort, A.; Huth, M., Fabrication and electrical transport properties of binary Co-Si nanostructures prepared by focused electron beam-induced deposition. *J. Appl. Phys* **2013,** *113* (5), 053707.
19. Porrati, F.; Pohlit, M.; Müller, J.; Barth, S.; Biegger, F.; Gspan, C.; Plank, H.; Huth, M., Direct writing of CoFe alloy nanostructures by focused electron beam induced deposition from a heteronuclear precursor. *Nanotechnology* **2015,** *26* (47), 475701.
20. Chini, P.; Colli, L.; Peraldo, M., *Gazz. Chim. Ital* **1960,** *90*, 1005-19.
21. Boyd, E. P.; Ketchum, D. R.; Deng, H.; Shore, S. G., Chemical vapor deposition of metallic thin films using homonuclear and heteronuclear metal carbonyls. *Chem. Mater* **1997,** *9* (5), 1154-1158.
22. Liu, D. K.; Lai, A. L.; Chin, R. J., Photochemical vapor deposition of mixed-metal thin films from organometallic precursors containing heteronuclear metal-metal bonds. *Mater. Lett* **1991,** *10* (7-8), 318-322.
23. Lübbe, A. S.; Alexiou, C.; Bergemann, C., Clinical applications of magnetic drug targeting. *J. Surg. Res* **2001,** *95* (2), 200-206.
24. Gazeau, F.; Baravian, C.; Bacri, J.-C.; Perzynski, R.; Shliomis, M., Energy conversion in ferrofluids: Magnetic nanoparticles as motors or generators. *Phys. Rev. E* **1997,** *56* (1), 614.
25. Childress, J. R.; Fontana, R. E., Magnetic recording read head sensor technology. *C. R. Phys* **2005,** *6* (9), 997-1012.

26. Fernández-Pacheco, A.; Streubel, R.; Fruchart, O.; Hertel, R.; Fischer, P.; Cowburn, R. P., Three-dimensional nanomagnetism. *Nature Communications* **2017,** *8*, 15756.
27. Silvis-Cividjian, N.; Hagen, C.; Kruit, P., Spatial resolution limits in electron-beam-induced deposition. *J. Appl. Phys* **2005,** *98* (8), 084905.
28. Mulders, J., Practical precursor aspects for electron beam induced deposition. *Nanofabrication* **2014,** *1* (1).
29. Lau, Y.; Chee, P.; Thong, J.; Ng, V., Properties and applications of cobalt-based material produced by electron-beam-induced deposition. *J. Vac. Sci. Technol. A* **2002,** *20* (4), 1295-1302.
30. Schößler, C.; Kaya, A.; Kretz, J.; Weber, M.; Koops, H., Electrical and field emission properties of nanocrystalline materials fabricated by electron-beam induced deposition. *Microelectron. Eng* **1996,** *30* (1-4), 471-474.
31. Rotkina, L.; Lin, J.-F.; Bird, J., Nonlinear current-voltage characteristics of Pt nanowires and nanowire transistors fabricated by electron-beam deposition. *Appl. Phys. Lett* **2003,** *83* (21), 4426-4428.
32. Fernández-Pacheco, A.; De Teresa, J.; Córdoba, R.; Ibarra, M., Magnetotransport properties of high-quality cobalt nanowires grown by focused-electron-beam-induced deposition. *J. Phys. D. Appl. Phys* **2009,** *42* (5), 055005.
33. Pierson, H. O., *Handbook of chemical vapor deposition: principles, technology and applications*. William Andrew: 1999.
34. Botman, A.; De Winter, D.; Mulders, J., Electron-beam-induced deposition of platinum at low landing energies. *J. Vac. Sci. Technol. B* **2008,** *26* (6), 2460-2463.
35. Silvis-Cividjian, N.; Hagen, C.; Leunissen, L.; Kruit, P., The role of secondary electrons in electron-beam-induced-deposition spatial resolution. *Microelectron. Eng* **2002,** *61*, 693-699.
36. Thorman, R. M.; T P, R. K.; Fairbrother, D. H.; Ingólfsson, O., The role of low-energy electrons in focused electron beam induced deposition: four case studies of representative precursors. *Beilstein. J. Nanotech* **2015,** *6* (1), 1904-1926.
37. Ingólfsson, O.; Weik, F.; Illenberger, E., The reactivity of slow electrons with molecules at different degrees of aggregation: gas phase, clusters and condensed phase. *Int. J. Mass. Spectrom* **1996,** *155* (1-2), 1-68.
38. Bald, I.; Langer, J.; Tegeder, P.; Ingólfsson, O., From isolated molecules through clusters and condensates to the building blocks of life. *Int. J. Mass. Spectrom* **2008,** *277* (1), 4-25.
39. Böhler, E.; Warneke, J.; Swiderek, P., Control of chemical reactions and synthesis by low-energy electrons. *Chem. Soc. Rev* **2013,** *42* (24), 9219-9231.
40. Christophoru, L. G., *Electron-Molecule Interactions and their Applications*. Academic Press: Orlando, Florida, 1984; Vol.; Vol. 1.
41. Arumainayagam, C. R.; Lee, H.-L.; Nelson, R. B.; Haines, D. R.; Gunawardane, R. P., Low-energy electron-induced reactions in condensed matter. *Surf. Sci. Rep.* **2010,** *65* (1), 1-44.
42. Fabrikant, I. I.; Eden, S.; Mason, N. J.; Fedor, J., Chapter Nine - Recent Progress in Dissociative Electron Attachment: From Diatomics to Biomolecules. In *Advances In Atomic, Molecular, and Optical Physics*, Ennio Arimondo, C. C. L.; Susanne, F. Y., Eds. Academic Press: 2017; Vol. Volume 66, pp 545-657.
43. T P, R. K.; Barth, S.; Bjornsson, R.; Ingólfsson, O., Dissociative electron attachment and dissociative ionization of bimetallic FEBID precursor $HFeCo_3(CO)_{12}$. *Manuscript in preparation* **2017**.
44. T P, R. K.; Bjornsson, R.; Barth, S.; Ingólfsson, O., Formation and decay of negative ion states up to 11 eV above the ionization energy of the nanofabrication precursor HFeCo3(CO)12. *Chem. Sci.* **2017,** *8*, 5949-5952.
45. T P, R. K.; Barth, S.; Bjornsson, R.; Ingólfsson, O., Structure and energetics in dissociative electron attachment to $HFeCo_3(CO)_{12}$. *Eur. Phys. J. D.* **2016,** *70* (8), 163.
46. T P, R. K.; Weirich, P.; Hrachowina, L.; Hanefeld, M.; Bjornsson, R.; Hrodmarsson, H. R.; Barth, S.; Fairbrother, D. H.; Huth, M.; Ingólfsson, O., Electron Interactions with the heteronuclear carbonyl

precursor (H2FeRu3(CO)13): from fundamental gas phase and surface science studies to focused electron beam induced deposition. *Manuscript submitted* **2017**.
47. Wnuk, J. D.; Gorham, J. M.; Rosenberg, S. G.; van Dorp, W. F.; Madey, T. E.; Hagen, C. W.; Fairbrother, D. H., Electron induced surface reactions of the organometallic precursor trimethyl (methylcyclopentadienyl) platinum (IV). *J. Phys. Chem. C* **2009,** *113* (6), 2487-2496.
48. Wnuk, J. D.; Gorham, J. M.; Rosenberg, S. G.; van Dorp, W. F.; Madey, T. E.; Hagen, C. W.; Fairbrother, D. H., Electron beam irradiation of dimethyl-(acetylacetonate) gold (III) adsorbed onto solid substrates. *J. Appl. Phys* **2010,** *107* (5), 054301.
49. Landheer, K.; Rosenberg, S. G.; Bernau, L.; Swiderek, P.; Utke, I.; Hagen, C. W.; Fairbrother, D. H., Low-energy electron-induced decomposition and reactions of adsorbed Tetrakis (trifluorophosphine) platinum [Pt (PF3) 4]. *J. Phys. Chem. C* **2011,** *115* (35), 17452-17463.
50. Rosenberg, S. G.; Barclay, M.; Fairbrother, D. H., Electron induced reactions of surface adsorbed tungsten hexacarbonyl (W (CO) 6). *Phys. Chem. Chem. Phys* **2013,** *15* (11), 4002-4015.
51. Rosenberg, S. G.; Barclay, M.; Fairbrother, D. H., Electron beam induced reactions of adsorbed cobalt tricarbonyl nitrosyl (Co (CO) 3NO) molecules. *J. Phys. Chem. C.* **2013,** *117* (31), 16053-16064.
52. Spencer, J. A.; Brannaka, J. A.; Barclay, M.; McElwee-White, L.; Fairbrother, D. H., Electron-Induced Surface Reactions of η 3-Allyl Ruthenium Tricarbonyl Bromide [(η 3-C3H5) Ru (CO) 3Br]: Contrasting the Behavior of Different Ligands. *J. Phys. Chem. C* **2015,** *119* (27), 15349-15359.
53. Spencer, J. A.; Wu, Y.-C.; McElwee-White, L.; Fairbrother, D. H., Electron Induced Surface Reactions of cis-Pt (CO) 2Cl2: A Route to Focused Electron Beam Induced Deposition of Pure Pt Nanostructures. *J. Am. Chem. Soc* **2016,** *138* (29), 9172-9182.
54. Tanuma, S.; Powell, C.; Penn, D., Calculations of electron inelastic mean free paths. *Surf. Interface. Anal* **2005,** *37* (1), 1-14.
55. Plummer, E.; Salaneck, W.; Miller, J. S., Photoelectron spectra of transition-metal carbonyl complexes: comparison with the spectra of adsorbed CO. *Phys. Rev. B* **1978,** *18* (4), 1673.
56. Barber, M.; Connor, J.; Guest, M.; Hall, M.; Hillier, I.; Meredith, W., High energy photoelectron spectroscopy of transition metal complexes. Part 1.—Bonding in substituted and unsubstituted first row carbonyls. *Faraday. Discuss. Chem. Soc* **1972,** *54*, 219-226.
57. Moulder, J. F., *Handbook of X-Ray Photoelectron Spectroscopy*. Chanhassen, 1995.
58. Engmann, S.; Stano, M.; Matejčík, Š.; Ingólfsson, O., Gas phase low energy electron induced decomposition of the focused electron beam induced deposition (FEBID) precursor trimethyl (methylcyclopentadienyl) platinum (iv)(MeCpPtMe 3). *Phys. Chem. Chem. Phys* **2012,** *14* (42), 14611-14618.
59. May, O.; Kubala, D.; Allan, M., Dissociative electron attachment to Pt (PF 3) 4—a precursor for Focused Electron Beam Induced Processing (FEBIP). *Phys. Chem. Chem. Phys* **2012,** *14* (9), 2979-2982.
60. Wnorowski, K.; Stano, M.; Matias, C.; Denifl, S.; Barszczewska, W.; Matejčík, Š., Low-energy electron interactions with tungsten hexacarbonyl–W (CO) 6. *Rapid. Commun. Mass. Sp* **2012,** *26* (17), 2093-2098.
61. Engmann, S.; Stano, M.; Papp, P.; Brunger, M. J.; Matejčík, Š.; Ingólfsson, O., Absolute cross sections for dissociative electron attachment and dissociative ionization of cobalt tricarbonyl nitrosyl in the energy range from 0 eV to 140 eV. *J. Chem. Phys* **2013,** *138* (4), 044305.
62. Marbach, H., Electron beam induced surface activation: a method for the lithographic fabrication of nanostructures via catalytic processes. *Appl. Phys. A* **2014,** *117* (3), 987-995.
63. Gazzadi, G.; Mulders, J.; Trompenaars, P.; Ghirri, A.; Rota, A.; Affronte, M.; Frabboni, S., Characterization of a new cobalt precursor for focused beam deposition of magnetic nanostructures. *Microelectron. Eng* **2011,** *88* (8), 1955-1958.
64. Gazzadi, G. C.; Mulders, H.; Trompenaars, P.; Ghirri, A.; Affronte, M.; Grillo, V.; Frabboni, S., Focused electron beam deposition of nanowires from cobalt tricarbonyl nitrosyl (Co (CO) 3NO) precursor. *J. Phys. Chem. C* **2011,** *115* (40), 19606-19611.

65. Koops, H.; Weiel, R.; Kern, D.; Baum, T., High-resolution electron-beam induced deposition. *J. Vac. Sci. Technol. B: Microelectronics Processing and Phenomena* **1988,** *6* (1), 477-481.
66. Porrati, F.; Sachser, R.; Huth, M., The transient electrical conductivity of W-based electron-beam-induced deposits during growth, irradiation and exposure to air. *Nanotechnology* **2009,** *20* (19), 195301.
67. Mulders, J.; Belova, L.; Riazanova, A., Electron beam induced deposition at elevated temperatures: compositional changes and purity improvement. *Nanotechnology* **2010,** *22* (5), 055302.
68. Ervin, M.; Nichols, B., Electron beam induced deposition of cobalt for use as single-and multiwalled carbon nanotube growth catalyst. *J. Vac. Sci. Technol. B* **2009,** *27* (6), 2982-2985.
69. Fernández-Pacheco, A.; Serrano-Ramón, L.; Michalik, J. M.; Ibarra, M. R.; De Teresa, J. M.; O'brien, L.; Petit, D.; Lee, J.; Cowburn, R. P., Three dimensional magnetic nanowires grown by focused electron-beam induced deposition. *Scientific reports* **2013,** *3*.
70. Córdoba, R.; Sesé, J.; De Teresa, J.; Ibarra, M., High-purity cobalt nanostructures grown by focused-electron-beam-induced deposition at low current. *Microelectron. Eng* **2010,** *87* (5), 1550-1553.

Article IV

Electron Interactions with the heteronuclear carbonyl precursor $H_2FeRu_3(CO)_{13}$: from fundamental gas phase and surface science studies to focused electron beam induced deposition

Ragesh Kumar T P, Paul Weirich, Lukas Hrachowina, Marc Hanefeld, Ragnar Bjornsson, Helgi Rafn Hrodmarsson, Sven Barth, D. Howard Fairbrother, Michael Huth and Oddur Ingólfsson.

Submitted to Beilstein journal of nanotechnology, 2017

Ragesh Kumar T P carried out the gas phase and surface experiments and analysed these datas, he wrote the first draft of the surface part of the paper and contributed to editing until submission.

BEILSTEIN JOURNAL OF NANOTECHNOLOGY

Electron Interactions with the heteronuclear carbonyl precursor ($H_2FeRu_3(CO)_{13}$): from fundamental gas phase and surface science studies to focused electron beam induced deposition

Ragesh Kumar T P[1], Paul Weirich[2], Lukas Hrachowina[3], Marc Hanefeld[2], Ragnar Bjornsson[1], Helgi Rafn Hrodmarsson[1], Sven Barth[3], D. Howard Fairbrother[4], Michael Huth[2], and Oddur Ingólfsson*[1]

Address

[1]Science Institute and Department of Chemistry, University of Iceland, Reykjavík, Iceland

[2]Physikalisches Institut, Max-von-Laue-Str. 1, Goethe-Universität, 60438 Frankfurt am Main, Germany

[3]Institute of Materials Chemistry, TU Wien, 1060 Vienna, Austria

[4]Department of Chemistry, Johns Hopkins University, Baltimore, Maryland, USA

Email: odduring@hi.is

* Oddur Ingólfsson

Abstract

In the current contribution we present a comprehensive study on the heteronuclear carbonyl complex $H_2FeRu_3(CO)_{13}$ covering its low energy electron induced fragmentation in the gas phase through dissociative electron attachment (DEA) and dissociative ionization (DI), its decomposition when adsorbed on a surface under controlled ultrahigh vacuum (UHV) conditions and exposed to irradiation with 500 eV electrons, and its performance in focused electron beam induced deposition (FEBID) at room temperature under HV conditions. The performance of this precursor is poor, resulting in maximum metal content of 26% under optimized conditions. Further, the Ru:Fe ratio in the FEBID deposit (≈ 3.5) is higher than the 3:1 ratio predicted. This is somewhat surprising as in recent FEBID studies on a structurally similar bimetallic precursor; $HFeCo_3(CO)_{12}$ metal contents of about 80% are achievable on a routine bases and the deposits are found to maintain the initial Co/Fe ratio. Low temperature (≈213K) surface science studies on thin films of $H_2FeRu_3(CO)_{13}$ demonstrate that electron stimulated decomposition leads to significant CO desorption (average of 8-9 CO groups per molecule) to form partially decarbonylated intermediates. However, once formed these intermediates are largely unaffected by either further electron irradiation or annealing to room temperature, with a predicted metal content similar to what is observed in FEBID. Furthermore, gas phase experiments indicate formation of $Fe(CO)_4$ from $H_2FeRu_3(CO)_{13}$ up on low energy electron interaction. This fragment could desorb at room temperature under high vacuum conditions, which may explain the slight increase in the Ru:Fe ratio of deposits in FEBID. With the combination of gas phase experiments, surface science studies and actual FEBID experiments, we can offer new insights into the low energy electron induced decomposition of this

precursor and how this is reflected in the relatively poor performance of $H_2FeRu_3(CO)_{13}$ as compared to the structurally similar $HFeCo_3(CO)_{13}$

Keywords

Heteronuclear FEBID precursors; Focused electron beam induced deposition; Surface Science; Dissociative electron attachment; Dissociative ionization; Electron molecule interaction; Electron induced deposition.

Introduction

Direct-write technologies using electron beams for nanostructure deposition can surpass the limitations of standard lithography techniques, such as the growth of three-dimensional nanostructures with complex geometries [1-2]. Focused electron beam induced deposition (FEBID) is a powerful technique relying on the decomposition of transiently adsorbed precursors under low vacuum conditions [3]. Different strategies have been used to identify suitable precursors for this process, which relies on electron-molecule interactions rather than the more common thermal fragmentation of precursor species, and results of FEBID using different classes of chemical compounds have been considered [4-5]. For instance, metalorganic precursors containing hydrocarbons and chelating ligands can result in stable precursors and simple handling, but these benefits come at the expense of incorporation of large amounts of carbon in the deposits by incomplete decomposition or co-deposition of the liberated ligands. Recent developments demonstrate elegantly a purification of the deposits to obtain pure, high quality metals such as Pt, Au by post-growth treatment or in situ injection of water for carbon removal [6-13]. These oxidative processes are suitable for precious metals, while other approaches such as annealing under vacuum [14] and hydrogen atmosphere [15-16] are suitable for metals such as Co. However, alternative precursors for the direct deposition of high-purity compounds are desired especially for non-precious metals and more complex compositions.

In FEBID the actual decomposition of the respective precursors is primarily induced by secondary electrons produced as the high-energy primary beam impinges on the substrates surface [17-18]. These secondary electrons span a wide energy range with significant contribution close to 0 eV, a peak intensity well below 10 eV

and a high energy tail extending well above 100 eV (see e.g., [19-21] and references therein). In this energy range fragmentation may be affected by four distinctly different processes, which are active within different energy ranges, and more importantly, lead to distinctly different processes; dissociative electron attachment (DEA), dissociative ionization (DI), and neutral and dipolar dissociation upon electron excitation (ND and DD). An account of the nature of these processes, their energy dependency and the resulting product formation in relation to their role in FEBID is given in a recent review by Thorman *et al* [22]. A more general, and detailed account on the nature of these processes can be found in [23-29] and references therein.

Gas phase experiments under controlled single collision conditions, where the incident electron energy may be varied within the relevant range, are ideal to study the extent and the product formation through the individual processes. Accordingly, such experiments have been used to map the energy dependency of the absolute and relative cross sections for low energy electron induced decomposition of a number of potential and currently used FEBID precursors. These include $Co(CO)_3NO$ [30-31], $Pt(PF_3)_4$ [32-33], $W(CO)_6$ [34], $MeCpPtMe_3$ [35], $Fe(CO)_5$ [36], and more recently $(\eta^3\text{-}\ C_3H_5)Ru(CO)_3Br$ [37-38] and the heteronuclear precursor $HFeCo_3(CO)_{12}$ [39-40]. However, though such gas phase experiments are well suited to map the extent and energy dependency of the individual processes, their predictive value is limited by the fact that these do not reflect the actual conditions when the precursor molecules are adsorbed on surfaces, as is the case in FEBID. Furthermore, current gas phase experiments rely on the detection of charged fragments, leaving the potentially significant neutral dissociation [22, 33, 41] upon electron excitation largely unexplored.

The single electron/molecule collision information obtained in the gas phase study may not be sufficient to understand all of the molecular level processes that occur in FEBID, because deposition does not occur in an isolated phase but on a surface. As a step towards understanding the reactions of adsorbed precursor molecules in FEBID, UHV-surface science studies have been performed, in which nanoscale thin films of precursor molecules adsorbed onto inert substrates have been irradiated with 500 eV electrons. Changes in the composition and bonding in the film can be analyzed with X-ray photoelectron spectroscopy (XPS), reflection-absorption IR spectroscopy (RAIRS), and/or high-resolution electron energy loss spectroscopy (HREELS), while mass spectrometry identifies gas phase species generated as a result of electron irradiation. As such the surface science experiments represent an increased level of complexity compared to gas phase experiments, with greater relevance to FEBID. However, such surface studies are conducted in UHV, at low temperatures and under non-steady state conditions and do thus not fully mimic the actual conditions in FEBID.

The surface science approach has none the less been proven effective in elucidating electron triggered decomposition of several FEBID precursors including $Pt(PF_3)_4$ [42], $W(CO)_6$ [43], $MeCpPtMe_3$ [44-45], $Co(CO)_3NO$ [46], $Fe(CO)_5$ [47] and potential new precursors such as cis-$Pt(CO)_2Cl_2$ [48] and (η^3- C_3H_5)$Ru(CO)_3Br$ [49]. From these surface science studies, it can be concluded that in general electron induced dissociation of surface adsorbed precursor molecules proceeds in two steps. Electron induced desorption of some ligands associated with the precursor occurs to some extent in the first step (e.g. desorption of one of the PF_3 groups in $Pt(PF_3)_4$ to form a $Pt(PF_3)_3$ surface bound intermediate [42]). In the second step, ligand decomposition typically dominates (e.g. decomposition of the residual PF_3 ligands in

the $Pt(PF_3)_3$ intermediate, the loss of fluoride ions and the formation of a Pt deposit contaminated by P), although thermal reactions of surface intermediates produced in the initial decomposition step can also be important (e.g. PF_3 desorption from the $Pt(PF_3)_3$ intermediate if the substrate temperature is sufficiently high [50]).

To date, the most popular precursor class for FEBID is homometallic metal carbonyls of homo-and heteroleptic nature with sufficient vapor pressure. For instance, $Fe(CO)_5$, [51-52] $Fe_2(CO)_9$ [53-54] and $Co_2(CO)_8$ [55] have been shown to yield deposits with high metal content (>60%). In addition, high resolution FEBID of metal nanostructures below 30 nm [56] and successful 3D growth [57] has been demonstrated; however, autocatalytic deposition by spontaneous dissociation on activated surfaces should be avoided for a selective deposition [58-59]. The potential of undesired non-electron induced autocatalytic decomposition illustrates the complexity of the task of identifying precursors yielding high metal content with sufficient stability towards autocatalytic dissociation. $Ru_3(CO)_{12}$ has been used for EBID in an earlier report on low temperature substrates [60]; however, the composition of the decomposition product remains unknown and FEBID using a substrate at room temperature could not replicate the earlier results based on chilled substrates [61]. Successful deposition of Ru containing structures has been demonstrated from an organometallic precursor leading to RuC_9 and required oxygen co-feeding to remove carbon resulting in RuO_2 [61]. Reports on a heteroleptic Ru carbonyl precursor suggest that the carbonyl ligands can be cleaved easier / more efficiently by low energy electrons than other ligands such as allyl and halogenide moieties [37, 49]. Therefore the investigation of Ru carbonyls as potential FEBID precursors is a promising route. Nowadays, deposition of heterometallic or composite materials containing more than one metal is usually realized by using

multiple injection systems [62-65]. Recently, an alternative strategy based on heterometallic $HFeCo_3(CO)_{12}$ precursor species has been demonstrated, which allows for direct writing of nanoscale deposits with high resolution, predefined metal ratio and high metal content (>80 at%) [66]. High purity of deposits and high resolution writing are essential to engineer geometries that are not accessible by crystallization or other template-based approaches. One field of interest in respect to such metallic deposits is the investigation of physical phenomena such as magnetism at the nanoscale. Magnetic nanostructures are fundamental building blocks for applications in data storage and processing as well as the potential successor technologies based on magnonics [67] and spintronics [68] combined with high integration density relying on 3D nanostructure formation. 2D and 3D structures of FEBID-derived magnetic nanostructures have been prepared, [16, 53, 56-57, 69-71] but alternative precursors are desired to predefine alternative compositions and increase the accuracy/spatial resolution of deposits.

The structure of molecular precursor species are required for theoretical treatment and calculation of orbital energies for the electronic ground state (highest occupied molecular orbital; HOMO) and as a base for calculation of singly occupied molecular orbital (SOMO) energies, which are formed as an anion upon electron attachment. The solid state structures of $HFeCo_3(CO)_{12}$ and $H_2FeRu_3(CO)_{13}$ have been obtained by single crystal X-ray diffraction (experimental section and as described in literature [66, 72]). Figure 1 shows both molecular structures side by side and illustrates the common tetrahedral framework of the metal atoms of these heterometallic clusters.

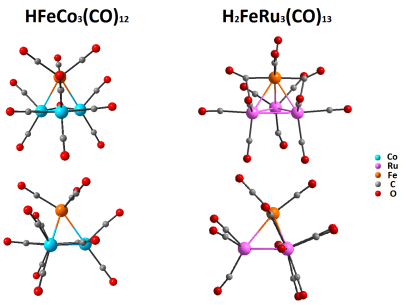

Figure 1: Structural arrangement of $HFeCo_3(CO)_{12}$ and $H_2FeRu_3(CO)_{13}$ illustrating differences in symmetry and ligand bonding shown in two orientations, the structures have been drawn using the crystal structure data determined for the two molecules. Hydrogen atoms are omitted because the position cannot be determined by single crystal XRD. Their location is in the center of the Co_3 basal plane for $HFeCo_3(CO)_{12}$ [66] and in bridging position between either equivalent Ru atom containing a CO bridge to the Fe apex and the one Ru Atom with exclusively terminal CO ligands in $H_2FeRu_3(CO)_{13}$ [72].

In $H_2FeRu_3(CO)_{13}$ and $HFeCo_3(CO)_{12}$ each tetrahedron contains one iron atom and three ruthenium and cobalt atoms, respectively. The coordination sphere contains the carbonyl as well as hydride ligands, which results in a highly symmetrical molecule for $HFeCo_3(CO)_{12}$ and a much less symmetrical arrangement for $H_2FeRu_3(CO)_{13}$. For instance, there are two non-equivalent Ru positions including one with three terminal CO ligands and two bridging to the two remaining Ru atoms in the plane, while all positions of the Co atoms are equivalent. Moreover, in contrast to exclusively terminal CO ligands on the Fe apex in $HFeCo_3(CO)_{12}$, the Fe apex in $H_2FeRu_3(CO)_{13}$ contains two bridging and two terminal CO ligands. In addition, the

bond lengths of the Fe apex to the three remaining metal atoms within the tetrahedron are in the range of 2.538-2.558 Å for $HFeCo_3(CO)_{12}$ and 2.655-2.705 Å in $H_2FeRu_3(CO)_{13}$. One of the Ru-Fe bonds in $H_2FeRu_3(CO)_{13}$, which does not contain any bridging CO ligand, is much longer than the other two and therefore it resembles the transition state upon electron capture as described in literature for $HFeCo_3(CO)_{12}$ [39]. Structural differences will be important for the electron induced decomposition and are discussed vide infra.

In the current contribution, we report on similarities and differences of the heterometallic precursors $H_2FeRu_3(CO)_{13}$ and $HFeCo_3(CO)_{12}$ using several techniques and allowing for comparison between the electron induced decomposition of these compounds in the gas phase, on the surface and during FEBID. The choice of $H_2FeRu_3(CO)_{13}$ was motivated by its structural similarities to those of $HFeCo_3(CO)_{12}$ which, in turn, has proven exceptionally good performance in FEBID of pure, stoichiometric metal alloy structures [66]. Furthermore, $H_2FeRu_3(CO)_{13}$ precursor is the only hydridocarbonyl with 1:3 Fe/Ru ratio. Other hydridocarbonyls, such as $H_3FeRu_2(CO)_{13}^-$ are only stable as anions that cannot be converted in neutral molecules. One other hydridocarbonyls for the Fe/Ru metal combination is known with an Fe_2Ru_2 tetrahedral metal core. However, this compound requires different synthesis conditions and is not expected to be better suited for FEBID. To the best of our knowledge, this is the first extensive report on a heteronuclear precursor providing well-rounded insight in fundamental electron-molecule interactions including electron induced decomposition characteristics in the gas phase and on surfaces as well as its performance in the actual FEBID process. These studies are highly interesting due to the excellent behavior of $HFeCo_3(CO)_{12}$ in the FEBID process including high metal content, predefined metal ratio and also the

high resolution deposition of nanostructures [66]. In contrast, depositions using $H_2FeRu_3(CO)_{13}$ have metal content of merely ~25% and varying metal ratios dependent on process parameters. We relate similarities and specific differences in structure and bonding and compare the fragmentation behavior of both heteronuclear precursors.

Results & Discussion

Gas-phase dissociative electron attachment and dissociative ionization of $H_2FeRu_3(CO)_{13}$.

In the current section we discuss decomposition of the heteronuclear complex $H_2FeRu_3(Co)_{13}$ through dissociative electron attachment (DEA) and dissociative ionization and we compare the fragmentation patterns observed to our previous work on $HFeCo_3(Co)_{12}$. In the energy range from about 0 eV up to about 25 eV DEA to both these potential precursors is characterized by a very rich fragmentation pattern. For $HFeCo_3(Co)_{12}$ [39-40, 73], 23 distinct, identifiable, negative ion fragments are observed in this energy range, along with the intact molecular anion, and for $H_2FeRu_3(CO)_{13}$ 29 fragments are assigned to discrete molecular compositions. Dissociative ionization of these compounds is also extensive with a dominating contribution from sequential CO loss, but also metal-metal bond cleavage and doubly charged cationic fragments are significant in DI of $H_2FeRu_3(Co)_{13}$ at 70 eV impact energy.

In the current DEA experiments the ion yield curves are recorded by scanning through the relevant electron energy range with the quadrupole mass spectrometer set to only allow transmission of one m/z ratio. However, to achieve sufficient signal intensity the mass resolution is kept fairly low, practically opening up a transmission window of about 2 mass units. The fragment assignment is fairly straight forward for

$HFeCo_3(Co)_{12}$ where the isotope distribution spans a mass range of 7 amu with one predominant isotope peak. This is to be compared to the mass of CO, i.e., 28 amu, which is the smallest neutral unit lost in the DEA process. For $H_2FeRu_3(CO)_{13}$, on the other hand, the isotope distribution spans about 30 mass units with about 10 mass units span of significant peaks. To demonstrate this situation, Figure 2 compares the isotope distribution for a) $HFeCo_3(CO)_{12}$ and b) $H_2FeRu_3(CO)_{13}$. It is clear from Figure 2 that an unambiguous assignment of contributions to the respective ion yield curves from $H_2FeRu_3(CO)_{13}$ from the m/z ratio alone is often not straight forward. This is further complicated by the fact that the principal mono-isotopic mass of iron is 56 amu, i.e., two times that of CO. Furthermore, DEA cross sections for individual fragments may vary by orders of magnitude and an insignificant m/z "spill-over" may thus dominate the respective ion yield curves.

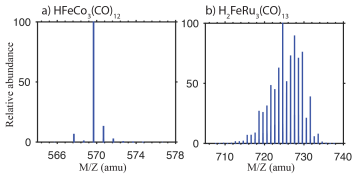

Figure 2: Isotope distribution for a) $HFeCo_3(CO)_{12}$, b) $H_2FeRu_3(CO)_{13}$, Isotope distribution for both compounds are adapted from [74].

To account for this we have calculated the threshold energy for the individual processes at the PBE0 [75-76] /ma-def2 TZVP [77-78] level of theory. We have previously compared the performance of PB86 to that of PBE0 for threshold calculations in DEA to $HFeCo_3(CO)_{12}$ [39] and found that while PB86 reproduced the structural parameters from the XDR measurements very well, this functional overestimated the threshold energies significantly, PBE0, on the other hand delivered threshold energies in good agreement with our experimental appearance energies.

We thus use the threshold energies calculated at the PBE0 level of theory along with the energy dependency of the fragment formation to assign the contributions in the individual ion yield curves to the respective fragments. Furthermore, to aid the discussion, signal identified as m/z spill over in the respective ion yield curves are presented in grey to be clearly distinguishable from the principal contributions under discussion. Finally, while we could state with fair confidence where the hydrogen is still attached to negative ion fragments formed from $HFeCo_3(CO)_{12}$ [39-40, 73] we have no means to verify this for $H_2FeRu_3(CO)_{13}$, this also applies to the DI spectra. Generally, we assume that the hydrogens remain attached to the Ru_3 base plane but in our discussion we do not explicitly account for their whereabouts, except where these are relevant for the calculation of the thresholds for the respective dissociation channels.

Dissociative electron attachment to $H_2FeRu_3(CO)_{13}$: Dissociative electron attachment to the heteronuclear complexes $H_2FeRu_3(CO)_{13}$ is characterized by two primary fragmentation pathways, the apex loss and the loss of a $Ru(CO)_n$. A further, minor channel leading to the formation of $[Ru_2(CO)_n]^-$ with n = 4 – 7 is also observed. The apex loss appears predominantly with charge retention on the iron containing moiety through the formation of $[Fe(CO)_4]^-$ and to a much lesser extent through the formation of $[Fe(CO)_3]^-$ and $[Fe(CO)_2]^-$, as is shown in Figure 3(a). The apex loss also leads to the formation of the complementary fragments $[M - Fe(CO)_4]^-$, $[M - Fe(CO)_3]^-$ and $[M - Fe(CO)_2]^-$ with appreciable intensity on the $[M - Fe(CO)_3]^-$ fragment. Charge retention on the remaining $Ru_3(CO)_n$ base-plane moiety is also observed along with further CO loss, up to 11 CO in total, as shown in Figure 4. Based on our threshold calculations we attribute these channels to the loss of a neutral $Fe(CO)_4$ and additional loss of up to 7 CO from the charge retaining moiety.

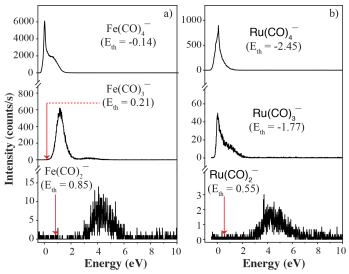

Figure 3: Negative ion yield curve for the formation of a) $[Fe(CO)_n]^-$ and b) $[Ru(CO)_n]^-$ up on electron attachment in the energy range from 0 – 10 eV. The thermochemical thresholds for the respective channels calculated at the PBE0/ma-def2 TZVP level of theory are given in parenthesis and indicated by red arrows.

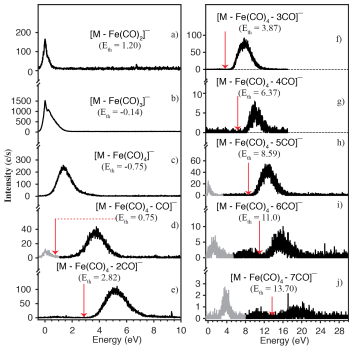

Figure 4: Loss of $Fe(CO)_2$ (panel a), $Fe(CO)_3$ (panel b), $Fe(CO)_4$ (panel c) and additional loss of up to 7 COs (from panel d to panel j) through dissociative electron attachment to $H_2FeRu_3(CO)_{13}$. The thermochemical thresholds for the respective channels calculated at the PBE0/ma-def2 TZVP level of theory are given in parenthesis and indicated by red arrows.

Similar to the apex loss, we also observe the formation of $Ru(CO)_4^-$ with significant intensity and the formation of $[Ru(CO)_3]^-$ and $[Ru(CO)_2]^-$ with considerably less intensity, as shown in Figure 3(b). Here we also observe the complementary ions $[M - Ru(CO)_4]^-$ and $[M - Ru(CO)_3]^-$ and further, sequential CO loss from the charge retaining, $FeRu_2$ containing moiety up to a total loss of 11 CO units. Similar to the apex loss we attribute these fragments to an initial loss of a neutral $Ru(CO)_4$ unit and an additional loss of up to 7 CO units from the charge-retaining moiety. The ion yield curves for these channels are shown in Figure 5.

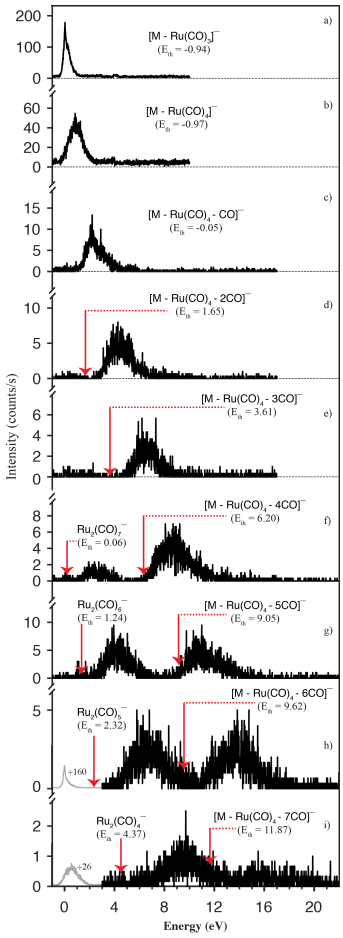

Figure 5: Negative ions formed through loss of $Ru(CO)_3$ (panel a), $Ru(CO)_4$ (panel b) and further loss of up to 7 COs (panel c to i) by electron attachment dissociation of $H_2FeRu_3(CO)_{13}$. Also the ion yield for $Ru_2(CO)_n$ with n = 7 – 4 appear in panels f) – i)

respectively, due to the overlap of the isotope distribution of these fragments with that of the respective $[M - Ru(CO)_4 - nCO]^-$ (n = 4 – 7) fragments. The thermochemical thresholds for the respective channels calculated at the PBE0/ma-def2 TZVP level of theory are given in parenthesis and indicated by red arrows.

The respective ion yield curves for the $[Fe(CO)_n]^-$ apex loss and the $[Ru(CO)_n]^-$, loss from $H_2FeRu_3(CO)_{13}$, shown in Figure 3, are almost identical to these observed from $HFeCo_3(CO)_{12}$ and reported earlier, and we have discussed these in detail elsewhere [39]. In brief, based on calculations at the BP86/def2 TZVP level of theory we find the LUMO of $HFeCo_3(CO)_{12}$ to have a strong Fe-Co antibonding character along the Fe-Co facets and the ground state negative ion formed up on single electron attachment to this molecule relaxes by substantial elongation of two of the three Fe−Co bonds and transformation of one of the terminal Co-COs to a Fe−CO−Co bridging ligand. Furthermore, the relative fraction of the spin density centered on the apical iron in the relaxed ground state $[HFeCo_3(CO)_{12}]^-$ anion is markedly larger than that on the cobalt atoms forming the base plane.

The situation is different for $H_2FeRu_3(CO)_{13}$ where the C_{3v} symmetry is broken with a bridging CO between two of the three base plane metal atoms (Ru) and the apex iron. The HOMO of $H_2FeRu_3(CO)_{13}$ shows a bonding character along the bridging COs between the base plane and the apex but no significant Ru−Fe bonding contribution is present. Also, the Ru−Fe anti-bonding character of the LUMO is not clear. This situation is demonstrated in Figure SI 1 within the supporting material which shows the iso-surfaces for the relevant MOs. Accordingly, single electron occupation of the LUMO of $H_2FeRu_3(CO)_{13}$ results in a moderate geometry change as compared to $HFeCo_3(CO)_{12}$ and the significant weakening of metal-metal bonds from the base plane to the apex observed for $HFeCo_3(CO)_{12}$ are not observed for

$H_2FeRu_3(CO)_{13}$. Rather, a moderate metal-metal bond weakening is observed, both within the Ru base plane and between the base plane and the apex, i.e., from 2.934 to 3.037 Å between the hydrogen-bridged rutheniums and from 2.687 to 2.781 Å between the iron and rutheniums, where these are carbonyl bridged. Also a moderate increase in distance between the none-hydrogen bridged rutheniums is observed, i.e., from 2.853 to 2.898 Å, but all further geometry changes are insignificant. For completeness all relevant, calculated bond lengths and angles for neutral $H_2FeRu_3(CO)_{13}$ and its anionic ground state are listed in table SI1 within the supporting material. Furthermore, as shown in Figure 6, the spin density calculated for the ground state $[H_2FeRu_3(CO)_{13}]^-$ anion, strained within the neutral geometry, is very similar on all metal atoms. Relaxation to the ground state anionic geometry (Figure 6(b)), however, leads to a relative increase in the spin density on the Ru base plane atoms as compared to the Fe-apex. It is clear that the comparison of the iso-surfaces for the respective MOs for $H_2FeRu_3(CO)_{13}$ and $HFeCo_3(CO)_{12}$, the spin density of their anions and the geometrical changes between the respective neutral and anionic ground states, does not offer a quantitative explanation of their different behavior with regards to DEA. However, the difference is significant, especially with regards to the relaxation of the metal-metal bonds between the base plane and the apex as well as within the base plane. While the relaxation of the ground state anion of $HFeCo_3(CO)_{12}$ leads to a spontaneous and significant weakening of the metal bonds from the base plane to the apex, the bond weakening within $H_2FeRu_3(CO)_{13}$ is much less significant and is similar within the Ru_3 base plane and between the base plane and the apex. Furthermore, the relative spin density on the apex iron is much more significant for the anionic ground state of $HFeCo_3(CO)_{12}$ than for $H_2FeRu_3(CO)_{13}$. This is in-line with the observation of the apex loss from

$HFeCo_3(CO)_{12}$ being restricted to charge retention on the Fe containing moiety while that from $H_2FeRu_3(CO)_{13}$ also leads to a considerable fraction with charge retention on the base plane fragment. Tentatively we offer the explanation that the apex loss from $HFeCo_3(CO)_{12}$ is a spontaneous process proceeding directly along a repulsive path on the respective potential energy surface of the ground state anion. For $H_2FeRu_3(CO)_{13}$, on the other hand, energy dissipation is more effective leading to more apparent competition between the apex loss and base plane fragmentation of the ground state $[H_2FeRu_3(CO)_{13}]^-$ anion.

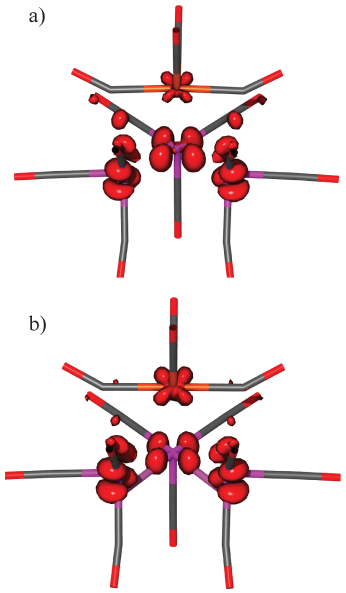

Figure 6: Calculated spin density of the $[H_2FeRu_3(CO)_{13}]^-$ anion; a) in the constrained geometry of neutral $H_2FeRu_3(CO)_{13}$ (vertical transition) b) in the relaxed ground state geometry of the anion.

Furthermore, fragmentation of the base plane is also observed through the formation of $[Ru_2(CO)_n]^-$ with n = 4 – 7, though with comparatively low intensity. The m/z ratios for the isotope distributions for these fragments overlap considerably with those for $[M - Ru(CO)_4 - nCO]^-$ with n = 7 – 4. These fragments, thus appear in the same ion yield curves displayed in panels (f)-(i) in Figure 5. The assignment of these fragments is based on their calculated thermochemical thresholds, which are displayed in the respective panels. As the $[Ru_2(CO)_n]^-$ n = 4 – 7 thresholds are lower, these could in principle contribute to the corresponding higher energy yields assigned to $[M - Ru(CO)_4 - nCO]^-$ with n = 7 – 4, respectively. We do, however, consider this unlikely as the threshold values for the respective fragments correspond very well with the respective onsets. These are distinct progressions of sequential CO loss and as is discussed here below we attribute these to metastable decay. As typical for such processes the onset of a proceeding channel (n+1 CO) coincides with the maximum probability for the preceding one (n CO), and correspondingly the onset should coincide with the thermochemical threshold.

Based on our analyzes, sequential loss of CO from $H_2FeRu_3(CO)_{13}$ with the remaining metal core intact is not observed. This is distinctly different for the fragmentation pattern observed for $HFeCo_3(CO)_{12}$ through DEA. While the apex loss through $[Fe(CO)_4]^-$, $[Fe(CO)_3]^-$ and $[Fe(CO)_2]^-$ formation is also observed from $HFeCo_3(CO)_{12}$ with similar relative cross sections as for $H_2FeRu_3(CO)_{13}$, for the respective fragments charge retention on the Co_3 base plane is not observed in $HFeCo_3(CO)_{12}$ [73], neither is the formation of $[Co(CO)_4]^-$ or $[Co(CO)_3]^-$. However,

similar to $H_2FeRu_3(CO)_{13}$ the loss of a single Co and 4-10 CO is observed from $HFeCo_3(CO)_{12}$, though with very low intensity [73]. We attributed this to insignificant neutral $Co(CO)_4$ loss associated with further CO loss. Furthermore, sequential CO loss from the intact metal core is the dominant channel in DEA to $HFeCo_3(CO)_{12}$, while, as stated above, this channel is not observed from $H_2FeRu_3(CO)_{13}$.

Figure 4 shows the ion yield curves for the formation of the fragments $[M - Fe(CO)_2]^-$, $[M - Fe(CO)_3]^-$, $[M - Fe(CO)_4]^-$ and $[M - Fe(CO)_4 - nCO]^-$ with n = 1 – 7, i.e., the apex loss with charge retention on the Ru_3 base plane and additional CO loss. The threshold for the corresponding channels are denoted in the respective panels, assuming neutral $Fe(CO)_n$ loss up to n = 4 and further sequential CO loss after that. In these calculations the hydrogens are retained on the respective ruthenium base plane fragments. We note in this context, that from the respective m/z ratios, these fragments could principally also be assigned as [M - (n+2)CO], however, the threshold for such sequential CO loss from the molecular anion are generally about 3 – 9 eV above the observed ones. These are listed in comparison with the thresholds for the corresponding [M - $Fe(CO)_4$ - nCO] fragments in Table SI2 with the supporting material.

For $H_2FeRu_3(CO)_{13}$ the loss of the neutral $Fe(CO)_2$ unit, i.e., the rupture of both Fe-CO bonds to the bridging CO ligands is observed with low intensity through a narrow contribution at around 0 eV (panel a, Figure 4). At the PBE0/ma-def2-TZVP level of theory the threshold for this channel is found to be 1.2 eV, and we thus, attribute this low intensity contribution to the high energy tail of the Maxwell Boltzmann inner energy distribution at the current experimental conditions, T = 338 to 343 K. We can, however, not exclude that we have missed the most stable anionic structure in our calculations, despite the consideration of a number of potential structures.

With regards to the charge retention, this is the complementary channel to the formation of $[Fe(CO)_2]^-$ which appearance energy is about 3 eV (Figure 3(a)) and for which we calculate the threshold to be about 0.85 eV. The next two channels i.e., the formation of $[M - Fe(CO)_3]^-$ and $[M - Fe(CO)_4]^-$ are found to be exothermic 0.14 and 0.75 eV, respectively, while the thresholds for the complementary channels leading to the formation of $[Fe(CO)_3]^-$ and $[Fe(CO)_4]^-$ (Figure 3(a)) are found to be 0.21 eV and exothermic by 0.14 eV, respectively. Comparing Figures 3(a) and Figure 4, it is clear that the ion yield curves for the fragments that are complementary with regards to the charge retention are also complementary with regards to the energy dependency and efficiency of their formation. Hence, while the $[M - Fe(CO)_3]^-$ formation is a dominant channel with a maximum contribution at about 0 eV the formation of $[Fe(CO)_3]^-$ is observed with moderate intensity and an appearance energy of about 0.5 eV. Conversely, $[M - Fe(CO)_4]^-$ is only observed with moderate intensity and an appearance energy at about 0.5 eV, while the complementary fragment $[Fe(CO)_4]^-$ is the highest intensity fragment observed from this compound, with the main contribution peaking at about 0 eV. In principle all exothermic channels are competing paths at 0 eV incident electron energy, however, the paired energy dependency of the $[M - Fe(CO)_3]^-$ and $[Fe(CO)_3]^-$ fragments as well as that of the $[M - Fe(CO)_4]^-$ and $[Fe(CO)_4]^-$ fragments implies that the rate determining step is strongly coupled to the charge retention. Tentatively we attributed this to two competing initial steps on the respective reaction paths, i.e., the initial rupture of a Fe−CO or a Ru−CO bond to one of the two Fe−CO−Ru bridging carbonyls. In this picture, the initial rupture of a Fe−CO bond to one of the two Fe−CO−Ru bridging carbonyls leads predominantly to charge retention on the iron containing moiety while

a Ru−CO bond rupture leads predominantly to charge retention at the Ru_3 base plane moiety.

In this context, and to aid the proceeding discussion, we note that the observation window of our experimental setup is about 10 µs, which is the extraction time from the electron-molecule interaction region. Fragments that dissociate further after extraction do not maintain stable trajectories within the quadrupole mass filter and are thus not detected. This is about 50 µs, which is the approximate lifetime required for a fragment to be observed.

We now turn to discuss the $[M - Fe(CO)_4 - nCO]^-$ and $[M - Ru(CO)_4 - nCO]^-$ fragments from $H_2FeRu_3(CO)_{13}$ with n = 1 – 7 (panels d – j in Figure 4 and c – i in Figure 5), and we compare these with sequential CO loss from $HFeCo_3(CO)_{12}$ leading to the fragments $[M - nCO]^-$ with n = 3 - 12. These regressions are remarkable for three different reasons, as is discussed in detail for $HFeCo_3(CO)_{12}$ elsewhere [40] and we believe that the same considerations hold equally for $H_2FeRu_3(CO)_{13}$. In brief, both these molecules show negative ion formation up to above 20 eV incident electron energy, which is more than 10 eV above their respective ionization limit. Furthermore, the lifetime of these ions with regards to autodetachment is long enough to allow for detachment of all CO units from $HFeCo_3(CO)_{12}$ and $Fe(CO)_4$ or $Ru(CO)_4$ along with additional loss of up to 7 CO units from $H_2FeRu_3(CO)_{13}$. In both cases the formation of individual fragments is confined to a well-defined energy range showing "resonance-like feature" in the ion yield curves. The onset of the respective contributions, however, agrees well with their expected thermochemical thresholds and the maxima of $[M - nCO]^-$ from $HFeCo_3(CO)_{12}$ and $[M - Fe(CO)_4 - nCO]^-$ and $[M - Ru(CO)_4 - nCO]^-$ from $H_2FeRu_3(CO)_{13}$ coincide with the succeeding $[M - (n+1)CO]^-$, $[M - Fe(CO)_4 -$

$(n+1)CO]^-$ and $[M - Ru(CO)_4 - (n+1)CO]^-$ fragments, respectively. This behavior is typical for sequential metastable loss, where $[M - nCO]^-$ is the precursor of $[M - (n+1)CO]^-$ and the extent of the fragmentation is determined by the available excess energy. This however, would require a quasi-continuous electron attachment over the energy range from around few eV up to above 20 eV for both compounds. For $HFeCo_3(CO)_{12}$ we postulated [40] that such a continuum is realized through a dense "*band*" of occupied and unoccupied molecular orbitals at the HOMO/LUMO gap of this molecule supporting electron attachment and the formation of long lived, transient negative ions at high energies through multiple electron excitations associated with the attachment process. *Id est*, the formation of "multi-particle-multi hole resonances". This is enabled through the poly-nuclear nature of these organometallic compounds providing a dense band of occupied, primarily metal-based orbitals (*d*-orbitals) and the high number and different nature of the carbonyl ligands (bridging and terminal) providing high density of unoccupied ligand CO π^* orbitals. Along with the appreciable mixing of these orbitals, this allows for multiple electronic excitations in conjunction with the electron attachment process.

Figure 7 compares the MO diagrams for $HFeCo_3(CO)_{12}$ showing that their MO structure is very similar in this respect, with both compounds possessing a dense band of occupied and unoccupied molecular orbitals at the HOMO/LUMO gap. These are spaced about 3 eV apart allowing for more than 6 electronic transitions at about 20 eV incident electron energy.

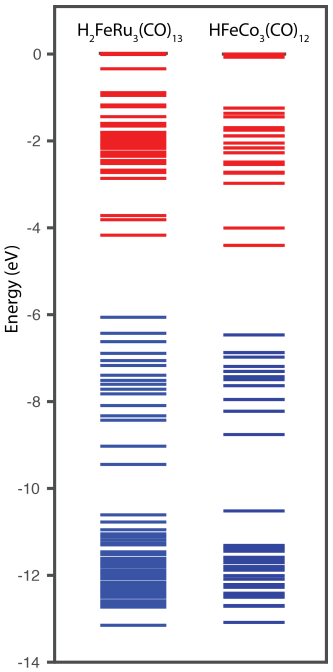

Figure 7: Calculated MO diagram of $H_2FeRu_3(CO)_{13}$ and $HFeCo_3(CO)_{12}$, red line represents the unoccupied molecular orbitals and blue line represents the occupied molecular orbitals.

In an intermediate extraction, we can conclude that the compounds $H_2FeRu_3(CO)_{13}$ and $HFeCo_3(CO)_{12}$ show a very similar electron attachment profile with a series of two to three low energy single particle resonances supporting negative ion formation in the energy range from 0 to about 2 - 3 eV. At intermediate energies the MO-structure of these compounds allows for negative ion formation supported through concomitant electronic excitation, i.e., one-hole two-particle

resonances and at high energies, i.e., up to about 20 eV we anticipate that long lived negative ion formation is supported by multiple electron excitations i.e., through "multi-particle-multi hole resonances" [40]. Together these resonances provide a quasi-continuous attachment profile from about 0 eV up to above 20 eV.

The main difference between these compounds, with regards to DEA, lies in the fragmentation process of the molecular anions formed, rather than the initial electron attachment process. For $HFeCo_3(CO)_{12}$ the two main channels are (i) the apex loss leading mainly to the formation $[Fe(CO)_4]^-$ but also $[Fe(CO)_3]^-$ and (ii) sequential CO loss from the molecular anion leading to the fragments $[M - nCO]^-$ with n = 1 - 12 [73]. Hence, there are two parallel paths where the initial CO loss competes with the apex loss in the low energy range:

$$[\mathrm{HFeCo_3(CO)_{12}}]^- \rightarrow \mathrm{Fe(CO)_n^-} + \mathrm{HCo_3(CO)_{12-n}} (\mathrm{n} = 2 - 4) \quad (1)$$

and

$$[\mathrm{HFeCo_3(CO)_{12}}]^- \rightarrow \mathrm{HFeCo_3(CO)_{12-n}^-} + \mathrm{nCO} (\mathrm{n} = 1 - 12) \quad (2)$$

For $H_2FeRu_3(CO)_{13}$, on the other hand, the apex loss (mainly as $Fe(CO)_4$) or the loss of a single ruthenium from the base plane (mainly as $Ru(CO)_4$) precedes all further fragmentation. Where the charge retention is on the metal tetracarbonyl ($M(CO)_4$) fragment, further fragmentation of the neutral fragment is not expected (predominantly at or close to 0 eV). However, when the charge retention is on the respective Ru_3 or $FeRu_2$ containing fragments further loss of up to 7 CO units is observed. This situation is shown in Eq. 3 and 4 for the apex loss as $Fe(CO)_4$ and further CO loss from the Ru_3 base plane fragment:

$$[\mathrm{H_2FeRu_3(CO)_{13}}]^- \rightarrow \mathrm{Fe(CO)_4^-} + \mathrm{H_2Ru_3(CO)_9} \quad (3)$$

and

$$[H_2FeRu_3(CO)_{13}]^- \rightarrow H_2Ru_3(CO)_9^- + Fe(CO)_4 \rightarrow H_2Ru_3(CO)_{9-n}^- + nCO (n = 1 - 7) \quad (4)$$

Furthermore, while insignificant base plane fragmentation is observed for $HFeCo_3(CO)_{12}$, base-plain fragmentation of $H_2FeRu_3(CO)_{13}$ is observed through $[Ru(CO)_n]^-$ and $[M - Ru(CO)_n]^-$ formation with n = 2 - 4, $[M - Ru(CO)_4 - nCO]^-$ with n =1 - 7 and $[Ru_2(CO)_n]^-$ with n = 4 - 7.

Dissociative ionization, different from DEA, is a non-resonant process with an onset at or slightly above the ionization limit of the respective compounds. At threshold, DI is generally characterized by single bond ruptures, i.e., the lowest energy channels. With increasing impact energy further channels open up and the DI cross sections for individual channels increases until the total cross section reaches a maximum in the range between 70 and 100 eV. At higher impact energies the energy transfer efficiency diminishes, reflected in a gradual decrease in the total cross section as the impact energy increases further. At about 70 eV all DI channels are generally close to their maxima and DI spectra at this energy generally give a good picture of the integral efficiency of the individual channels, though they do not accurately reflect the onset region where different channels are opening up and the branching ratios are markedly different. This difference is typically only significant in the energy range 10-20 eV above the ionization energy of the respective compounds.

Figure 8 shows DI spectra of $H_2FeRu_3(CO)_{13}$ recorded at an impact energy of 70 eV. Panel (a) shows the m/z range from about 50 to 315 while panel (b) shows the m/z range from about 280 to 670. The fragmentation of $H_2FeRu_3(CO)_{13}$ at 70 eV impact energy is very rich and characterized by broad contributions and significant overlap resulting from the wide isotope distribution of ruthenium. The accurate interpretation of the spectra is further complicated due to the fact that the mass of the principal iron isotope (56 amu) is two times that of CO not allowing for differentiation between Fe loss and the loss of two CO from the m/z ratios alone. Furthermore, in

the lower m/z range we observe contributions from doubly charged fragment ions, though with comparably low intensity. For the low m/z range up to about 300, the dominating regression can be unambiguously assigned to $[Fe(CO)_n]^+$ with n = 0 - 5. The higher m/z range, on the other hand, is characterized by two main regressions which cannot be unambiguously assigned to defined molecular composition from the m/z ratios alone. The first regression may be assigned as $[M - nCO]^+$ with n = 3 - 13, but may also be attributed to $[M - Fe - (n - 2)CO]^+$. The second regression is $[M - Ru - nCO]^+$ with n = 6 - 11 which similarly may also be attributed to $[M - Ru - Fe - (n - 2)CO]^+$. Further significant contributions are observed from $[M - 2Ru - 6CO]^+$ and $[M - 2Ru - 7CO]^+$ in this m/z range. Again, these m/z fragments may also be assigned to the respective $[M - 2Ru - Fe - 4CO]^+$ and $[M - 2Ru - Fe - 5CO]^+$ ions.

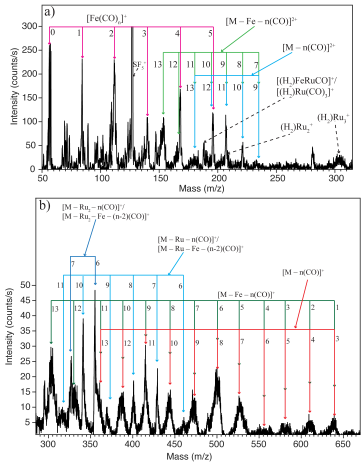

Figure 8. electron impact ionization spectra of $H_2FeRu_3(CO)_{13}$ recorded at electron energy of 70 eV, upper panel shows the positive ion fragments formed in the mass

range 50 to 315 amu and the lower panel shows positive ion fragments in the mass range 280 to 670 amu. The label M in the figure is used for $H_2FeRu_3(CO)_{13}$.

To enable better comparison with the surface experiments discussed in the next section and specifically to try to identify whether DEA or DI are likely to play the dominating role in the decomposition of $H_2FeRu_3(CO)_{13}$ physisorbed on a substrates surface, we have estimated the average CO loss per incident electron for both the DI and DEA process. For DEA this is estimated by multiplying the integrated intensity of the individual channels with the number of CO lost in the process, summing this up for all channels and dividing the derived total CO loss with the total DEA intensity. For DI the same procedure is used, however, the respective integral intensities are estimated from the peak intensities at the m/z ratios for the respective principal isotopes. The measured intensities are then divided by the fractional contribution of the principal isotope to the total isotope distribution. For simplification only the isotope distribution of the metal content of the respective fragments is considered.

The main problem with these estimations is that we do not have any information on the fragmentation of the neutral counterparts; this is especially true for DI where we have no information on the available excess energy.

To account for this, we have calculated a lower limit and a higher limit for the CO loss from $H_2FeRu_3(CO)_{13}$ per incident, both for the DI and the DEA process. For the lower limit in DI we presume the high m/z regressions to be associated with neutral iron loss as neutral $Fe(CO)_4$, i.e., loss of the apex iron with both the bridging carbonyls and both terminal carbonyls. For the $[Fe(CO)_n]^+$ regression we presume that the neutral counterpart stays intact. For the higher limit we presume that the high m/z ratios are not associated with iron loss and that the neutral counterparts to the $[Fe(CO)_n]^+$ regression fragment through complete CO loss. Similarly, for DEA we

estimate the upper limit by assuming additional CO loss from the neutral counterparts formed in the individual processes. However, here we have a fair estimation of the excess energy available as we have calculated the thermochemical thresholds for the individual processes. For the neutral $Fe(CO)_4$ and $Ru(CO)_4$ loss and additional CO loss the onset of the individual contributions is mostly close to the calculated thermochemical threshold of the individual processes but the respective contributions generally stretch over a range of about 4 - 5 eV. On the high energy side of the respective contribution further loss of 2 - 3 CO from the respective metal neutral tetra carbonyl is thus principally possible. Accordingly, we calculate the lower limit for CO loss through DEA by presuming the intact neutral Fe and Ru carbonyls (mainly tetra carbonyls). For the higher limit we simply presume additional loss of two CO from these.

From these estimations we derive the bracketing numbers 0.5 - 3 for CO loss from $H_2FeRu_3(CO)_{13}$ per incident through DEA and 3 - 9 for DI. In this context we note that all DEA channels are associated with metal-metal bond ruptures, while in DI this number is somewhere about 50 - 100% depending on how large a fraction of the m/z ratios matching the $[M - nCO]^+$ regression are actually due to the formation of $[M - Fe - (n - 2)CO]^+$. For $HFeCo_3(CO)_{12}$ the same estimations give the bracketing numbers 4 - 9 for CO loss per incident through DI and 2 - 3 for DEA, while metal-metal bond rupture 50% of the DI intensity and about 30% of the DEA intensity.

Finally, we emphasize that we are only able to account for DEA and DI in the current experiments and we are blind on all fragmentation caused by neutral dissociation up on electron excitation. For $Pt(PF_3)_4$, it has been shown that the cross sections for electronic excitations are very significant [33] and it is reasonable to assume that the cross sections for such fragmentation is comparable to the

fragmentation observed in DEA. This assumption is derived from the notation that the underlying electronic excitations correspond to the respective resonances observed in DEA, i.e., a single particle resonance in DEA has a corresponding one-hole one-particle resonance in electronic excitation and the same is true for core excited one-hole two particle DEA resonances as well as the postulated multi-particle resonances recently discussed in conjunction with CO loss from $HFeCo_3(CO)_{12}$ through DEA [40].

Electron Induced Surface Reactions of $H_2FeRu_3(CO)_{13}$.

The surface reactions of adsorbed $H_2FeRu_3(CO)_{13}$ molecules were studied under UHV conditions (P_{base} < 4 x 10^{-9} mbar). Ultra-thin (< 2 - 3nm) $H_2FeRu_3(CO)_{13}$ films were deposited onto a cooled sputter cleaned Au substrate before being exposed to 500 eV incident electrons generated by a commercial flood gun source. The effect of electron irradiation on the adsorbed $H_2FeRu_3(CO)_{13}$ molecules as monitored in situ by X-ray Photoelectron Spectroscopy (XPS) and mass spectrometry.

Figure 9 shows the evolution of O(1s), Fe(2p) and Ru(3d)/C(1s) XPS regions of a nanometer thick film of $H_2FeRu_3(CO)_{13}$ adsorbed onto a gold substrate at 213 K, plotted as a function of increasing electron dose. Area analysis reveals that prior to electron irradiation, the O:Ru ratio is ~4.8 and the O:Fe ratio is ~14.5. These measured O:Ru and O:Fe ratios, in addition to the absence of any peaks in the O(1s) or C(1s) regions that would be indicative of CO decomposition, all support the idea that upon deposition at 213 K the precursor is molecularly intact prior to electron irradiation.

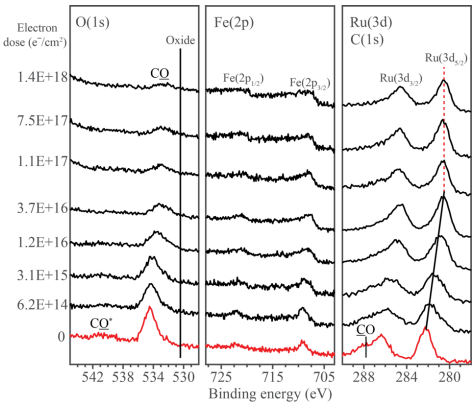

Figure 9: Evolution of O(1s), Fe(2p) and Ru(3d)/C(1s) XPS regions of a $H_2FeRu_3(CO)_{13}$ film exposed to electron doses up to $1.4x10^{18}$ e^-/cm^2.

Prior to electron irradiation, the O(1s) region consists of two peaks centered at 534.5 and 540.6 eV, which can be ascribed to the O(1s) peak and the higher binding energy/lower intensity π-π* shake up features associated with CO ligands, respectively [79-80]. Electron irradiation produces a significant decrease in intensity within the O(1s) XPS region for electron doses < $\approx 5x10^{16}$ e^-/cm^2, although thereafter it remains relatively constant in peak position and intensity. During the course of irradiation there is no evidence of oxide formation which would be expected to produce an asymmetric profile with a peak position at ≈530.5 eV [81].

In the Fe(2p) region two peaks are observed prior to electron irradiation, which correspond to the $Fe2p_{3/2}$ and $Fe2p_{1/2}$ transitions of $H_2FeRu_3(CO)_{13}$, centered at 709.1 eV and 722.3 eV respectively. Upon electron irradiation, there is a decrease in the Fe(2p) peak position (≈0.6 eV) accompanied by a change in the spectral profile from a fairly symmetric peak, indicative of iron atoms in a molecular entity such as $H_2FeRu_3(CO)_{13}$ to a peak shape more indicative of metallic iron, likely caused by an

increase in the degree of metal-metal bonding between fragments formed by the dissociation of the precursor and/or between fragments and the substrate. Careful analysis of the Fe(2p) region reveals that although there is a change in the peak shape there is no statistically significant change in the integrated area of the Fe(2p) peaks.

In the Ru(3d)/ C(1s) region, the spectral envelop can be fit with three peaks prior to electron irradiation (fitting can be seen in Fig. SI2 within the supporting material). Peaks at 286.2 eV and 282.2 eV correspond to the $Ru3d_{3/2}$ and $Ru3d_{5/2}$ transitions respectively, while another peak centered at 287.7 which appears as a shoulder to the higher binding energy side of the $Ru3d_{5/2}$ peak can be ascribed to the C(1s) peak of the CO ligands [82]. It should be noted that the π-π* shake up feature in the C(1s) peak for CO ligands expected at ~293.2 eV was not observed due to its low intensity. Upon electron irradiation, the $Ru3d_{3/2}$ and $Ru3d_{5/2}$ peak positions decrease measurably to lower binding energy, and the CO peak, at least qualitatively decreases in intensity. Spectral fitting of the Ru(3d)/C(1s) XPS region measured after an electron irradiation of dose $1.4x10^{18}$ e^-/cm^2 reveals an absence of any graphitic carbon (peak position 284.5 eV). As a consequence of electron irradiation the $Ru3d_{5/2}$ peak shape changes in a fashion analogous to the one observed for the Fe(2p) peaks without any change in the integrated area of the Ru peaks. Thus, electron irradiation does not cause any desorption of metal from the adsorbed $H_2FeRu_3(CO)_{13}$ film, under these low temperatures (≈213K).

During XPS analysis, secondary electrons will be generated and can also cause changes to the adsorbate molecules. As a result, separate control studies were conducted to determine the effect of X-ray irradiation alone on the adsorbate layer. Results from these experiments are shown in Figure SI 3 within the Supporting

Information, where a $H_2FeRu_3(CO)_{13}$ film was continuously exposed to X-rays and simultaneously analyzed using XPS. Comparison with electron irradiated films reveal that X-ray irradiation produces the same changes as electron irradiation, but at a much slower rate. Based on the variation in the O(1s) area we estimate that the time taken to acquire one XPS scan of the O(1s), Fe(2p) and C(1s)/Ru(3d) regions corresponds to an electron dose of ≈ $6.3x10^{14}$ e^-/cm^2. Consequently, the effect of X-ray irradiation during the experiments described in Figure 9 is minimal except for the shortest electron doses, where the measured dose based on electron irradiation alone is somewhat underrepresented.

Figure 10 shows that the fractional decrease in the coverage of oxygen atoms and the change in Ru($3d_{5/2}$) binding energies both follow a similar dependence on the electron dose; specifically, they both decrease significantly for comparatively short electron doses (<≈$6x10^{16}$ e^-/cm^2) but remain constant thereafter. In the case of the Ru($3d_{5/2}$) peak the binding energy decreases systematically from 282.2 eV initially to 280.6 eV (close to the Ru metal binding energy of 280.1 eV) after an electron dose of ≈ $6x10^{16}e^-/cm^2$, implying a partial reduction of Ru in the decomposition process. Over the course of the same electron dose the fractional coverage of oxygen atoms is reduced by ≈ 70% of its initial value.

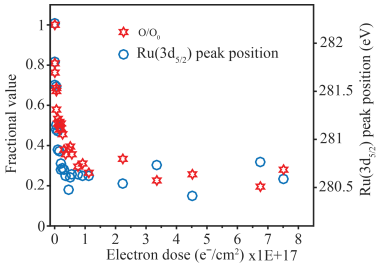

Figure 10: Change in fractional coverage of oxygen atoms (red stars) and, Ru($3d_{5/2}$) peak position (blue open circle) for $H_2FeRu_3(CO)_{13}$ films, all plotted as a function of electron dose.

Figure 11 shows the mass spectrum recorded during the electron irradiation (dose ~$1.2x10^{17}e^-/cm^2$) of a $H_2FeRu_3(CO)_{13}$ film. The only signals observed were at m/z 12 (C), 16 (O) and 28 (CO), along with some hydrogen and residual water vapor in the UHV chamber.

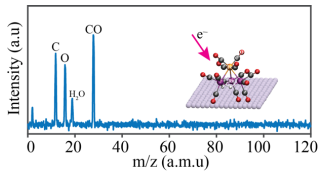

Figure 11: Mass spectrum of neutral gas phase species desorbed from the $H_2FeRu_3(CO)_{13}$ film during the course of an electron dose ~$1.2x10^{17}e^-/cm^2$.

Figure 12 shows the evolution of the O(1s), Fe(2p) and Ru(3d)/C(1s) XPS regions of a $H_2FeRu_3(CO)_{13}$ film adsorbed at 213 K (bottom set of spectra), after exposure to an electron does of $1.3x10^{17}e^-/cm^2$ (middle spectra) and then subsequently annealed to RT (298 K) (topmost spectra). An initial electron dose of $1.3x10^{17}e^-/cm^2$ was chosen because it closely corresponds to the minimum electron dose required to complete the initial stage of the reaction, in the regime where changes were observed in both the coverage of oxygen-containing species and the Ru peak position (see Figures 9 and 10). In Figure 12 the changes in the O(1s), Fe(2p) and Ru(3d)/C(1s) XPS regions for this electron dose ($1.3x10^{17}e^-/cm^2$) are seen to be similar to those shown in Figure 9, with the dominant effects being the loss of signal intensity in the O(1s) region (~70% of its initial value) and a decrease of ≈1.6 eV in the binding energy of the Ru atoms. Upon annealing this irradiated film to

RT, the O(1s) area decreased by a relative small amount (~22% in intensity) but did not disappear; moreover, a slight shoulder was still visible on the higher binding energy side of the $Ru3d_{3/2}$ peak, supporting the idea of some residual CO ligands. No change was observed in the Ru(3d) peak positions although there is a suggestion of slight broadening in the Fe(2p) region.

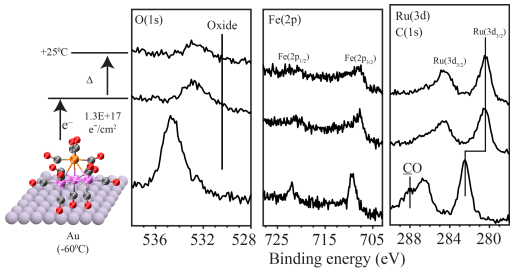

Figure 12: Changes in O(1s), Fe(2p) and Ru(3d)/C(1s) XPS regions when an $H_2FeRu_3(CO)_{13}$ film was exposed to electron dose of $1.3x10^{17}$ e^-/cm^2 (middle set of spectra) and then subsequently heated to room temperature (298 K) (uppermost set of spectra)

Discussion of surface science results: Previous UHV-surface science studies on organometallic precursors have shown that the initial step in FEBID involves electron stimulated decomposition of the precursor accompanied by ligand desorption [43-44, 46, 49-50]. This causes the deposition of non-volatile metal-containing fragments that become incorporated into the deposit. In the present study, analysis of Figures 9 and 10 reveals that this initial decomposition/deposition step is complete for electron doses on the order of $1.0x10^{17}$ e^-/cm^2 where the fraction of CO ligands present in the $H_2FeRu_3(CO)_{13}$ film is reduced to about 30% of its initial value. This is evidenced by the decrease in intensity within the O(1s) region and the evolution of CO detected by

MS (Figure 11). Further, this electron stimulated $H_2FeRu_3(CO)_{13}$ decomposition leads to decrease in the binding energy of the Fe $2p_{3/2}$ (709.1 eV to 708.5 eV) and $Ru3d_{5/2}$ (from 282.2 eV to 280.6 eV) peaks as the metal atoms are reduced; indeed, the $Ru3d_{5/2}$ binding energy of 280.6 eV after irradiation is close to the binding energy of Ru metal (280.1 eV), suggesting extensive CO desorption from the Ru atoms.

When comparing the extent of CO desorption from $H_2FeRu_3(CO)_{13}$ [83] during the electron stimulated decomposition, it is apparent from Figure 10 that 65-70% of the CO groups present in the precursor desorb in the initial decomposition step. Based on the precursor's stoichiometry we can therefore estimate that on average 8 - 9 of the 13 CO ligands present in $H_2FeRu_3(CO)_{13}$ desorb during its electron stimulated decomposition. From the gas phase experiments described earlier we infer that the average CO loss per DI incident is in the range from about 3 - 9. Similar analysis of the gas phase DEA data an average CO loss of 0.5 - 3 CO in the decomposition of $H_2FeRu_3(CO)_{13}$ up on electron attachment. These two processes, along with neutral dissociation up on electron excitation are expected to be responsible for the bulk of precursor decomposition in FEBID. Unfortunately, the extent and product formation in ND of FEBID precursors cannot be determined with the currently available instrumentations, though the first steps in this direction have recently been taken [84]. However, as discussed in the gas phase section of this contribution we expect the extent of decomposition through neutral dissociation (ND) to be similar to that effected through dissociative electron attachment (DEA), rather than dissociative ionization (DI). From the comparison of the gas phase and surface data we thus expect DI to dominate the initial electron induced decomposition process observed for $H_2FeRu_3(CO)_{13}$. However, it should be noted that the initial

fragmentation of the precursor through DEA or DI could be followed by subsequent surface induced fragmentation, which cannot be excluded.

During precursor decomposition, CO desorption occurs in the absence of any CO decomposition, which previous studies have shown would lead to the appearance of a lower binding energy peak in the O(1s) region (see Figure 9) as oxides are formed. Consequently, we can conclude that the parent $H_2FeRu_3(CO)_{13}$ molecules are initially converted into partially decarbonylated, surface bound intermediates as shown in Figure 13. This schematic also highlights the fact that DI is an inherently statistical process. As a result, we do not expect that a single partially decarbonylated intermediate is formed, but rather a distribution of $H_2FeRu_3(CO)_x$(x = 4,5) species with a coverage averaged stoichiometry of $H_2FeRu_3(CO)_x$/ (x=4.5). Unfortunately, XPS cannot detect hydrogen and H_2 is a ubiquitous background gas in UHV chambers. As a result, the surface science studies do not provide any insights into the fate of the hydrogen atoms in the precursor.

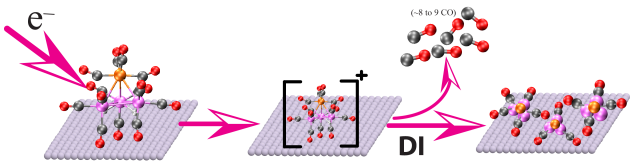

Figure 13: Initial decomposition/deposition of surface adsorbed $H_2FeRu_3(CO)_{13}$ precursor, mediated by dissociative ionization. The mixture of partially decarbonylated intermediates shown on the right side represents the statistical nature of DI, each generated by the loss of a different number of CO groups from the parent molecule.

Fate of the Partially Decarbonylated Intermediate: In FEBID, deposition is typically conducted in an electron microscope at ambient temperatures under steady state conditions, where the partially decarbonylated intermediates formed by the decomposition of precursor will be subjected either to the effects of further electron beam irradiation and/or undergo thermally stimulated reactions. In the UHV-surface science studies we can independently probe the fate of the partially decarbonylated intermediates towards further electron beam irradiation as well as their thermal stability at ambient temperatures.

Stability towards further electron irradiation: After an electron dose of ≈1x10^{17} e^{-}/cm^{2} essentially all of the parent precursor molecules have undergone electron stimulated decomposition as evidenced by the absence of any Ru(3d$^{5/2}$) peak at 282.2 eV associated with the parent compound as well as the invariance of the Ru(3d) spectral envelope for electron doses in excess of ≈1x10^{17} e^{-}/cm^{2}. At this stage the precursor molecules have been converted into partially carbonylated fragments as shown in Figure 13 with an average stoichiometry of $H_2FeRu_3(CO)_{4.5}$. The XPS results shown in Figures 9 and 10 for electron doses > ≈1x10^{17} e^{-}/cm^{2} therefore reflect the effect of further electron irradiation on these partially carbonylated fragments. In typical FEBID experiments, surface bound intermediates will often be exposed to the effects of electron irradiation as deposition occurs in the presences of a constant flux of electrons. Analysis of XPS data for electron doses > ≈1x10^{17} e^{-}/cm^{2} revealed no noticeable changes in the O(1s), Fe(2p) and Ru(3d)/C(1s) region. This suggests that the CO ligands of these partially decarbonylated intermediates are relatively stable towards electron irradiation. This is in contrast to previous studies of CO containing FEBID precursors (e.g. $W(CO)_6$ [43]) where the partially decarbonylated intermediates formed as the precursor

decomposed were susceptible to electron induced decomposition of the CO ligands and the formation of metal oxides and graphitic carbon ($M(CO)_{y(ads)} + e^- \rightarrow MO(ads) + C(ads)$). The reasons for the apparent stability of the CO ligands in the $H_2FeRu_3(CO)_x$(x = 4,5) intermediates is unclear and somewhat surprising. In the context of its influence on the metal content in FEBID structures, however, the apparent persistence of these CO ligands under the influence of electron irradiation is no different to the effect of CO decomposition as both routes will cause the associated carbon and oxygen atoms to remain in the deposit as it grows.

Thermal stability: In contrast to the low temperature (213 K) UHV surface science studies where experiments in this study are principally conducted, FEBID occurs at ambient temperatures (≈298 K). In FEBID, although the initial step must involve electron mediated decomposition/deposition of the precursor, the surface bound intermediates formed as a result of precursor decomposition could subsequently react thermally. To assess the potential for this to occur it is necessary to assess the thermal stability of the partially decarbonylated intermediates generated from $H_2FeRu_3(CO)_{13}$. Experimentally we accomplish this in Figure 12 using XPS by first exposing $H_2FeRu_3(CO)_{13}$ films to an electron dose sufficient to create the partially decarbonylated intermediates, and then annealing these species to RT. Analysis of Figure 12 reveals that there is loss of some of the O(1s) intensity (O(1s) area reduced by ~22%), but most of the CO groups in the $H_2FeRu_3(CO)_x$(x = 4,5) intermediates still remain with average stoichiometry of $H_2FeRu_3(CO)_x$(x = 3,4).

FEBID nanostructures made from $H_2FeRu_3(CO)_{13}$ under steady state conditions have metal contents <26at% as discussed *vide infra*. From the surface science results discussed so far, it is clear that the partially carbonylated intermediates generated from $H_2FeRu_3(CO)_{13}$ ($H_2FeRu_3(CO)_x$ will not change significantly in terms of their

chemical composition, regardless of whether they are subject to the effects of further electron beam irradiation (Figure 10) or thermal processing (Figure 12). Consequently, most of the associated carbon and oxygen atoms residual in the partially decarbonylated intermediates will be incorporated into the growing deposits. Indeed, the overall sequence of elementary reaction steps $H_2FeRu_3(CO)_{13}$ precursor molecules will experience in FEBID can be represented as:

$H_2FeRu_3(CO)_{13}$ (physisorbed) + e^- → $H_2FeRu_3(CO)_x$(x = 4,5) (chemisorbed) + 8.5 (CO) ↑(g)

$H_2FeRu_3(CO)_x$(x = 4,5) (chemisorbed) + e^- / Δ → most CO ligands are retained

This overall process is shown schematically in Figure 14, where the partially decarbonylated intermediates are incorporated into the FEBID nanostructure. From the stoichiometry of the film formed after irradiation and annealing of surface adsorbed $H_2FeRu_3(CO)_{13}$ film, one can estimate the metal content and the estimated value is <31%. These values match very well with the composition obtained in the current FEBID experiments with $H_2FeRu_3(CO)_{13}$. As is discussed in the next section the metal content varies in the range 21 to 26 at% with optimized deposition parameters in FEBID of $H_2FeRu_3(CO)_{13}$..

Related experiments on the electron induced decomposition of surface adsorbed $HFeCo_3(CO)_{12}$ indicate a similar behavior with regards to the initial electron induced decomposition. However, for $HFeCo_3(CO)_{12,}$ thermal CO desorption from the partially decarbonylated intermediates is essentially complete at room temperature, in contrast to the behavior of $H_2FeRu_3(CO)_{13}$.

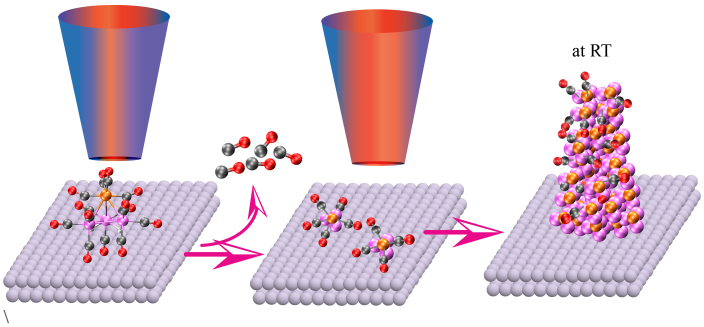

\

Figure 14: Schematic showing the incorporation of partially decarbonylated intermediate of $H_2FeRu_3(CO)_{13}$ into the deposit in FEBID.

Focused electron beam induced deposition of $H_2FeRu_3(CO)_{13}$

Heteronuclear precursors are attractive for FEBID of alloys and intermetallic compounds, in particular, if the deposit metal composition is in accordance with the stoichiometric proportions of the metal species in the precursor and if the precursor leads to deposits which are, ideally, fully metallic.

Prominent applications fields are nano-magnetism, in particular with regard to the advent of 3D nano-magnetic structures [85-86], or superconducting nanostructures for studying finite-size and (quantum) phase slip effects or the direct-writing of device structures based on tunneling or Andreev reflection [87-89].

In recent work we have shown that $HFeCo_3(CO)_{12}$ is a rather ideal precursor with regard to preserving the metal composition in FEBID and leading to deposits with high metal content (typically above 80 at%) for a wide range of deposition conditions, in particular those which are suitable for high-resolution structure formation [66].

In the following we present new results concerning the performance of $H_2FeRu_3(CO)_{13}$ as precursor in FEBID and compare this to our previous results on $HFeCo_3(CO)_{12}$.

Dependence of gas flux on deposit composition for $H_2FeRu_3(CO)_{13}$: In a first series of experiments we followed the evolution of the deposits' composition as we increased the precursor temperature in several discrete steps under otherwise fixed deposition conditions of 5 keV beam energy and 1.6 nA beam current. The pitch was set to 20 nm in both, x and y direction, and the dwell time was fixed to 1 µs. In Tab. 1 we present an overview of the composition evolution for different precursor temperatures in the first-time heating process after the initial precursor loading, and in a follow-up experiment, when the precursor had already reached the highest temperature of 338 K accessible in our setup. In these experiments we also varied the distance of the gas injection capillary to the substrate surface and field of view.

Temperature (K)	**GIS**		**Chemical composition (at%)**			
	LDFOV (µm)	DS (µm)	C	O	Fe	Ru
1st experiment: First heating of precursor after initial precursor loading						
313	90	100	23.4	75.5	0	1.1
315	90	100	30.3	67.8	0.3	1.6
323	90	100	35.1	62.3	0.4	2.2
338	65	110	40.9	51.4	1.6	6.1
2nd experiment: Heating after initial precursor conditioning up to 65 °C						

Temperature (K)	GIS		Chemical composition (at%)			
298	103	85	24.7	75.0	0.3	0.0
303	100	90	17.8	82.0	0.2	0.0
313	104	85	27.0	72.2	0.8	0.0
323	101	90	27.0	69.6	1.1	2.3
333	100	93	43.8	42.7	3.0	10.5
338	100	80	44.4	34.4	4.7	16.5

Tab. 1: Determination of the optimal gas injection system (GIS) temperature. For the confirmation of the precursor's stability under heating, the experiments were repeated after the precursor had once been heated to 338 K. The deposits were written with 5 kV, 1.6 nA, 20 nm pitch and a dwell time of 1 µs. The chemical deposition was determined via EDX. Signal contributions from the substrate, Si/Si_3N_4, as visible by the spectral contributions of Si, were taken out from the EDX quantification. LDFOV: lateral distance to center of field of view. DS: vertical distance to substrate.

From the data presented in Tab. 1 it is apparent that the highest metal content is obtained for the highest precursor flux, i.e. at 338 K. This is in clear correspondence to $HFeCo_3(CO)_{12}$ for which also sufficient precursor flux can only be obtained above 333 K. However, already at this stage a clear difference to $HFeCo_3(CO)_{12}$ is noticeable. Even at the highest flux the overall metal content of Fe-Ru does only reach 21 at%, which is far below the typical value of 80 at% of Fe-Co under the beam conditions employed here.

FEBID growth optimization: In a next step the FEBID process was optimized with regard to the metal composition by varying the beam current, x and y pitches and the dwell time. This was done with support from a semi-automatic non-linear optimization routine using a genetic algorithm (GA), as described in [90]. As a general trend, from

the GA we find short dwell times and rather large pitches to result in the highest conductance for the deposits. A more detailed account is given in Tab. 2, which summarizes the results for a subset of the growth conditions investigated in this work.

Current (nA)	**Dwell time (µs)**	**x pitch (nm)**	**y pitch (nm)**	**Chemical composition**				**resistivity (Ωcm)**
				C	O	Fe	Ru	
Standard writing parameters								
1.6	0.2	20	20	51.7	32.3	3.6	12.4	1.8×10^{5}
1.6	1	20	20	49.2	41.6	1.9	7.3	9.2×10^{3}
1.6	100	20	20	47.9	41.0	2.1	9.0	650
1.6	500	20	20	53.0	37.5	2.5	7.0	332
6.3	0.2	20	20	52.8	28.4	5.1	13.7	135
6.3	1	20	20	48.1	29.8	5.4	16.7	45.6
6.3	100	20	20	49.6	25.8	5.2	19.4	57.3
6.3	500	20	20	49.5	24.2	5.1	21.2	70.7
Optimized writing parameters								
1.6	0.3	80	74	40.5	36.5	4.7	18.3	2.55
1.6	3.7	80	74	42.2	33.9	5.1	18.8	4.38
6.3	0.4	29	31	37.8	40.8	5.0	16.4	2.46
6.3	1.1	29	31	40.5	38.7	4.3	16.5	3.66

Current (nA)	Dwell time (µs)	x pitch (nm)	y pitch (nm)	Chemical composition	resistivity (Ωcm)

Tab. 2: Overview of sample composition and room-temperature resistivity employing a set of standard writing parameters, as well as optimized parameters, as indicated. For the EDX experiments dedicated reference structures of sufficient thickness were fabricated. For these we employed the same deposition parameters as for the structures used for the transport measurements.

Three main results can be stated using $H_2FeRu_3(CO)_{13}$: (i) The largest metal content for carefully optimized deposits does not reach beyond 26 at%, which is significantly higher than the metal content obtained for other Ru-based precursors (~10%) [61] but also very low when compared to $HFeCo_3(CO)_{12}$ (>80%) [66]. (ii) The resistivity, however, is not lowest for the highest metal content but reaches its minimum for [Fe-Ru] ~21 at%, namely about 2.5 Ωcm. (iii) There is a significant variation in the Ru-to-Fe ratio, reaching from 2.7 to 4.3. This is again in stark contrast to our observations for deposits obtained from $HFeCo_3(CO)_{12}$ for which the lowest resistivities, of below 100 µΩcm, nicely correlate with the largest metal content. Moreover, the large resistivity values of the Fe-Ru deposits clearly indicate that these are not metallic but are in the thermally-assisted tunneling regime; see ref. [91] for a discussion of the electronic transport regimes of nanogranular FEBID materials. This is also clearly seen in the temperature-dependent conductivity, which we discuss in the last part of this section. We conclude this paragraph by commenting on the observed strong variability of the Ru-to-Fe ratio. Here significant deviations from the 3-to-1 ratio expected from the precursor composition are observed. In most instances the ratio exceeds 3, which indicates a partial loss of Fe during the dissociation and fragment desorption processes at work in FEBID for this precursor. With a view to the

results from the gas phase experiments, this may be a consequence of the significant apex loss as neutral $Fe(CO)_4$ in $H_2FeRu_3(CO)_{13}$, as apparent in the current gas phase studies while the loss of anionic $Fe(CO)_4^-$ is the predominant apex loss channel in $HFeCo_3(CO)_{12}$. Furthermore metal-metal bond rupture, to a large extent through apex loss, is a pre-requisite for further fragmentation of $H_2FeRu_3(CO)_{13}$ in the gas phase, but is only a parallel process to sequential CO loss in $HFeCo_3(CO)_{12}$.

Deposit morphology and co-deposit formation: Utilizing the deposition parameters from the optimization process described in the previous paragraph, we have fabricated rectangular reference structures for getting insight into the morphology of the deposits and the manifestation of co-deposit. In Figure 15(a) we show AFM cross section profiles of two deposits defined as a rectangle of size 6×2 μm^2 for two different dwell times. The beam parameters were set to 5 keV and 6.3 nA.

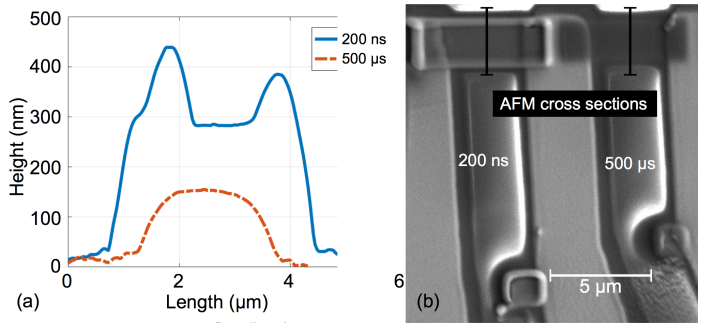

Figure 15:(a) AFM cross sections of deposits shown in the SEM micrograph (b) at the positions indicated by the black bars. The deposits were written with 5 kV, 6.3 nA and 20 nm pitch. The lateral shape of the patterns was set to be rectangular of size 6×2 µm². For short dwell time (200 ns) the deposit's dimensions exceed the pattern size by about a factor of two due to co-deposit formation.

Considering the extremely pronounced edge bulging for the short dwell time of 200 ns and the rounded shape for longer dwell times (500 µs), we attribute these morphological changes to a transition from a reaction-rate limited (RRL) to a mass-transport limited (MTL) regime with increasing dwell time. This goes in analogy to our previous results for the precursor $W(CO)_6$ described in [92]. For short dwell times the dish-shape is particularly strongly pronounced and does in fact lead to a lateral inflation of the targeted size by a factor of two. This indicates that the morphological evolution is not only the consequence of the RRL growth regime but also of a strongly pronounced co-deposit formation. This is again in stark contrast to our observations regarding the deposit shape of Fe-Co structures obtained from $HFeCo_3(CO)_{12}$. Here we find only very small co-deposit contributions and nice shape fidelity under growth conditions optimized for both, high metal content and high-resolution writing.

Electronic transport regime of Fe-Ru FEBID structures: In the last part of this section we briefly summarize our observations regarding the temperature-dependent conductivity of Fe-Ru FEBID nano-stripes optimized for high metal content and being subject to a sequence of electron irradiation steps. For nano-granular Pt FEBID structures post-growth irradiation has been shown to be very efficient in increasing the conductivity by up to four orders of magnitude, even up to the transition from a thermally activated to metallic transport [93-94]. In Figure 16 we show the temperature-dependent conductivity of Fe-Ru nano-stripes prepared at 5 keV and 6.3 nA beam energy and current, respectively. The dwell time was set to 400 ns at a symmetric pitch of 80 nm.

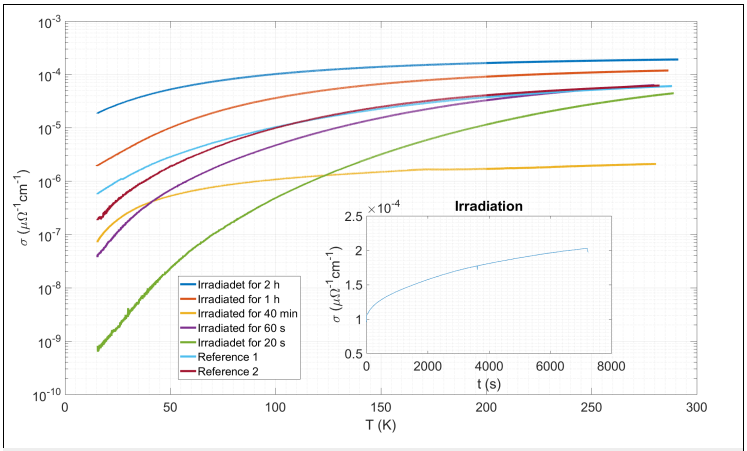

Figure 16: Transport measurements of as-grown Fe-Ru deposit and deposits grown under identical conditions after being subjected to different electron post-growth treatments, as indicated. The samples irradiated for 1 h and 2 h show the highest room-temperature conductivities, associated with the smallest reduction in conductivity as the temperature is lowered. Inset: Time-dependent evolution of the in-situ conductivity as a sample is electron irradiated in the electron microscope after growth.

As is apparent from the inset of Figure 16, the effect of post-growth electron irradiation on the conductivity of Fe-Ru deposits is noticeable, but even for extended irradiation times (2 h) the increase is just below a factor of two. The main plot in Figure 16 gives an overview of the overall temperature-dependence of Fe-Ru nano-stripes written under identical conditions but being subject to irradiation times of 20 s up to 2 h. A comparison of any of the two as-grown reference structures with the nano-stripe irradiated for only 20 s indicates that the overall variability in the activation temperature of these semiconducting / insulating deposits is rather large. The observation of a strongly activated transport, dominated by tunneling, is again in clear contrast to our observations on Fe-Co for which we routinely observe metallic

behavior, i.e. increasing conductivity as the temperature is lowered, at room-temperature resistivity levels which are at least 4 orders of magnitude lower than those observed for optimized Fe-Ru.

Conclusions

A comprehensive investigation of electron interactions with the FEBID precursor $H_2FeRu_3(CO)_{13}$ was conducted under different experimental conditions, using gas phase and UHV surface-based studies as well as focused electron beam induced deposition (FEBID).

In the current FEBID of $H_2FeRu_3(CO)_{13}$, considerable effort was given to optimize the resulting metal content of the deposit, however, only a maximum metal content of about 26 at% was achieved. Moreover, the metal content was generally found to be lower than 26 at%. This is a quite poor performance compared to the structurally similar precursor $HFeCo_3(CO)_{12}$, where stoichiometric metal content of 80 at% was routinely achieved [66]. EDX analysis of the deposits also produced a Ru/Fe ratio that was higher (average Ru/Fe $\approx$3.5 : 1) than the stoichiometric ratio of 3:1 in the intact precursor.

In gas phase electron interaction with $H_2FeRu_3(CO)_{13}$ all CO loss through DEA is preceded by metal-metal bond ruptures, with a significant apex loss in the form of neutral $Fe(CO)_4$. In DI, metal-metal bond rupture is also significant and is observed for more than 50% of all dissociation events. The average CO loss from $H_2FeRu_3(CO)_{13}$ through DI is found to be between 3 and 9 per incident and in DEA these numbers are about 0.5 to 3. In the surface experiments, decomposition of the parent molecules leads to an average loss of 8 - 9 CO groups and the formation of partially decarbonylated intermediates. The partially decarbonylated fragments

(average stoichiometry $H_2FeRu_3(CO)_{4.5}$) formed as a result of the precursor's decomposition are relatively unaffected by further electron irradiation or thermal annealing to room temperature (where typical FEBID experiments are conducted).

Comparing the extent of the CO loss through DEA and DI in the gas phase experiments with the observed CO loss in the surface experiments indicates that DI, rather than DEA is the dominating process for this precursor. However, we note that ND is not accounted for in current gas phase experiments and this process may be significant. Fragmentation through ND is expected to be more similar to DEA than DI, and should be manifested in a similar extent of CO loss. The fact that no desorption of metal containing fragments is observed in the surface experiments despite the fact that these dominate the gas phase fragmentation observed may readily be explained by the low substrate temperature in the surface experiments (213 K).

The main difference in the gas phase fragmentation of $H_2FeRu_3(CO)_{13}$ as compared to $HFeCo_3(CO)_{12}$ is the significantly more pronounced metal-metal bond ruptures observed for $H_2FeRu_3(CO)_{13}$. Especially the apparently significant apex loss through the formation of neutral $Fe(CO)_4$ is of interest as this fragment could desorb at room temperature during FEBID. Related surface studies on $HFeCo_3(CO)_{12}$ reveal that the initial electron induced decomposition of this precursor is similar to that of $H_2FeRu_3(CO)_{13}$. However, post exposure annealing to room temperature apparently allows for more efficient removal of the remaining CO ligands than is the case for $H_2FeRu_3(CO)_{13}$ [81].

With the observations from the surface science and gas phase studies we can attribute the low metal content achieved with $H_2FeRu_3(CO)_{13}$ predominantly to the persistence of the CO ligands that remain after the initial electron induced

decomposition. *Id est*, for $H_2FeRu_3(CO)_{13}$ these are not effectively removed through annealing to room temperature in the surface experiments. Consequently, the associated carbon and oxygen atoms are likely to be incorporated in FEBID nanostructures, decreasing the metal content. Moreover, the final metal content of the deposits observed for $H_2FeRu_3(CO)_{13}$ in the surface experiments is very similar to that achieved in FEBID under optimal conditions, i.e., 31 vs 26%. The vapor pressure of $H_2FeRu_3(CO)_{13}$ is also very low in FEBID experiments as compared to the background gases. This will increase the relative importance of deposition from background gases, which likely explains the observation that the metal content was often significantly less than the maximum value of 26% observed. Gas phase studies suggest that the slight increase in the Ru/Fe ratio of deposits from that of the molecular stoichiometry, could be a reflection of the desorption of neutral, iron containing ligands, predominantly $Fe(CO)_4$.

Experimental

Preparation of the heterometallic carbonyl precursors was conducted through modified procedures described in literature [95-96]. Our modified procedure for $HFeCo_3(CO)_{12}$ has been described in the literature [66], while the procedure for the synthesis of $H_2FeRu_3(CO)_{13}$ was conducted as follows (CIF file with refined data for $H_2FeRu_3(CO)_{13}$ can be provided on request).

All handling and synthesis procedures have been carried out under inert atmosphere using Schlenk and glove box techniques to prevent oxidation. $Fe(CO)_5$, $Ru_3(CO)_{12}$, H_3PO_4, benzene, hexane, 1,4-dioxane, and acetone have been purchased from Sigma Aldrich. All solvents have been deoxygenated before use. $Na_2[Fe(CO)_4]$ is formed by reduction of $Fe(CO)_5$ in THF using a sodium/benzophenone mixture as

described in literature [97]. The solid product is filtered, washed with hexane, dried under vacuum and stored in a glovebox. In a typical synthesis, 200 mg $Ru_3(CO)_{12}$ in 70 ml THF are added dropwise to a refluxing solution of 140 mg $Na_2[Fe(CO)_4]$ in 80 ml THF. The colorless solution turned red upon the first addition of the $Ru_3(CO)_{12}$ and was refluxed for additional 75 mins after complete mixing of the compounds. The solvent was subsequently removed from the solution under reduced pressure. Hexane was added to the residue and the further addition of 30 ml 20% H_3PO_4 lead to a coloration of the hexane phase due to phase transfer. The organic phase was pipetted in another flask containing anhydrous $MgSO_4$, filtered and concentrated under reduced pressure. The concentrate was chromatographically purified under argon atmosphere using silica gel (column length 30 cm; Ø 3 cm) and hexane as eluent with the column length being sufficient to clearly separate the different fractions containing other metal carbonyls. Three fractions of distinct color (yellow, green and purple) were eluted with hexane and discarded. The red product was finally stripped from the column using benzene and the solvent was removed. The crude product was crystallized from hexane to obtain sheet-like crystals of $H_2FeRu_3(CO)_{13}$, which were dried under reduced pressure. ^{1}H-NMR identified a small concentration of impurity hexanes with very low concentration in a saturated solution. These are however removed under reduced pressure. Crystals were checked by single crystal XRD (with R=2.8 %) without any solvent molecules incorporated in the crystals. Unit cell parameters were determined for different crystals and gave the same results. IR spectra are recorded, and were found to be in accordance with literature data. The thermal stability of $H_2FeRu_3(CO)_{13}$ was investigated by thermogravimety with a heating rate of 5 K min^{-1}. The onset of thermal decomposition for the precursor is at ~390 K. Since the stability at elevated temperatures is

important for the evaporation of the precursor, isotherms at different temperatures under nitrogen were recorded. The most important one for the evaporation procedure showed a mass loss of <1.5 % during heating for 4h at 343 K.

Gas phase experiments were conducted in a crossed electron/molecular beam instrument under single collision condition, a full description of the experimental setup can be found in [98] and thus only a brief description is given here. An electron beam with energy resolution of ~110 meV was generated using a trochoidal electron monochromator and crossed with an effusive beam of $H_2FeRu_3(CO)_{13}$ provided by subliming the precursor molecule into the collision chamber through a capillary tube. The flow of the molecular beam can be precisely controlled with a leak valve. Prior to the measurement, the background pressure of the collision chamber was ~$6x10^{-8}$ mbar, with heating of the inlet system to 338 - 343 K, the precursor pressure increased to 2 - $4x10^{-7}$ mbar. In order to avoid charging of the electrical lense components of the monochromator due to condensation on its surfaces, the monochromator was maintained at a temperature of about 393 K. The electron energy scale was calibrated based on the SF_6^-/SF_6 formation at 0 eV, the energy resolution of the electron beam was estimated from the FWHM of the SF_6^-/SF_6 signal at 0 eV. Both positive and negative ions formed by the interaction of electrons with $H_2FeRu_3(CO)_{13}$ were analyzed and detected using a quadrupole mass spectrometer (Hiden EPIC1000).

Compared to $HFeCo_3(CO)_{12}$ the handling of $H_2FeRu_3(CO)_{13}$ was more demanding. Maintaining sufficient pressure for acceptable signal to noise ratios and acquisition times required temperatures above 338 K, preferably higher while heating above 348 - 353 K caused decomposition of $H_2FeRu_3(CO)_{13}$ (identified by decrease of relevant fragment ion signals). For $HFeCo_3(CO)_{12}$, on the other hand, it was easy

to maintain sufficient working pressure and no change in the behavior of this compound was observed, even at temperatures as high as 358 K.

The quantum chemical calculations of the thermochemical thresholds for the negative ion fragment formation was performed using the ORCA computational chemistry software [99]. In most of the calculations we tried different ways of removing CO ligands and other respective fragments, then for each possibility we optimized the structures at the BP86 [100-101]/def2-TZVP [77] level of theory. It will optimize to the most probable and minimally energetic structure. However, it is not practical to consider all the possibilities. After geometry optimizations, the single point energies were calculated with the hybrid DFT functional PBE0 [75-76] and the basis set ma-def2-TZVP [77-78]. The energetics and threshold calculations reported in the current work are the best optimized values obtained in our quantum chemical calculations. Since the $H_2FeRu_3(CO)_{13}$ precursor molecule was heated during the experiments, we included the thermal energy of the neutral molecule in the calculation (at 343 K, the calculated thermal energy of $H_2FeRu_3(CO)_{13}$ at this temperature is 1.16 eV). We note, that this is the most probable internal energy and does not account for the actual Maxwell Boltzmann distribution of internal energies at the current temperature. The molecular orbitals and spin density of $H_2FeRu_3(CO)_{13}$ was plotted using VMD [102].

The surface science experiments were performed in a UHV-chamber equipped with XPS and MS (more details can be found in [44, 103]). A gold substrate was used because it is chemically inert and because there are no Au XPS or AES peaks which overlap with any Ru (3d)/C(1s), Fe(2p) and O(1s) XPS peaks. Prior to each experiment, the Au surface was cleaned by sputtering with 4 keV Ar^+ ions. To create $H_2FeRu_3(CO)_{13}$ films, $H_2FeRu_3(CO)_{13}$ was sublimed into the UHV- chamber

from a glass finger through heating to 338 - 343 K. The heating increased the chamber pressure from ≈$9x10^{-9}$ mbar to ≈$4x10^{-7}$ mbar. $H_2FeRu_3(CO)_{13}$ deposited onto a cooled (153 K) Au substrate. To get sufficiently thick films, it was necessary to dose the precursor continuously for 4 hr. The thickness of the film was determined from the attenuation of the Au(4f) XPS signal, using an inelastic mean free path of 2 nm for the Au(4f) photoelectrons [104]. Typical $H_2FeRu_3(CO)_{13}$ film thickness ranged from 1.1 to 1.4 nm. Based on the effective size of the $H_2FeRu_3(CO)_{13}$ molecule (estimated from the computed structure of $H_2FeRu_3(CO)_{13}$) this film thickness corresponds to 1 to 2 monolayers. The composition of the film was determined from analysis of the Ru (3d)/C(1s), Fe(2p) and O(1s) XPS transitions.

Following deposition, the substrate temperature was increased from 153 K to 213 K to ensure that any co-adsorbed water has desorbed prior to electron irradiation. A commercial flood gun (Spec FG 15/40) was used to irradiate the adsorbed film of $H_2FeRu_3(CO)_{13}$. For all surface science experiments, we used an electron (primary) beam energy of 500 eV. This value corresponds to the sum of the flood gun electron energy and a positive bias of +20 eV applied to prevent the escape of secondary electrons generated in the surface by the impact of primary electrons. Electron flux was measured based on the target current, which was held constant during a particular experiment by adjusting the electron current as needed. Changes in the film's composition and bonding as a result of electron irradiation was determined by measuring the Ru(3d)/C(1s), Fe(2p) and O(1s) transitions in terms of electron dose (electron dose = target current x exposure time).

All XPS data were recorded by a PHI 5400 XPS using Mg K_α X-rays (hv = 1253.6 eV). The measured spectra were de-convoluted using commercial software CASA XPS. The Ru(3d)/C(1s), Fe(2p) and O(1s) regions were calibrated by aligning

the measured Au($4f_{7/2}$) substrate XPS peak to 84 eV. Gas phase species which desorbed from the surface as a result of electron irradiation were monitored using a quadrupole mass spectrometer (Stanford research system, 0 to 200 amu).

The FEBID experiments were performed in a dual beam microscope (FEI Nova NanoLab 600) equipped with a Schottky electron emitter. The base pressure of the system was 4×10^{-6}mbar. An Omniprobe gas injector with inner diameter of the capillary of 0.5 mm was used. The distances of the capillary to the substrate surface and the center of the field of view were 100 µm (vertically) and 90 to 100 µm (laterally), respectively. The precursor $HFeCo_3(CO)_{12}$ was heated to 337 K leading to an increase of the chamber pressure by about 1×10^{-7} mbar. The precursor $H_2FeRu_3(CO)_{13}$ was heated in several steps up to 338 K leading to a hardly detectable increase of the chamber pressure. The deposition experiments were done on p-doped Si(100) substrates with native oxide, thermally grown SiO_2 (200 nm) or Si_3N_4 (100 nm). We did not observe an appreciable influence of the different substrate materials on the results of the deposition experiments. The substrate temperature was 296 K for all deposition experiments. After some preliminary experiments we set the beam energy to 5 keV for the deposition experiments with $H_2FeRu_3(CO)_{13}$, as we observed a strong reduction in both, deposition yield and metal content at higher beam energies. For $HFeCo_3(CO)_{12}$ we have shown in previous work that high metal contents can be obtained for a wide range of beam energies and currents [66].

Energy-dispersive x-ray analysis (EDX) experiments were performed in-situ directly after growth at 5 keV beam energy and 1 nA beam current.

Transport measurements were performed in the temperature range from 2 to 300 K under fixed bias voltage conditions in two- or four-probe configuration

employing Cr/Au electrode structures prepared by dc magnetron sputtering and standard UV lithography.

Atomic force microscopy (Nanosurf EasyScan 2) in dynamic, non-contact mode was done on selected samples.

Supporting Information File 1:

File name: Supporting Information H2FeRu3CO13_Gasphase_surface_FEBID

Title: Supporting Information for Electron Interactions with the heteronuclear carbonyl precursor ($H_2FeRu_3(CO)_{13}$): from fundamental gas phase and surface science studies to focused electron beam induced deposition

Acknowledgements

The authors acknowledge the fruitful and productive environment provided by the COST Action CELINA CM1301 and we like to take the opportunity to extend our thanks to Prof. Petra Swiderek for running this Action exceptionally well. Marc Hanefeld and Michael Huth acknowledge financial support by the Deutsche Forschungsgemeinschaft (DFG) through Priority Program SPP 1928, project HU 752/12-1. DHF thanks the National Science Foundation for support of this work through the linked collaborative grants CHE-1607621 and CHE-160754. 7OI acknowledges supported from the Icelandic Center of Research (RANNIS) Grant No. 13049305(1-3) and the University of Iceland Research Fund. R K T P acknowledges a doctoral grant from the University of Iceland Research Fund and financial support from the COST Action CM1301; CELINA, for short term scientific missions (STSMs)

References

1. Fowlkes, J. D.; Winkler, R.; Lewis, B. B.; Stanford, M. G.; Plank, H.; Rack, P. D., Simulation-Guided 3D Nanomanufacturing via Focused Electron Beam Induced Deposition. *ACS Nano* **2016,** *10* (6), 6163-6172.
2. Bret, T.; Utke, I.; Hoffmann, P., Influence of the beam scan direction during focused electron beam induced deposition of 3D nanostructures. *Microelectron. Eng.* **2005,** *78*, 307-313.
3. Huth, M.; Porrati, F.; Schwalb, C.; Winhold, M.; Sachser, R.; Dukic, M.; Adams, J.; Fantner, G., Focused electron beam induced deposition: A perspective. *Beilstein J. Nanotech.* **2012,** *3*, 597-619.
4. Utke, I.; Hoffmann, P.; Melngailis, J., Gas-assisted focused electron beam and ion beam processing and fabrication. *J. Vac. Sci. Technol. B.* **2008,** *26* (4), 1197-1276.
5. van Dorp, W. F.; Hagen, C. W., A critical literature review of focused electron beam induced deposition. *J. Appl. Phys.* **2008,** *104* (8), 081301.
6. Shawrav, M. M.; Taus, P.; Wanzenboeck, H. D.; Schinnerl, M.; Stöger-Pollach, M.; Schwarz, S.; Steiger-Thirsfeld, A.; Bertagnolli, E., Highly conductive and pure gold nanostructures grown by electron beam induced deposition. *Scientific Reports* **2016,** *6*, 34003.
7. Mehendale, S.; Mulders, J. J. L.; Trompenaars, P. H. F., Purification of Au EBID structures by electron beam post-irradiation under oxygen flux at room temperature. *Microelectron. Eng.* **2015,** *141*, 207-210.
8. Winkler, R.; Schmidt, F.-P.; Haselmann, U.; Fowlkes, J. D.; Lewis, B. B.; Kothleitner, G.; Rack, P. D.; Plank, H., Direct-Write 3D Nanoprinting of Plasmonic Structures. *ACS Appl. Mater. Inter.* **2017,** *9* (9), 8233-8240.
9. Sachser, R.; Reith, H.; Huzel, D.; Winhold, M.; Huth, M., Catalytic Purification of Directly Written Nanostructured Pt Microelectrodes. *ACS Appl. Mater. Inter.* **2014,** *6* (18), 15868-15874.
10. Mehendale, S.; Mulders, J. J. L.; Trompenaars, P. H. F., A new sequential EBID process for the creation of pure Pt structures from MeCpPtMe 3. *Nanotechnology* **2013,** *24* (14), 145303.
11. Plank, H.; Noh, J. H.; Fowlkes, J. D.; Lester, K.; Lewis, B. B.; Rack, P. D., Electron-Beam-Assisted Oxygen Purification at Low Temperatures for Electron-Beam-Induced Pt Deposits: Towards Pure and High-Fidelity Nanostructures. *ACS Appl. Mater. Inter.* **2014,** *6* (2), 1018-1024.
12. Lewis, B. B.; Stanford, M. G.; Fowlkes, J. D.; Lester, K.; Plank, H.; Rack, P. D., Electron-stimulated purification of platinum nanostructures grown via focused electron beam induced deposition. *Beilstein. J. Nanotech.* **2015,** *6*, 907-918.
13. Geier, B.; Gspan, C.; Winkler, R.; Schmied, R.; Fowlkes, J. D.; Fitzek, H.; Rauch, S.; Rattenberger, J.; Rack, P. D.; Plank, H., Rapid and Highly Compact Purification for Focused Electron Beam Induced Deposits: A Low Temperature Approach Using Electron Stimulated H2O Reactions. *J. Phys. Chem. C.* **2014,** *118* (25), 14009-14016.
14. Puydinger dos Santos, M. V.; Velo, M. F.; Domingos, R. D.; Zhang, Y.; Maeder, X.; Guerra-Nuñez, C.; Best, J. P.; Béron, F.; Pirota, K. R.; Moshkalev, S.; Diniz, J. A.; Utke, I., Annealing-Based Electrical Tuning of Cobalt–Carbon Deposits Grown by Focused-Electron-Beam-Induced Deposition. *ACS Appl. Mater. Inter.* **2016,** *8* (47), 32496-32503.
15. Begun, E.; Dobrovolskiy, O. V.; Kompaniiets, M.; Sachser, R.; Gspan, C.; Plank, H.; Huth, M., Post-growth purification of Co nanostructures prepared by focused electron beam induced deposition. *Nanotechnology* **2015,** *26* (7), 075301.
16. Dobrovolskiy, O. V.; Kompaniiets, M.; Sachser, R.; Porrati, F.; Gspan, C.; Plank, H.; Huth, M., Tunable magnetism on the lateral mesoscale by post-processing of Co/Pt heterostructures. *Beilstein. J. Nanotech.* **2015,** *6*, 1082-1090.
17. Silvis-Cividjian, N.; Hagen, C. W.; Leunissen, L. H. A.; Kruit, P., The role of secondary electrons in electron-beam-induced-deposition spatial resolution. *Microelectro. Eng.* **2002,** *61*, 693-699.
18. Botman, A.; De Winter, D. A. M.; Mulders, J. J. L., Electron-beam-induced deposition of platinum at low landing energies. *J. Vac. Sci. Technol. B.* **2008,** *26* (6), 2460-2463.
19. Schaefer, J.; Hoelzl, J., A contribution to the dependence of secondary electron emission from the work function and Fermi energy. *Thin Solid Films* **1972,** *13* (1), 81-86.

20. Ohya, K.; Harada, A.; Kawata, J.; Nishimura, K., Monte Carlo simulation of yield and energy distribution of secondary electrons emitted from metal surfaces. *Japn. J. Appl. Phys.* **1996,** *35* (12A), 6226-6232.
21. Schou, J., Transport theory for kinetic emission of secondary electrons from solids. *Phys. Rev. B.* **1980,** *22* (5), 2141.
22. Thorman, R. M.; Kumar T. P, R.; Fairbrother, D. H.; Ingólfsson, O., The role of low-energy electrons in focused electron beam induced deposition: four case studies of representative precursors. *Beilstein J. Nanotech.* **2015,** *6*, 1904-1926.
23. Ingólfsson, O.; Weik, F.; Illenberger, E., The reactivity of slow electrons with molecules at different degrees of aggregation: gas phase, clusters and condensed phase. *Int. J. Mass. Spectrom. Ion Processes* **1996,** *155* (1-2), 1-68.
24. Bald, I.; Langer, J.; Tegeder, P.; Ingólfsson, O., From isolated molecules through clusters and condensates to the building blocks of life. *IJMS* **2008,** *277* (1), 4-25.
25. Bohler, E.; Warneke, J.; Swiderek, P., Control of chemical reactions and synthesis by low-energy electrons. *Chem. Soc. Rev.* **2013,** *42* (24), 9219-9231.
26. Christophoru, L. G., *Electron-Molecule Interactions and their Applications*. Academic Press: Orlando, Florida, 1984; Vol.; Vol. 1.
27. Hotop, H.; Ruf, M.-W.; Allan, M.; Fabrikant, I., Resonance and threshold phenomena in low-energy electron collisions with molecules and clusters. *Adv. Atom. Mol. Opt. Phys.* **2003,** *49*, 85-216.
28. Arumainayagam, C. R.; Lee, H.-L.; Nelson, R. B.; Haines, D. R.; Gunawardane, R. P., Low-energy electron-induced reactions in condensed matter. *Surf. Sci. Rep.* **2010,** *65* (1), 1-44.
29. Fabrikant, I. I.; Eden, S.; Mason, N. J.; Fedor, J., Chapter Nine - Recent Progress in Dissociative Electron Attachment: From Diatomics to Biomolecules. In *Advances In Atomic, Molecular, and Optical Physics*, Ennio Arimondo, C. C. L.; Susanne, F. Y., Eds. Academic Press: 2017; Vol. Volume 66, pp 545-657.
30. Engmann, S.; Stano, M.; Matejčík, Š.; Ingólfsson, O., The role of dissociative electron attachment in focused electron beam induced processing: a case study on cobalt tricarbonyl nitrosyl. *Angew. Chem. Int. Edit.* **2011,** *50* (40), 9475-9477.
31. Engmann, S.; Stano, M.; Papp, P.; Brunger, M. J.; Matejčík, Š.; Ingólfsson, O., Absolute cross sections for dissociative electron attachment and dissociative ionization of cobalt tricarbonyl nitrosyl in the energy range from 0 eV to 140 eV. *J. Chem. Phys.* **2013,** *138* (4), 044305.
32. May, O.; Kubala, D.; Allan, M., Dissociative electron attachment to Pt $(PF_3)_4$—a precursor for Focused Electron Beam Induced Processing (FEBIP). *Phys. Chem. Chem. Phys.* **2012,** *14* (9), 2979-2982.
33. Allan, M., Electron scattering in Pt $(PF_3)_4$: Elastic scattering, vibrational, and electronic excitation. *J. Chem. Phys.* **2011,** *134* (20), 204309.
34. Wnorowski, K.; Stano, M.; Matias, C.; Denifl, S.; Barszczewska, W.; Matejčík, Š., Low-energy electron interactions with tungsten hexacarbonyl–W $(CO)_6$. *Rapid. Commun. Mass. Sp.* **2012,** *26* (17), 2093-2098.
35. Engmann, S.; Stano, M.; Matejčík, Š.; Ingólfsson, O., Gas phase low energy electron induced decomposition of the focused electron beam induced deposition (FEBID) precursor trimethyl (methylcyclopentadienyl) platinum (iv)(MeCpPtMe 3). *Phys. Chem. Chem. Phys.* **2012,** *14* (42), 14611-14618.
36. Lacko, M.; Papp, P.; Wnorowski, K.; Matejčík, Š., Electron-induced ionization and dissociative ionization of iron pentacarbonyl molecules. *Eur. Phys. J. D.* **2015,** *69* (3), 84.
37. Thorman, R. M.; Brannaka, J. A.; McElwee-White, L.; Ingolfsson, O., Low energy electron-induced decomposition of η^3-C_3H_5)$Ru(CO)_3Br$, a potential focused electron beam induced deposition precursor with a heteroleptic ligand set. *Phys. Chem. Chem. Phys.* **2017,** *19* (20), 13264-13271.
38. Thorman, R. M.; Bjornsson, R.; Ingólfsson, O., Computational study of dissociative electron attachment to π-allyl ruthenium (II) tricarbonyl bromide. *Eur. Phys. J. D.* **2016,** *8* (70), 1-7.
39. T P, R. K.; Barth, S.; Bjornsson, R.; Ingólfsson, O., Structure and energetics in dissociative electron attachment to $HFeCo_3(CO)_{12}$. *Eur. Phys. J. D.* **2016,** *70* (8), 163.

40. T P, R. K.; Bjornsson, R.; Barth, S.; Ingólfsson, O., Formation and decay of negative ion states up to 11 eV above the ionization energy of the nanofabrication precursor $HFeCo_3(CO)_{12}$. *Chem. Sci.* **2017,** *8* (9), 5949-5952.
41. Zlatar, M.; Allan, M.; Fedor, J., Excited States of Pt $(PF_3)_4$ and Their Role in Focused Electron Beam Nanofabrication. *J. Phys. Chem. C.* **2016,** *120* (19), 10667-10674.
42. Landheer, K.; Rosenberg, S. G.; Bernau, L.; Swiderek, P.; Utke, I.; Hagen, C. W.; Fairbrother, D. H., Low-Energy Electron-Induced Decomposition and Reactions of Adsorbed Tetrakis(trifluorophosphine)platinum $[Pt(PF_3)_4]$. *J. Phys. Chem. C.* **2011,** *115* (35), 17452-17463.
43. Rosenberg, S. G.; Barclay, M.; Fairbrother, D. H., Electron induced reactions of surface adsorbed tungsten hexacarbonyl (W(CO)6). *Phys. Chem. Chem. Phys.* **2013,** *15* (11), 4002-4015.
44. Wnuk, J. D.; Gorham, J. M.; Rosenberg, S. G.; van Dorp, W. F.; Madey, T. E.; Hagen, C. W.; Fairbrother, D. H., Electron Induced Surface Reactions of the Organometallic Precursor Trimethyl(methylcyclopentadienyl)platinum(IV). *J. Phys. Chem. C.* **2009,** *113* (6), 2487-2496.
45. Hedhili, M.; Bredehöft, J.; Swiderek, P., Electron-induced reactions of $MeCpPtMe_3$ investigated by HREELS. *J. Phys. Chem. C.* **2009,** *113* (30), 13282-13286.
46. Rosenberg, S. G.; Barclay, M.; Fairbrother, D. H., Electron Beam Induced Reactions of Adsorbed Cobalt Tricarbonyl Nitrosyl $(Co(CO)_3NO)$ Molecules. *J. Phys. Chem. C.* **2013,** *117* (31), 16053-16064.
47. Hauchard, C.; Rowntree, P. A., Low-energy electron-induced decarbonylation of $Fe(CO)_5$ films adsorbed on Au(111) surfaces. *Can. J. Chem.* **2011,** *89* (10), 1163-1173.
48. Spencer, J. A.; Wu, Y.-C.; McElwee-White, L.; Fairbrother, D. H., Electron Induced Surface Reactions of cis-$Pt(CO)_2Cl_2$: A Route to Focused Electron Beam Induced Deposition of Pure Pt Nanostructures. *J. Am. Chem. Soc.* **2016,** *138* (29), 9172-9182.
49. Spencer, J. A.; Brannaka, J. A.; Barclay, M.; McElwee-White, L.; Fairbrother, D. H., Electron-Induced Surface Reactions of η^3-Allyl Ruthenium Tricarbonyl Bromide $[(\eta^3\text{-}C_3H_5)Ru(CO)_3Br]$: Contrasting the Behavior of Different Ligands. *J. Phys. Chem. C.* **2015,** *119* (27), 15349-15359.
50. Spencer, J. A.; Rosenberg, S. G.; Barclay, M.; Wu, Y.-C.; McElwee-White, L.; Fairbrother, D. H., Understanding the electron-stimulated surface reactions of organometallic complexes to enable design of precursors for electron beam-induced deposition. *Appl. Phys. A.* **2014,** *117* (4), 1631-1644.
51. Masaki, T.; Masayuki, S.; Kazuo, F., Fabrication of magnetic nanostructures using electron beam induced chemical vapour deposition. *Nanotechnology* **2005,** *16* (8), 1321.
52. Lukasczyk, T.; Schirmer, M.; Steinrück, H.-P.; Marbach, H., Electron-Beam-Induced Deposition in Ultrahigh Vacuum: Lithographic Fabrication of Clean Iron Nanostructures. *Small* **2008,** *4* (6), 841-846.
53. Rodríguez, L. A.; Deen, L.; Córdoba, R.; Magén, C.; Snoeck, E.; Koopmans, B.; De Teresa, J. M., Influence of the shape and surface oxidation in the magnetization reversal of thin iron nanowires grown by focused electron beam induced deposition. *Beilstein. J. Nanotech.* **2015,** *6*, 1319-1331.
54. Lavrijsen, R.; Córdoba, R.; Schoenaker, F. J.; Ellis, T. H.; Barcones, B.; Kohlhepp, J. T.; Swagten, H. J. M.; Koopmans, B.; Teresa, J. M. D.; Magén, C.; Ibarra, M. R.; Trompenaars, P.; Mulders, J. J. L., Fe:O:C grown by focused-electron-beam-induced deposition: magnetic and electric properties. *Nanotechnology* **2011,** *22* (2), 025302.
55. Fernández-Pacheco, A.; Teresa, J. M. D.; Córdoba, R.; Ibarra, M. R., Magnetotransport properties of high-quality cobalt nanowires grown by focused-electron-beam-induced deposition. *J. Phys. D. Appl. Phys.* **2009,** *42* (5), 055005.
56. Serrano-Ramón, L.; Córdoba, R.; Rodríguez, L. A.; Magén, C.; Snoeck, E.; Gatel, C.; Serrano, I.; Ibarra, M. R.; De Teresa, J. M., Ultrasmall Functional Ferromagnetic Nanostructures Grown by Focused Electron-Beam-Induced Deposition. *ACS Nano* **2011,** *5* (10), 7781-7787.
57. Córdoba, R.; Sharma, N.; Kölling, S.; M. Koenraad, P.; Koopmans, B., High-purity 3D nano-objects grown by focused-electron-beam induced deposition. *Nanotechnology* **2016,** *27* (35), 355301.
58. Vollnhals, F.; Woolcot, T.; Walz, M. M.; Seiler, S.; Steinruck, H. P.; Thornton, G.; Marbach, H., Electron Beam-Induced Writing of Nanoscale Iron Wires on a Functional Metal Oxide. *J. Phys. Chem. C.* **2013,** *117* (34), 17674-17679.

59. Muthukumar, K.; Jeschke, H. O.; Valentí, R.; Begun, E.; Schwenk, J.; Porrati, F.; Huth, M., Spontaneous dissociation of $Co_2(CO)_8$ and autocatalytic growth of Co on SiO_2: A combined experimental and theoretical investigation. *Beilstein. J. Nanotech.* **2012,** *3*, 546-555.
60. Scheuer, V.; Koops, H.; Tschudi, T., Electron beam decomposition of carbonyls on silicon. *Microelectron. Eng.* **1986,** *5* (1), 423-430.
61. Noh, J. H.; Stanford, M. G.; Lewis, B. B.; Fowlkes, J. D.; Plank, H.; Rack, P. D., Nanoscale electron beam-induced deposition and purification of ruthenium for extreme ultraviolet lithography mask repair. *Appl. Phys. A.* **2014,** *117* (4), 1705-1713.
62. Porrati, F.; Kämpken, B.; Terfort, A.; Huth, M., Fabrication and electrical transport properties of binary Co-Si nanostructures prepared by focused electron beam-induced deposition. *J. Appl. Phys.* **2013,** *113* (5), 053707.
63. Winhold, M.; Schwalb, C. H.; Porrati, F.; Sachser, R.; Frangakis, A. S.; Kämpken, B.; Terfort, A.; Auner, N.; Huth, M., Binary Pt–Si Nanostructures Prepared by Focused Electron-Beam-Induced Deposition. *ACS Nano* **2011,** *5* (12), 9675-9681.
64. Porrati, F.; Begun, E.; Winhold, M.; Ch, H. S.; Sachser, R.; Frangakis, A. S.; Huth, M., Room temperature L 1 0 phase transformation in binary CoPt nanostructures prepared by focused-electron-beam-induced deposition. *Nanotechnology* **2012,** *23* (18), 185702.
65. Porrati, F.; Sachser, R.; Gazzadi, G. C.; Frabboni, S.; Huth, M., Fabrication of FeSi and Fe3Si compounds by electron beam induced mixing of [Fe/Si]2 and [Fe3/Si]2 multilayers grown by focused electron beam induced deposition. *J. Appl. Phys.* **2016,** *119* (23), 234306.
66. Porrati, F.; Pohlit, M.; Müller, J.; Barth, S.; Biegger, F.; Gspan, C.; Plank, H.; Huth, M., Direct writing of CoFe alloy nanostructures by focused electron beam induced deposition from a heteronuclear precursor. *Nanotechnology* **2015,** *26* (47), 475701.
67. Kruglyak, V. V.; Demokritov, S. O.; Grundler, D., Magnonics. *J. Phys. D. Appl. Phys.* **2010,** *43* (26), 264001.
68. Joshi, V. K., Spintronics: A contemporary review of emerging electronics devices. *Engineering Science and Technology, an International Journal* **2016,** *19* (3), 1503-1513.
69. Pablo-Navarro, J.; Sanz-Hernández, D.; Magén, C.; Fernández-Pacheco, A.; Teresa, J. M. d., Tuning shape, composition and magnetization of 3D cobalt nanowires grown by focused electron beam induced deposition (FEBID). *J. Phys. D. Appl. Phys.* **2017,** *50* (18), 18LT01.
70. Pohlit, M.; Porrati, F.; Huth, M.; Ohno, Y.; Ohno, H.; Müller, J., Magnetic stray-field studies of a single Cobalt nanoelement as a component of the building blocks of artificial square spin ice. *J. Magn. Magn. Mater.* **2016,** *400*, 206-212.
71. Pohlit, M.; Stockem, I.; Porrati, F.; Huth, M.; Schröder, C.; Müller, J., Experimental and theoretical investigation of the magnetization dynamics of an artificial square spin ice cluster. *J. Appl. Phys.* **2016,** *120* (14), 142103.
72. Gilmore, C. J.; Woodward, P., Crystal and molecular structure of $H_2FeRu_3(CO)_{13}$; a tetrahedral hydridocarbonyl of iron and ruthenium containing asymmetric carbon bridges. *J. Chem. Soc. A.* **1971,** (0), 3453-3458.
73. T P, R. K.; Barth, S.; Bjornsson, R.; Ingólfsson, O., Dissociative electron attachment and dissociative ionization of bimetallic FEBID precursor $HFeCo_3(CO)_{12}$. *Manuscript in preparation* **2017**.
74. Patiny, L.; Borel, A., ChemCalc: a building block for tomorrow's chemical infrastructure. ACS Publications: 2013.
75. Perdew, J. P.; Burke, K.; Ernzerhof, M., Generalized gradient approximation made simple. *Phys. Rev. Lett.* **1996,** *77* (18), 3865.
76. Adamo, C.; Barone, V., Toward reliable density functional methods without adjustable parameters: The PBE0 model. *J. Chem. Phys.* **1999,** *110* (13), 6158-6170.
77. Weigend, F.; Ahlrichs, R., Balanced basis sets of split valence, triple zeta valence and quadruple zeta valence quality for H to Rn: Design and assessment of accuracy. *Phys. Chem. Chem. Phys.* **2005,** *7* (18), 3297-3305.
78. Zheng, J.; Xu, X.; Truhlar, D. G., Minimally augmented Karlsruhe basis sets. *Theor. Chem. Acc.* **2011,** *128* (3), 295-305.

79. Barber, M.; Connor, J.; Guest, M.; Hall, M.; Hillier, I.; Meredith, W., High energy photoelectron spectroscopy of transition metal complexes. Part 1.—Bonding in substituted and unsubstituted first row carbonyls. *Faraday. Discuss. Chem. Soc* **1972,** *54*, 219-226.
80. Plummer, E. W.; Salaneck, W. R.; Miller, J. S., Photoelectron spectra of transition-metal carbonyl complexes: comparison with the spectra of adsorbed CO. *Phys. Rev. B* **1978,** *18* (4), 1673.
81. T P, R. K.; Unlu, I.; Barth, S.; Ingólfsson, O.; Fairbrother, D. H., Electron Induced Surface Reactions of $HFeCo_3(CO)_{12}$, a Bimetallic Precursor for Focused Electron Beam Induced Deposition (FEBID). *J. Phys. Chem. C., submitted* **2017**.
82. Moulder, J. F.; Chastain, J., *Handbook of X-ray Photoelectron Spectroscopy: A Reference Book of Standard Spectra for Identification and Interpretation of XPS Data*. Physical Electronics: Chanhassen, 1995.
83. Johannesson, G. H.; Wang, H. S.; Kvaran, A., REMPI Spectra of Cl_2: Vibrational and Rotational Analysis of the 2^1P_g Rydberg States of $^{35}Cl_2$, $^{35}Cl^{37}Cl$, and $^{37}Cl_2$. *J. Mol. Spectrosc.* **1996,** *179* (2), 334-341.
84. Li, Z.; Milosavljević, A. R.; Carmichael, I.; Ptasinska, S., Characterization of neutral radicals from a dissociative electron attachment process. *Phys. Rev. Lett.* **2017,** *119* (5), 053402.
85. Fernandez-Pacheco, A.; Streubel, R.; Fruchart, O.; Hertel, R.; Fischer, P.; Cowburn, R. P., Three-dimensional nanomagnetism. *Nat. Commun.* **2017,** *8*, 14.
86. Keller, L.; Mamoori, M. A.; Pieper, J.; Gspan, C.; Stockem, I.; Schröder, C.; Barth, S.; Winkler, R.; Plank, H.; Pohlit, M.; Muller, J.; Huth, M., Direct-write of free-form building blocks for artificial magnetic 3D lattices. *Submitted to Nature Commun.* **2017**.
87. Bezryadin, A., *Superconductivity in Nanowires - Fabrication and Quantum Transport*. Wiley-VCH: 2012; p 282.
88. Sangiao, S.; Morellon, L.; Ibarra, M. R.; De Teresa, J. M., Ferromagnet-superconductor nanocontacts grown by focused electron/ion beam techniques for current-in-plane Andreev Reflection measurements. *Solid State Commun.* **2011,** *151* (1), 37-41.
89. Winhold, M.; Weirich, P. M.; Schwalb, C. H.; Huth, M., Superconductivity and metallic behavior in PbxCyO delta structures prepared by focused electron beam induced deposition. *Appl. Phys. Lett.* **2014,** *105* (16), 5.
90. Weirich, P. M.; Winhold, M.; Schwalb, C. H.; Huth, M., In situ growth optimization in focused electron-beam induced deposition. *Beilstein J. Nanotech.* **2013,** *4*, 919-926.
91. Huth, M.; Porrati, F.; Dobrovolskiy, O. V., Focused electron beam induced deposition meets materials science. *Microelectron. Eng.* **2017**.
92. Winhold, M.; Weirich, P. M.; Schwalb, C. H.; Huth, M., Identifying the Crossover between Growth Regimes via in-situ Conductance Measurements in Focused Electron Beam Induced Deposition. *Nanofabrication* **2014,** *1*, 86-95.
93. Porrati, F.; Sachser, R.; Schwalb, C. H.; Frangakis, A. S.; Huth, M., Tuning the electrical conductivity of Pt-containing granular metals by postgrowth electron irradiation. *J. Appl. Phys.* **2011,** *109* (6), 7.
94. Sachser, R.; Porrati, F.; Schwalb, C. H.; Huth, M., Universal Conductance Correction in a Tunable Strongly Coupled Nanogranular Metal. *Phys. Rev. Lett.* **2011,** *107* (20), 5.
95. Chini, P.; Colli, L.; Peraldo, M., Preparazione a proprietà dell'idrocarbonile $HFeCo_3(CO)_{12}$ e di alcuni composti derivati dall'anione $[FeCo_3(CO)_{12}]^-$. *Gazz. Chim. Ital* **1960,** *90*, 1005-1020.
96. Geoffroy, G. L.; Gladfelter, W. L., Synthesis of tetrahedral mixed-metal clusters of the iron triad. Preparation and characterization of tridecacarbonyldihydroironosmiumdiruthenium and tridecacarbonyldihydroirondiosmiumruthenium. *J. Am. Chem. Soc.* **1977,** *99* (23), 7565-7573.
97. Herrmann, W. A., *Synthetic Methods of Organometallic and Inorganic Chemistry, Volume 7, 1997: Volume 7: Transition Metals*. Thieme: 2014.
98. Bjarnason, E. H.; Ómarsson, B.; Engmann, S.; Ómarsson, F. H.; Ingólfsson, O., Dissociative electron attachment to titatinum tetrachloride and titanium tetraisopropoxide. *Eur. Phys. J. D* **2014,** *68* (5), 1-8.
99. Neese, F., The ORCA program system. *Wires. Comput. Mol. Sci.* **2012,** *2* (1), 73-78.

100. Becke, A. D., Density-functional exchange-energy approximation with correct asymptotic behavior. *Phys. Rev. A.* **1988,** *38* (6), 3098.
101. Perdew, J. P., Density-functional approximation for the correlation energy of the inhomogeneous electron gas. *Phys. Rev. B.* **1986,** *33* (12), 8822.
102. Humphrey, W.; Dalke, A.; Schulten, K., VMD: visual molecular dynamics. *J. Mol. Graphics.* **1996,** *14* (1), 33-38.
103. Wnuk, J. D.; Gorham, J. M.; Rosenberg, S. G.; van Dorp, W. F.; Madey, T. E.; Hagen, C. W.; Fairbrother, D. H., Electron beam irradiation of dimethyl-(acetylacetonate) gold (III) adsorbed onto solid substrates. *J. Appl. Phys.* **2010,** *107* (5), 054301.
104. Tanuma, S.; Powell, C. J.; Penn, D. R., Calculations of electorn inelastic mean free paths. II. Data for 27 elements over the 50–2000 eV range. *Surf. Interface. Anal.* **1991,** *17* (13), 911-926.

Article V

Electron beam induced deposition of silacyclohexane and dichlorosilacyclohexane; the role of dissociative ionization and dissociative electron attachment in the deposition process

Ragesh Kumar T P, Sangeetha Hari, Krishna K Damodaran, Oddur Ingólfsson and Cornelis W. Hagen.

Beilstein Journal of Nanotechnology, **8** 2376-2388 (2017)

Ragesh Kumar T P carried out most of the experiments and analysed the data, he wrote the first draft of the paper and contributed to editing until publication.

BEILSTEIN JOURNAL OF NANOTECHNOLOGY

Electron beam induced deposition of silacyclohexane and dichlorosilacyclohexane: the role of dissociative ionization and dissociative electron attachment in the deposition process

Ragesh Kumar T P[1], Sangeetha Hari[2], Krishna K Damodaran[1], Oddur Ingólfsson[*1] and Cornelis W. Hagen[*2]

Full Research Paper

Open Access

Address:
[1]Department of Chemistry and Science Institute, University of Iceland, Dunhagi 3, 107 Reykjavik, Iceland and [2]Department of ImPhys, Delft University of Technology, Lorentzweg 1, 2628CJ Delft, Netherlands

Email:
Oddur Ingólfsson[*] - odduring@hi.is; Cornelis W. Hagen[*] - C.W.Hagen@tudelft.nl

* Corresponding author

Keywords:
dichlorosilacyclohexane; dissociative electron attachment; dissociative ionization; electron beam induced deposition; low-energy electrons; silacyclohexane

Beilstein J. Nanotechnol. **2017,** *8,* 2376–2388.
doi:10.3762/bjnano.8.237

Received: 12 July 2017
Accepted: 09 October 2017
Published: 10 November 2017

This article is part of the Thematic Series "Chemistry for electron-induced nanofabrication".

Guest Editor: H. Marbach

Abstract

We present first experiments on electron beam induced deposition of silacyclohexane (SCH) and dichlorosilacyclohexane (DCSCH) under a focused high-energy electron beam (FEBID). We compare the deposition dynamics observed when growing pillars of high aspect ratio from these compounds and we compare the proximity effect observed for these compounds. The two precursors show similar behaviour with regards to fragmentation through dissociative ionization in the gas phase under single-collision conditions. However, while DCSCH shows appreciable cross sections with regards to dissociative electron attachment, SCH is inert with respect to this process. We discuss our deposition experiments in context of the efficiency of these different electron-induced fragmentation processes. With regards to the deposition dynamics, we observe a substantially faster growth from DCSCH and a higher saturation diameter when growing pillars with high aspect ratio. However, both compounds show similar behaviour with regards to the proximity effect. With regards to the composition of the deposits, we observe that the C/Si ratio is similar for both compounds and in both cases close to the initial molecular stoichiometry. The oxygen content in the DCSCH deposits is about double that of the SCH deposits. Only marginal chlorine is observed in the deposits of from DCSCH. We discuss these observations in context of potential approaches for Si deposition.

Introduction

Focused electron beam induced deposition (FEBID) [1,2] is a 3-D direct writing method suitable for the fabrication of nanostructures, even on non-planar surfaces. This approach is in many ways complementary to current mask-based lithography methods and has high potential in areas where these are not applicable. Focused electron beam induced deposition is based

Beilstein J. Nanotechnol. **2017,** *8,* 2376–2388.

on the exposure of precursor molecules, physisorbed on a substrates surface, to a narrowly focused high-energy electron beam. Ideally these precursor molecules fully decompose under the electron beam and a well-defined deposit is formed from the non-volatile fragments while the volatiles are pumped away. The ideal case would be that the primary electron beam alone is responsible for the decomposition of these molecules through effective impulsive energy transfer. Then, the decomposition of the precursor molecules would be confined within the diameter of the primary electron beam and a spatial resolution better than 1 nm would be achievable on a routine basis.

However, when a high-energy electron beam impinges on a solid substrate, significant inelastic and elastic scattering will take place at the surface and within the substrate along the penetration depth of the beam [3,4]. Furthermore, a significant number of secondary electrons are produced through inelastic ionizing scattering of the primary beam and its scattered electrons [3]. On a flat surface the spatial distribution of these secondary electrons will be defined by the angular distribution of the back-scattered primary electrons [5-7]. During the growth of structures with aspect ratios greater than zero, however, the forward component will also play a role, generating a flux of secondary electrons on the surface of objects with high aspect ratio as these are grown [8,9]. The energy distribution of the secondary electrons produced depends largely on the nature of the substrate [10,11], but also on the primary electron energy. However, it normally has similar features: a maximum well below 10 eV with still a significant contribution close to 0 eV and a high-energy tail extending well above 100 eV [3,5,12]. In this energy range electron induced molecular fragmentation may proceed through four different processes: dissociative electron attachment (DEA; Equation 1), dissociative ionization (DI; Equation 2), neutral dissociation (ND; Equation 3) and dipolar dissociation (DD; Equation 4) [13-20]. The respective reaction schemes for each of these pathways are:

$$\mathrm{AB} + e^- \longrightarrow \mathrm{AB}^{(\ddagger)-} \longrightarrow \mathrm{A}^{(\ddagger)-} + \mathrm{B}^{(\ddagger)}, \quad (1)$$

$$\mathrm{AB} + e^- \longrightarrow \mathrm{AB}^{(\ddagger)+} + 2e^- \longrightarrow \mathrm{A}^{(\ddagger)+} + \mathrm{B}^{(\ddagger)} + 2e^-, \quad (2)$$

$$\mathrm{AB} + e^-(\varepsilon_1) \longrightarrow [\mathrm{AB}]^{*-} + e^-(\varepsilon_2 < \varepsilon_1) \longrightarrow \mathrm{A}^{(\ddagger)} + \mathrm{B}^{(\ddagger)}, \quad (3)$$

$$\mathrm{AB} + e^-(\varepsilon_1) \longrightarrow [\mathrm{AB}]^{*-} + e^-(\varepsilon_2 < \varepsilon_1) \longrightarrow \mathrm{A}^{(\ddagger)+} + \mathrm{B}^{(\ddagger)-}. \quad (4)$$

The double dagger (‡) signifies vibrational or electronic excitation, the asterisk identifies electronically excited species and ε_1 and ε_2 are the energies of the electron before and after the inelastic scattering event, respectively. These reactions have very different energy dependencies, their cross sections also have different dependencies on the respective molecular constellation, and the product formation through these channels is very different.

In recent years significant, concerted effort has been taken to de-convolute the effect of these different processes to better understand the physics and chemistry behind the FEBID process and to purposely turn that knowledge into applicable design criteria for superior FEBID precursors. In this context a considerable number of gas-phase studies have been conducted, mainly on DEA and DI of different organometallic FEBID precursors. Complementary surface science studies have been carried out to better relate the gas-phase observations to the actual conditions in FEBID. A fairly comprehensive account of these studies up to early 2015 is given in [13]. This is however a fast-moving field and a considerable number of studies have appeared recently [21-29], including studies on a mononuclear heteroleptic precursor [21,24-26] and on large heteronuclear carbonyl cluster compounds [22,23,30] that have partly proven to perform well in the FEBID deposition of magnetic alloys [31]. In fact, both DEA and DI cross sections of typical metal-containing FEBID precursors can be very high [32,33]. The same is true for electronic excitation upon electron impact [34]. However, no experimental information is available on actual cross sections for neutral dissociation upon such electronic excitations. This is due to the difficulties associated with the detection of the resulting neutral species and current experiments are thus largely confined to DEA and DI of FEBID precursors. Despite this, significant insight has been provided by the gas-phase and surface-science studies and in individual cases a distinction between the role of DEA and DI in the deposition process has been achieved.

Silacyclohexane (SCH) and dichlorosilacyclohexane (DSCH), shown in Figure 1, are cyclohexane derivatives where one of the carbon atoms is replaced by a silicon atom, and in DCSCH two chlorine atoms are attached to that silicon atom.

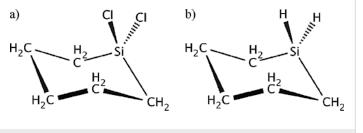

Figure 1: Molecular structure of (a) 1,1-dichloro-1-silacyclohexane (cyclo-$C_5H_{10}SiCl_2$) and (b) silacyclohexane (cyclo-$C_5H_{10}SiH_2$). Adapted from [35].

Beilstein J. Nanotechnol. **2017,** *8,* 2376–2388.

In a fairly recent gas phase study [35], where these molecules were exposed to low-energy electrons under single-collision conditions, it was shown that while appreciable decomposition of DCSCH was affected through DEA, SCH was inert with regards to this process. Dissociative ionisation, on the other hand, leads to similar fragmentation of both these molecules. For reference, Figure 2 shows the ion yield curves for the principal DEA channels observed for DCSCH and Figure 3 compares the DI spectra for DCSCH and SCH at an electron impact energy of 70 eV.

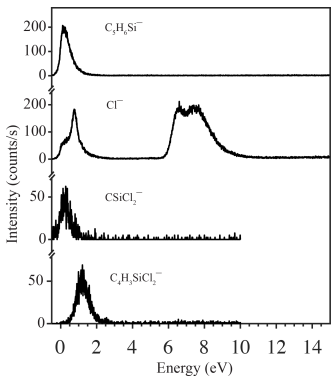

Figure 2: Negative ion yield curve for the principal fragments formed by the electron attachment dissociation of DCSCH in the energy range from 0–14 eV. Adapted from [35].

Motivated by the absolute difference in the sensitivity of these compounds towards fragmentation induced by DEA, we have conducted the first EBID experiments with DCSCH and SCH, and we discuss these in the context of potential effects on the growth dynamics through the very different sensitivity of these molecules towards electrons of very low energy (<10 eV). Furthermore, both molecules are potential precursors for the deposition of SiO_2, especially in conjunction with oxidizing agents such as oxygen or water. Specifically such deposits are of interest due to the broad transparency and the high diffractive index of SiO_2, but may also be of interest in the fabrication of protective or isolating layers/components [2]. Specifically, FEBID deposition of SiO_2 is of interest for the repair of deep ultraviolet (DUV) masks [36], but also for the deposition of transparent nano-optics [37-39].

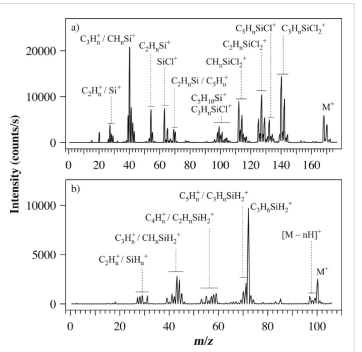

Figure 3: Positive ion mass spectra of (a) DCSCH and (b) SCH, both spectra are recorded at an electron impact energy of 70 eV. Adapted from [35].

Results and Discussion

Deposition from SCH and DCSCH

To our knowledge, the precursor molecules SCH and DCSCH have not been used for EBID so far. Hence, the first experiment that was performed was just to observe whether something can be deposited from each of these precursor molecules. The precursor was introduced via a leak valve into the specimen chamber of a scanning electron microscope (SEM) (see Experimental section for details), raising the pressure from below 9×10^{-7} mbar to (2–3) $\times 10^{-5}$ mbar. Subsequently, an electron beam was focused on a silicon substrate and it was observed whether or not a pillar grows under a stationary electron beam. Both precursor molecules were seen to easily dissociate and to form solid deposits. Figure 4 shows two pillars grown from DCSCH (left) and SCH (right) at the same precursor pressure of ca. 3×10^{-5} mbar and with the same total deposition time of 180 s. The first observation is that the height of both pillars is about the same but the SCH pillar has a smaller base diameter than the DCSCH pillar. Also, both pillars are characterised by a cylindrical lower part and a conical upper part. To study the growth characteristics of both precursors, pillars were grown for a range of deposition times, keeping all other parameters, such as precursor pressure, beam energy and beam current, the same. Figure 5a shows the pillar base diameter as a function of the total beam exposure time for SCH and DCSCH. The diameters were measured from the SEM images, as described in the Experimental section. Pillars deposited with a beam exposure time below 600 ms (SCH) and below 300 ms (DCSCH) could hardly be imaged anymore. Therefore those pillar diameters are not

Beilstein J. Nanotechnol. **2017,** *8,* 2376–2388.

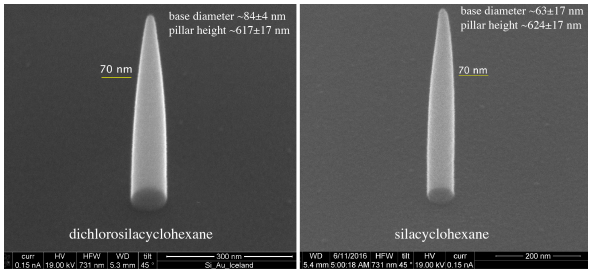

Figure 4: Pillars grown by EBID from the precursors DCSCH (left) and SCH (right). The precursor pressure was 3 × 10^{-5} mbar and the total deposition time was 180 s for both DCSCH and SCH. Electron beam energy of 20 keV and current of 150 pA was used for the deposition. The base diameters and heights are given in the images.

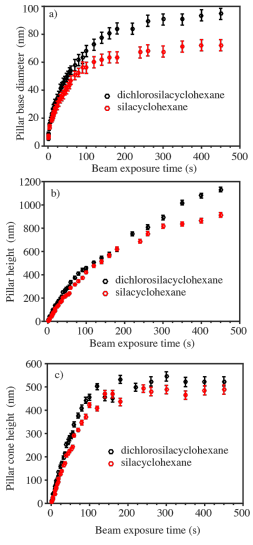

Figure 5: Measured (a) pillar base diameter, (b) pillar height and (c) heights of the cone-shaped upper part of the pillars as a function of electron beam exposure time for two precursors DCSCH and SCH as black and red circles, respectively. The experimental parameters such as precursor pressure, electron beam energy, current were kept constant during the experiment.

included in Figure 5. For both precursors an abrupt increase in pillar base diameter is seen at the initial growth stage, and after about 300 s the pillar base diameter starts saturating. The highest initial lateral growth rate we could measure for DCSCH and SCH was 12 nm/s (measured at 300 ms) and 8 nm/s (measured at 600 ms beam exposure time). After 300 s, the lateral growth rate decreases significantly and saturates at a base diameter of ca. 90 nm and ca. 70 nm, respectively. The diameters of the DCSCH pillars are larger than those of the SCH pillars over the entire range of deposition times. Figure 5b shows how the pillar height develops for increasing deposition time for both precursor molecules. Both curves show a linearly increasing height for small exposure times and a slightly decreasing vertical growth rate at higher exposure times.

The composition of the deposits was determined using energy-dispersive X-ray analysis (EDX) on large and thick deposits. The deposits were grown on a gold sample to be able to distinguish the elements in the deposit from the substrate material.

For the precursor molecule DCSCH, respectively SCH, measurements at four, respectively three, different sites were performed, the results of which were averaged. The ratio of Si/O/C in the SCH deposits was found to be 1.0/1.1/6.0. The ratio of Si/O/C/Cl in the DCSCH deposits was found to be 1.0/2.4/5.8/0.2. In both cases the Si/C ratio is close to that of the precursor molecules (1/5) and the additional carbon content is likely to result from the background gas. No significant chlorine content is observed for DCSCH. However, the oxide content in the deposits formed from DCSCH is significantly larger than that in deposits from SCH. In fact, the Si/O ratio from DCSCH is 1/2.4 indicating a complete oxidation to SiO_2. For SCH this ratio is only 1/1.2 indicating a much more incomplete oxidation. Silicon

chlorides are generally very sensitive towards hydrolysis leading to the formation of silicon oxide and hydrochloric acid. We thus anticipate that the significantly larger oxygen content in the deposits formed from DCSCH is the result of hydrolysis in reactions with residual water in the background gas and at the surfaces.

In EBID pillar growth one can distinguish three stages: the nucleation stage, a fast-growth stage and a saturation stage [4,40]. In the nucleation stage a dot-like deposit will form, predominantly due to the scattered electrons emitted from the substrate surface. In the fast-growth stage, a cone shaped pillar grows with maximum lateral and vertical growth rate. During the fast growth stage, the growth is enhanced by forward- and backscattered electrons (FSEs and BSEs) generated in the growing deposit, as well as by secondary electrons (SE2s) created by FSEs + BSEs [40]. The evolution of the cone morphology depends upon the spatial extent and the location of the primary electron beam interaction volume, and also depends on the material [40]. Eventually, when the interaction volume is limited to the pillar volume the lateral growth saturates. The cone will no longer change shape and the pillar will grow taller in a cylindrical fashion. The cone angles measured from SEM tilt images at the beginning stage of pillar growth for DCSCH and SCH were 71° and 74°. After 80 to 100 s, the angles reduce to a constant value of 13° and 11°, respectively. In Figure 5c the heights of the cone-shaped upper parts of the pillars deposited with SCH and DCSCH are shown for varying exposure times. It is seen that the tip cone height for DCSCH and SCH saturates at about 500 nm. This value is significantly lower than the spatial extent of the interaction volume of bulk Si. Using the equation of Kayana and Okayama [41] a value for the spatial extent of the interaction volume in Si is estimated as 4.7 µm (at 20 keV). However, the size of the interaction volume in a pillar does not necessarily have to be the same as in the bulk, because of the reduced scattering in a pillar. For example, the Monte Carlo simulated mean electron penetration depth for 20 keV electrons in a flat aluminium substrate is 3200 nm [42] while the simulated electron penetration depth for 20 keV electrons in a pillar with a cone angle of 10° is only 240 nm [42]. Similarly, the simulated depth of the interaction volume for 20 keV electrons in bulk SiO_2 is ca. 3 µm [43], while the calculated averaged depth of the interaction volume for 20 keV electrons in a 350 nm pillar is ca. 500 nm [43]. Assuming that the EBID pillars consist of SiO_2 (ignoring the large carbon content found) the interaction volume for an 80 nm SiO_2 pillar might be below 500 nm, in agreement with the tip cone height saturation value of Figure 5c. At exposure times larger than 180 s the lower part of the pillars grows in a cylindrical shape. Since the pillar base diameter (Figure 5a) and the tip cone height (Figure 5c) saturate at about 180 s for DCSCH and SCH, one could define this as the saturation region, where the lateral growth rate diminishes to zero but the pillar height keeps increasing.

From the measured pillar dimensions the pillar volume can now be estimated. Figure 6a shows the pillar volume as a function of the exposure time for SCH and DCSCH, the volume being larger for DCSCH over the entire range. Interestingly, a closer inspection of the volume increases at exposure times below 100 s reveals that the growth is quadratic rather than linear. This becomes better visible looking at the volume growth rate, which is plotted in Figure 6b, showing a significantly larger growth rate for DCSCH than for SCH.

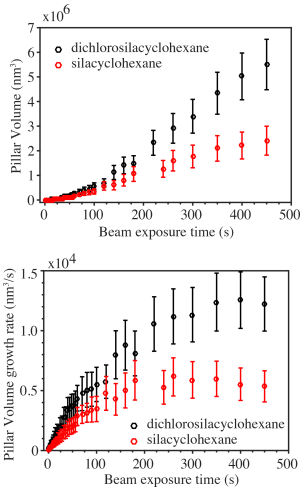

Figure 6: (a) Pillar volume determined from the measured pillar diameter, pillar height, tip cone height and cone angle, versus exposure time for DCSCH and SCH. (b) the pillar volume growth rate versus exposure time for DCSCH and CSH.

A linear increase in pillar height with beam exposure time [43-46] is usually taken as an indication that the deposition is carried out in the electron-limited regime, i.e., there is always sufficient coverage of the surface with precursor molecules. This is also observed for DCSCH and SCH pillars. However, the pillar volume growth is faster, and rather quadratic than linear with exposure time. Were the deposition process in the precursor-limited regime, a slower growth with exposure time

Beilstein J. Nanotechnol. 2017, 8, 2376–2388.

would be expected. As the deposits may be insulating or, at best, be very bad electrical conductors, electron-induced heating of the pillars may occur. This would lower the residence time of precursor molecules, and thereby decrease the growth rate. This is, for instance, observed at larger exposure times in the experiments. Also surface diffusion of the precursor molecules would rather slow down the growth with increasing exposure time than increase the growth.

Charging could play a role in case the deposits are insulating, although it is not straightforward to predict its influence on the volume growth, and no conclusive explanation for the increasing volume growth rate can be offered yet.

Comparing the lateral growth of DCSCH and SCH pillars below 180 s exposure time, the DCSCH pillars were seen to have a larger base diameter than the SCH pillars. The difference in diameter is ca. 1.3 nm in the beginning and gradually increases with beam exposure time to ca. 20 nm at 180 s. From Figure 6b it is seen that the volume growth rate of DCSCH is twice that of SCH, in the early growth stage and the same enhancement in volume growth rate of DCSCH occurs at higher beam exposure times (i.e., DCSCH volume growth rate is about two times that of SCH). As the pillar diameter is determined mainly by the FSEs and BSEs and the SE2s [15], one could expect a smaller growth in pillar width when DEA channels are not available, as is the case for SCH.

From the DEA study of DCSCH (Figure 2 and [35]), one can see that DEA is mainly active below 2 eV, and in the range of 6–9 eV, with the integral cross section being similar for both these energy ranges. This means that the inert behaviour of SCH towards DEA, as compared to DCSCH, only concerns electrons of energies below 2 eV and in the range of 6–9 eV. The effective dissociation yield of DEA in the DCSCH EBID process, however, depends not only on the DEA cross sections, but also on the available number of electrons within the respective energy ranges. From the secondary electron emission spectra of Si irradiated at 1 keV [47], the integrated contribution of emitted electrons with energies below 2 eV and in the energy range from 6 to 9 eV can be estimated to be close to 50% of the total emitted SEs below 20 eV and extrapolation of the secondary electron yield to 100 eV would lower this value to some extent. Since we do not have estimates of the DEA and DI cross sections for DCSCH and SCH, it is difficult to know how much DEA contributes to the deposition compared to DI. In the early pillar-growth stage, the difference in pillar base diameter between DCSCH and SCH is still small. But at later stages the difference increases and grows to a maximum at the saturation point (i.e., at 180 s). At this saturation point, the SE yield will be maximum as shown in [9,40], and the observed diameter difference might be attributed to the electrons below 2 eV and in the range of 6–9 eV if they amount to 30% of all SE events, with the other effects being the same for both compounds.

In summary, DEA would cause additional lateral growth and a higher volume growth rate for DCSCH compared to SCH, but insufficient evidence is obtained to fully ascribe the observed additional lateral growth to this effect only. The electron scattering in deposits from DCSCH and SCH may be different, resulting in different electron yields. Also, the two types of precursor molecules may behave differently when introduced in the specimen chamber, e.g., they may have different sticking coefficients and different surface densities.

In the next section, experiments are presented where deposits are grown in close proximity of each other to further study the role of the low-energy secondary electrons in EBID using DCSCH and SCH as precursors.

Proximity effect comparison between DCSCH and SCH precursors

When growing a pillar close to an earlier deposited pillar, SEs and BSEs + FSEs and SE2s are emitted from the newly deposited pillar, inducing additional deposition on the earlier deposited pillar. This is called a proximity effect and it is believed that, especially for shallow deposits in the early stage of growth, the proximity effect is predominantly caused by the low-energy SEs emitted from the neighbouring deposit. Therefore, the presence or absence of effective DEA channels in the precursor dissociation may be reflected in the extent of the proximity effect. The proximity effect is usually observed as a variation of dot diameters within an array of deposited dots, depending on the order in which they are deposited. Dots were deposited from DCSCH and SCH in two different geometries. In Figure 7a, a schematic is shown for a circular arrangement of dots. The first pillar is deposited in the centre of a circle and the other pillars are deposited surrounding the central pillar. The order in which they are deposited is indicated in Figure 7a as 1 to 9. The expected additional broadening due to the proximity effect is indicated in the schematic by the red filled circles. The red arrows indicate the pillars causing the additional deposition. The number of red circles around the blue dots gives an impression of the expected broadening when proximity effects are present. In the absence of proximity effects, all dots are expected to have almost the same diameter after deposition. In Figure 7b, a different arrangement is shown in which dots are deposited in a square array. The blue filled circles represent the pillars with no additional broadening and the numbers in the blue filled circles indicate the order of pillar deposition. The red and green filled circles represent the expected additional deposition due to the proximity effect and the red and green arrows in-

Beilstein J. Nanotechnol. **2017,** *8,* 2376–2388.

dicate the origin of the effect. For example, pillar 2 can have additional deposition during the deposition of pillar 3 (red arrow), pillar 7 (red arrow), pillar 8 (green arrow) and pillar 6 (green arrow).

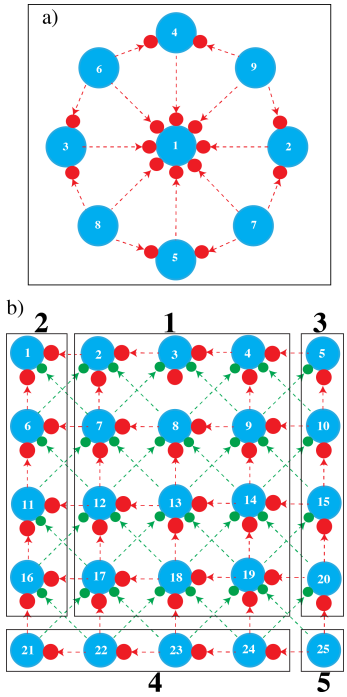

Figure 7: a) Schematic showing the order of pillar deposition in a circular array around a central dot; b) schematic showing the order of pillar deposition in a square array. Blue filled circles represent the diameter of the pillars with no proximity effect, red filled circles represent the lateral broadening induced by the deposition of pillars in close proximity (nearest neighbours) and green filled circles represent the lateral broadening induced by the deposition of pillars that are not as close, but still capable of inducing additional deposition. In the circular configuration these were not indicated and in the square configuration these are the next diagonal neighbours. The bold numbers, shown for the square configuration, represent the areas with the same expected pillar diameters.

From the drawing in Figure 7a, it is seen that in the presence of proximity effects, the largest dot is expected to be dot 1, the second largest dots should be 2–5, and the smallest dots should be 6–9. Similarly, in Figure 7b areas where similar diameters are expected are grouped, indicated by the areas numbered from 1 to 5. The broadening due to the proximity effect should decrease from area 1 to 5. All pillars were grown very close to each other in an area much smaller than the backscattered electron range of Si at 20 keV (4–5 micrometres), such that the backscattered electrons of the substrate have approximately the same effect on all dots.

Figure 8a shows two sets of nine closely spaced pillars deposited with DCSCH in a circular arrangement. Both a top-down SEM image and a 45° tilt image are shown. The beam exposure time and the separation between the central pillar and the surrounding pillars are given in the figure. Figure 8b shows the dots deposited with SCH, all other parameters are exactly the same as for Figure 8a. The diameters of all pillars deposited in the circular arrangement are tabulated in Table 1. It is clearly seen in both figures that a proximity effect is present. As expected, dots 2–5 and dots 6–9 indeed have almost the same diameter, and the order from small to large is as predicted. The dot base plane diameters were measured as described in the Experimental section.

In the case of DCSCH, the first pillar deposited in a circular arrangement, with a beam exposure time of 4 s, has a diameter of 17.9 ± 3 nm, the average diameter of pillars 2 to 5, with the same beam exposure time, is 15.0 ± 1 nm, for pillars 6 to 9 an average diameter of 12.4 ± 1 nm is observed. A similar analysis of the SCH deposits results in a diameter of 18.8 ± 3 nm for the first deposited pillar, the pillars 2–5 have an average diameter of 16.0 ± 1 nm, and pillars 6–9 have an average diameter of 13.8 ± 1 nm. The observed relative broadening of the central pillar with respect to the average diameter of pillars 6–9 is 5.5 ± 1 nm for DCSCH, and 5.0 ± 1 nm for SCH. For an exposure time of 8 s the same analysis results in a relative broadening for DCSCH and SCH of 8.0 ± 1 and 7.7 ± 1 nm, respectively.

The square arrangement of deposited pillars is shown in Figure 9. Two sets of square arrays of pillars are shown, for both DCSCH and SCH. The first set is deposited with a beam exposure time of 2 s and the distance between the pillars is 15 nm. In the second set, pillars were deposited with a beam exposure time of 4 s and the distance between the pillars is 20 nm. The order of deposition is the same as in the schematic shown in Figure 7b. The diameters of all pillars deposited in the square arrangement are tabulated in Table 2 along with the average diameter within each section.

Beilstein J. Nanotechnol. **2017,** *8,* 2376–2388.

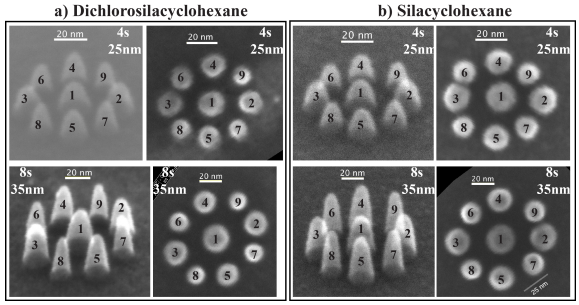

Figure 8: Tilted (45°) and normal view of two sets of nine closely spaced pillars deposited in a circular arrangement; (a) deposited with DCSCH and (b) deposited with SCH. The beam exposure time and the distance between nearby pillars are marked in the corner of each image.

Table 1: Measured pillar base diameter (nm) of DCSCH and SCH pillars deposited in a circular arrangement. The method for measuring the pillar base diameter is described in the Experimental section.

	DCSCH				SCH			
	4 s, 25 nm		8 s, 35 nm		4 s, 25 nm		8 s, 35 nm	
pillar	45° view	normal view	45° view	normal view	45° view	normal view	45° view	normal view
1	19.2 ± 4	16.5 ± 4	24.6 ± 4	22.5 ± 4	19.7 ± 4	17.9 ± 4	26.1 ± 4	24.5 ± 4
2	15.0 ± 4	14.5 ± 4	20.8 ± 4	19.5 ± 4	17.2 ± 4	16.0 ± 4	23.7 ± 4	21.5 ± 4
3	16.3 ± 4	15.2 ± 4	21.0 ± 4	19.5 ± 4	16.0 ± 4	16.1 ± 4	23.7 ± 4	21.2 ± 4
4	14.5 ± 4	14.9 ± 4	18.3 ± 4	18.4 ± 4	15.9 ± 4	15.4 ± 4	22.0 ± 4	20.2 ± 4
5	16.0 ± 4	13.4 ± 4	20.5 ± 4	18.0 ± 4	16.9 ± 4	14.8 ± 4	23.0 ± 4	20.7 ± 4
6	13.2 ± 2	13.0 ± 2	16.0 ± 2	15.4 ± 2	14.4 ± 2	13.4 ± 2	19.7 ± 2	18.2 ± 2
7	13.8 ± 2	11.2 ± 2	17.3 ± 2	15.0 ± 2	14.7 ± 2	13.6 ± 2	18.7 ± 2	17.9 ± 2
8	13.2 ± 2	11.2 ± 2	15.3 ± 2	14.5 ± 2	14.7 ± 2	12.8 ± 2	18.7 ± 2	17.5 ± 2
9	12.2 ± 2	11.0 ± 2	15.4 ± 2	15.0 ± 2	13.9 ± 2	13.2 ± 2	17.7 ± 2	17.5 ± 2

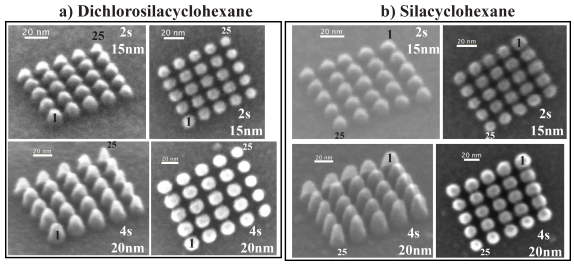

Figure 9: Square arrays of pillars deposited with the indicated beam exposure time and neighbouring pillar distance from (a) DCSCH and (b) SCH. The first (1) and last (25) pillars are indicated and the order of deposition is as shown in Figure 7b.

Beilstein J. Nanotechnol. **2017,** *8,* 2376–2388.

Table 2: Measured pillar base diameter (nm) of DCSCH and SCH pillars deposited in a square array. There are five different areas in the square array within which the pillars are expected to have the same base diameter. The average pillar base diameter is shown at the bottom row of each area. The method for measuring the pillar base diameter is described in the Experimental section.

		DCSCH		SCH	
	pillar	2 s, 15 nm	4 s, 20 nm	2 s, 15 nm	4 s, 20 nm
area 1	2	12.8 ± 4	16.8 ± 4	13.5 ± 4	18.4 ± 4
	3	12.3 ± 4	16.3 ± 4	13.6 ± 4	18.6 ± 4
	4	12.5 ± 4	17.4 ± 4	12.9 ± 4	17.9 ± 4
	7	12.0 ± 4	16.0 ± 4	12.5 ± 4	16.3 ± 4
	8	12.6 ± 4	16.1 ± 4	12.3 ± 4	17.4 ± 4
	9	12.6 ± 4	16.1 ± 4	12.4 ± 4	16.5 ± 4
	12	12.0 ± 4	16.3 ± 4	12.1 ± 4	16.4 ± 4
	13	11.9 ± 4	16.4 ± 4	12.2 ± 4	16.9 ± 4
	14	11.9 ± 4	16.1 ± 4	12.0 ± 4	16.0 ± 4
	17	11.9 ± 4	16.1 ± 4	12.3 ± 4	17.0 ± 4
	18	11.6 ± 4	15.9 ± 4	11.9 ± 4	16.5 ± 4
	19	11.5 ± 4	15.8 ± 4	12.0 ± 4	16.5 ± 4
area 1 average pillar diameter		12.1 ± 1	16.3 ± 1	12.5 ± 1	17.0 ± 1
area 2	1	13.4 ± 4	16.9 ± 4	13.9 ± 4	19.6 ± 4
	6	12.3 ± 4	16.5 ± 4	12.7 ± 4	18.5 ± 4
	11	12.1 ± 4	16.3 ± 4	13.0 ± 4	18.6 ± 4
	16	11.7 ± 4	15.8 ± 4	12.8 ± 4	17.4 ± 4
area 2 average pillar diameter		12.4 ± 2	16.4 ± 2	13.1 ± 2	18.5 ± 2
area 3	5	12.5 ± 2	15.6 ± 2	11.9 ± 2	16.4 ± 2
	10	11.9 ± 2	15.3 ± 2	11.9 ± 2	16.6 ± 2
	15	11.4 ± 2	14.9 ± 2	11.8 ± 2	17.0 ± 2
	20	11.1 ± 2	14.8 ± 2	11.9 ± 2	16.4 ± 2
area 3 average pillar diameter		11.7 ± 1	15.2 ± 1	11.9 ± 1	16.6 ± 1
area 4	21	10.5 ± 2	12.6 ± 2	11.5 ± 2	17.5 ± 2
	22	10.3 ± 2	13.5 ± 2	11.6 ± 2	15.9 ± 2
	23	10.6 ± 2	12.9 ± 2	11.0 ± 2	15.6 ± 2
	24	10.2 ± 2	12.4 ± 2	10.5 ± 2	15.1 ± 2
area 4 average pillar diameter		10.4 ± 1	12.9 ± 1	11.2 ± 1	16.0 ± 1
area 5	25	9.6 ± 2	12.5 ± 2	10.6 ± 2	14.8 ± 2

In Figure 9a, for DCSCH, the proximity effect is clearly visible for pillars deposited with beam exposure times of 2 and 4 s. For a beam exposure time of 2 s, DCSCH pillars deposited in area 1 (Figure 7b) have an average diameter of 12.1 ± 1 nm, the average diameter of pillars deposited in area 2 is 12.4 ± 2 nm. Pillars deposited in area 3 have an average diameter of 11.7 ± 1 nm. In the second smallest area (area 4) the average diameter is 10.4 ± 1 nm, and the last deposited pillar (25 in Figure 7b) has the smallest diameter of 9.6 ± 2 nm. The average pillar base diameters for DCSCH pillars deposited in the various areas 1 to 5, with a beam exposure time of 4 s and a neighbouring pillar distance of 20 nm, are listed in Table 2.

Similar square arrays were fabricated using SCH, as shown in Figure 9b. The upper set of pillars in Figure 9b was deposited with a beam exposure time of 2 s, and the distance between neighbouring pillars is 15 nm. The square array of pillars in the lower panel was deposited with a beam exposure time of 4 s, and the distance between neighbouring pillars is 20 nm. Measured base diameters of all pillars are tabulated in Table 2. The square array pillar deposition of SCH is analysed in the same manner as DCSCH. Based on the schematic shown in Figure 7b, the SCH square array pillar deposition shows five areas of different pillar diameters. The estimated average diameter of pillars deposited in area 1 is 12.5 ± 1 nm, in area 2 the

Beilstein J. Nanotechnol. **2017,** *8,* 2376–2388.

average diameter is 13.1 ± 2 nm. Similarly in areas 3 and 4, the estimated average pillar diameters are 11.9 ± 1 and 11.2 ± 1 nm, respectively. The smallest base diameter pillar (area 5) obtained for SCH with a beam exposure time of 2 s and a neighbouring pillar distance of 15 nm is 10.6 ± 2 nm. The average diameters of the SCH square arrays of pillars deposited with a beam exposure time of 4 s and a neighbouring pillar distance of 20 nm, categorized into areas 1–5, are also included in Table 2. The broadening of the pillars in area 1 with respect to the pillar in area 5 results in a diameter increase of 2.5 ± 0.5 nm for DCSCH at a beam exposure time of 2 s and a neighbouring pillar distance of 15 nm. Similarly for a beam exposure time of 4 s and neighbouring pillar distance of 20 nm the diameter increase is 3.8 ± 0.5 nm. For SCH these numbers are 1.9 ± 0.5 nm and 2.2 ± 0.5 nm, respectively.

It is clear that both DCSCH and SCH show appreciable broadening through the proximity effect. However, considering the errors associated with the calculations of the relative broadening, the difference observed between DCSCH and SCH is not significant. Nonetheless, we find the relative broadening of deposits due to the proximity effect to be consistently more pronounced for DCSCH than for SCH. The difference between these compounds ranges from about 8% to about 40%, calculated as the increase in broadening when proceeding from SCH to DCSCH.

As discussed above, DEA to DCSCH is active for electrons of energies below 2eV and in the range from 6 to 9 eV. In order to contribute to deposit broadening through DEA, these low-energy electrons, generated in the growing pillar, need to reach the neighbouring dots. To obtain a better estimate of the number of low-energy electrons in the relevant energy range, a Monte Carlo simulation of the angular distribution of electrons escaping from a Si half sphere on the top of a Si surface was conducted. The sample for the simulation was a flat Si substrate with a 1 nm diameter Si half sphere on top, resembling a tiny Si deposit on a Si substrate (Figure 10a). The simulator contains the best possible physics models and runs on a GPU [48,49]. A "zero-diameter" 20 keV incident electron beam is directed on top of the half sphere, and subsequently all electrons emitted from the sample are recorded. For each emitted electron the energy, the direction and the location where it was emitted, is stored.

In Figure 10b the angular distribution of the electrons is shown, where the angle theta is the angle between the emitted electron and the incident electron beam. The top curve contains electrons of all energies up to 20 keV. The lower curves contain electrons of energy up to a maximum energy, as indicated in the figure. Integrating the intensity of electrons with energies below 2eV and in the range from 5 to 10 eV shows that the total number of electrons in this energy range is about 50% of the total number of electrons below 20 keV.

Considering the large number of secondary electrons emitted in the energy range relevant for DEA of DCSCH, and under the assumption that the DI cross sections are similar for both compounds, it is rather surprising that the difference between these compounds with respect to their relative broadening through the proximity effect is not more significant. However, as stated earlier, we do not know the absolute DEA or DI cross sections. Furthermore, these deposits are electrical isolators and during dot deposition, SEs and BSEs emitted from the growing dot

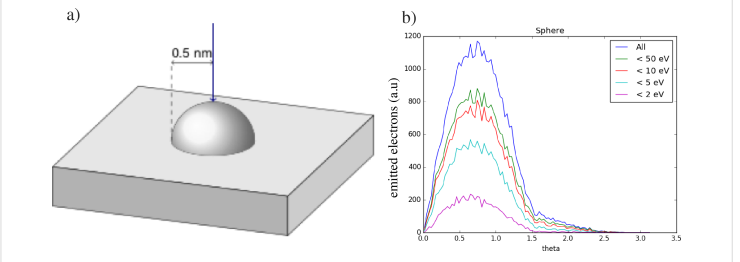

Figure 10: Monte Carlo simulation of the angular distribution of electrons emitted from a flat Si substrate with a 1 nm diameter Si half sphere on top (a), upon exposure with a "zero-diameter" 20 keV electron beam at the location of the top of the half sphere. b) The different curves are for emitted electrons with energy only below the indicated values. Theta is the angle between the emitted electron direction and the direction of the incident beam.

Beilstein J. Nanotechnol. **2017,** *8,* 2376–2388.

may induce negative charges in neighbouring pillars. The trajectories of 2 eV electrons having to reach the neighbouring pillars may in turn be heavily influenced by the charging and may be prevented from reaching the pillar.

Conclusion

Here we have presented the first study on electron beam induced deposition of SCH and DCSCH. We have characterized and compared the growth dynamics of these compounds and the composition of the deposits formed, as well as the extent of the proximity effect under different deposition conditions and geometrical deposition arrangements. We have further discussed the performance of these precursors in the context of their very different sensitivity towards DEA. That is, whereas DCSCH shows appreciable DEA cross sections, SCH is inert in this respect.

Fast initial lateral growth rates are observed for both precursors, but for DCSCH the lateral growth rate is found to be significantly higher than for SCH and the saturation diameter is about 30% larger for DCSCH as compared to SCH (90 nm as compared to 70 nm). Furthermore, in the early growth stage the volume growth rate of DCSCH is twice that of SCH. This meets the expectations that DEA should cause additional lateral growth and a higher volume growth rate. However, due to insufficient data on the absolute cross sections for these processes (DEA and DI) and for ND, as well as potential effects through the different chemical and physical properties of these molecules, we do not consider these results as conclusive in this respect. Potential approaches to achieve clearer differentiation between these two processes would be through targeted design of precursors with higher stability with respect to DI and increased sensitivity with respect to DEA. Such precursors should include predetermined breaking points where the DEA process is exothermic, as the attachment cross section is highest at threshold (close to 0 eV) and preferably the DEA process should lead to destabilization of the remaining moiety after the initial DEA process. In this context, the formation of hydrogen fluoride (bond dissociation energy (BDE) of about 6 eV [50]) has proven to increase molecular fragmentation through DEA considerably [51,52]. Combined with perfluorination of ligands to increase the attachment cross sections at threshold, this could be a viable approach to probe the relevance of DEA by very low energy (0+ eV) SEs produced by the primary electron beam in FEBID.

Composition analyses of the deposits by means of EDX reveal a close to stoichiometric Si/C ratio for both compounds and only a marginal amount of chlorine remains in the deposits formed with DCSCH. However, the Si/O ratio of the DCSCH deposits (2.4) is twice that observed for SCH deposits (1.2), indicating an efficient and complete formation of SiO_2. We attribute this to an efficient hydrolysis of the Si–Cl bonds through residual water in the chamber and at the substrates surface. This is also consistent with the low chlorine content observed in the DCSCH deposits (desorption of HCl). Furthermore, such efficient hydrolysis of DCSCH is likely to reduce its susceptibility towards DEA by offering a competing channel for Si–Cl bond cleavage.

The proximity effect for both compounds is appreciable and although the relative broadening observed is consistently larger for DCSCH than for SCH, this difference is still within the accuracy of our measurements, and we do not consider this observation to give any conclusive information on the role of DEA, beyond that of DI in this process. According to the current Monte Carlo simulations, about 50% of all secondary electrons emitted below 20 keV falls within the energy range where DEA to DCSCH is active. Nonetheless, it is clear from this study that DI is very significant in the deposition of these precursors and the presence or absence of DEA is not a game changer in these cases. This may be due to efficient DI for both molecules blurring the additional effect expected due to the open DEA channels in DCSCH, or simply through a comparable total dissociation cross section of both compounds in the relevant secondary-electron energy range.

Independent of the ambiguity of the current results with respect to the role of DEA and DI, from this study there emerge two approaches worth exploring in the deposition of silicon containing nanostructures. First, the fact that the initial stoichiometric Si/C ratio is maintained in the deposit indicates that the deposition of silicon carbide may be achieved with a similar precursor with a higher Si/C ratio. We have identified the commercially available candidate trisilacyclohexane (TSCH) in which the stoichiometric Si/C ratio is 1:1, i.e., that of silicon carbide. We are currently studying this precursor. The oxygen content observed in the deposits of SCH, however, indicates that the formation of silicon carbide from the potential precursor TSCH might be further promoted through deposition under reductive conditions, e.g., in the presence of hydrogen. Secondly, the observable promotion of SiO_2 formation from DCSCH, through hydrolysis of the Si–Cl bonds is a well-known process and might be purposely taken advantage of in the deposition of structurally intact SiO_2 deposits.

Experimental

The electron beam induced deposition and the inspection of the deposits was done in an FEI NovaNanoLab 650 dual beam scanning electron microscope. The precursor molecules were introduced into the SEM specimen chamber using a custom-built inlet system consisting of a stainless steel container with

the precursor molecules and a leak valve. With the leak valve the pressure of the precursor molecules in the chamber could be precisely controlled.

The precursor dichlorosilacyclohexane (DCSCH, CAS No. 2406-34-0) was purchased from Gelest Inc, Morrisville PA, US. Silacyclohexane (SCH) was synthesized from DCSCH by following our reported procedure with a slight modification [35]. Briefly, a solution of 1,1-dichloro-1-silacyclohexane in diethyl ether was added dropwise to a lithium aluminium hydride solution (1.0 M in diethyl ether) at 0 °C and the mixture was stirred overnight at room temperature. The reaction mixture was then refluxed for three hours and excess $LiAlH_4$ was quenched by treating with acidic solution (H_2SO_4). The organic layer was separated, dried over anhydrous Na_2SO_4 and filtered. The solvent was removed by distillation under reduced pressure to yield the crude product. The crude product was purified via condensation onto a liquid N_2 cooled finger to yield the pure product and the analytical data matched with our previous report.

All deposition experiments were performed at room temperature. The background pressure of the system prior to deposition was (7–9) × 10^{-7} mbar. By leaking precursor molecules into the SEM chamber a precursor pressure was set to ca. 3 × 10^{-5} mbar for both precursor molecules. Both deposition and imaging were performed in ultra-high resolution mode, at a primary beam energy of 20 keV and a probe current of 150 pA. Pillar growth was achieved by spot exposure of the substrate at normal incidence. The primary electron beam exposure time and position was controlled using a stream file generated with the help of MATLAB. In all EBID experiments the working distance was 5.3 mm, close to the eucentric height of the system. The substrate material used for pillar deposition was silicon. All pillars were imaged top-down as well as under a tilt angle of 45°. Before imaging the deposits, the SEM chamber was pumped at least for 90 min after deposition to avoid unwanted further deposition due to remaining precursor molecules. This waiting time was sufficient to lower the background pressure to below 9 × 10^{-7} mbar. Pillar dimensions (height and base diameter) are estimated using the programme imageJ [53]. The base diameter was measured by fitting an ellipse to the base plane in the tilt images. The height was measured from the tilt images as well, and measured from the centre of the base plane to the apex of the deposit. The diameter of very shallow deposits arranged in arrays was measured by fitting circles to the perimeter of the deposits in the top-down SEM images. The pillar cone angle was measured by fitting straight lines to the edge of the cylindrical part of the pillar and the cone-shaped upper part using the imageJ programme [53]. The volumes of the pillars are estimated by approximating the pillar shape as a combination of a cylindrical lower part and a conical upper part of the pillar. From the estimated volume, the volume growth rate can be found by dividing the volume by the corresponding beam exposure time. The elemental composition of the deposited material was determined by energy-dispersive X-ray analysis of large volume deposits on gold substrates, using an Oxford Instruments 80 mm^2 detector. EDX was performed at two different incident energies of 5 keV and 20 keV, at beam currents of 1.6 nA and 240 pA, respectively.

Acknowledgements

CWH likes to thank Luc van Kessel, Kerim Arat and Sebastiaan Lokhorst for their assistance with the Monte Carlo simulations of Figure 10. OI acknowledges supported from the Icelandic Center of Research (RANNIS) Grant No. 13049305(1-3) and the University of Iceland Research Fund. RKTP acknowledges a doctoral grant from the University of Iceland Research Fund and financial support from the COST Action CM1301; CELINA, for short term scientific missions (STSMs)

References

1. Van Dorp, W. F.; Hagen, C. W. *J. Appl. Phys.* **2008,** *104,* 081301. doi:10.1063/1.2977587
2. Utke, I.; Hoffmann, P.; Melngailis, J. *J. Vac. Sci. Technol., B* **2008,** *26,* 1197–1276. doi:10.1116/1.2955728
3. Reimer, L. *Scanning Electron Microscopy;* Springer-Verlag: Berlin, Germany, 1998. doi:10.1007/978-3-540-38967-5
4. Silvis-Cividjian, N.; Hagen, C. W.; Leunissen, L. H. A.; Kruit, P. *Microelectron. Eng.* **2002,** *61–62,* 693–699. doi:10.1016/S0167-9317(02)00515-4
5. Seiler, H. *J. Appl. Phys.* **1983,** *54,* R1–R18. doi:10.1063/1.332840
6. Allen, T. E.; Kunz, R. R.; Mayer, T. M. *J. Vac. Sci. Technol., B* **1988,** *6,* 2057–2060. doi:10.1116/1.584111
7. Everhart, T. E.; Chung, M. S. *J. Appl. Phys.* **1972,** *43,* 3707–3711. doi:10.1063/1.1661794
8. Silvis-Cividjian, N.; Hagen, C. W.; Kruit, P. *J. Appl. Phys.* **2005,** *98,* 084905. doi:10.1063/1.2085307
9. Smith, D. A.; Fowlkes, J. D.; Rack, P. D. *Nanotechnology* **2007,** *18,* 265308. doi:10.1088/0957-4484/18/26/265308
10. Schaefer, J.; Hoelzl, J. *Thin Solid Films* **1972,** *13,* 81–86. doi:10.1016/0040-6090(72)90158-7
11. Knights, A. P.; Coleman, P. G. *Appl. Surf. Sci.* **1995,** *85,* 43–48. doi:10.1016/0169-4332(94)00306-8
12. Ding, Z. J.; Tang, X. D.; Shimizu, R. *J. Appl. Phys.* **2001,** *89,* 718–726. doi:10.1063/1.1331645
13. Thorman, R. M.; Kumar T. P., R.; Fairbrother, D. H.; Ingólfsson, O. *Beilstein J. Nanotechnol.* **2015,** *6,* 1904–1926. doi:10.3762/bjnano.6.194
14. Ingólfsson, O.; Weik, F.; Illenberger, E. *Int. J. Mass Spectrom. Ion Processes* **1996,** *155,* 1–68. doi:10.1016/S0168-1176(96)04392-3
15. Bald, I.; Langer, J.; Tegeder, P.; Ingólfsson, O. *Int. J. Mass Spectrom.* **2008,** *277,* 4–25. doi:10.1016/j.ijms.2008.06.013
16. Böhler, E.; Warneke, J.; Swiderek, P. *Chem. Soc. Rev.* **2013,** *42,* 9219–9231. doi:10.1039/c3cs60180c

17. Christophoru, L. G. *Electron-Molecule Interactions and their Applications;* Academic Press: Orlando, FL, U.S.A., 1984; Vol. 1.
18. Hotop, H.; Ruf, M.-W.; Allan, M.; Fabrikant, I. I. *Adv. At., Mol., Opt. Phys.* **2003,** *49,* 85–216. doi:10.1016/S1049-250X(03)80004-6
19. Arumainayagam, C. R.; Lee, H.-L.; Nelson, R. B.; Haines, D. R.; Gunawardane, R. P. *Surf. Sci. Rep.* **2010,** *65,* 1–44. doi:10.1016/j.surfrep.2009.09.001
20. Fabrikant, I. I.; Eden, S.; Mason, N. J.; Fedor, J. *Adv. At., Mol., Opt. Phys.* **2017,** *66,* 545–657. doi:10.1016/bs.aamop.2017.02.002
21. Thorman, R. M.; Bjornsson, R.; Ingólfsson, O. *Eur. Phys. J. D* **2016,** *70,* 164. doi:10.1140/epjd/e2016-70166-9
22. Kumar T. P., R.; Barth, S.; Bjornsson, R.; Ingólfsson, O. *Eur. Phys. J. D* **2016,** *70,* 163. doi:10.1140/epjd/e2016-70164-y
23. Kumar T. P., R.; Bjornsson, R.; Barth, S.; Ingólfsson, O. *Chem. Sci.* **2017,** *8,* 5949–5952. doi:10.1039/C7SC01927K
24. Thorman, R. M.; Brannaka, J. A.; McElwee-White, L.; Ingólfsson, O. *Phys. Chem. Chem. Phys.* **2017,** *19,* 13264–13271. doi:10.1039/C7CP01696D
25. Spencer, J. A.; Wu, Y.-C.; McElwee-White, L.; Fairbrother, D. H. *J. Am. Chem. Soc.* **2016,** *138,* 9172–9182. doi:10.1021/jacs.6b04156
26. Spencer, J. A.; Brannaka, J. A.; Barclay, M.; McElwee-White, L.; Fairbrother, D. H. *J. Phys. Chem. C* **2015,** *119,* 15349–15359. doi:10.1021/acs.jpcc.5b03775
27. Neustetter, M.; Jabbour Al Maalouf, E.; Limão-Vieira, P.; Denifl, S. *J. Chem. Phys.* **2016,** *145,* 054301. doi:10.1063/1.4959278
28. Neustetter, M.; Silva, F. F.; Denifl, S. *Rapid Commun. Mass Spectrom.* **2016,** *30,* 1139–1144. doi:10.1002/rcm.7542
29. Lengyel, J.; Fedor, J.; Fárník, M. *J. Phys. Chem. C* **2016,** *120,* 17810–17816. doi:10.1021/acs.jpcc.6b05852
30. T P, R. K.; Unlu, I.; Barth, S.; Ingólfsson, O.; Fairbrother, D. H. *J. Phys. C* **2017,** submitted.
31. Porrati, F.; Pohlit, M.; Müller, J.; Barth, S.; Biegger, F.; Gspan, C.; Plank, H.; Huth, M. *Nanotechnology* **2015,** *26,* 475701. doi:10.1088/0957-4484/26/47/475701
32. Engmann, S.; Stano, M.; Papp, P.; Brunger, M. J.; Matejčík, Š.; Ingólfsson, O. *J. Chem. Phys.* **2013,** *138,* 044305. doi:10.1063/1.4776756
33. May, O.; Kubala, D.; Allan, M. *Phys. Chem. Chem. Phys.* **2012,** *14,* 2979–2982. doi:10.1039/C2CP23268E
34. Zlatar, M.; Allan, M.; Fedor, J. *J. Phys. Chem. C* **2016,** *120,* 10667–10674. doi:10.1021/acs.jpcc.6b02660
35. Bjarnason, E. H.; Ómarsson, B.; Jónsdóttir, N. R.; Árnason, I.; Ingólfsson, O. *Int. J. Mass Spectrom.* **2014,** *370,* 39–43. doi:10.1016/j.ijms.2014.06.020
36. Perentes, A.; Hoffmann, P.; Munnik, F. *Proc. SPIE* **2007,** *6533,* 65331Q. doi:10.1117/12.736918
37. Perentes, A.; Bachmann, A.; Leutenegger, M.; Utke, I.; Sandu, C.; Hoffmann, P. *Microelectron. Eng.* **2004,** *73,* 412–416. doi:10.1016/j.mee.2004.02.079
38. Babin, S.; Weber, M.; Koops, H. W. P. *J. Vac. Sci. Technol., B* **1996,** *14,* 4076–4079. doi:10.1116/1.588594
39. Koops, H. W. P.; Hoinkis, O. E.; Honsberg, M. E. W.; Schmidt, R.; Blum, R.; Böttger, G.; Kuligk, A.; Liguda, C.; Eich, M. *Microelectron. Eng.* **2001,** *57–58,* 995–1001. doi:10.1016/S0167-9317(01)00565-2
40. Smith, D. A.; Fowlkes, J. D.; Rack, P. D. *Small* **2008,** *4,* 1382–1389. doi:10.1002/smll.200701133
41. Kanaya, K.; Okayama, S. *J. Phys. D: Appl. Phys.* **1972,** *5,* 43. doi:10.1088/0022-3727/5/1/308
42. Weber, M. *J. Phys. D: Appl. Phys.* **1994,** *27,* 1363. doi:10.1088/0022-3727/27/7/004
43. Choi, Y. R.; Rack, P. D.; Randolph, S. J.; Smith, D. A.; Joy, D. C. *Scanning* **2006,** *28,* 311–318. doi:10.1002/sca.4950280603
44. Hübner, U.; Plontke, R.; Blume, M.; Reinhardt, A.; Koops, H. W. P. *Microelectron. Eng.* **2001,** *57–58,* 953–958. doi:10.1016/S0167-9317(01)00476-2
45. Lau, Y. M.; Chee, P. C.; Thong, J. T. L.; Ng, V. *J. Vac. Sci. Technol., A* **2002,** *20,* 1295–1302. doi:10.1116/1.1481040
46. Silvis-Cividjian, N.; Hagen, C. W.; Kruit, P.; v. d. Stam, M. A. J.; Groen, H. B. *Appl. Phys. Lett.* **2003,** *82,* 3514–3516. doi:10.1063/1.1575506
47. Dapor, M. *Nucl. Instrum. Methods Phys. Res., Sect. B* **2009,** *267,* 3055–3058. doi:10.1016/j.nimb.2009.06.025
48. Verduin, T. Quantum Noise Effects in e-Beam Lithography and Metrology. Ph.D. Thesis, Delft University of Technology, Delft, Netherlands, 2017.
49. Verduin, T.; Lokhorst, S. R.; Hagen, C. W. *Proc. SPIE* **2016,** *9778,* 97780D. doi:10.1117/12.2219160
50. Luo, Y.-R. *Comprehensive handbook of chemical bond energies;* CRC Press: Boca Raton, FL, U.S.A., 2007.
51. Ómarsson, B.; Bjarnason, E. H.; Haughey, S. A.; Field, T. A.; Abramov, A.; Klüpfel, P.; Jónsson, H.; Ingólfsson, O. *Phys. Chem. Chem. Phys.* **2013,** *15,* 4754–4766. doi:10.1039/C3CP44320E
52. Ómarsson, B.; Engmann, S.; Ingólfsson, O. *RSC Adv.* **2014,** *4,* 33222–33235. doi:10.1039/C4RA04451G
53. Schneider, C. A.; Rasband, W. S.; Eliceiri, K. W. *Nat. Methods* **2012,** *9,* 671–675. doi:10.1038/nmeth.2089

Article VI

Gas phase study and focused electron beam induced deposition of 1,3,5-trisilacyclohexane

Ragesh Kumar T P, Sangeetha Hari, Oddur Ingólfsson and Cornelis W. Hagen.
Manuscript in progress, 2017

Ragesh Kumar T P carried out most of the experiments and analysed the data, he wrote the first draft of the paper that shown here

Gas phase study and focused electron beam induced deposition of 1,3,5-trisilacyclohexane (TSCH)

Ragesh Kumar T P[1], Sangeetha Hari[2], Oddur Ingolfsson[1] and Cornelis W. Hagen*[2]

Address:

[1]Department of Chemistry and Science Institute, University of Iceland, Dunhagi 3,

107 Reykjavik, Iceland

[2]Department of ImPhys, Delft University of Technology, Lorentzweg 1, 2628CJ Delft, The Netherlands

Abstract:

1. Introduction

Silicon based FEBID precursor molecules are mostly using for fabricating Si, SiC and SiO_2 nanostructures. Different silicon-based precursor molecules used in FEBID thus far are SiH_4 [1], Si_2H_6 [2], tetraethoxysilane (TEOS, $Si(OCH_2CH_3)_4$) [3], tetramethoxysilane (TMOS, $Si(OCH_3)_4$) [3], tetramethylsilane (TMS, $Si(CH_3)_4$ [3], triphenylsilanol [4].

Although there are reports of silicate deposition in 1960 [5], the first detailed study of silica deposition from triphenylsilanol due to electron induced-dissociation was carried out by Woodman *et al* in 1965 [4]. Silica deposition from electron-induced dissociation of surface-adsorbed tetramethylsilane and deposit characterization was carried out by Faber *et al* in 1969 [6]. An electron beam assisted SiO_2 deposition from silane (SiH_4) was reported in 1983 [7]. The first FEBID of pure SiO_2 in an ultrahigh-vacuum SEM was reported by Nakano *et al* in 1996 [8]. By monitoring the current flowing through the sample, Bret *et al* [9] performed a controlled FEBID of SiO_2 from TEOS. Using room temperature FEBID, Perentese *et al* [3] fabricated contamination-free transparent silicon-based nanostructures from precursor molecules such as TEOS, TMOS and TMS in the presence of a controlled O_2 flow. From this study, they also found that TMS has many advantages over TEOS and TMOS in fabricating denser silicon material. The complications of introducing a silicon precursor and O_2 into a FEBID system through different gas injection needles to fabricate pure SiO_2 was addressed in a recent study of Riazanova *et al* [10] by intermixing a silicon precursor (TEOS) and O_2 in a single gas injection system. Since SiO_2 is an insulating material, deposition of SiO_2 in FEBID may create some issues with regards to accumulation of charges; De Boer *et al* [11] studied the charging effect of depositing SiO_2 material in FEBID using the precursor molecule 2,4,6,8,10-pentamethyl-cyclopenta-siloxane (PMCPS).

Most of the precursor molecules mentioned above behaved quite well in FEBID and were capable of creating contamination-free silicon-based nanostructures; however, there is still a need for new silicon-based FEBID precursor molecules, which may give qualitatively and quantitatively good deposition, which may ultimately be applicable for nanophotonics, nanoplasmonics and many other applications.

The structure of TSCH is shown in Figure 1. TSCH is an intermediate compound between cyclohexane and cyclohexasilane with a Si/C stoichiometric ratio of 1:1 Compared to other commonly used organic silicon precursor molecules like SiH_4, Si_2H_6, TEOS, TMOS, TMS, and triphenylsilanol, the precursor TSCH has a higher Si:C ratio. This might be an advantage of using TSCH as a silicon-based precursor in FEBID. TSCH is a liquid at room temperature and is sufficiently volatile under these conditions to use as a FEBID precursor. There have been two patents filed for fabricating silicon carbide from TSCH using plasma-enhanced CVD and plasma-enhanced ALD [12, 13].

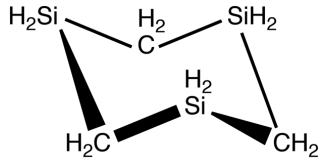

Figure 1: Molecular structure of 1,3,5-trisilacyclohexane.

2. Experimental

2.1 Gas phase experiments

The gas phase experiments of TSCH were performed using a crossed electron/molecule beam instrument under single collision condition. Detailed description of the instrument can be found in ref. [14], thus only a brief description is provided here. The gas phase instrument mainly consists of a collision chamber under high vacuum (order of $1x10^{-8}$ mbar), trochoidal electron monochromator (TEM), effusive gas inlet system and a quadrupole mass spectrometer (HIDEN EPIC 1000). The TEM in the instrument produce an electron beam of well-defined energy with energy resolution of ~120 meV. The energy selected electron collides with TSCH in the collision chamber and produce ions. Both positive and negative ions can be analyzed using the quadrupole mass spectrometer attached to the collision chamber. The TSCH was introduced into the collision chamber through a gas inlet system and a precursor pressure of $1x10^{-6}$ mbar was used for the measurements.

2.2 FEBID experiments

All FEBID experiments were conducted in an FEI NovaNanoLab 650 dual beam scanning electron microscope. Due to the high volatility of TSCH, it was not possible to introduce TSCH using a commercial GIS system, a home-built inlet system was used to introduce TSCH into FEBID system. The precursor flow was controlled using a leak valve attached to the inlet system. The background pressure of the system was $7 – 9x10^{-7}$ mbar, by leaking the precursor molecule the pressure increased to ~$3x10^{-5}$ mbar. The pillar deposition from TSCH was

achieved by keeping the primary electron beam in stationary mode, pillar deposition from TSCH was performed with three different primary electron beams of energy 1 keV (current 30 pA), 5 keV (current 98 pA) and 20 keV (current 150 pA). The position and exposure time of primary electron was controlled using a stream file generated with the help of MATLAB. All the deposited pillars were imaged using the same scanning electron microscope with primary electron beam of energy 20 keV and current 150 pA. In order to avoid any further deposition from remaining residual TSCH gas, 90-minute pump out time was allowed before imaging the pillars. The pillar parameters like pillar base diameter, height, volume are estimated from the SEM image of pillars using image J program [15].

3. Results and discussions

3.1 Gas phase study of TSCH

In the negative ion mass scan of TSCH with different electron energies, we couldn't detect any negative ion species from TSCH. The most efficient mechanism to form a negative ion fragment is DEA, the other relatively inefficient mechanism is DD. Although neutral dissociation of TSCH cannot be measured in our instrument, the absence of negative ion species in the mass scan of TSCH indicates that TSCH is most likely inert to secondary electrons in the energy range of 0 to about 6 eV. This may be an advantage of using TSCH in FEBID, as low energy SEs have been found to cause lateral broadening of deposited structures and co-deposition of impurities.

The positive ion mass spectrum of TSCH recorded at an incident electron energy of 70 eV is shown in Figure 2. Relatively intense fragment observed in the positive ion mass spectrum of TSCH is Si^+ (28), the peak at m/z of 28 shown in the Figure 1 however have contribution (30%) from N_2 (28). The fragments $[SiCH_n]^+$ (m/z = 40 – 44) are also observed with significant contribution. Other fragments identified along with molecular ion $[Si_3C_3H_{12}]^+$ (m/z of 132) are $[SiC_2H_n]^+$/$[Si_2H_n]^+$ (m/z =.55 - 60), $[Si_2CH_n]^+$ (m/z = 69 - 74), $[Si_2C_2H_n]^+$ (m/z = 83 - 88) and $[Si_2C_3H_n]^+$ (m/z = 99 - 103).

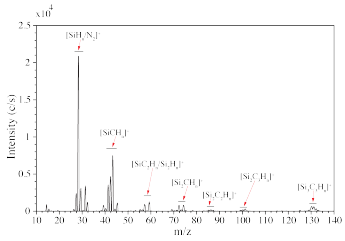

Figure 2: *Positive ion mass spectrum of TSCH recorded with electron impact energy of 70 eV.*

Nanopillar formation from TSCH

Pillars deposited from TSCH using focused electron beams of 1, 5 and 20 keV in FEBID are shown in Figure 3. Each pillar shown in Figure 3 was deposited with a total beam exposure time of 16 s and the pillar deposition was achieved using spot exposure mode. Generally, in FEBID, the pillar deposition can be characterized by pillar base diameter, pillar height and

volume of deposited material. The estimated values for these parameters are shown in Figure 3. As we can see from Figure 3, the diameters of pillars deposited with 1 keV (~53.1 nm) is larger than those deposited with 5 keV (~46.6 nm) and 20 keV (~40.0 nm). The diameter of TSCH pillars deposited with varying beam exposure times for 1, 5 and 20 keV are shown in Figure 3a. Series of pillar depositions are achieved by incrementally increasing the beam exposure time from 300 ms to 300 s.

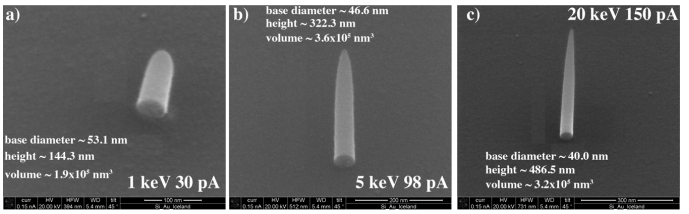

Figure 3: *Nanopillars fabricated from TSCH precursor using focused electron beams of (a) 1 keV, 30 pA, (b) 5 keV, 98 pA and (c) 20 keV, 150 pA. All pillars were deposited with beam exposure time of 16 s.*

There are mainly three regions in typical pillar growth: nucleation stage, fast growth stage and saturation stage. The nucleation stage of TSCH pillar growth can be seen as the starting point of the curve in Figure 3a, i.e. ~300 ms or below. The fast growth stage of TSCH pillars occurs between 300 ms and 24 s and is quite visible in Figure 4a for all 3 beam energies (i.e. 1, 5 and 20 keV). Although there should not be further lateral growth after the fast growth regime has finished, we could clearly see some increase in lateral growth after this point for TSCH as shown in Figure 4a. This lateral growth most likely originates from deposition produced by forward scattered electrons (FSEs). The saturated pillar base diameter for TSCH is higher for 1 keV compared to 5 and 20 keV primary electrons (see Figure 4a). The difference in pillar diameter can be mainly attributed to the different penetration depth of 1, 5 and 20 keV primary electrons. Electrons with an energy of 20 keV can penetrate deeper into a substrate compared to those with energies of 5 and 1 keV, as a result SE yield on the surface will be lesser for 20 keV, which reduces the spatial distribution of SEs for 20 keV. This means that the lateral broadening due to SEs emitted by the impact of 20 keV electrons will be comparatively smaller than by 5 or 1 keV electrons. At 24 s, where the fast growth regime ends, the pillar base diameter for 20 keV is ~ 43 nm, that for 5 keV is 47 nm and for 1 keV is 54 nm. From the pillar base diameter vs beam exposure time plot of TSCH (shown in Figure 4a) we can estimate the lateral growth rate by dividing the pillar base diameter with corresponding beam exposure time. The lateral growth rate of TSCH pillars measured at the nucleation stage (i.e. at ~ 300 ms) for 1 keV is 35 nm/s, that for 5 keV is 33 nm/s and that for 20 keV is 30 nm/s respectively.

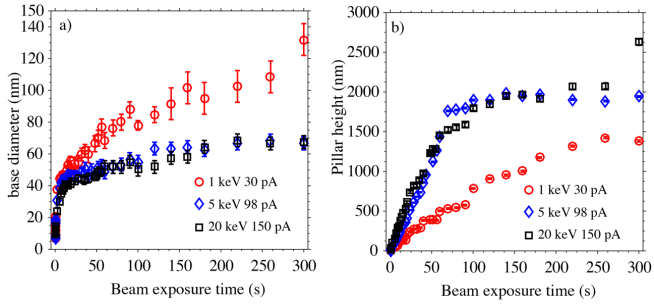

Figure 4: *Evolution of a) base diameter and b) height with respect to electron beam exposure time for TSCH pillars fabricated with 1 keV, 30 pA; 5 keV, 98 pA and 20 keV, 150 pA electron beams. Pillar diameter and heights are measured from the SEM images of the pillars.*

The vertical growth of TSCH pillars is shown in Figure 4b in terms of pillar height and beam exposure time. A linear relationship between pillar height and beam exposure time is observed for 1 keV over the beam exposure time of 300 ms to 260 s, similar behaviour is observed for 5 and 20 keV over the beam exposure time of 300 ms to 90 s. After about 90 s, the pillar height remains almost constant for 5 and 20 keV. The different vertical growth for 5 and 20 keV compared to 1 keV most likely due to the change in regime from the current-limited regime to the precursor-limited regime. In the precursor-limited regime, the number of precursor molecules in the area of deposition will be significantly less and thus a slower growth rate with beam exposure time is expected. During the FEBID process, the supply of precursor molecules is replenished by surface diffusion of adsorbed precursor molecules to the area of the primary electron beam [16]. With the increase in pillar height, the number of precursor molecules diffusing to the top of the pillar is reduced, leading to conversion of the regime to the precursor-limited regime. At 100 s, the height of pillars deposited with 5 and 20 keV is > 1.8 µm; at this height, significantly fewer precursor molecules will be available on the pillar tip. Further, at increased pillar height, the electron dose (i.e. number of primary electrons interacting on the surface) on the pillar tip will be reduced due to defocusing of the primary electron beam. This will also slow down vertical growth. In the case of the TSCH pillars deposited with 1 keV, the electron-molecule interaction regime remains current-limited regime even after 100 s because the pillar height is comparatively smaller. From the measured pillar heights, we can calculate the vertical growth rate by dividing the pillar height with corresponding beam exposure time. the average vertical growth rate calculated over the beam exposure time of 300 ms to 300 s for 1 keV is 10.8 nm/s, that for 5 keV is 19.3 nm/s and that for 20 keV is 25.4 nm/s.

In a typical pillar growth of FEBID, the initial pillar growth will have conical shape, and with continuing electron irradiation a cylindrical section grows under the conical region. Therefore, from the SEM images of pillars deposited with TSCH, we can calculate the deposited volume by assuming the deposited pillar as a combination of conical and cylindrical shapes. Figure 5a shows the volume of TSCH pillars deposited with varying beam exposure times for 1, 5 and 20 keV electron beams. From the measured volume of pillars, we can estimate the volume growth rate by dividing the pillar volume with corresponding beam exposure time. the TSCH volume growth rate for 1, 5 and 20 keV are shown in Figure 5b. the TSCH pillar volume growth rate with change in beam exposure time show similar profile for 5 and 20 keV, in both cases

the volume growth rate increases up to about 80 s and then decreases. The decrease in pillar volume growth rate is most likely due to change in growth regime from current limited regime to precursor limited regime. In the case of 1 keV, volume growth rate increases for the entire beam exposure time (i.e 300 ms to 300 s), which indicates that for 1 keV the pillar growth over the beam exposure time 300 ms to 300 s is in current limited regime.

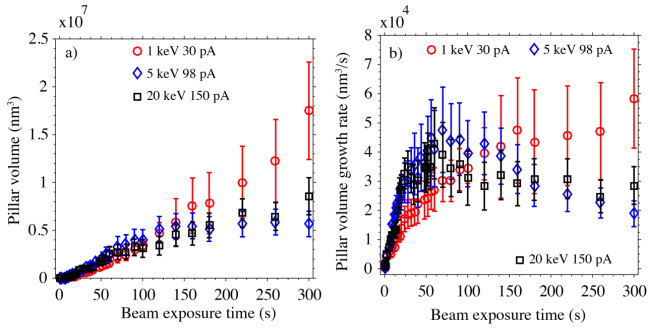

Figure 5: *Change in (a) deposited volume and (b) volume growth rate with respect to beam exposure time for pillars fabricated from TSCH with 1 keV, 30 pA; 5 keV, 98 pA and 20 keV, 150 pA incident electron beams. The deposited volume is measured from the SEM image of the pillars.*

From Figure. 6, one can see that the tip of TSCH pillar deposited with 5 keV have a round bulged shape. However, it is absent for 1 and 20 keV. This bulged shape in the TSCH pillar for 5 keV starts to appear at an electron beam exposure time of ~ 70 s. The volume of the bulged shape then increases with increased electron beam exposure time. The evolution of the bulged structure with increased electron beam exposure is shown in Figure 7. As we can see from Figure 7, in the initial stage the bulged structure has an elliptical shape; however, with increasing electron beam exposure, it becomes more spherical in shape. At 70 s, the calculated volume of the bulged structure is ~ 2.5 x 10^4 nm^3, and at 300 s it has increased to 1.3 x 10^5 nm^3.

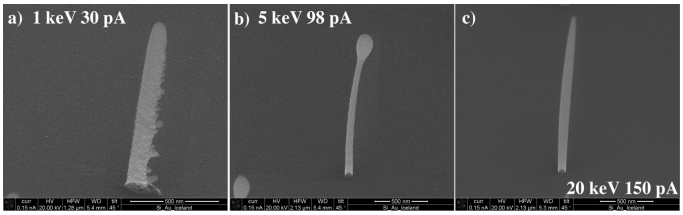

Figure 6: *Pillars deposited from TSCH with a) 1 keV 30 pA, b) 5 keV 98 pA and c) 20 keV 150 pA, only the pillar deposited with 5 keV shows the bulged structure in the tip of pillar. All pillars are deposited with electron beam exposure time of 220 s*

The bulged shape on the TSCH pillar tip may be understood from the electron induced heating at the tip of deposited pillar. When primary electrons (PEs) interact with material, some amount of PE energy can deposit into the material and convert to thermal energy. The dissipation of thermal energy in the material depends upon the material's thermal conductivity. The thermal effect has significant influence in high aspect ratio nanopillars, because the primary electron energy is localized on the tip of pillars. Using the Monte Carlo electron-solid interaction model, Randolph *et al* [17] studied the effect of electron beam-induced heating in FEBID. In the model, they calculated the thermal energy distribution profile of bulk and SiO_2 nanostructures. In the case of pillar geometry, their model suggests that the pillar tip temperature increases sharply with pillar height; therefore, the temperature will be maximized for taller pillars. Their model also suggests that the tip temperature is slightly higher for 5 keV (~5% higher) incident electron beams compared to 20 keV incident electron beams. For a pillar with a height of 2 μm, 5 keV electrons can create electron-induced heating with temperatures in the range of 150 to 200 ^{0}C [17]. At these temperatures, TSCH may thermally decompose and contribute some deposition in addition to electron-induced deposition. This may lead to increased deposition on the pillar tip for taller pillars. It is most likely the reason for the appearance of the bulged structure on the taller TSCH pillars deposited with a 5 keV incident electron beam.

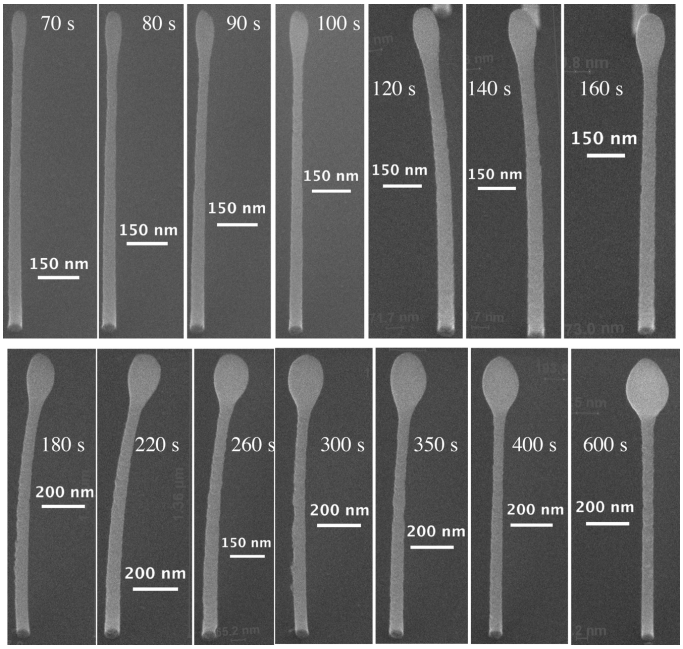

Figure 7: *Pillars deposited from TSCH with a 5 keV, 98 pA primary electron beam. The beam exposure time used for depositing each pillar is shown on the top side of each image.*

Since TSCH is inert to low energy (0 – 6 eV) SEs, we compared the effect of SEs during the deposition of very close pillars for 1, 5 and 20 keV incident electron beams. When a pillar is deposited in close proximity to a previously deposited pillar, the SEs produced during deposition of the new pillar will induce additional deposition on the previously deposited pillar. This effect is called proximity effect (see ref. [18]). Figure 8 compares the proximity effect of depositing very close TSCH pillars (distance between neighbouring pillars are marked in the figure) for 1, 5 and 20 keV incident electron beams. From the measured base diameter of the first and last deposited pillar, we can calculate the relative broadening. The calculated relative broadening for deposition with a 1 keV primary electron beam is ~ 20 nm, that for 5 keV is ~ 10 nm and that for 20 keV is 2 nm.

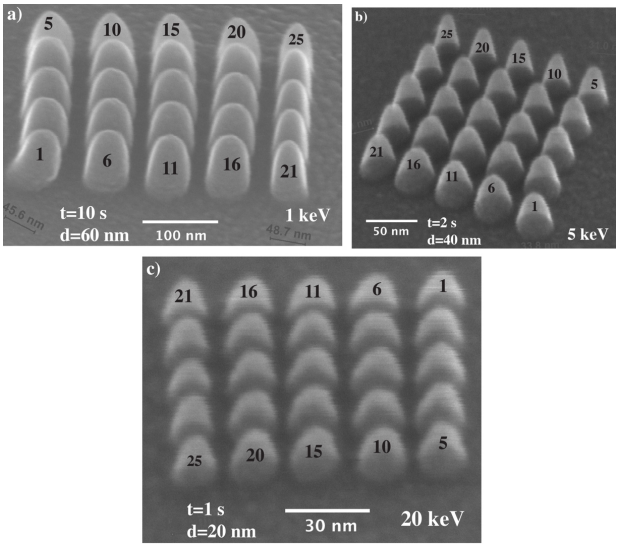

Figure 8: *Array of closely spaced pillars deposited from TSCH with (a) 1 keV, 30 pA; (b) 5 keV, 98 pA and (c) 20 keV, 150 pA incident electron beams. The beam exposure time (t), distance between adjacent pillars (d) and order of depositions (1 – 25) are marked in the image.*

Conclusions

A study of the gas phase electron-induced decomposition and electron beam-induced deposition of the silicon-based precursor molecule TSCH has been discussed here. In the gas phase study of TSCH, no negative ion fragments were detected from the mass spectrum of TSCH.

In the positive ion mass spectrum of TSCH, relatively intense fragments Si^+ (28) and $[SiCH_n]^+$ (m/z = 40 – 44) are observed along with molecular ion $[Si_3C_3H_{12}]^+$ (m/z of 132).

The growth dynamics of TSCH in FEBID were characterized by measuring the base diameter, height and deposited volume of a series of pillars deposited with varying incident electron beam energies and exposure times. Three different primary electron beam energies: 1, 5 and 20 keV, were used to deposit pillars from TSCH, the pillars were subsequently characterized. The observed TSCH pillar diameter (for entire beam exposure time) was higher for 1 keV compared to 5 and 20 keV, this we attributed to different penetration depth and spatial distribution of emitted SEs of 1, 5 and 20 keV primary electron beams. The fast growth regime of TSCH ends at 24 s and the TSCH pillar base diameter estimated at that point is ~ 43 nm for the 20 keV primary electron beam, 47 nm for 5 keV and 54 nm for 1 keV. The initial lateral growth (at 300 ms) of TSCH pillars is higher for 1 keV primary electron beam (35 nm/s) compared to 20 keV (30 nm/s) and 5 keV (33 nm/s). The vertical growth of TSCH pillars shows linear behavior with respect to deposition time for the 1 keV primary electron beam; however, for 5 and 20 keV, the linear behavior is observed only for beam exposure times of < 90 s. Above 90 s, the pillar height remains constant, which we attributed to the change in growth regime from current-limited to precursor-limited. The deposited volume of TSCH pillars was estimated from the SEM image of pillars and subsequently the volume growth rate was estimated.

The TSCH pillars deposited with a 5 keV incident electron beam shows an interesting feature at higher electron beam exposure time (> 70 s). The tips of the TSCH pillars deposited with electron beam exposure time of > 70 s have a bulged shape, however this bulged shape is absent for pillars deposited using 1 and 20 keV primary electron beams. We attributed this to the effect of electron beam-induced heating.

The proximity effect when growing close TSCH pillars was also investigated for 1, 5 and 20 keV primary electron beams. In the proximity effect, the relative broadening is higher for the 1 keV primary electron beam (~20 nm) compared to 20 keV (~2 nm) and 5 keV (~2 nm).

References:

1. T. Sato, M. Mitsui, J. Yamanaka, K. Nakagawa, Y. Aoki, S. Sato and C. Miyata, *Thin solid films*, **2006**, 508, 61-64.
2. F. Bozso and P. Avouris, *Applied physics letters*, **1988**, 53, 1095-1097.
3. A. Perentes and P. Hoffmann, *Chemical Vapor Deposition*, **2007**, 13, 176-184.
4. T. P. Woodman, *British Journal of Applied Physics*, **1965**, 16, 359.
5. K. R. Shoulders, *Stanford Res. Inst. Rept., p. 124*, **1960**,
6. E. S. Faber, R. N. Tauber and B. Broyde, *Journal of Applied Physics*, **1969**, 40, 2958-2964.
7. L. R. Thompson, J. J. Rocca, K. Emery, P. K. Boyer and G. J. Collins, *Applied Physics Letters*, **1983**, 43, 777-779.
8. K. Nakano, T. Horie and H. Sakamoto, *Japanese Journal of Applied Physics*, **1996**, 35, 6570.
9. T. Bret, I. Utke, A. Bachmann and P. Hoffmann, *Applied Physics Letters*, **2003**, 83, 4005-4007.
10. A. V. Riazanova, B. N. Costanzi, A. Aristov, Y. G. M. Rikers, V. Ström, J. J. L. Mulders, A. V. Kabashin, E. D. Dahlberg and L. M. Belova, *Nanotechnology*, **2014**, 25, 155301.
11. S. K. De Boer, W. F. van Dorp and J. T. M. De Hosson, *Journal of Vacuum Science & Technology B, Nanotechnology and Microelectronics: Materials, Processing, Measurement, and Phenomena*, **2011**, 29, 06FD01.

12. T. W. Weidman and T. Schroeder, Methods for deposition of silicon carbide and silicon carbonitride films, 2013
13. R. P. Mandal, Very low dielectric constant plasma-enhanced CVD films, 2003
14. E. H. Bjarnason, B. Ómarsson, N. R. Jónsdóttir, I. Árnason and O. Ingólfsson, *International Journal of Mass Spectrometry*, **2014**, 370, 39-43.
15. C. A. Schneider, W. S. Rasband and K. W. Eliceiri, *Nat Methods*, **2012**, 9, 671-675.
16. L. Reimer and M. Wächter, *Ultramicroscopy*, **1978**, 3, 169-174.
17. S. Randolph, J. Fowlkes and P. Rack, *Journal of applied physics*, **2005**, 97, 124312.
18. R. K. TP, S. Hari, K. K. Damodaran, O. Ingólfsson and C. W. Hagen, *Beilstein Journal of Nanotechnology*, **2017**, 8, 2376-2388.